A Study of Soft X-ray Diffuse Background with Suzaku: from the Geocorona to the Galactic Halo

Tomotaka Yoshino

Department of Physics, Graduate School of Science,
The University of Tokyo

Institute of Space and Astronautical Science,
Japan Aerospace Exploration Agency

December, 2008

Abstract

A major fraction of the soft X-ray diffuse background (SXDB) below ~1 keV is considered to be produced by hot components of the interstellar medium (ISM) at our neighborhood and in or around our Galaxy. However, limited by the insufficient energy resolutions of the previous instruments, the structure of the hot phase ISM has not been understood well, in spite of the long observation history since the early discovery in 1970's. The superior energy resolution and well-understood background of *Suzaku* below 1 keV offer new approaches to investigation of the SXDB. In this thesis, we present the X-ray observations with *Suzaku* for 16 fields which are apart from local Galactic emission structures, such as North Polar Spur and Cygnus supperbubble, together with two additional fields previously analyzed by other authors. After carefully removing the contamination from the Geocoronal solar wind charge exchange (SWCX), the O VII emission intensities of all the observation fields were determined with small systematic errors. The intensities were in the rage of $\sim 2-9$ photons s^{-1} cm^{-2} str^{-1} (LU). The O VIII emission were also detected from most of the fields (from < 0.6 LU upper limit to 4 LU). The O VII line emission shows and intensity floor at $\sim$ 2 LU, and the high latitude O VIII emission shows a tight correlation with excess of O VII emission above the floor. The correlation was well approximated with the relation, (O VIII intensity) $\sim 0.5 \times$((O VII intensity) - 2 LU). This suggests that line-of-sight averaged temperature of the excess component has a narrow distribution around $kT = 0.2$ keV. We consider that the intensity floor of O VII ($\sim$ 2 LU) arises from the Heliospheric SWCX with some small contribution from the local hot bubble (LHB), since the floor intensity is consistent with that of other observational direction in which the mean free path of O VII is shorter than several hundred pc. The excess O VII emission (2-7 LU) is likely to arise from more distant part of our galaxy = transabsorption emission (TAE). In order to consistently explain the observed spectra in 0.4 - 1 keV range, it was found that we need to assume high (2-3 solar) Fe and Ne abundances, or a higher temperature ($kT = 0.6-0.9$ keV) component for four fields. The R45-band counting rates expected form the *Suzaku* best-fit models were statistically consistent with the counting rate of *ROSAT* All Sky Survey map. The upper limit difference was 17×10^{-6}c s^{-1} arcmin^{-2}. This places an upper limit of 2 LU for the difference between the Heliospheric SWCX O VII emissions during solar maximum (*ROSAT*) and solar minimum (*Suzaku*). The constant apparent temperature of the TAE is consistent with the thick hot disk model. However, the hot gas must be very patchy because of the large field-to-field intensity variation. The total bolometric luminosity of the TAE component were estimated to be $\sim 1 \times 10^{39}$ erg s^{-1}, assuming a cylindrical and plane-parallel distribution of the hot gas with a Galactocentric radius of 10 kpc and the vertical scale height of 2.8 kpc, and a temperature of 0.2 keV. This is within the range of luminosities observed in halo of some nearby normal galaxies. The hot gas must be heated or supplied within the radiative cooling time scale of 0.5 G years. The specific temperature, $kT = 0.2$ keV, of the TAE component may be related to the virial temperature of our Galaxy.

Acknowledgment

In the five years for this work, I have been supported by many people and think that I would not complete this thesis without their help.

Firstly I am very grateful for my supervisor Professor K. Mitsuda, who has guided and encouraged me to write this doctor thesis. I feel myself fortunate to be given his valuable advice and knowledge about astrophysics. I have learned a lot of things from his strict attitude for deriving and treating scientific result.

And I would like to thank associate professor N. Yamasaki, who always gave accurate instructions to me, and assistant professor Y. Takei who is one of the most reliable person.

Dr. R. Fujimoto, who is the associate professor, always encouraged me and gave useful advice not only about astrophysics but life as a researcher. Whenever I was depressed, he cheer up me with singing "Youngman", which is a extremely positive song. I would appreciation for his assistance.

Professor Dan Mccammon has great knowledge and experience about interstellarmedium research, I would thank for useful discussion with him.

I also wish to thank S. Ito who is a secretary of our laboratory. I always feel comfortable with her tasty tea and sweet cake.

I thank colleagues and friends at ISAS: T. Oshima, Y. Ezoe, K. Shinozaki, K. Futamoto, K. Yoshida, H. Kawahara, K. Masui, A. Tsuchiya, M. Koshiishi, S. Kimura, T. Hagihara, K. Mukai, H. Yoshitake, I. Mitsuishi. A little discussion and a lot of trivial talk with them is precious memory for my life.

And I am grateful to Mr. Y. Miyakubo, who is the chief of my supplementary private school in my hometown, for giving the motivation for studying mathematics and physics when I was a child. I wanted to show him this thesis while he was alive.

Finally, I would acknowledge my father, mother and sister for their great help. The support of my mind when I seem to fail is always their kindness and tenderness.

Contents

Chapter 1

Introduction

In the diffuse background emission from radio to gamma ray bands, early rockets observations followed by the *SAS-3*, *HEAO-1*, and *ROSAT* all sky surveys (RASS) showed that the whole sky is shining much more brightly in the 0.1 – 1 keV X-ray band than could be explained by the extragalactic background seen at higher energies. It was gradually realized that this is produced by previously unsuspected hot components of the interstellar medium (ISM) at our neighborhood and in or around our Galaxy. Now we recognize the central role of these hot phases of the ISM in feedback control of star formation and the life cycles of the elements. The creation of elements within stars is rather well understood and their ejection into the ISM by supernovae and other stellar processes only somewhat less so, but their transport once they are in the ISM is nearly pure speculation. The first and most important stage of this transport occurs within the hot plasma phases of the ISM, and it is indicative of our current level of understanding of these that serious and well-respected ISM models currently have filling factors for the hot gas ranging from 10% to 90%. This research field was limited by the insufficient energy resolution of the RASS and the very small coverage of high resolution observation by sounding rockets. The superior energy resolution and well-understood background of *Suzaku* below 1 keV offer new approaches to investigate Galactic diffuse emission where we are assisted by a detailed analysis of the emission lines, part of which has been revealed to be charge-exchange process origin.

In this thesis, we will investigate the physical conditions and distribution of the hot ISM in our Galaxy. As the tracer of hot ISM and indicator of the temperature we utilize emission from O ions of two ionization states, O VII and O VIII. O is the fourth most abundant element in the universe following, H, He, and C. O VII and O VIII emissivity have peak at kT = 0.2 keV and kT = 0.3 keV, respectively. Therefore, these emission lines are most important for the study of thermal emission of temperature in the range $kT = 0.1 - 0.4$ keV. The X-ray CCD camera on board *Suzaku* , the XIS, has a much better energy spread function and much lower background below 1 keV than the X-ray CCD cameras on-board *Chandra* and *XMM-Newton* . The back illuminated CCD (XIS1), in particular, has a high efficiency in the energy range 0.4 to 1 keV. Both O VII and O VIII emission consist of plural lines of fine structure. Although X-ray CCD cannot resolve the fine structures of lines, it can separate emission from different elements and different ionization states.

Solar-wind charge exchange (SWCX) produces emission lines from EUV to soft X-ray, and is recognized as one of the important ingredients in the EUV to soft X-ray diffuse background. As we will show in Chapter 2, the SWCX induced X-ray emission originates from two distinct regions. We will try to remove one of the two emission components, Geocoronal SWCX induced emission, as much as possible, utilizing the time variations correlated with the solar wind flux and the relation between the *Suzaku* 's sight line and the geomagnetic field which reflects the interaction between the interplanetary and Earth's magnetic fields.

This thesis consists of the following structure. Past observation of soft X-ray diffuse background are reviewed in Chapter 2. Chapter 3 describe the instrumentation. In Chapter 4 and 5, we respectively explain the data reduction as well as the observed fields and present the results of spectral analysis. The discussion and conclusion are given in Chapter 6 and 7.

In this thesis, errors are quoted at 90% confidence level in the text and tables, while they are at 68% (1σ) confidence level in the figures, unless otherwise described.

Chapter 2

Review

2.1 Properties of Interstellar Medium

In this section, we will briefly review the ingredients of interstellar medium. We owe most of the contents in this section to the review paper by Ferrière (2001). All physical parameters were rescaled for the galactocentiric distance of the sun $R_{\odot} = 8.5$ kpc by Ferrière (2001).

2.1.1 Overview

About $10 - 15$ % of the total mass of the Galactic disk is occupied by interstellarmatter, which mainly exist in the Galactic plane, in particular, along the spiral arms. Interstellar clouds, which has about half of interstellarmass and occupy $\sim 1 - 2$ % of its volume, can be divided into three types: the dark clouds, which consist of very cold molecular gas (T ∼10-20 K), the diffuse clouds which are made of cold atomic gas (T ∼100 K) and the translucent clouds, which contains both of molecular and atomic clouds. Between these clouds the rest of interstellarmatter exists in three different forms: warm atomic($T \sim 6000 - 10^4$ K) , warm ionized (T ∼8000 K) and hot ionized ($T \sim 10^6$ K). The parameters of these interstellarmatter is tabulated in Table 2.1. In the vicinity of Sun, the density of interstellarmatter varies from $\sim 1.5 \times 10^{-26}$ gcm^{-3} in the hot ionized to $\sim 2 \times 10^{-20} - 2 \times 10^{-18}$ gcm^{-3} in the molecular regions. The space-averaged number density is about one hydrogen atom per cubic centimeter. The chemical composition of interstellarmatter is considered to be close to that inferred from the abundance measurements in the Sun, in other disk stars, and in meteorites, which consists of 90.8 % by number (70.4 % by mass) of hydrogen, 9.1 % (28.1 %) of helium, and 0.12 % (1.5 %) of heavier elements. However, a significant fraction of the heavy elements are shown to be depleted by the observation of absorption line. About 0.5-1 % of the interstellarmatter by mass is considered to be in the form of dust rather than gas.

We summarize the different forms of interstellarmedium in the following sections.

2.1.2 Molecular gas

H_2 molecules do not emit detectable electromagnetic signals except in extraordinary conditions such as shocks, because they are symmetric and therefore have no electric dipole moment. Instead, the rotational transition line of CO molecule , which is a J=1→ 0 at a

Table 2.1: Descriptive parameters of the different components of the interstellar gas.T is the temperature, n is the true (as opposed to space-averaged) number density of hydrogen nuclei near the Sun, $\Sigma_\odot$ is the azimuthally-averaged mass density per unit area at the solar circle, $\mathcal{M}$ is the mass contained in the entire Milky Way and ξ is the volume filling factor. Both $\Sigma_\odot$ and $\mathcal{M}$ include 70.4 % of hydrogen, 28.1 % of helium, and 1.5 % of heavier elements. All values were rescaled to $R_\odot = 8.5$ kpc. Table is extracted from Ferrière (2001) and Cox (2005).

Component	T (K)	n (cm^{-3})	$\Sigma_\odot$ ($M_\odot$ pc^{-2})	$\mathcal{M}$ (10^9 $M_\odot$)	ξ	$<n>$ (cm^{-3})
Molecular	$10-20$	10^2-10^6	~ 2.5	~ 1.3 - 2.5	$\sim 10^{-4}$	~ 0.58
Cold atomic	$50-100$	$20-50$	~ 3.5	} $\gtrsim 6.0$	0.013	~ 0.40
Warm atomic	$6000-10^4$	$0.2-0.5$	~ 3.5		0.368[a]	~ 0.17
Warm ionized	~ 8000	$0.2-0.5$	~ 1.4	$\gtrsim 1.6$	0.083	~ 0.04
Hot ionized	$\sim 10^6$	~ 0.0065			$\sim$0.46	~ 0.003

[a] The sum of 0.194 for about 5000 K component and 0.174 for 8000 K.

radio wave length of 2.6 mm, is used as the main tracer of molecular interstellargas. The horizontal distribution map of molecular cloud is dominated by the molecular ring peaking at a Galactic radius R $\sim$ 4.5 kpc and by two discrete features closely associated with 21-cm spiral arms (Clemens et al., 1988). And the density of H_2 in interarm regions is a factor of $\sim$ 3.6 lower than in arms. In the outer Galaxy ($R > R_\odot$), the molecular surface density in spiral arms is 13 times larger than that in interarm region, which indicate that the bulk of the molecular gas belongs to the spiral arms. And beyond the solar circle, the H_2 column density averaged over azimuthal angle drops off rapidly.

For the vertical direction, most of the moleculer cloud exists in low galactic latitude, i.e., along the Galactic plane, and the space averaged distribution of it can be expressed by a Gaussian function. At $R_\odot$, the space-averaged number density of hydrogen nuclei in molecular form is expressed as

$$\langle n_m\rangle(Z) \;=\; \langle n_m\rangle(0)\;\exp\left[-\left(\frac{Z}{H_m}\right)^2\right] \;, \tag{2.1}$$

with $\langle n_m\rangle(0) = 0.58$ cm^{-3} and $H_m = 81$ pc by Clemens et al. (1988). They modeled with the observational fact that the FWHM of the moleculer layer , averaged over azimuthal angle in $0° < l < 90°$, becomes larger with increasing radius as $R^{0.58}$ and has a value of 136$\pm$17 pc, which is consistent with a decreasing stellar mass surface density. On the other hand, Bronfman et al. (1988) construct the axisymmetric model, using the Galactic data in $-90° < l < 90°$, which is independent of R and has a FWHM value of 120$\pm$18 pc and expressed as equation 2.1 with $\langle n_m\rangle(0) = 0.53$ cm^{-3} and $H_m = 71$ pc.

Molecular clouds are divided into two classes by mass: Giant complex with $\sim 10^5 - 10^6$ $M_\odot$ and hydrogen number density $\sim$ 100-1000 cm^{-3}, and small dense cores $0.3-10^3$ $M_\odot$ and hydrogen number density $\sim 10^4 - 10^6$ cm^{-3}. The moleculer clouds are bound by self-gravity, therefore satisfy the virial balance, i.e., $G\ M/R \sim \sigma^2$ where M, R and σ are the mass, radius and velocity dispersion of moleculer cloud, and G is gravitational constant.

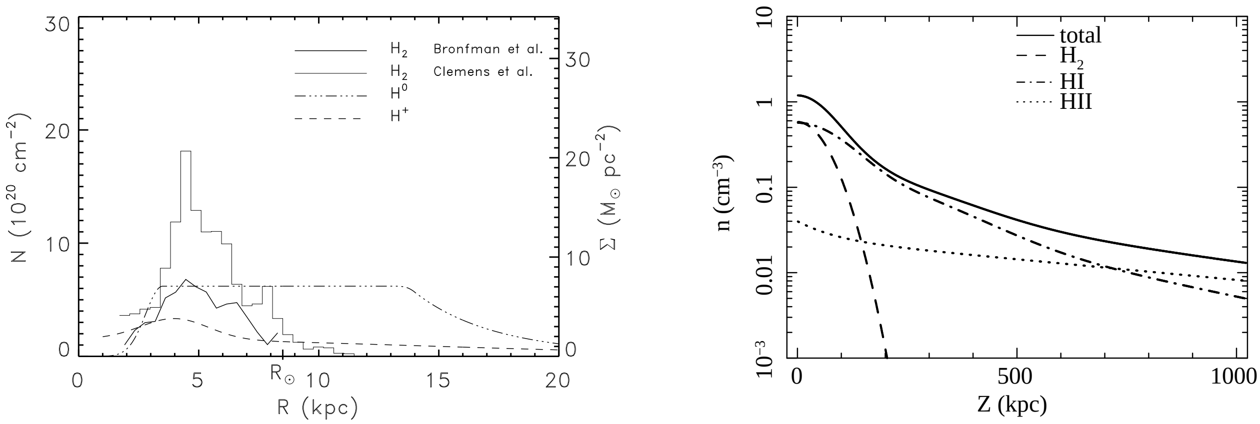

Figure 2.1: Left: Column density of interstellarhydrogen through the Galactic disk and surface mass density averaged over the Galactocentric azimuthal angle, as a function of Galactic radius R for the different gas components. Solid line, triple-dot-dashed line and dashed line is contribution from molecular gas, cold+warm atomic gas and ionized gas, respectively. Figure is taken from Ferrière (2001): Right: Space averaged hydrogen number density as a function of z from the Galactic plane at the solar circle for the different state of interstellargas: dashed line is contribution from molecular gas, dot-dashed line is contribution from cold and warm atomic gas, dotted line is contribution from warm ionized gas and solid line is total of them.

The temperature of moleculer cloud measured by the intensity of CO emission line is $10 - 20$ K. The thermal velocity calculated from it is smaller than observed velocity dispersion, therefore the turbulent motions is dominant in the pressure of moleculer cloud. This temperature can be explained by the thermal balance between heating by cosmic rays and cooling by moleculer line emission.

2.1.3 Cold and Warm atomic gas

One of the method of detecting the neutral atomic hydrogen is using Lyα transition in the UV band. The number of Lyα absorption line study revealed that H I is deficient in the vicinity of the Sun. The cavity of H I is known as Local Hot Bubble (LHB) which is filled by rarefied hot gas at $\sim 10^6$ K and spreads to a few hundred pc scale around the Sun. The H I cavity has a radius in the plane $\sim 60 - 100$ pc and a vertical extent from plane $\sim 120 - 180$. Although Lyα is a useful tool for detecting neutral atomic hydrogen , it is not suited to map the H I in galactic scale due to the absorption by interstellarmedium. The other detecting method is tracing the 21 cm hyper-fine-structure transition line of hydrogen atoms in radio band, which has the advantage of penetrating into the deep ISM and therefore can study the outside of our galaxy.

In the radial direction, H I gas extends to more than 30 kpc from the Galactic center, and the azimuthly averaged column density of it is characterized by a depression inside 3.5 kpc, a relatively flat through the solar circle, and out to $\sim$ 14 kpc and exponential fall off beyond 14 kpc(Diplas & Savage, 1991). However, the exponential fall off has an uncertainty due to the poorly confidence of the shape of the rotation curve outside the solar circle.

In the vertical direction, the H I distribution is roughly uniform for 3.5 kpc $< R < R_\odot$ (Lockman, 1984). In this radial interval, the H I gas lies in a flat layer with a FWHM of 230 pc (almost twice the FWHM of the molecular gas at $R_\odot$), and its space-averaged number density can be approximated by the sum of two Gaussians and an exponential tail:

$$\begin{aligned}\langle n_n\rangle(Z) &= (0.57\ \mathrm{cm}^{-3})\left\{0.70\ \exp\left[-\left(\frac{Z}{127\ \mathrm{pc}}\right)^2\right]\right.\\ &\left.+0.19\ \exp\left[-\left(\frac{Z}{318\ \mathrm{pc}}\right)^2\right]+0.11\ \exp\left(-\frac{|Z|}{403\ \mathrm{pc}}\right)\right\} \qquad (2.2)\end{aligned}$$

(Dickey & Lockman, 1990). The thickness of the H I layer drops to $\lesssim 100$ pc inside 3.5 kpc (Dickey & Lockman, 1990), and it grows more than linearly with R outside $R_\odot$, reaching ~ 3 kpc at the outer Galactic boundary (Diplas & Savage, 1991). Structure so-called warp, which can be expected from the decrease of the vertical gravitation, is that the midplane of the H I layer lies above the Galactic equatorial plane in $0° < l < 180°$, with a maximum displacement of ~ 4 kpc, and below the Galactic plane in $180° < l < 360°$ with a maximum displacement of ~ -1.5 kpc

The emission and absorption spectra in the nearby direction is different: while the emission contains both the narrow peaks and broader feature, the absorption has only narrow peaks. The interpretation of the difference is that the narrow peaks is produced by discrete cold H I clouds (50 - 100 K), and broad structure is due to warm H I gas ($\sim 6000 - 10^4$ K) that is widespread and does not show the detectable 21-cm absorption line. In the solar neighborhood, the column density of cold and warm H I is shown to be almost same by the comparison of absorption and emission line study. Outside the solar circle, H I is expected to be mainly dominated by warm gas, as suggested by the 21-cm emission line distribution of face-on extra galaxy. From that hydrogen density in cold H I is estimated to be $\sim 20 - 50\mathrm{cm}^{-3}$, which is two orders larger than that of warm phase, cold and warm phase of interstellarmedium is roughly in the thermal pressure equilibrium. These two states of H I are generated by the process that once the atomic interstellargas is heated by the low energy cosmic rays and cooled by the deexcitation of collisionally excited line of heavy elements for a cold phase, and by Lα cooling at about 8000 K for warm phase, respectively(Field et al., 1969).

2.1.4 Warm ionized gas

Around the massive stars such as O and B star, the H II region where hydrogen are fully ionized by UV photon from the star is expanded to Strömgren radius described by the number of ionizing photon from central star and the density of hydrogen and electron. The equilibrium temperature of H II region is $\simeq 8000$ K by the balance of photoelectric heating and radiative cooling.

In H II region, the main radiative processes are radio continuum emission of bremsstrahlung as the reaction of free electrons with Coulomb field by positive ions, and line emission in radio, infrared and optical band due to the recombination of free electrons and hydrogen and helium ions or to the deexcitation of collisionally excited ions. For the observation of warm ionized medium, Hα transition line is most important which is the Balmer line from the excited state n = 3.

Near the Sun, the space-averaged density of free electrons can be approximated by

$$\langle n_e\rangle(Z) = (0.015\ \mathrm{cm}^{-3})\ \exp\left(-\frac{|Z|}{70\ \mathrm{pc}}\right) + (0.025\ \mathrm{cm}^{-3})\ \exp\left(-\frac{|Z|}{900\ \mathrm{pc}}\right) \qquad (2.3)$$

(Reynolds, 1991), where the contribution from H II regions (first term) is taken from Manchester and Taylor (1981), while the diffuse component (second term) relies on the midplane density deduced from a limited sample of low-latitude pulsars by Weisberg et al.(1980) and on the column densities toward newly-discovered pulsars inside high-$|Z|$ globular clusters. As Reynolds (1991) himself admitted, the exponential scale height of the extended component in Eq. 2.3 may have been underestimated by up to a factor of 2, due to a probable deficiency inside the Local Bubble in which the Sun is located.

2.1.5 Hot ionized gas

As shown in Table 2.1, about half of interstellar space is now believed to be occupied by hot interstellar of $T \sim 10^6$ K in volume. Existence of this hot component of interstellarmedium was first recognized by the rocket observations in 1970's to observe the soft X-ray diffuse background (see Tanaka & Bleeker (1977), McCammon & Sanders (1990) for review).

In the following sections of this chapter, we will review the present understandings of the soft X-ray diffuse background and the hot interstellar medium.

2.2 Soft X-ray Diffuse Background

In this thesis we use the word, the soft X-ray diffuse background (SXDB), to mean the emission below ~ 1 keV which is spatially unresolved to individual sources. Above 2 keV, unresolved X-ray emission is called the cosmic X-ray background (CXB). We now believe that the most of the CXB comes from numerous faint extragalactic sources; active galactic nuclei. With the deep observations of the *Chandra* and *XMM-Newton* observatories, about 80 % of the CXB has been actually resolved into point sources.

A certain fraction of the SXDB also comes from extragalactic faint sources which is just an extension of the CXB to the lower energy range. However, the SXDB cannot be explained just by the extension and the remaining emission is considered to consist of emission from highly ionized ions, such as C V, O VII, O VIII, Fe XVII, and Ne IX, in solar neighborhoods, in our Galaxy, and possibly in the intergalactic space.

2.2.1 Brief History: Early observations to spectroscopy with a microcalorimeter

Existence of excess above the extension of the CXB was first noted by sounding rockets experiments in 1970s. The observations were conducted by using proportional counters with thin entrance windows and slats collimators. From these early observations, it was noted that the intensity in the carbon band (C band), the energy band below the C K edge (284 eV) is anticorrelated with Galacitc neutral hydrogen column density of the direction. Since the X-rays in the C band are not transparent to the Galactic neutral medium, the anticorrelation cannot be explained by the absorption of emission outside the bulk of Galactic neutral medium. It was interpreted as an displacement of neutral matter by hot plasma; the solar system is surrounded by a hot plasma of $T \sim 10^6$ K, and in the directions in which the hot plasma is more extended, the column density of the neutral matter is smaller (Tanaka & Bleeker, 1977). The cavity was called the Local Hot Bubble (LHB, see Section 2.1.3).

All sky maps of the SXDB have been made by several experiments: a University of Wisconsin sounding-rocket survey (7° angular resolution, McCammon et al. (1983)), SAS-3 survey (4.5 °, Marshall & Clark (1984)), HEAO 1 map (3 °, Garmire et al. (1992)). The most important map nowadays is the map by the *ROSAT* all sky survey (*RASS* , Snowden et al. (1994, 1997)).

The *RASS* carried out in 1990 to 1991 by the *ROSAT* improved the angular resolution of the SXDB to $\sim 12'$ by using an X-ray focusing mirror and a position sensitive detector. Because of the high spatial resolution of the system ($\sim 1'$) point sources up to 4×10^{-13}erg s^{-1} cm^{2} in 0.47-1.21 keV band had been removed from the map.

The *ROSAT* all-sky survey (*RASS*) is designed to map the sky with high sensitivity for the detection of discrete sources as well as diffuse background in the 0.1-2.4 keV band. This survey was executed from July 1990 to Jan 1991 with the Position Sensitive Proportional Counter of the X-ray telescope. In *RASS*, the space craft spun about an axis perpendicular to the line of site once per orbital. The great circle on the sky which includes the ecliptic poles was observed in each orbit because the satellite's spin axis which is normal to the solar panel lay in the ecliptic plane, within $\leq 15°$ from the Sun-earth line. Figure 2.2 shows the soft X-ray diffuse background maps by *RASS* in the 1/4 keV band (also known as the R12 band, approximately equal to the C band) and 3/4 keV band (the R45 band and approximately equal to M band), which are approximately 0.12–0.284 keV and 0.47–1.21 keV, respectively (Energy response of *ROSAT* PSPC is shown in Figure 2.3), where the contribution of X-ray point sources, long-term-enhancement (LTEs) by geocoronal solar wind charge exchange (see Section 2.2.5.2), solar scattered X-ray and particle background are excluded as far as possible.

The SXDB was clearly resolved into line emissions with the sounding rocket experiment conducted by the Wisconsin and NASA/GSFC group (McCammon et al., 2002). The rocket carried an X-ray microcalorimeter array operated at the cryogenic temperature of 60 mK. The field of view the detector was confined by a collimator to the sky area of ~ 1 str shown in Figure 2.2. By virtue of high energy resolution, the X-ray spectrum was resolved into number of emission lines (Figure 2.4). Comparing the line intensities and the previous SXDB and CXB observations, McCammon et al. (2002) estimated that about 40 % of the emission in the *ROSAT* R45 band are the extragalactic continuum emission, i.e. the CXB.

2.2.2 Emission lines from hot gas

As shown in the bottom panel of Figure 2.4, there are many complex lines such as L-branch in the energy range below the C K edge at 284 eV. On the other hands, in the energy range between 0.3 - 1 keV, there are Kα lines such as C VI, O VII, O VIII and Ne IX. Hot ionized gas of a temperature of about 10^6 K can be characterized by these lines. Figure 2.5 shows ionization fraction and emissivity of these representative lines for a gas in collisional ionization equilibrium state adopting the solar abundance by Anders & Grevesse (1989), which are calculated by using publicly available routine SPEX. As shown in Figure 2.6, the intensity ratio of O VIII and O VII are sensitive to the temperature in the range from 10^6 K to 10^7 K. As the oxygen is abundant elements, spectroscopic study of oxygen lines is the powerful tool to reveal the nature of these hot plasma.

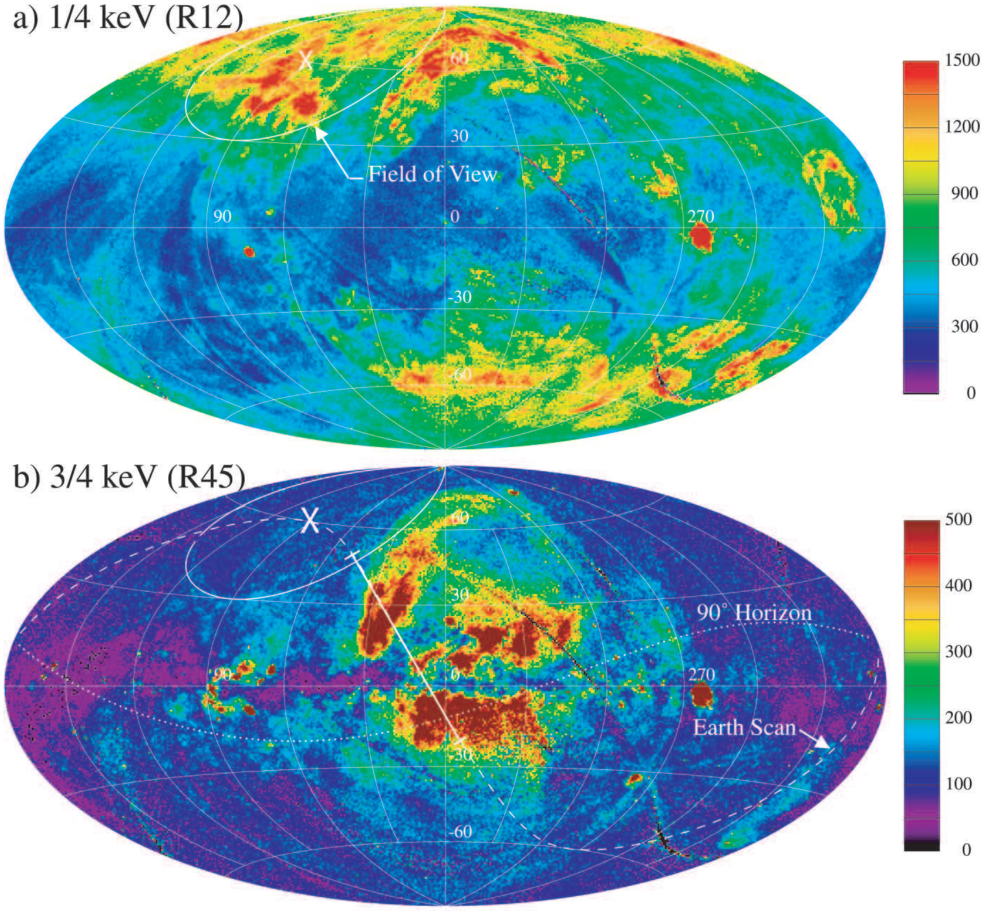

Figure 2.2: *ROSAT* maps of the (a) R12 (1/4 keV) band and (b) R45 (3/4 keV) band diffuse background in Galactic coordinates by *ROSAT* intensity units are 10^{-6} counts s^{-1} arcmin^{-2}. The field of view of their microcalorimeter sounding rocket experiment is also shown. Figures are taken from McCammon et al. (2002).

2.2.3 Galactic absorption and the C K edge

The energy band of *ROSAT* is shown in Figure 2.3. There is a clear energy gap between R12 and R45 bands. This is due to C K edge in the entrance window of the position sensitive proportional counter. Since C is the third abundant element in interstellar space, C K edge affects the absorption length of X-ray photons traveling in the interstellar medium.

In the left panel of Figure 2.7, we show the column density of neutral medium at which the optical depth for photo absorption becomes unity as a function the X-ray energy. In the right panel of the figure, we show the line of sight length where the optical depth for absorption becomes unity for several typical X-ray energies as a function of galactic latitude. We assumed the average neutral matter distribution described in Section 2.1.2 and 2.1.3, and calculated for the galactic longitude of $\lesssim |90°|$. From this we can see that the Galaxy is not transparent for X-ray photons in the R12 band even in high latitude, while in R45 band, in particular above O VII emission, the Galaxy is transparent in high latitude ($b >\sim 20°$). Only in selected directions where the Galactic absorption is extremely low, e.g. the Lockman hole

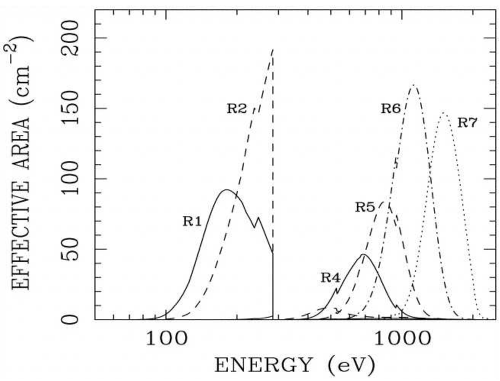

Figure 2.3: Energy response curve of *ROSAT* .

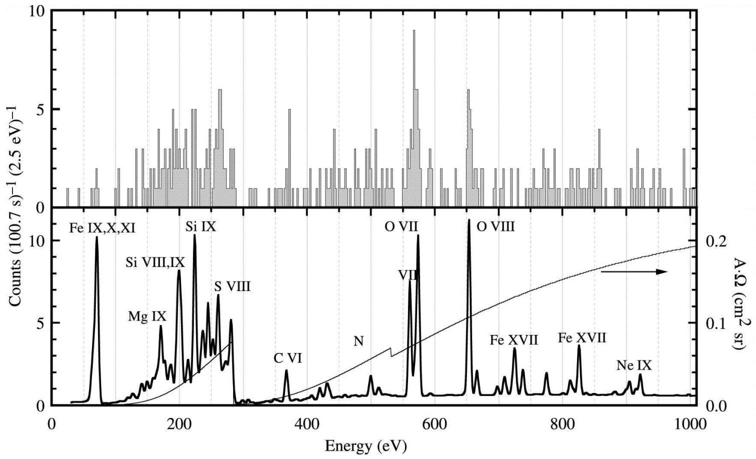

Figure 2.4: Observed spectrum from high latitude region with X-ray microcalorimeter(top) and the normal abundance two-temperature thin thermal model(bottom). Figure is taken from McCammon et al. (2002).

direction, extragalactic R12-band X-ray photons can reach to the Solar system. Therefore, the most of X-ray photons in the R12 band map in Figure 2.2 originate within $\sim$ 100 pc from the earth, while a significant fraction can be from more distant part of the Galaxy and extragalactic sources for direction with small galactic absorption.

2.2.4 Local Hot Bubble

Constraining distance of objects is an important issue in astronomy. Shadowing observations are a useful tool to constrain the emitters of the SXDB. The MBM-12 molecular cloud is located in the direction well outside the local Galactic structures and in a reasonably high latitude ($(\ell, b) = (159°.2, -34°.5)$). The distance is about 100 pc, although there is uncertainty from 60 ± 30 to 275 ± 65 pc (Smith et al., 2005). Thus it is likely located inside the LHB and in front of the bulk of Galactic absorption, while the column density of the cloud itself is high enough($N_{\rm H} = 4 \times 10^{21}$cm^{-2}) to block X-rays below 1 keV. Thus this cloud is very useful to estimate the emission within $\sim$ 100 pc from the earth.

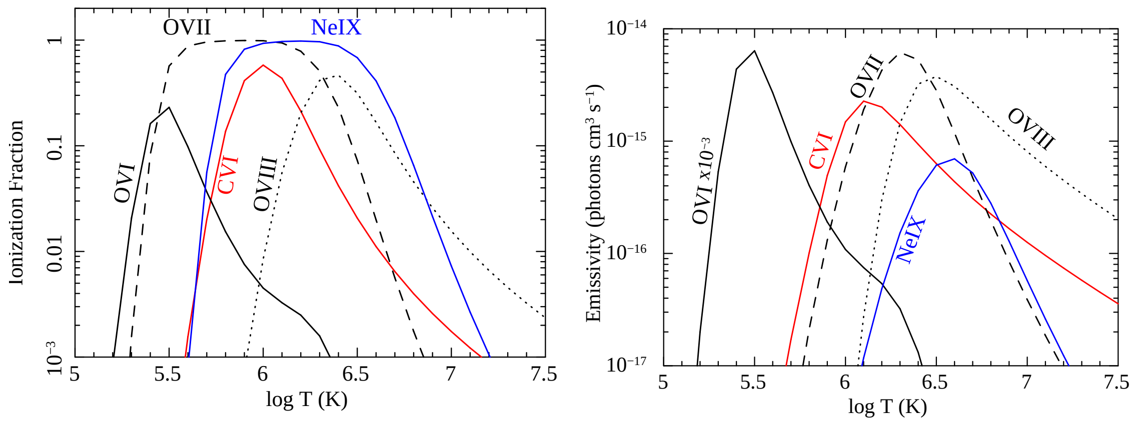

Figure 2.5: Ionization fraction (left) and the emissivity (right) of C VI, O VI, O VII, O VIII and Ne IX line as a function of temperature for a gas in the collisional ionization equilibrium state. The emissivity of O VI is scale down by a factor of 1000 for demonstration purpose.

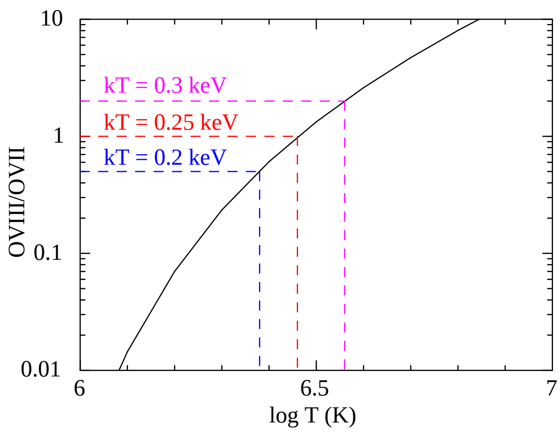

Figure 2.6: The line intensity ratio of O VIII to O VII as a function of temperature. Dashed line shows that O VIII/O VII are 0.5, 1.0 and 1.5.

A *ROSAT* PSPC pointing observation was carried out in 1991 in the direction of this cloud (Snowden et al., 1993). The X-ray intensity in the R45 band showed a decrease well correlated with the 100 μm IR intensity, which is proportional to the column density of dust grains, thus the neutral matter density of the cloud. On the other hand the intensity in R12 band showed little shadowing. Thus the most of R12 band emission arises from distance closer than $\sim$ 100 pc while a part of R45 band emission is from beyond the cloud. Snowden et al. (1993) estimated the emission measure of the hot gas emitting the R12 band to be 0.0024 cm^{-6} pc $= 5.9 \times 10^{14}$ cm^{-5} str^{-1} assuming a temperature of $10^{6.0}$ K.

A *Suzaku* observation of the MBM12 on-cloud direction was carried out in 2006 (Smith et al., 2007b). The *Suzaku* XIS1 spectrum clearly detected O VII line and the intensity was determined to be 2.93 ± 0.45 LU (LU = photons s^{-1} cm^{-2} str^{-1}). The spectrum above 0.4 keV was well represented by a thin-thermal emission model with $kT = 0.109^{+0.006}_{-0.012}$ keV ($T = 10^{5.97}$ K) and emission measure $=13.4^{+6.1}_{-2.4} \times 10^{14}$ cm^{-5} str^{-1} (0.0054 cm^{-6} pc)(Masui et al. 2009). Comparing the emission measure obtained from the *ROSAT* R12 band observation,

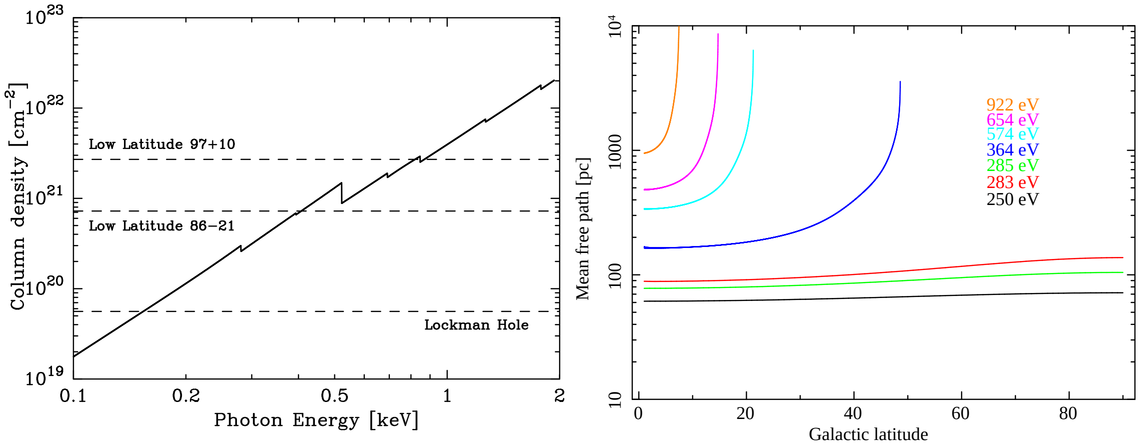

Figure 2.7: Left:Energy dependence of column density at which the optical depth is equal to unity assumed solar abundance. Typical values of column density in the directions of the observed fields in the present thesis are also indicated as dotted lines.Right: The galactic latitude dependence of mean free path for photon at energy of 250 eV, 283 eV and 285 eV which are lower and higher side around the carbon edge, 364 eV for C VI line, 574 eV for O VII line, 654 eV for O VIII line, 922 eV for Ne IX line.

we find that about half of emission in the R45 band ($\sim$ *Suzaku* 0.4-1 keV) must have different origins from the R12 band emission.

A more stringent constraint on the emission measure of the hot component in the LHB was obtained from diffuse EUV iron line observations with CHIPS (Cosmic Hot Interstellar Plasma Spectrometer). Hurwitz et al. (2005) placed a 90 % upper limit of 0.0004 cm^{-6} pc $= 9.8 \times 10^{13}$ cm^{-5} str^{-1} on the emission measure of $10^{6.0}$ K hot gas in the LHB, assuming the solar abundance. This is by a factor of six smaller than the emission measure of the R12 band emission.

As shown in Figure 2.8, a part of the R12 band emission shows clear anti-correlation to the neutral matter column density. Thus at least a part of R12 band emission must come from the LHB. However, we notice that there exists a large amount of offset counts in the correlation plot. If all the interpretations of the three observations are correct, only reasonable explanation is that only $\lesssim 1/6$ of R12 band emission and $\lesssim 1/10$ of R45 band emission arise from the LHB and remaining dominant part of emission is from somewhere else. The most likely candidate of the origin is the solar wind charge exchange (SWCX) induced X-ray emission from the interplanetary space, which we call the Heliospheric SWCX.

2.2.5 Solar Wind Charge Exchange (SWCX)

2.2.5.1 Brief history of SWCX

Mysterious time variations of X-ray count rates that lasted a few hours to a few days were discovered during the *ROSAT* survey (Snowden et al., 1994). The temporal variations were called "long-term enhancements (LTEs)". At that time, the origin of the LTEs was not known at all. Then the comet Hyakutake was found to emit X-rays (Lisse et al., 1996), which was surpringing because copious X-ray was emitted from such a cold object. Soft X-ray

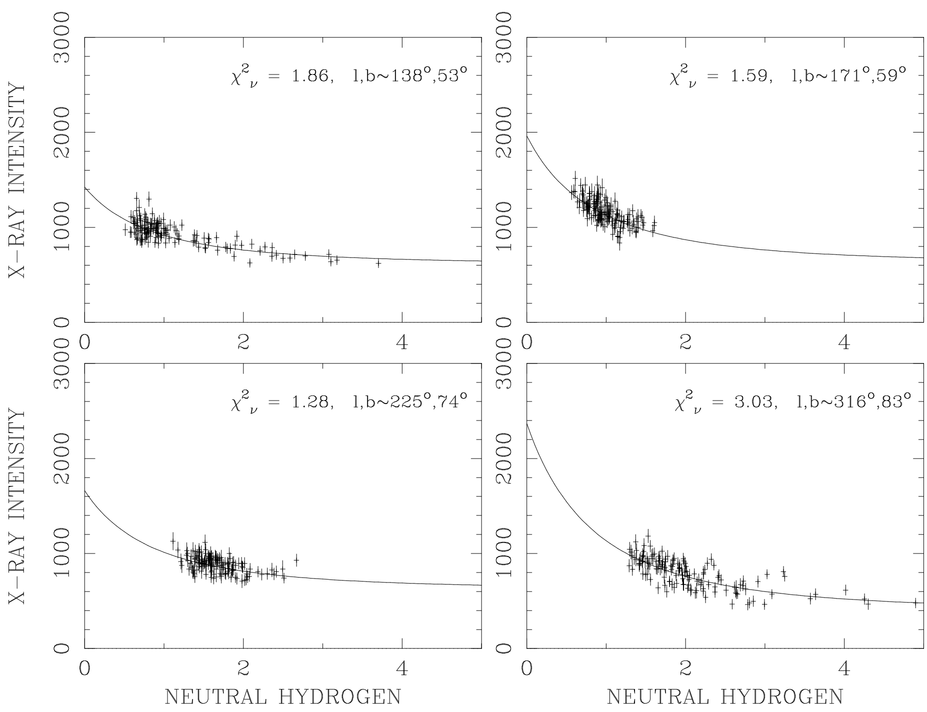

Figure 2.8: Scatter plot of R12 band intensity and corrected and scaled *IRAS* 100 μm data plus fitted model curve for the typical four northern hemisphere regions. Figures are taken from Snowden et al. (1998)

emissions were detected from other comets. Several emission mechanisms were proposed. It is now believed that the dominant X-ray emission mechanism is charge transfer from cometary neutrals to heavy solar wind ions (Cravens, 1997; Krasnopolsky et al., 2004). This discovery became a great hint for the origin of the LTEs. The LTEs were found to be correlated with the solar activity (Freyberg, 1994) and with the solar wind events (Cravens, 2000) . It is now understood that LTEs are mainly due to the interaction of strong solar wind with the geocoronal atomic hydrogen. Cox (1998) and Cravens (2000) suggested that a significant fraction of the SXDB can be explained by the SWCX in the interplanetary space. Lallement (2004b) constructed a model for the Heliospheric SWCX. Her model could explain the whole R12 band emission in the directions of low R12 band intensity, thus of high neutral column density, but leaves interstellar emission in directions of high R12 band intensity.

2.2.5.2 Geocoronal and Heriospheric SWCX

The SWCX is considered to be emitted from two distinct regions. The first one is neutral matter in Earth's magnetosphere, i.e. geocorona. We call this component Geocoronal SWCX. As shown in Figure 2.9, the H atom density in geocorona is as high as 1000 cm^{-3} at $2R_{\rm E}$ and decreases exponentially with increasing geocentric distance, where $R_{\rm E}$ is the Earth's radius.

If O^{7+} ions of solar wind can penetrate down to the geocentric distance R, then the expected O VII intensity is,

$$F_{\mathrm{OVII}} = \frac{1}{4\pi}\sigma_{\mathrm{ce}} A(\mathrm{O}^{7+}) f_{\mathrm{sw}} \int_R^\infty ds\; n_{\mathrm{H}}(s) \tag{2.4}$$

$$= \left\{ \begin{array}{ll} 0.33\ (\mathrm{LU}) & \text{for } R = 10R_{\mathrm{E}} \\ 1.0\ (\mathrm{LU}) & \text{for } R = 3R_{\mathrm{E}} \end{array} \right\} \left(\frac{3.4\times10^{-15}\mathrm{cm}^{-2}}{\sigma_{\mathrm{ce}}}\right)\left(\frac{0.2/1780}{A(\mathrm{O}^{7+})}\right)\left(\frac{1\times10^{8}\ \mathrm{cm}^{-2}\ \mathrm{s}^{-1}}{f_{\mathrm{sw}}}\right) \tag{2.5}$$

where σ_{ce}, $A(\mathrm{O}^{7+})$, and f_{sw} are, respectively, the charge exchange reaction cross section, O^{7+} to proton number density ratio in solar wind, and the solar wind flux. The values are typical value for slow wind (Table A.1). We used the equation shown in Figure 2.9 for the H atom density, n_{H}. The integration by ds has to be done along a line of sight. However, in the above equation, we integrated radially to estimate a typical value. In Equation 2.4, we assumed that the solar wind flux is conserved when it passes the bow shock of magnetosphere. Solar wind penetrates usually down to $\sim 10R_{\mathrm{E}}$, while depending on the interplanetary plasma condition it can go down to lower altitude in the polar region of the geomagnetic fields. Since the O VII intensity in MBM-12 on-cloud direction is ~ 3 LU, Equation 2.5 indicates that the Geocoronal SWCX will not be negligible compared to the SXDB if the solar wind penetrate down to $\sim 3R_{\mathrm{E}}$ or the solar wind flux becomes as high as $\sim 4\times10^{8}\ \mathrm{cm}^{-2}\ \mathrm{s}^{-1}$.

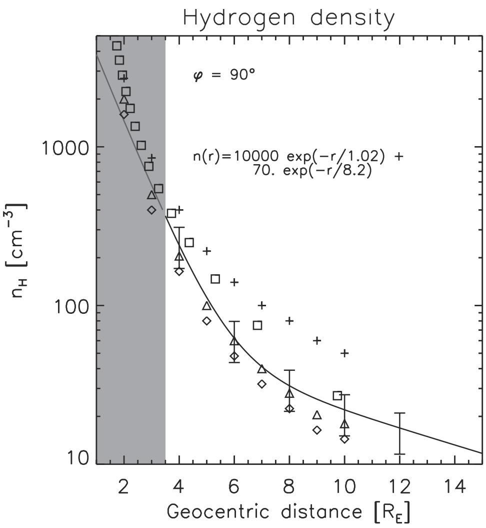

Figure 2.9: The H atom density in geocorona (Østgaard et al., 2003) ϕ is the solar zenith angle, and $\phi = 90°$ is the dawn side.

The solar system is moving against the local interstellar medium (LISM) with a velocity of ~ 200 km s^{-1}, and thus neutral matter in LISM flows into the heliosphere. The flow of the neutral matter, mostly H and He atoms, is affected by the radiation pressure and the gravity of the Sun. H and He atoms are also ionized by UV photons from the Sun. Consequently, the H atom density at 1 AU from the Sun becomes as low as 0.05 cm^{-3} while it is 1 cm^{-3} at > 10 AU (Lallement et al., 1985). Although both the neutral and solar-wind densities are much lower than geocoronal case, charge exchange interaction of the solar-wind ions and H and He atoms in the heliosphere produces non-negligible intensity X-ray photons, because of the long sight line. We call this heliospheric SWCX. Cravens et al. (2007) estimated the intensity of Heliosheric SWCX for the first time assuming H density profile of $\propto \exp(-\lambda/r)$, where r is the heliocentric distance and λ is a constant. Lallement (2004a,b) and Koutroumpa et al. (2006, 2007, 2008) constructed Heliospheric SWCX model. In Lallement (2004a,b), the change in characteristics of the solar wind associated with solar cycle is considered. In the model simulation by Koutroumpa et al. (2007), the relation between the propagation front of the intense solar winds triggered by solar flares in the planetary space and the line of sight of X-ray observations are considered. Koutroumpa et al. (2007) and Henley & Shelton (2008) also argued that the O VII and/or O VIII intensities determined by early *Chandra* and *XMM-Newton* observations are not consistent with those obtained by *Suzaku* observations of the same directions. They suggested that the difference is due to the different solar activity; early *Chandra* and *XMM-Newton* observations were conducted near the solar maximum, while after launch of *Suzaku* , the sun went into extended low activity phase. However, the line intensities determined by *Chandra* and *XMM-Newton* observations are less reliable than those by *Suzaku* because of the high non X-ray background and complicated energy response function of the detectors on board *Chandra* and *XMM-Newton* (e.g. Smith et al. (2007b)). We thus consider that the long-term variations of the line intensity is not well established yet.

The models of the Heliospheric SWCX suggest that the SXDB in R45 band can be entirely explained by the Heliospheric SWCX, while a part of the R12 band emission can be from the LHB.

2.2.5.3 Contamination of Geocoronal SWCX in *Suzaku* data

Since the altitude of the *Suzaku* orbit is 600 km, the line of sight always passes through the Earth's magnetosphere. During the observation of the blank field near the North Ecliptic Pole in September 2005, *Suzaku* detected a strong flare in 0.4-1 keV energy band. Fujimoto et al. (2007) concluded that the increase of the X-ray flux during the flare is mostly due to emission lines from C VI (357 eV) to Mg XI (1329 eV). They detected the C VI Ly γ emission (459 eV) in the flare spectrum. This line is expected to be enhanced in charge exchange process compared to thermal emission. Thus this is a strong evidence that the emission arises from charge exchange process. During the flare the X-ray intensity varied on times scales as short as 10 min. They concluded that the short time variation is related to the movement of the sight line associated with the orbital motion of the satellite. At this time the solar-wind ions penetrated down to the geocentric distance of $2R_{\rm E}$ along the geomagnetic fields of the northern polar cap. Thus when the line of sight passes polar cap region of low altitudes, the SWCX is enhanced.

Strong geocoronal SWCX can be observed even when the sight line does not pass through the Earth's polar cap region. An example of this observation is the observation for the Galactic ridge X-ray emission (GRXE) conducted in October, 2005. During this observation O VII emission as strong as 11 LU was observed and was strongly correlated with the solar wind flux. The observed O VII intensity is by a factor of $\sim$ 10 stronger than that expected from Equation 2.5. Yamasaki et al. (2008a) discussed that the neutral density in the geocorona increases during solar flare. Liu & Lühr (2005) reported a change of the density of a factor of 4–8 within a few hours at an altitude of $\sim$ 400 km due to the growth of the Joule heat. Since the neutrals in the geocorona are supplied from the outer atmosphere, the density there can also be enhanced during and after solar flares.

These two are extreme cases in which time variation is easily found in the X-ray light curve. In most cases, the spectra can be contaminated by the Geocoronal SWCX which is too weak to be identified in the X-ray light curve but cannot be neglected compared to the SXDB (e.g. > 1 LU in O VII emission). The the Geocoronal SWCX should be variable on time scales of 10 minutes to hours and correlated with the solar wind flux and the geocentric distance of the magnetopause on the sight line. Here we define the magnetopause as a lowest-altitude point along the sight line whose geomagnetic field is open to the interplanetary space. In chapter 4, we will try to remove time interval in which the data could be contaminated by the Geocoronal SWCX, utilizing the time variations and the correlations.

The charge exchange process, typical solar wind parameters, and the cross sections for charge exchange interaction are summarized in Appendix A.

2.2.6 Emission from distant part of the Galaxy

The shadowing experiments using the MBM-12 cloud clearly shows that a significant fraction of the SXDB in R45 band arises from behind the cloud. It is likely to arise from distant part of the galaxy; mostly above or beyond the bulk of absorption in the Galactic disk. Kuntz & Snowden (2000) called this component the "transabsorption" emission (TAE) and separated it in the *ROSAT* all sky map utilizing the directional dependence of the absorption column density. They argued that the emission spectrum can be described by a two-temperature thermal emission model of temperatures k$T \sim 0.10$ and 0.25 keV. However, because there is no constraint on distance other than absorption, it is hard to constrain the origins conclusively.

A new insight was obtained from combined analysis of the absorption lines observed in the energy spectra of extragalactic objects and emission lines of the same ion species observed in the energy spectra of nearby skies. Yao et al. (2009) analyzed the absorption spectra of LMC X-3 obtained with the transmission grating (HETG) on board *Chandra* , and the emission spectra from the blank fields about 30' away from LMC X-3 observed with the CCD camera (XIS) on board *Suzaku* . The joint spectral fit of the data shows the hot gas attributed to the TAE component can not be isothermal. Instead, a thick Galactic hot gaseous disk whose temperature and density decreases exponentially from the Galactic midplane can consistently explain the observations. They obtained scale heights of $1.4\xi^{-1}$ and $2.8\xi^{-1}$ kpc, and the midplane values of 0.31 keV and 1.4×10^{-3}cm^{-3} for the temperature and the density, respectively. Here, ξ is the volume filling factor of the hot gas.

A similar result was obtained for the sight line toward Mrk 421, although the the X-ray emission is mostly based on the *ROSAT* All Sky Survey data, thus the emission lines are not resolved spectroscopically (Yao & Wang, 2007).

2.2.7 Observation of O_{VI} line

We would like to mention about O VI absorption and emission, which traces gas at a temperature of $\sim 10^5$ K. O VI absorption lines were detected in OB stars and in the extragalactic objects. Based on absorption lines detected by *FUSE* , Savage et al. (2003) proposed a model for O VI distribution; a plane-parallel patchy absorbing layer with an average O VI midplane density of n_0(O VI) $= 1.7 \times 10^{-8}$ cm^{-3}, a scale height of 2.3 kpc, and a $\sim$0.25 dex excess of O VI in the northern Galactic polar region. However this model does not provide a good fit to the O VI-emission observation with *FUSE* . The distribution of O VI emission over the sky is poorly correlated with other tracers of gas in the halo, including low- and intermediate-velocity H I, H_α emission from the warm ionized gas at $\sim 10^4$ K, and hot X-ray-emitting gas at $\sim 10^6$ K.

The thick Galactic hot gaseous disk model in the previous subsection can account for the O VI line absorption observed in *FUSE* spectrum. This model predicts that most of the O VI absorption arises from the kpc scale diffuse gas distributed narrow region compared to O VII emission. On the other hand, the thick Galactic hot gaseous disk model only predicts less than one tenth of the O VI line emission intensity typically observed at high Galactic latitude. Yao et al. (2009) suggested that there exist high density region at the interfaces between hot and cool media and that O VI emission arises mainly from such regions.

If the thermal pressure of gas at 3×10^5 K, at which the ionization fraction of O^{+5} shows the peak, is half the average midplane value, 1.5×10^{-12} dyn cm^{-2}, the local density of O^{+5} is about 2.2×10^{-6} cm^{-3}. Compared with the observed value above, 1.7×10^{-8} cm^{-3}, the filling factor of the material emitting O VI is only less than about 0.8 %.

2.2.8 Emission from galactic disk

As mentioned in subsection 2.2.1, about 40 % of the SXDB in the *ROSAT* R45 band is extragalactic continuum emission. As we also showed in Figure 2.7, the X-ray photons in this energy band is completely blocked by the neutral matter in the Galactic plane ($N_{\rm H} \sim 10^{22}$ cm^{-2}). Nevertheless, the R45 band X-ray surface brightness decreases only by 20 % or less from high Galactic latitude to midplane. This issue has been known as the "M band problem" (McCammon & Sanders, 1990; Cox, 2005). The M band is the name of a similar energy band in the Wisconsin and the Nagoya-Leiden rocket programs. Since X-ray photons below 1 keV can travel only about 1 kpc in the Galactic disk, there must be emission in the midplane within 1 kpc which compensates partly the decrease of the extragalactic emission. Nousek et al. (1982) and Sanders et al. (1983) suggested hot gas of $\sim 3 \times 10^6$ K as the origin, while Rosner et al. (1981) pointed out emission from dM stars can contribute ~ 20 % of the total diffuse emission. Cox (2005) showed that if a significant fraction ($\gtrsim 1/2$) of emission originates from hot gas in the temperature range of 2.5×10^6 to 6.3×10^6 K, the hot gas must expand because of its high pressure. He suggested young expanding superbubbles or supernova remnants evolving in low density region as candidates for the emission.

As an example, the surface brightness averaged over rectangular areas of $(\Delta\ell, \Delta b) = (10^\circ, 2^\circ)$ along the line of $\ell = 235^\circ$ is plotted as a function of b in Figure 2.10. A model surface brightness profile consisting of an unabsorbed constant emission and the CXB absorbed by the average column density is plotted together with the observational data. For $|b| \lesssim 10^\circ$, there is 20×10^{-6}counts s^{-1}arcmin^{-2} of excess over the model. This corresponds to about 20 % of the total diffuse emission at high latitudes. Note that the model curve is for the minimum possible absorption: if the other 60 % of the R45 emission at high latitudes is produced by a hot halo, then this too would be largely absorbed in the plane, depending on its scale height structure. The surface brightness profile suggests asymmetry between the profiles for $b > 0^\circ$ and $b < 0^\circ$, which is more pronounced in R4 band. In this paper, however, we concentrate on the excess flux at $b = 0^\circ$. In Appendix D, we will construct a model which can consistently explain the excess at $b = 0^\circ$, although we will find the model cannot explain the excess in $b \sim 2 - 10^\circ$.

The origin of the excess midplane emission is not known yet although this problem has been known for more than 25 years. One major reason is that there has been no energy

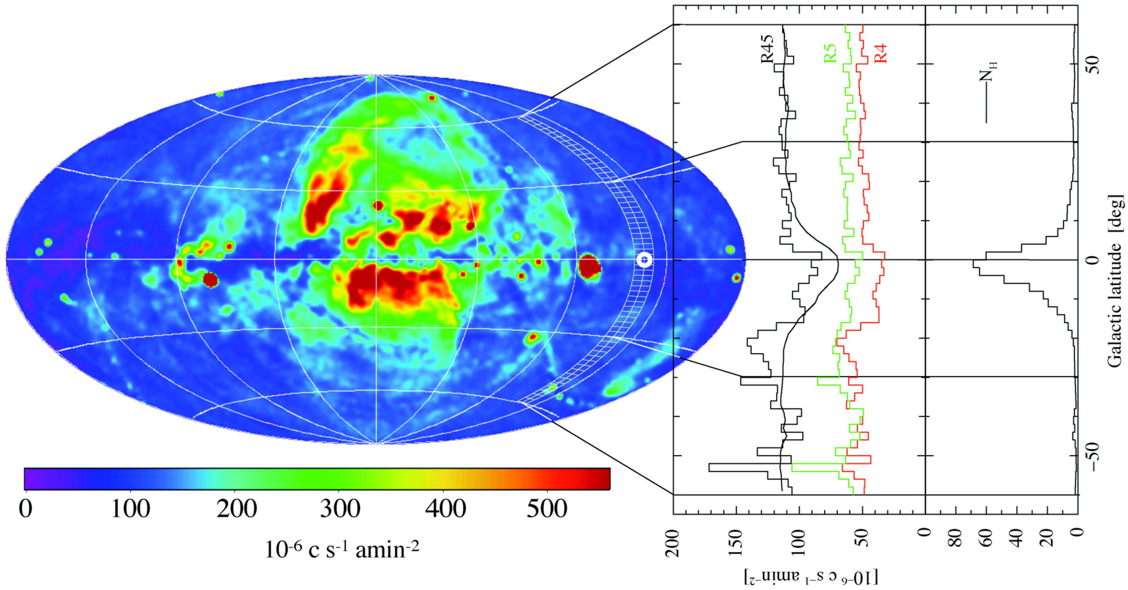

Figure 2.10: *ROSAT* diffuse X-ray R45 band map (Snowden et al., 1997), and the surface brightness and neutral hydrogen column density as functions of b along $\ell \sim 230°$. The thick white circle in the map indicates the pointing direction of the present observation. The surface brightness and the hydrogen column density were averaged over rectangular areas of size $(\Delta\ell, \Delta b) = (10°, 2°)$. The surface brightnesses in R4, R5, and R45 bands are plotted as step functions. A model surface brightness for R45 band which consists of an unabsorbed constant emission (65×10^{-6}counts s^{-1}arcmin^{-2}) and the cosmic X-ray background emission ($10\ (E/1\ \mathrm{keV})^{-1.4}$ photons s^{-1} cm^{-2} str^{-1} keV^{-1}) absorbed by the average column density is shown with a thick curve. There exists about 20×10^{-6}counts s^{-1}arcmin^{-2} of excess over the model at midplane. The excess in $b = -20°$ to $-30°$ is partly due to one of the streaks of bright areas which meet together at the South Ecliptic Pole. Thus it could be due to the so-called long term enhancement (Snowden et al., 1994) or scattered solar X-rays. Taken from Masui et al. 2009.

spectrum available in which emission line structures are resolved. A new insight was also obtained from *Suzaku* observations. Masui et al. (2009) observed a nominal midplane direction (ℓ, b) = (235°, 0°) with *Suzaku* for 160 ks. The direction was selected because this point is well outside the Galactic bulge and north polar spur, and because the direction is an average midplane direction without any special features, i.e. no bright X-sources in the XIS field of view, a typical neutral Hydrogen density, and a typical counting rate in the *ROSAT* all sky survey map. They found that the O VII Kα emission intensity was comparable with that of the MBM-12 on-cloud observation and that a narrow bump peaked at $\sim$ 0.9 keV was compensating the decrease of the extragalactic component. This strong feature, presumably due to a blend of Ne-K and Fe-L lines, makes the $b = 0°$ spectrum qualitatively unlike empty-field spectra at other latitudes and requires plasma at higher temperatures than generally seen in Galactic diffuse emission. They discussed that because the pressure exceeds the total midplane pressure the emission can not be truly diffuse hot gas, but that the emission is from spatially unresolved faint young dM stars. They constructed a model spectrum based on the average properties and density of dM stars in solar neighborhood and showed it could consistently explain both the spectrum and the absolute intensity. The source number expected for dM stars, typically 60 in the *Suzaku* XIS field of view, was found to be consistent with the source number count from the *Chandra* plane survey project. However, they found that the excess emission in $|b| = 2 - 10°$ cannot be explained if they assume the vertical distribution of young dM stars from the Galaxy dynamical model.

2.3 Summary of the Review

Understanding of the SXDB and the hot phase interstellarmatter has been gradually increased since early observations in 1970's. The *ROSAT* all sky survey was a great step which provided the all sky map with 12' spatial resolution, although the energy resolution was poor. The discovery of the SWCX brought new insights in interpretation of the emission. *Suzaku* is now bringing another great step in the research of SXDB above the C K edge (= 3/4 keV band = R45 band), with low and stable non X-ray background, medium spatial resolution, and good energy resolution. The present status may be summarized as below.

- The SXDB above the C K edge consists of at least two components: near ($\lesssim$ 100 pc) and far components ($\gtrsim$ 100 pc).
- A large fraction ($\gtrsim$9/10) of the near component arises from the Heliospheric SWCX and the $\sim 10^6$ hot gas in the LHB contribute only a small fraction. However, below the C K edge (=1/4 keV band = R12 band) it may have more contribution ($\lesssim$ 1/6). Early *Suzaku* observation was already a large step to new understanding,
- The far component is likely to arise from hot gas. However, we do not know how they are distributed in the Galaxy. Its temperature may be higher than that of LHB ($\sim 2 \times 10^6$ K). However, both the temperature and density are not well constrained yet. The major part of the hot gas is considered to locate beyond the bulk of neutral matter in our Galaxy. As a possible configuration, a thick hot disk with vertical scale height of $\sim 2\xi$ kpc, where ξ is the volume filling factor of the hot gas, was proposed.
- An emission component which has a significantly higher temperature ($\sim 6 \times 10^6$ K) than other directions exists in midplane. The emission is compensating the decrease of extragalactic emission by the Galactic absorption. A sum of faint young dM stars is a candidate of the source.

Chapter 3

Instruments

This thesis deals with soft X-ray diffuse background, which would be dominated by the composition of line emission. We utilize a satellite *Suzaku*, which is most suitable for investigating soft X-ray diffuse background because of its unprecedented energy resolution below ~ 1 keV for spatially extended source. The first section in this chapter outlines the *Suzaku* instrumentation. In the second section, we show brief description of *ACE* and *WIND* satellite used as a monitor of proton flux of the solar wind which induced the solar wind charge exchange emission that contributes to the soft X-ray diffuse background.

3.1 The *Suzaku* satellite

3.1.1 Mission Description

Suzaku is placed in a near-circular orbit with an apogee of 568 km, an inclination of 31.9 degrees, and an orbital period of about 96 minutes. The maximum slew rate of the spacecraft is 6 degrees/min, and settling to the final attitude takes $\sim$ 10 minutes, using the star trackers.

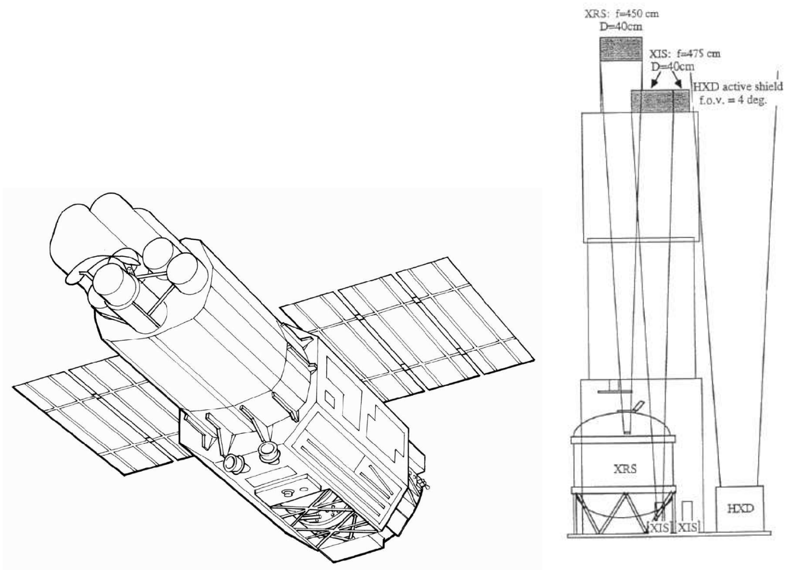

Figure 3.1: [Left] Schematic picture of the bottom of the *Suzaku* satellite. [Right] A side view of the instrument and telescopes on *Suzaku* .

The scientific payload of *Suzaku* (Fig. 3.1) initially consisted of three distinct co-aligned scientific instruments. There are four X–ray sensitive imaging CCD cameras (X–ray Imaging Spectrometers, or XISs), three front-illuminated (FI; energy range 0.4-12 keV) and one back-illuminated (BI; energy range 0.2-12 keV), capable of moderate energy resolution. Each XIS is located in the focal plane of a dedicated X–ray telescope. The second instrument is the non-imaging, collimated Hard X–ray Detector (HXD), which extends the bandpass of the observatory to much higher energies with its 10–600 keV pointed bandpass. The X–Ray Spectrometer (XRS) is no longer operational. And one of the X–ray Imaging sensor XIS-S2 became disabled. XRT–XIS modules and HXD operate simultaneously. In the study of this thesis, only XRT/XIS were used. The description of the HXD is hence omitted.

Table 3.2 summarizes the calibration items of XRT and XIS, the current status, and their expected accuracy. These values are the 90% limits, equivalent to 1.6σ. Note that the values listed are those required from the scientific purpose and ultimate goals which are possible to be realized on the basis of the instrument design, and are not measurement results.

3.1.2 X–Ray Telescopes (XRTs)

Suzaku has five light-weight thin-foil X–Ray Telescopes (XRTs). These are grazing-incidence reflective optics consisting of compactly nested, thin conical elements. Because of the reflectors' small thickness, they permit high density nesting and thus provide large collecting

Table 3.1: Overview of *Suzaku* capabilities

S/C	Orbit Apogee	568 km
	Orbital Period	96 minutes
	Observing Efficiency	$\sim 45\%$
XRT	Focal length	4.75 m
	Field of View	$17'$ at 1.5 keV
		$13'$ at 8 keV
	Plate scale	0.724 arcmin/mm
	Effective Area	440 cm^2 at 1.5 keV
		250 cm^2 at 8 keV
	Angular Resolution	$2'$ (HPD)
XIS	Field of View	$17.8' \times 17.8'$
	Bandpass	0.2–12 keV
	Pixel grid	1024×1024
	Pixel size	24 μm× 24 μm
	Energy Resolution	~ 130 eV at 6 keV
	Effective Area	340 cm^2 (FI), 390 cm^2 (BI) at 1.5 keV
	(incl XRT-I)	150 cm^2 (FI), 100 cm^2 (BI) at 8 keV
	Time Resolution	8 s (Normal mode), 7.8 ms (P-Sum mode)

Table 3.2: Error Budgets of Scientific Instrument Calibrations

	Calibration Item	October 2005	Requirement	Goal
XRT−I/XIS	On-axis effective area [a]	∼10%	5%	5%
	Vignetting	∼50%	5%	2%
	On-axis EEF [b]	∼20%	5%	1%
	Off-axis EEF [c]	∼30%	20%	2%
	Optical axis position in XIS	$\sim 0.5'$	$< 0.2'$	$<0.2'$
	Energy scale	0.3%	0.1%	0.1%
	Energy resolution (FWHM) at 5.9 keV	5%	1%	1%

Note ··· All the values quoted are preliminary.

a: Valid in the 1–8 keV band. Calibration uncertainty may become larger outside this energy range, especially below 0.3 keV (BI chip) and above 10 keV.

b: For all integration radii from $1'$-$6'$. No error on attitude control is included.

c: As on-axis but for all XIS f.o.v. No calibration is currently scheduled.

efficiency with a moderate imaging capability in the energy range of 0.2-12 keV, all accomplished in telescope units under 20 kg each.

Four XRTs on-board *Suzaku* (XRT-I) are used on the XIS, and the other XRT (XRT-S) is for the XRS. XRT-S is no more functional. The XRTs are arranged on the Extensible Optical Bench (EOB) on the spacecraft in the manner shown in Figure 3.2. The external dimensions of the 4 XRT-Is, however, are the same (See Table 3.3).

The angular resolutions of the XRTs range from $1.8'$ to $2.3'$, expressed in terms of half-power diameter, which is the diameter within which half of the focused X–ray is enclosed.

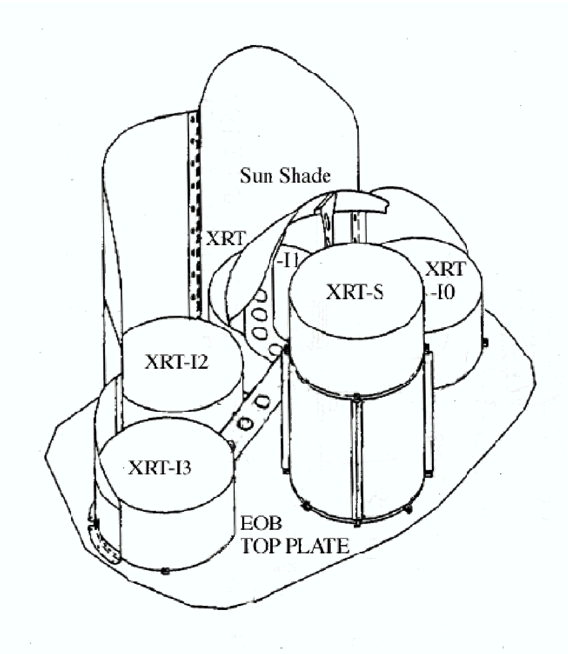

Figure 3.2: Layout of the XRTs on the *Suzaku* spacecraft.

Figure 3.3: A *Suzaku* X–Ray Telescope

Table 3.3: Telescope Dimensions and Parameters of XRT-I

Number of telescopes	4
Focal length	4.75 m
Inner Diameter	118 mm
Outer Diameter	399 mm
Height	279 mm
Mass/Telescope	19.5 kg
Number of nested shells	175
Reflectors/Telescope	1400
Geometric area/Telescope	873 cm^2
Reflecting surface	Gold
Substrate material	Aluminum
Substrate thickness	155 μm
Reflector slant height	101.6 mm

The angular resolution does not significantly depend on the energy of the incident X–ray in the energy range of *Suzaku* , 0.2-12 keV. The effective areas are typically 440 cm^2 at 1.5 keV and 250 cm^2 at 8 keV. The focal lengths are 4.75 m for the XRT-I. Individual XRT quadrants have their component focal lengths deviated from the design values by a few cm. The optical axes of the quadrants of each XRT are aligned within $2'$ from the mechanical axis. The field of view for XRT-Is is about $17'$ at 1.5 keV and $13'$ at 8 keV. (see also Table 3.1)

3.1.2.1 Basic Components of XRT

The *Suzaku* X–Ray Telescopes (XRTs) consist of closely nested thin-foil reflectors, reflecting X–ray at small grazing angles. An XRT is a cylindrical structure, having the following layered components: a thermal shield at the entrance aperture to help maintain a uniform temperature; a pre-collimator mounted on metal rings for stray light elimination; a primary stage for the first X–ray reflection; a secondary stage for the second X–ray reflection; a base ring for structural integrity and interface with the EOB of the spacecraft. All these components, except the base rings, are constructed in 90° segments. Four of these quadrants are coupled together by interconnect-couplers and also by the top and base rings (Figure 3.3). The telescope housings are made of aluminum for an optimal strength to mass ratio. Each reflector consists of a substrate also made of aluminum and an epoxy layer that couples the reflecting gold surface to the substrate.

3.1.2.2 Reflectors

In shape, each reflector is a 90° segment of a section of a cone. The cone angle is designed to be the angle of on-axis incidence for the primary stage and 3 times that for the secondary stage. They are 101.6 mm in slant length and with radii extending approximately from 60 mm at the inner part to 200 mm at the outer part. The reflectors are nominally 178 μm in thickness. All reflectors are positioned with grooved alignment bars, which hold the foils at their circular edges. There are 13 alignment bars at each face of each quadrant, separated at approximately 6.4° apart.

To properly reflect and focus X–ray at grazing incidence, the precision of the reflector figure and the smoothness of the reflector surface are important aspects. Since polishing of thin reflectors is both impractical and expensive, reflectors in *Suzaku* XRTs acquire their surface smoothness by a replication technique and their shape by thermo-forming of aluminum. In the replication method, metallic gold is deposited on extrusion glass mandrel ("replication mandrel"), of which the surface has sub-nanometer smoothness over a wide spatial frequency, and the substrate is subsequently bonded with the metallic film with a layer of epoxy. After the epoxy is hardened, the substrate-epoxy-gold film composite can be removed from the glass mandrel and the replica acquires the smoothness of the glass. The replica typically has $\sim$0.5 nm rms roughness in the mm or smaller spatial scale, which is sufficient for excellent reflectivity at incident angle less than the critical angle. The *Suzaku* XRTs are designed with on-axis reflection at less than critical angle, which is approximately inversely proportional to X–ray energy.

In the thermo-forming of the substrate, pre-cut, mechanically rolled aluminum foils are pressed onto a precisely shaped "forming mandrel", which is not the same as the replication mandrel. The combination is then heated until the aluminum softened. The aluminum foils acquire the figure of the properly shaped mandrel after cooling and release of pressure. In

Table 3.4: Design Parameters for Pre-collimator

	XRT-I
Number of Collimators	4
Height	32 mm
Blade Substrate	Aluminum
Blade Thickness	120 μm
Blade Height	22 mm
Height from Blade Top to Reflector Top	30 mm
Number of nested shells	175
Blade/Telescope	700
Mass/Collimator	2.7 kg

the *Suzaku* XRTs, the conical approximation of the Wolter-I type geometry is used. This approximation fundamentally limits the angle resolution achievable. More significantly, the combination of the figure error in the replication mandrels and the imperfection in the thermo-forming process (to about 4 micrometers in the low frequency components of the figure error in the axial direction) limits the angular resolution to about 1 minute of arc.

3.1.2.3 Pre-collimator

The pre-collimator, which blocks off stray light that otherwise would enter the detector at a larger angle than intended, consists of concentrically nested aluminum foils similar to that of the reflector substrates. They are shorter, 22 mm in length, and thinner, 120 micrometers in thickness. They are positioned in a fashion similar to that of the reflectors, by 13 grooved aluminum plates at each circular edge of the pieces. They are installed on top of their respective primary reflectors along the axial direction. Due to their smaller thickness, they do not significantly reduce the entrance aperture in that direction more than the reflectors already do. Pre-collimator foils do not have reflective surfaces (neither front nor back). The relevant dimensions are listed in Table 3.4.

3.1.2.4 Thermal Shields

The *Suzaku* XRTs are designed to function in a thermal environment of 20±7.5°C. The reflectors, due to its composite nature and thus its mismatch in coefficients of thermal expansion, suffer from thermal distortion that degrades the angular resolution of the telescopes in temperature outside this range. Thermal gradient also distorts the telescope in a larger scale. Even though sun shields and other heating elements on the spacecraft help in maintaining a reasonable thermal environment, thermal shields are integrated on top of the pre-collimator stage to provide the needed thermal control.

3.1.2.5 XRT-I Performance in Orbit

The four XISs (cf. Fig. 3.12) are true imagers, with a large field of view ($\sim 18' \times 18'$), and moderate spectral resolution. Each of the co-aligned XRTs features an X–ray mirror with an angular resolution (expressed as Half-Power Diameter, or HPD) of $\sim 2'$. Figure 3.5 shows the total effective area of the XIS+XRT, which includes features due to the elemental

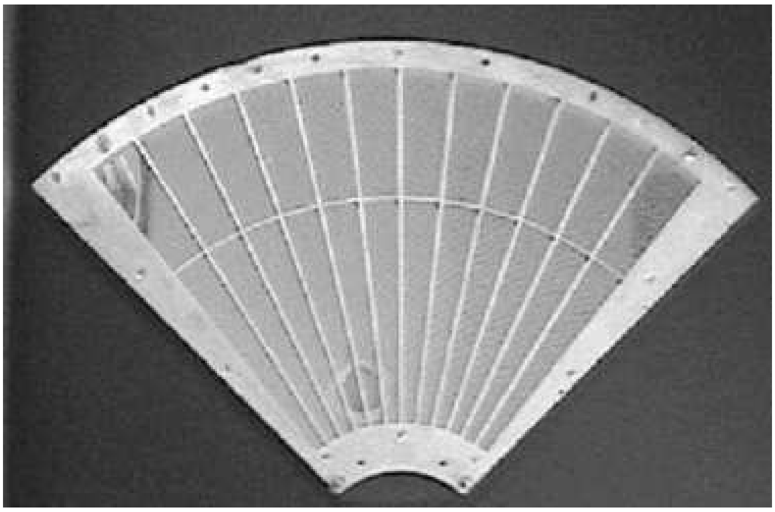

Figure 3.4: A thermal shield.

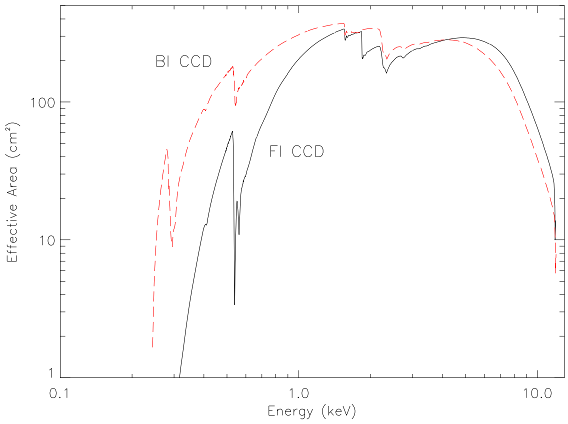

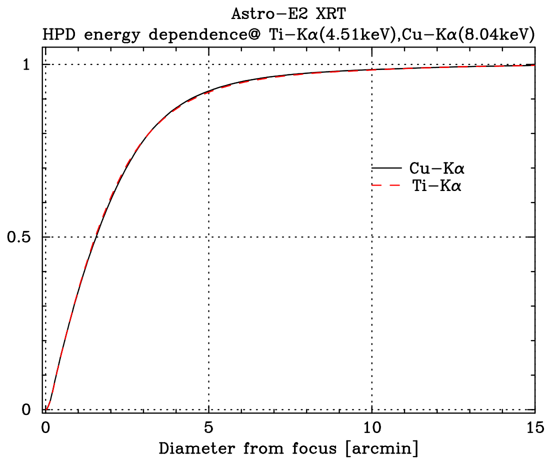

Figure 3.5: Left: XIS Effective area of one XRT + XIS system, for both the FI and BI chips. Right: The Encircled Energy Function (EEF) showing the fractional energy within a given radius for one quadrant of the XRT-I telescopes on *Suzaku* at 4.5 and 8.0 keV.

composition of the XIS and XRT. K-shell absorption edges from the oxygen (0.54 keV) and aluminum (1.56 keV) in the blocking filters are present, as well as a number of weak M-shell features between 2–3 keV arising from the gold in the XRT.

Fig. 3.6 shows the point spread functions (PSFs) of all the XRT-I+XIS modules, measured using a observation of a point-like source MCG−6−30-15. The preliminary HPD, with a typical statistical error of $\sim 0'.1$, ranges from $1'.8 \sim 2'.3$. Figure 3.7 shows the focal position of the XRT-Is, that the source is focused when the satellite points at the XIS aimpoint. The focal positions locate roughly within $0'.5$ from the detector center with an deviation of $\sim 0'.3$. This implies that the fields of view of the XIS coincides each other within $\sim 0'.3$.

A series of offset observations of the Crab observations were carried out in August and September at various off-axis angles of $0'$, $3'.5$, $7'$. The intensity of the Crab nebula is evaluated for each pointing and for each XIS module separately. By finding the maximum throughput angle, we also have obtained a direction of the optical axis of each telescope. The result is shown in Fig. 3.8. The optical axes locate roughly within $1'$ from the XIS aim

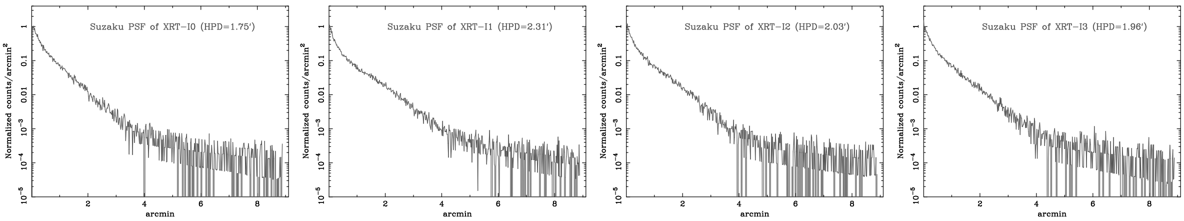

Figure 3.6: Point spread functions of the XRT–XIS modules for the XRT-I0 through XRT-I3 from left to right. Each PSF is normalized by the number of total photons collected over the entire XIS aperture.

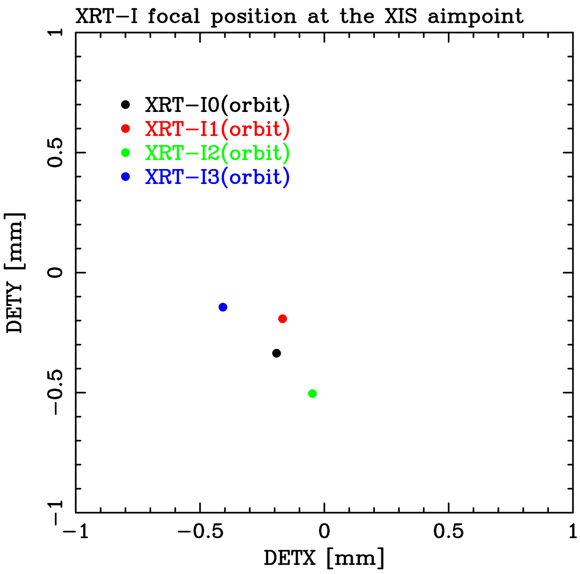

Figure 3.7: Focal positions at the XISs when the satellite points MCG−6−30-15 at the XIS aimpoint.

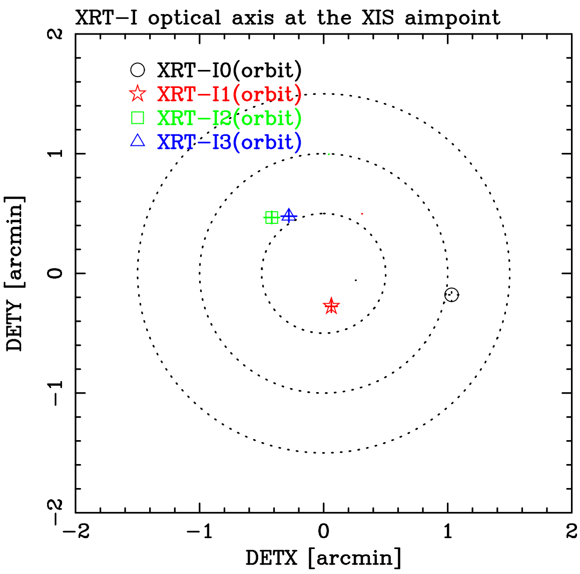

Figure 3.8: Optical axis directions of the XIS-S0 through S3. The optical axis of the XRT-I0 (XIS-S0), for example, locates at $(1'.0,\ -0'.2)$, which implies that the maximum throughput is achieved for XRT-I0 when the satellite points at the XIS aimpoint.

point. This implies that the efficiency of all the XRT-Is is more than 97 % even at 10 keV when we observe a point source on the XIS aimpoint. By assuming the detector efficiency is constant over the field of view, we determined the vignetting function as shown in Figure 3.9. The vignetting function is narrower in higher energy. The averaged effective area over the detector size of XIS ($17.8'$x$17.8'$) is 60%, 60% and 50% of the E.A on axis at 1.5, 4.5 and 8.0 keV, respectively.

In-flight stray-light observations were carried out with Crab at off-axis angles of $20'$ (4 pointings), $50'$ (4 pointing) and $120'$ (4 pointing) in August and September. It was found that the pre-collimator works for reducing the stray light in orbit. Figure 3.10 shows angular responses of the XRT-I at 1.5 and 4.5 keV up to 2 degrees. The effective area is normalized at on-axis. The integration area is corresponding to the detector size of XIS ($17'.8 \times 17'.8$). The three solid lines in the plots correspond to different parameters of ray-tracing program

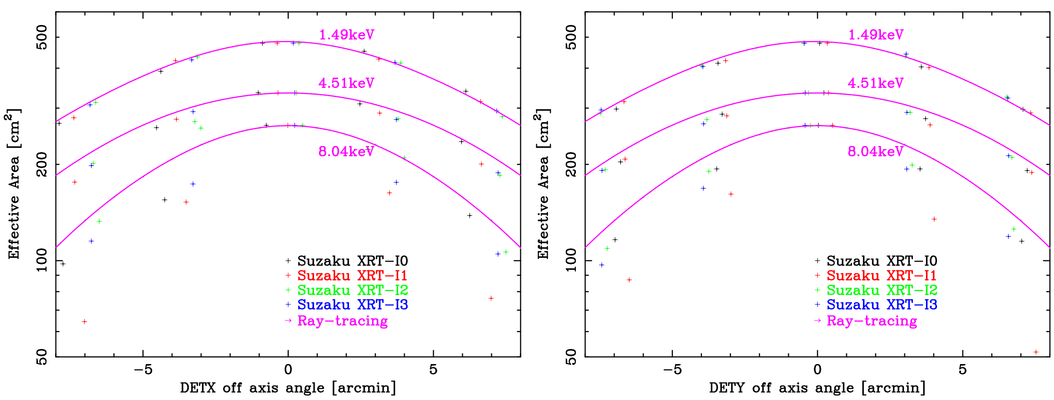

Figure 3.9: Vignetting curves of XRT-I at three different energies of 1.5, 4.5 and 8.0 keV. The three solid lines in the plots correspond to a parameter of ray-tracing program while the crosses are the preliminary XRT-I effective area "inferred" from the Crab pointings with some assumptions. The XRT-I effective area shown here does not includes either the quantum efficiency of the detector or transmissivity of the thermal shield and the optical blocking filter.

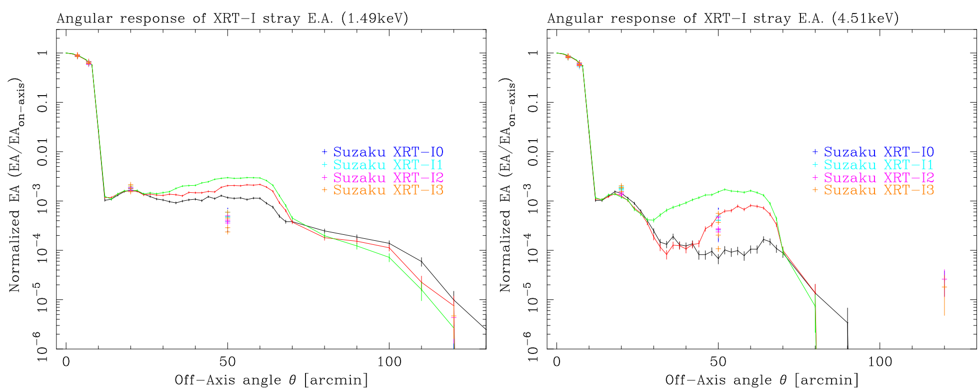

Figure 3.10: Angular responses of the XRT-I at 1.5 (left) and 4.5 keV (right) up to 2 degrees. The effective area is normalized at on-axis. The integration area is corresponding to the detector size of XIS ($17'.8 \times 17'.8$). The three solid lines in the plots correspond to different parameters of ray-tracing program while the crosses are the normalized effective area using the Crab pointings.

while the crosses are the normalized effective area using the Crab pointings. For example, the effective area of the stray lights at 1.5 keV is $\sim 10^{-3}$ at angles smaller than 70 arcmin off axis and $< 10^{-3}$ at angles larger than 70 arcmin off. The measured flux of stray lights are in good agreement with that of raytracing within an order.

3.1.3 X–ray Imaging Spectrometer (XIS)

3.1.3.1 Overview of the XIS

Suzaku has four X–ray Imaging Spectrometers (XISs), which are shown in Figure 3.11. These employ X–ray sensitive silicon charge-coupled devices (CCDs), which are operated in

Figure 3.11: The four XIS detectors before installation onto *Suzaku* .

a photon-counting mode, similar to that used in the ASCA SIS, *Chandra* ACIS, and *XMM-Newton* EPIC. The four *Suzaku* XISs are named XIS-S0, S1, S2 and S3, each located in the focal plane of an X–ray Telescope; those telescopes are known respectively as XRT-I0, XRT-I1, XRT-I2, and XRT-I3. Each CCD camera has a single CCD chip with an array of 1024×1024 picture elements ("pixels"), and covers an $18' \times 18'$ region on the sky. Each pixel is 24 μm square, and the size of the CCD is 25 mm $\times$ 25 mm. One of the XISs, XIS-S1, uses a back-side illuminated CCDs, while the other three use front-side illuminated CCDs.

A CCD has a gate structure on one surface to transfer the charge packets to the readout gate. The surface of the chip with the gate structure is called the "front side". A front-side illuminated CCD (FI CCD) detects X-ray photons that pass through its gate structures, i.e. from the front side. Because of the additional photo-electric absorption at the gate structure, the low-energy quantum detection efficiency (QDE) of the FI CCD is rather limited. Conversely, a back-side illuminated CCD (BI CCD) receives photons from "back," or the side without the gate structures. For this purpose, the undepleted layer of the CCD is completely removed in the BI CCD, and a thin layer to enhance the electron collection efficiency is added in the back surface. A BI CCD retains a high QDE even in sub-keV energy band because of the absence of gate structure on the photon-detection side. However, a BI CCD tends to have a slightly thinner depletion layer, and the QDE is therefore slightly lower in the high energy band. The decision to use only one BI CCD and three FI CCDs was made because of both the slight additional risk involved in the new technology BI CCDs and the need to balance the overall efficiency for both low and high energy photons. To minimize the thermal noise, the sensors need to be kept at $\sim -90°$C during observations.

To reduce contamination of the X–ray signal by optical and UV light, each XIS has an

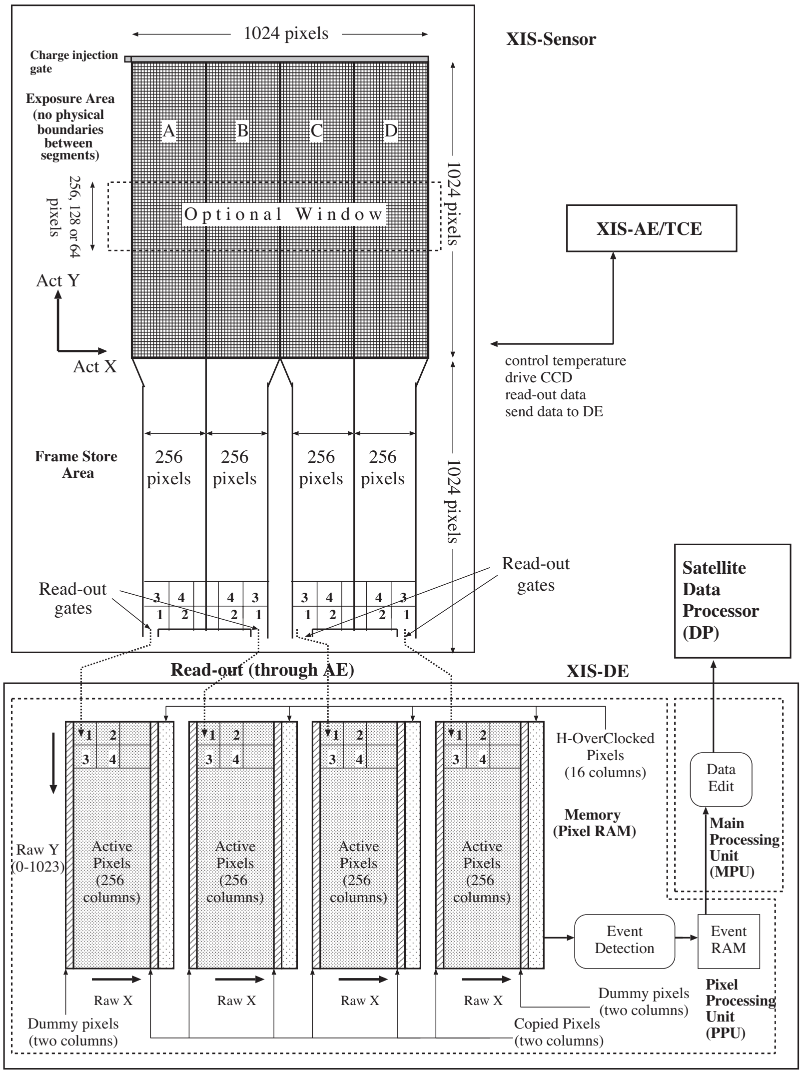

Figure 3.12: One XIS instrument. Each XIS consists of a single CCD chip with 1024×1024 X–ray sensitive cells, each 24 μm square. *Suzaku* contains four CCD sensors (XIS-S0 to S3), two AE/TCUs (AE/TCE01 and AE/TCE23), two PPUs (PPU01 and PPU23), and one MPU. AE/TCU01 and PPU01 service XIS-S0 and XIS-S1, while AE/TCE23 and PPU23 service XIS-S2 and XIS-S3. Three of the XIS CCDs are front-illuminated (FI) and one (XIS-S1) is back-illuminated (BI).

Optical Blocking Filter (OBF) located in front of it. The OBF is made of polyimide with a thickness of 1000 Å, coated with a total of 1200 Å of aluminum (400 Å on one side and 800 Å on the other side). To facilitate the in-flight calibration of the XISs, each CCD sensor has two ^{55}Fe calibration sources. One is installed on the door to illuminate the whole chip, while the other is located on the side wall of the housing and is collimated in order to illuminate two corners of the CCD. The door-mounted source will be used for initial calibration only; once the door is opened, it will not illuminate the CCD. The collimated source can easily be seen in two corners of each CCD. A small number of these X–rays scatter onto the entire CCD. In addition to the emission lines created by these sources, we can utilize a new feature of the XIS CCDs, "charge injection capability," to assist with calibration. This allows an arbitrary amount of charge to be input to the pixels at the top row of the imaging region (exposure area), i.e. the far side from the frame-store region. The charge injection capability may be used to measure the CTI (charge transfer inefficiency) of each column, or even to reduce the CTI. The latter usage, so-called spaced-row CI, is successfully demonstrated in 2006.

Fig. 3.12 provides a schematic view of the XIS system. Charge clouds produced in the CCD by the X–rays focused by the XRT are accumulated on the exposure area for a certain exposure period (typically 8 s in the "normal" mode), and the data are transferred to the Frame Store Area (FSA) after each exposure. Data stored in the Frame Store Area are read-out sequentially by the AE, and sent to the PPU after the conversion to the digital data. The data are put into the memory in PPU named Pixel RAM. Subsequent data processing is done by accessing the Pixel RAM.

3.1.3.2 Pulse Height Determination, and Hot Pixels

When a CCD pixel absorbs an X–ray photon, the X–ray is converted to an electric charge, which in turn produces a voltage at the analog output of the CCD. This voltage ("pulse-height") is proportional to the energy of the incident X–ray. In order to determine the true pulse-height corresponding to the input X–ray energy, it is necessary to subtract *Dark Levels* and correct possible *optical Light Leaks*. XIS has capability to measure them on-board.

Hot pixels are pixels which always output over threshold pulse-heights even without input signals. Hot pixels are not usable for observation, and their output has to be disregarded during scientific analysis. In the case of XIS, hot pixels are detected on-board and their positions and pulse-heights are stored in the Hot-pixel RAM and sent to the telemetry. Thus, hot pixels can be recognized on-board, and they are excluded from the event detection processes. It is also possible to specify the hot pixels manually. There are, however, some pixels which output over threshold pulse-heights intermittently. Such pixels are called flickering pixels. It is difficult to identify and remove the flickering pixels on board; they are inevitably output to the telemetry and need to be removed during the ground processing. Flickering pixels sometimes cluster around specific columns, which makes it relatively easy to identify.

3.1.3.3 Pulse Height Distribution Function

Pulse hight distribution function for a monochromatic X-ray line can be represented by a Gaussian-like peak and low energy tail component. Energy resolution for Oxygen K_α line at 0.525 keV is about 50 eV (FWHM) for BI and 40 eV for FI (Koyama et al., 2007). The fraction of the low energy tail component of *Suzaku* XIS is very small in comparison with other X-ray CCDs used in X-ray satellite mission. Figure 3.13 shows energy spectra (pulse height distribution) for a monochromatic X-ray line emission at $E = 0.5$ keV, in comparison with X-ray CCDs on-board *XMM-Newton*. Clear peaks are shown by *Suzaku* FI/BI CCDs. Actual energy spectra of a SNR 1E0102-72 is shown in Figure 3.14. K_α lines of O VII (0.57 keV) and O VIII (0.65 keV) are clearly resolved with excellent energy resolution. Thus *Suzaku* is the most suitable to study diffuse hot plasma which can be characterized by emission lines.

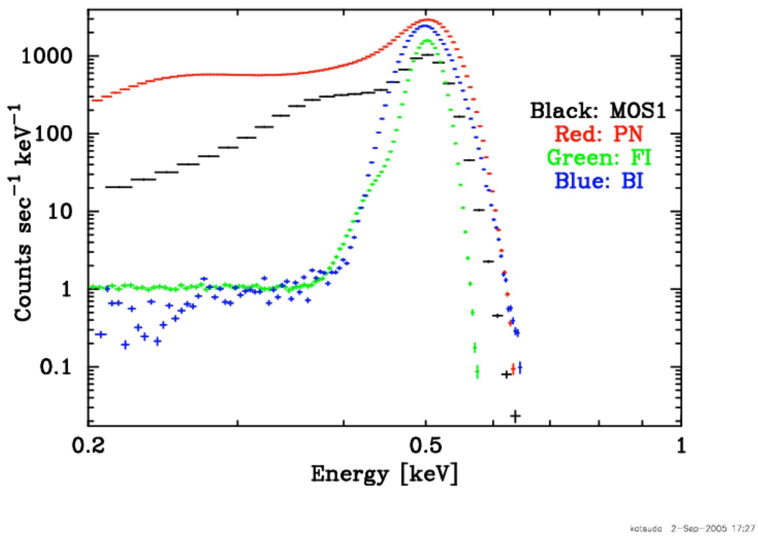

Figure 3.13: Energy spectra for monochromatic line by *Suzaku* FI/BI sensors and PN and MOS1 CCD onboard *XMM-Newton*.

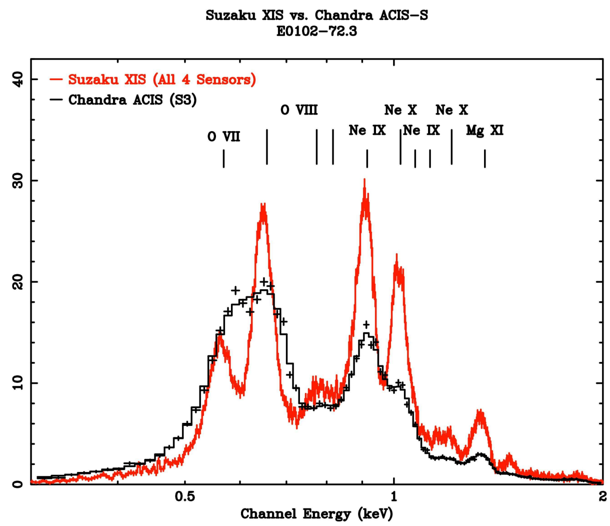

Figure 3.14: Energy spectra of SNR 1E0102-72 by a sum of 4 XIS of *Suzaku* and S3 CCD onboard *Chandra*. The O VII and O VIII lines are clearly resolved by *Suzaku* .

3.1.3.4 Photon pile-up

The XIS is essentially a position-sensitive integrating instrument, with the nominal interval between readouts of 8 s. If during the integration time one or more photons strike the same CCD pixel, or one of its immediate neighbors, these cannot be correctly detected as independent photons: this is the phenomenon of photon pile-up. Here, the modest angular resolution of the *Suzaku* XRT is an advantage: the central 3×3 pixel area receives 2% of the total counts of a point source, and $\sim$10% of the counts fall within $\sim$0.15 arcmin of the image center. The pile-up effect is negligible for the object studied in this thesis.

3.1.3.5 XIS background rate

All four XISs have low backgrounds, due to a combination of the *Suzaku* orbit and the instrumental design. Below 1 keV, the high sensitivity and energy resolution of the XIS-S1 combined with this low background means that *Suzaku* is the superior instrument for observing soft sources with low surface brightness.

In the XIS, the background originates from the cosmic X–ray background (CXB) combined with charged particles (the non-X–ray background, or NXB). When observing the dark earth (*i.e.* the NXB), the background rate between 1-12 keV in is 0.11 cts/s in the FI CCDs and 0.40 cts/s in the BI CCD; see Figure 3.15. Note that these are the fluxes after the grade selection is applied with only grade 0, 2, 3, 4 and 6 selected. There are also fluorescence features arising from the calibration source as well as material in the XIS and XRTs. The Mn lines are due to the scattered X-rays from the calibration sources. As shown in Table 3.5 the Mn lines are almost negligible except for XIS-S0. The O lines are mostly contamination from the day earth (3.1.3.5.2). The other lines are fluorescent lines from the material used for the sensor. Table 3.5 shows the current best estimates for the strength of these emission features, along with their 90% upper and lower limits.

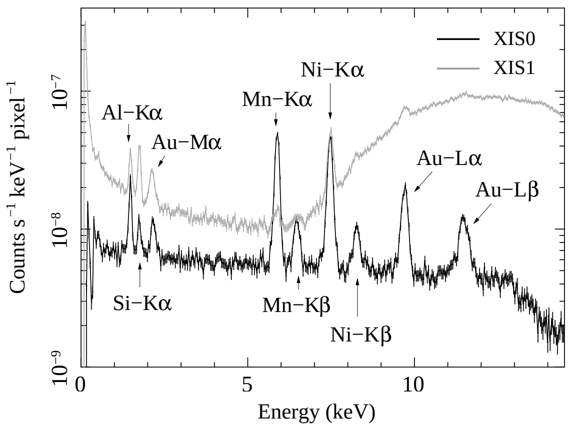

Figure 3.15: The night earth X-ray background (NXB) spectra for XIS-S0 and XIS-S1. The prominent fluorescent lines marked (See Table 3.5).

3.1.3.5.1 Out-of-time events X-ray photons detected during the frame-store transfer do not correspond to the true image, but instead appear as a streak or blur in the readout

Table 3.5: Energies and count rates of the line components in the NXB spectra.

Line	Energy (keV)	Count rate (10^{-9} cts s^{-1} pixel^{-1}) XIS0	XIS1	XIS2	XIS3
Al-Kα	1.486	1.45 ± 0.11	1.84 ± 0.14	1.41 ± 0.10	1.41 ± 0.10
Si-Kα	1.740	0.479 ± 0.081	2.27 ± 0.15	0.476 ± 0.080	0.497 ± 0.082
Au-Mα	2.123	0.63 ± 0.093	1.10 ± 0.13	0.776 ± 0.097	0.619 ± 0.092
Mn-Kα	5.895	6.92 ± 0.19	0.43 ± 0.14	1.19 ± 0.13	0.76 ± 0.11
Mn-Kβ	6.490	1.10 ± 0.11	0.26 ± 0.13	0.40 ± 0.11	0.253 ± 0.094
Ni-Kα	7.470	7.12 ± 0.19	7.06 ± 0.37	8.01 ± 0.20	7.50 ± 0.20
Ni-Kβ	8.265	0.96 ± 0.10	0.75 ± 0.22	1.16 ± 0.11	1.18 ± 0.11
Au-Lα	9.671	3.42 ± 0.15	4.15 ± 0.49	3.45 ± 0.15	3.30 ± 0.15
Au-Lβ	11.51	2.04 ± 0.14	1.93 ± 0.48	1.97 ± 0.14	1.83 ± 0.14

The count rates are obtained from the whole CCD chip excluding the calibration source regions. Errors are 90 % confidence level.

Table 3.6: Origins of the fluorescence lines in the NXB spectra.

Line	Origin
Al-Kα	Optical blocking filter, housing, alumina substrate to mount CCD
Si-Kα	CCD (Si fluorescence line)
Au-Mα, Lα, Lβ	Housing, CCD substrate, heatsink
Mn-Kα, Kβ	Scattered X-rays from calibration sources
Ni-Kα, Kβ	Housing, heatsink

direction. These events are called out-of-time events., and they are an intrinsic feature of CCD detectors. Similar streaks are seen from bright sources observed with *Chandra* and *XMM-Newton* . Out-of-time events produce a tail in the image, which can be an obstacle to detecting a low surface brightness feature in an image around a bright source. Thus the out-of-time events reduce the dynamic range of the detector. Since XIS spends 25 ms in the frame-store transfer, about 0.3% (= $0.025/8 \times 100$) of all events will be out-of-time events. However, because the orientation of the CCD chip is different among the sensors, one can in principle distinguish a true feature of low surface brightness and the artifact due to the out-of-time events by comparing the images from two or more XISs.

3.1.3.5.2 Day Earth Contamination When the XIS field of view is close to the day earth (i.e. Sun lit Earth), fluorescent lines from the atmosphere contaminate low-energy part of the XIS data, especially in the BI chip. Most prominent is the oxygen line, but the nitrogen line may be also noticed (see Fig. 3.15–right). These lines are mostly removed when we apply the standard data screening criteria (XIS FOV is at least 20 degree away from the day earth) during the ground processing. However, small amount of contamination can remain. This contamination may be further reduced if we subtract appropriate background. This subtraction, however, may be imperfect.

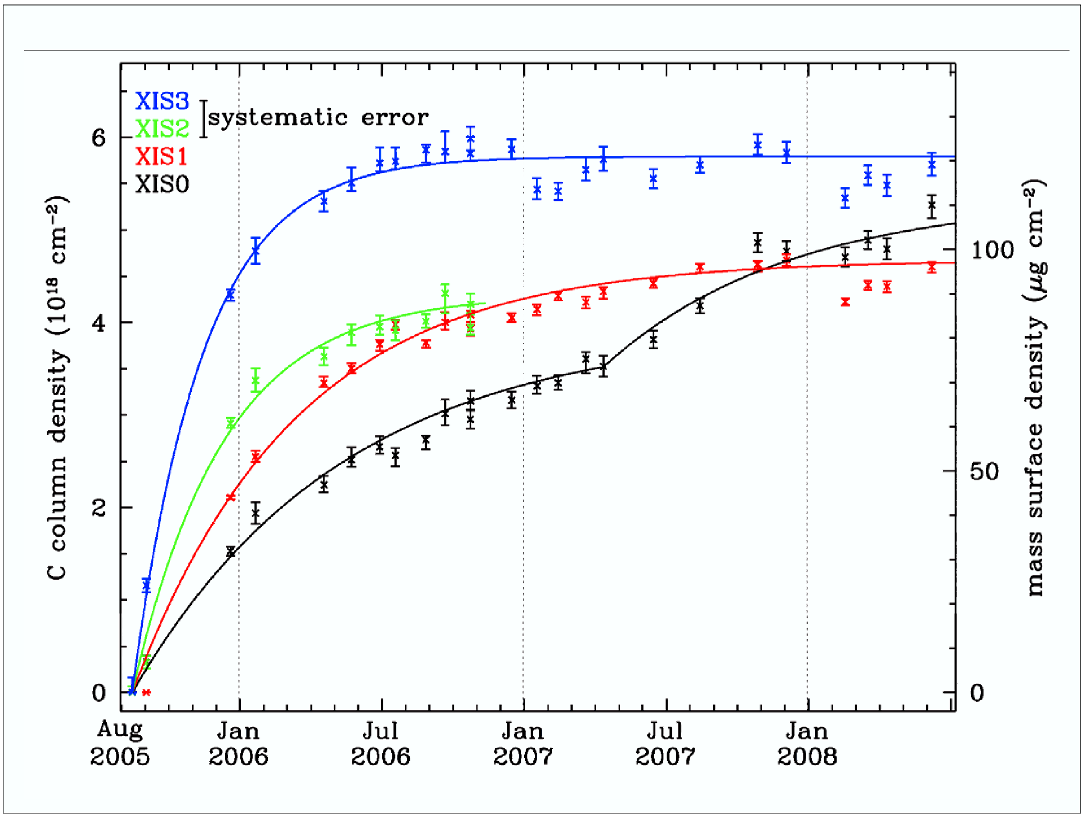

Figure 3.16: Trend plot of contamination column density (carbon) and mass surface density for each XIS sensor.

3.1.3.6 Radiation Damage and On-board Calibration of the XIS

The performance of X-ray CCDs gradually degrades in the space environment due to the radiation damage. This generally causes an increase in the dark current and a decrease of the charge transfer efficiency (CTE). In the case of XIS, the increase of the dark current is expected to be small due to the low (–90°C) operating temperature of the CCD. However, a decrease in CTE is unavoidable. Thus, continuous calibration of CCD on orbit is essential to the good performance of the XIS. This is calibrated using a radio isotope source and charge injection as explained below:
(i) Each XIS carries ^{55}Fe calibration sources near the two corners of the chip, which will be used to monitor the instrument gain.
(ii) Each XIS CCD is equipped with charge injection capability, which may be useful to measure and even suppress CTI.

3.1.3.7 Contamination on the OBFs

After the launch of *Suzaku*, a time and position dependent contamination of the XIS optical blocking filter (OBF) was found. The source is probably outgassing from the satellite. The level of contamination increases with time and is different from sensor to sensor. The *Suzaku* team investigated possible materials that caused the contamination and found DEHP (a kind of rubber), which evaporates in high temperature is a candidate. The composition of DEHP is $C_{24}H_{38}O_4$, i.e., C/O=6. The time and position dependence of the contamination thickness has been empirically modeled by the XIS team as shown in Figure 3.16, assuming C/O=6. The uncertainties in composition, thickness and position dependence produce the largest systematic uncertainty on the effective area and response functions, in particular for diffuse emissions, at the time of this study.

3.1.3.8 On-ground event selection

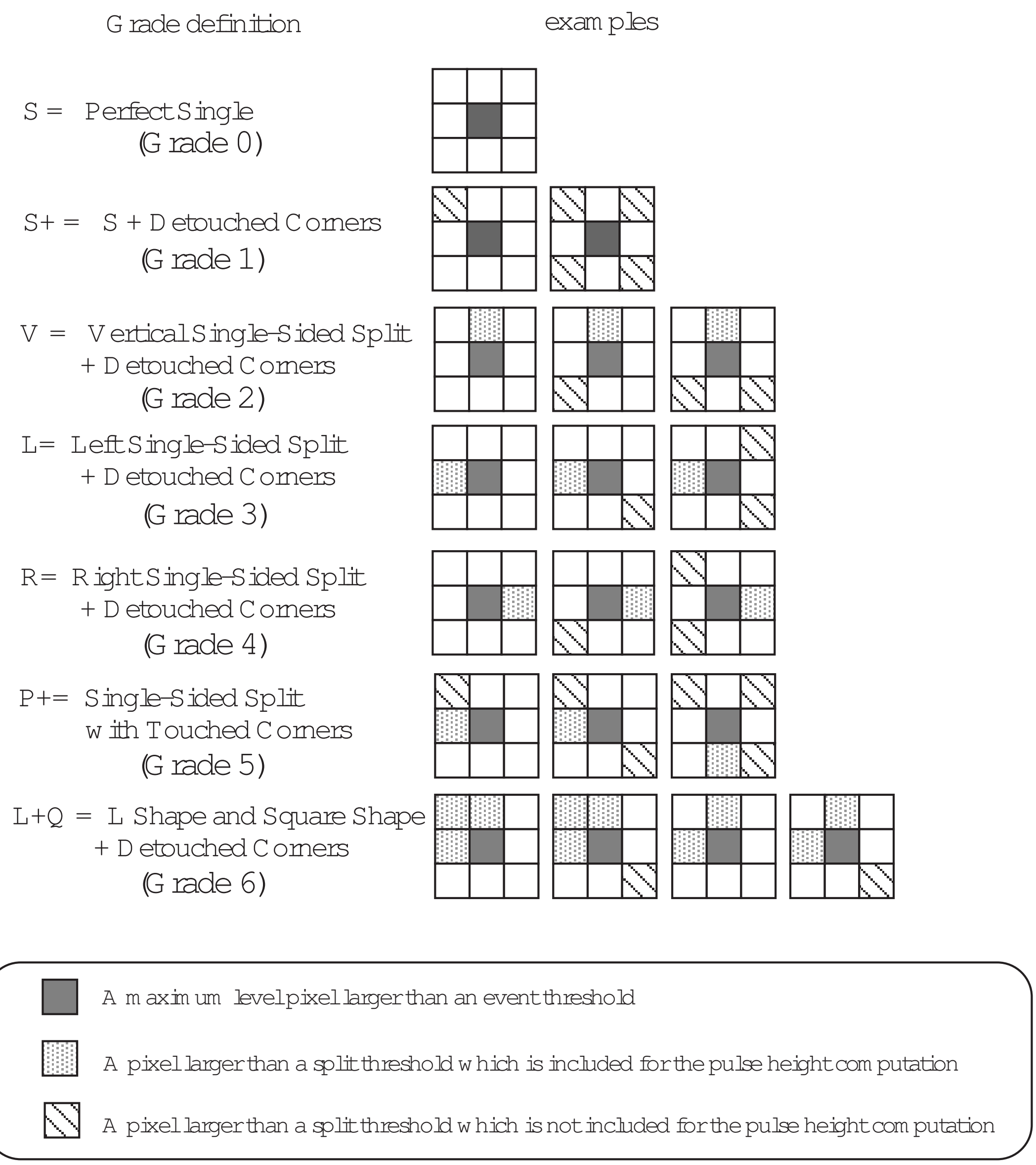

Figure 3.17: Definition of GRADE of CCD events.

Internal (non X-ray) background events can be effectively removed using the pattern on CCD pixels (GRADE), the position (STATUS) and time of an event. The definition of GRADE is shown in Figure 3.17. Most of X-ray events take GRADE = 0, 2, 3, 4, or 6. On the other hand, most of the events of other GRADEs are dominated by non X-ray events, and should be excluded. STATUS parameter stores the information of pixel quality of an event. Known hot pixels, bad CTE columns, flickering pixels, and pixels on the segment boundaries can be removed by selecting the events with STATUS$<$ 131072. The parameters used in good time interval (GTI) selection are shown in Table 3.7. The signal to noise ratio can be improved with an appropreate GTI criteria, indicated in Table 3.7.

Table 3.7: Parameters used in GTI selection of *Suzaku*

Parameter	Definition	Recommended value to use
SAA	Whether the satellite was in the SAA[a] or not	eq.0
T_SAA	Time after the last SAA duration (s)	> 255
ELV	Elevetion angle from the Earth limb (degree)	> 5
DYE_ELV	Elevation angle from the day Earth limb (degree)	> 20
COR	Cut off rigidity of the cosmic ray (GeV/c/particle)	> 8

[a]: South Atlantic anomaly

3.2 The *ACE* and *WIND* satellite for monitoring solar-wind parameters

3.2.1 *ACE* satellite

The Advanced Composition Explorer (ACE) was launched August 25, 1997 by a McDonnell-Douglas Delta II 7920 launch vehicle from the Kennedy Space Center in Florida. *ACE* orbits the Lagrangian 1 point which is a point of Earth-Sun gravitational equilibrium about 1.5 $\times 10^6$ km from the Earth and 1.485 $\times 10^8$ km from the Sun(see Figure 3.18 left). By orbiting the L1 point, *ACE* stays in a relatively constant position with respect to the Earth as the Earth revolves around the sun.

ACE carries nine major scientific instruments for sampling low-energy particles of solar origin and high-energy galactic particles ; Cosmic Ray Isotope Spectrometer (CRIS); Electon, Proton, and Alpha Monitor (EPAM); Magnetometer (MAG); Solar Energetic Particle Ionic Charge Analyzer (SEPICA); Solar Isotope Spectrometer (SIS); Solar Wind Ionic Charge Spectrometer (SWICS); Solar Wind Ion Mass Spectrometer (SWIMS); Ultra Low Energy Isotope Spectrometer (ULEIS) and Solar Wind Electon, Proton, and Alpha Monitor (SWEPAM). The spacecraft spins at 5 rpm, with the spin axis generally pointed along the Earth-sun line and most of the scientific instruments on sunward deck (see Figure 3.18 right). In this thesis, we mainly used the data of SWEPAM on-board *ACE* for obtaining the proton density and speed to calculate the proton flux level.

3.2.2 *WIND* satellite

WIND satellite was launched on November 1, 1994 and is the first of two NASA spacecraft in the Global Geospace Science initiative and part of the International Solar Terrestrial Physics Project. *WIND* orbits the Lagrangian 1 point. Wind carries an array of scientific

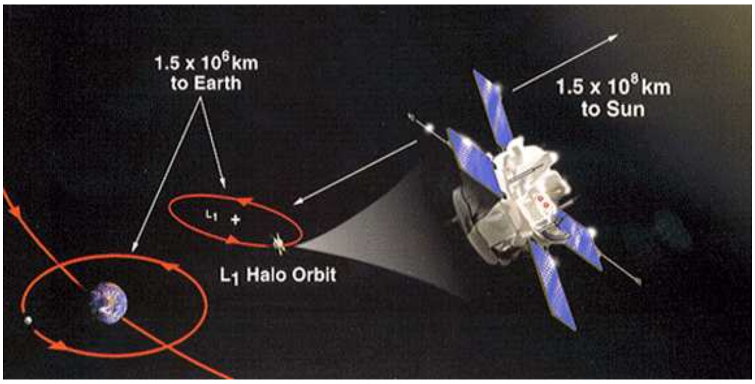

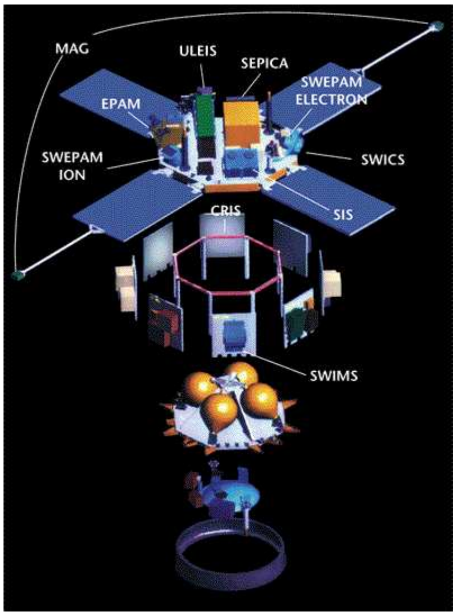

Figure 3.18: Left: The orbit of ACE satellite. Earth and Lunar orbit are also shown. Right: A schematic view of the ACE satellite, showing the configuration of its onboard instrument.

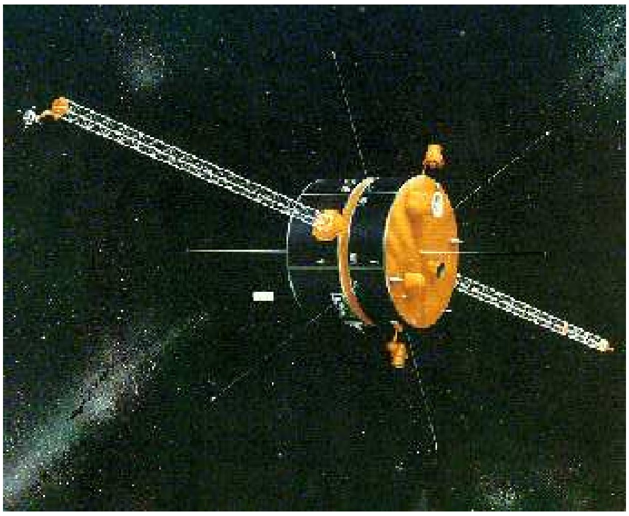

Figure 3.19: A schematic vies of $WIND$ satellite.

instruments for measuring the charged particles and electric and magnetic fields that characterize the interplanetary medium, solar wind and a plasma environment. WIND provides nearly continuous monitoring of the solar wind conditions near Earth. In the WIND data, we mainly used Solar Wind Experiment (SWE) data, which provides the high time resolution 3 dimensional velocity distributions of the ion component of the solar wind, for ions with energies ranging from 200 eV to 8.0 keV.

Chapter 4

Observations and Data reduction

4.1 Observations

In order to study soft X-ray diffuse background, we selected the observation fields that are apart from local diffuse emission structures such as North Polar Spur or Cygnus Superbubble, and are separated from bright X-ray point sources like X-ray binaries and blazars. The observation fields analyzed in this paper are shown in Figure 4.1, and observation log and position are summarized in Tables 4.1 and 4.2, respectively.

GB1428+4217 (ID 1) is the observation for aiming high-z blazar, however the point source contained in this data is not so bright in the soft energy band where we are interested, and has no line emission feature in the spectrum. This could have little effect on the soft X-ray diffuse background emission, thus in data reduction we removed the region which contains this point source and utilized the outside region which are usually used as a background region in point source analysis. The detail criteria of point source exclusion is shown in later.

The directions of PKS2155_obs1(ID 7) and PKS2155_obs2(ID 6) are inside the Radio Loop I. However, the R45 band intensity in the *ROSAT* map is weaker than that in the Northern Hemisphere, that is the North Polar Spur, we thus decided to use these observations. We need to keep it in mind that these regions might be contaminated by emission from Loop I. Although the emission of these targets may be influenced by the local one, we analyzed the data since its effect is expected to be small due to their high galactic latitude, these can be used as a reference of low galactic longitude region.

The emission feature of MBM12 on cloud (ID R1) and Midplane235 (ID R2) are different from the other observations. MBM12 on cloud (ID R1) is the observation towards the molecular cloud MBM12 at the distance estimated to in the range from 60 ± 30 to 275 ± 65 pc. Since the column density in this direction is $4 \times 10^{21}\mathrm{cm}^{-2}$, whose transmission of O VII and O VIII emission is ~ 5 % and 10 % respectively, the detected emission thus arise from $\lesssim$ 100 pc. As for Midplane235 (ID R2) observation towards galactic latitude $b = 0$, the column density in this direction is estimated to 9×10^{21} which is opaque to O VII and O VIII line emission. The mean free path of O VII emission in this direction is ~ 400 pc assuming the galactic midplane hydrogen density to be 1 cm^{-3}, this emission is from within 400 pc.

The analysis results of the seven data sets North Ecliptic Pole 1 (NEP1), MBM12 off cloud (M12off), LMC X-3 Vicinity (LX-3), Off Filament(Off-FIL), On Filament(On-FIL), MBM12 on cloud (M12on) and Midplane235 (MP235) have been already published. For data sets M12on and MP235, we simply adopt the results from Masui et al. (2008) since the data screening criteria and reduction procedure of them are the same as those in this paper. For data LX-3, all the data reduction done by Yao et al. (2009) is consistent with that shown in this section. Since Fujimoto et al. (2007) (NEP1, data ID 13) and Smith et al. (2007b) (M12off, data ID 11) used the data processed with older (version 0.7) software, we re-analyzed the data from the data reduction.

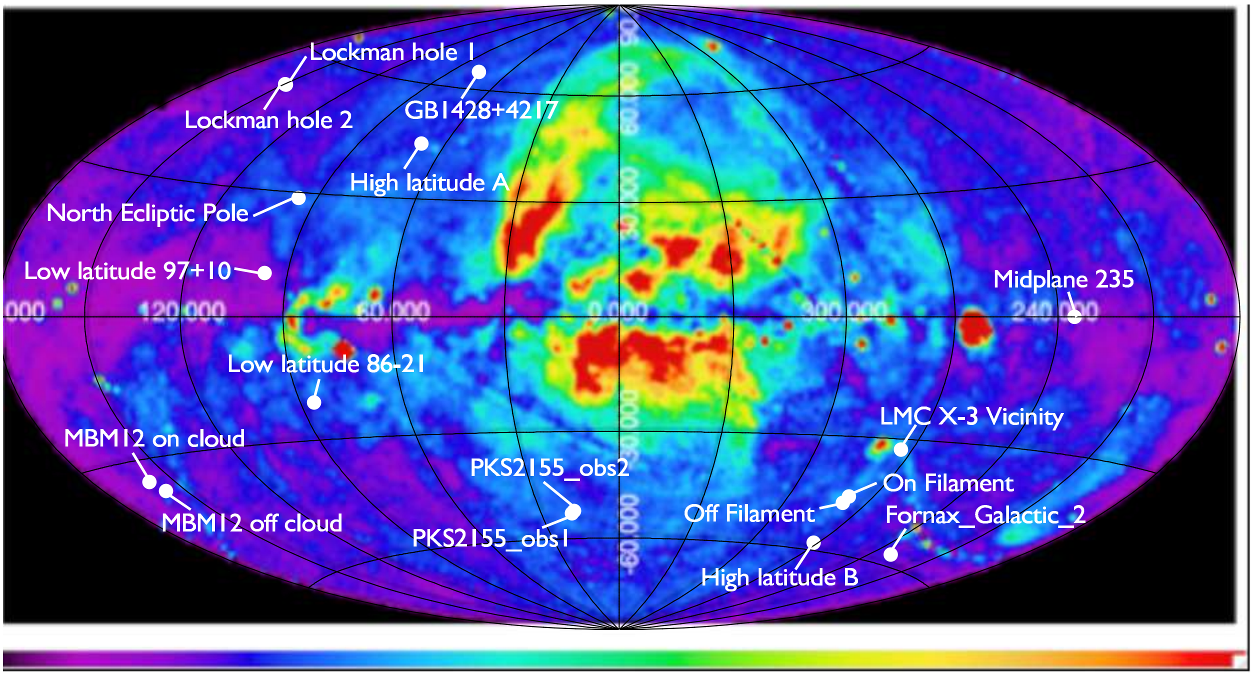

Figure 4.1: *Suzaku* observation fields studied in this thesis are presented as circles, which are plotted in Aitoff projection of the sky with the Galactic center at the center of the figure and Galactic longitude increasing to the left. The backside color map is *ROSAT* R45 band image.

Table 4.1: Observation log

Data set ID	Filed Name (Short Name)	Obs ID(phase[g])	Date (start, end)	Exposure (ks) Total	Filtered
1	GB1428+4217 (GB)	701092010(AO1)	(2006-06-12T17:11:37 , 2006-06-13T20:00:24)	48.7	34.9
2	High latitude B (HL-B)	500027020(SWG)	(2006-02-17T22:24:49 , 2006-02-20T12:30:24)	103.6	29.7
3	FORNAX (FOR)	802040010(AO2)	(2007-06-29T08:05:04 , 2007-06-29T23:45:14)	21.0	16.4
4	Lockman hole 2 (LH-2)	101002010(CAL)	(2006-05-17T17:44:06 , 2006-05-19T19:03:18)	80.4	40.0
5	Lockman hole 1 (LH-1)	100046010(CAL)	(2005-11-14T05:41:37 , 2005-11-15T19:55:18)	77.0	61.7
6	PKS2155_obs2* (PKS2)	503083010(AO3)	(2008-05-02T08:31:41 , 2008-05-04T17:30:19)	87.3	58.2
7	PKS2155_obs1* (PKS1)	503082010(AO3)	(2008-04-29T18:32:39 , 2008-05-02T08:30:08)	90.2	46.9
8	Off Filament[a] (Off-FIL)	501001010(AO1)	(2006-03-01T16:56:01 , 2006-03-02T22:29:14)	80.1	59.6
9	On Filament[a] (On-FIL)	501002010(AO1)	(2006-03-03T20:52:00 , 2006-03-06T08:01:19)	101.4	59.2
10	High latitude A (HL-A)	500027010(SWG)	(2006-02-14T07:01:24 , 2006-02-15T23:08:14)	73.6	53.2
11	MBM12 off cloud[b] (M12off)	501104010(SWG)	(2006-02-06T15:33:59 , 2006-02-08T14:50:19)	75.3	51.0
12	LMC X-3 Vicinity[c] (LX-3)	500031010(SWG)	(2006-03-17T14:25:12 , 2006-03-19T22:00:12)	82.0	56.1
13	North Ecliptic Pole 1[d] (NEP1)	100018010(SWG)	(2005-09-02T14:43:43 , 2005-09-04T15:00:14)	106.2	58.7
14	North Ecliptic Pole 2 [d] (NEP2)	500026010(SWG)	(2006-02-10T06:08:12 , 2006-02-12T02:00:24)	75.6	16.5
15	Low latitude 86-21 (LL21)	502047010(AO2)	(2007-05-09T01:56:32 , 2007-05-10T23:55:14)	81.5	57.0
16	Low latitude 97+10 (LL10)	503075010(AO3)	(2008-04-15T03:10:45 , 2008-04-16T21:20:14)	79.8	40.8
R1	MBM12 on cloud[e] (M12on)	500015010(SWG)	(2006-02-03T23:02:29 , 2006-02-06T15:30:18)	102.9	68.0
R2	Midplane 235[f] (MP235)	502021010(AO2)	(2007-04-22T20:39:20 , 2007-04-25T10:04:24)	89.6	53.0

Results previously published by [a] Henley & Shelton (2008), [b] Smith et al. (2007b), [c] Yao et al. (2009), [d] Fujimoto et al. (2007), [e] Smith et al. (2007b); Masui et al. (2008), [f] Masui et al. (2008)
[g] Observation phase. AO1, AO2, AO3 is for first, second and third announcement of opportunity. SWG is for Science Working Group. CAL is for calibration observation

Table 4.2: Position of Observations

ID	Filed Name	(RA, Dec)	(ℓ, b)	(Lon, Lati)
1	GB	(217.6 , 42.1)	(75.9 , 64.9)	(194.2 , 52.7)
2	HL-B	(38.7 , -52.3)	(272.4 , -58.3)	(4.4 , -61.4)
3	FOR	(50.0 , -32.1)	(230.8 , -57.5)	(35.2 , -48.2)
4	LH-2	(162.9 , 57.3)	(149.7 , 53.2)	(137.1 , 45.1)
5	LH-1	(163.4 , 57.6)	(149.0 , 53.2)	(137.2 , 45.5)
6	PKS2[a]	(330.2 , -30.0)	(18.2 , -52.6)	(321.7 , -16.7)
7	PKS1[a]	(329.2 , -30.5)	(17.2 , -51.9)	(320.7 , -16.9)
8	Off-FIL	(50.0 , -62.4)	(278.7 , -47.1)	(354.8 , -72.6)
9	On-FIL	(53.2 , -63.5)	(278.6 , -45.3)	(354.1 , -74.4)
10	HL-A	(246.2 , 43.5)	(68.4 , 44.4)	(228.8 , 63.5)
11	M12off	(41.3 , 18.3)	(157.3 , -36.8)	(44.5 , 2.3)
12	LX-3	(83.5 , -63.9)	(273.4 , -32.6)	(41.2 , -86.2)
13	NEP1	(272.8 , 66.0)	(95.8 , 28.7)	(334.8 , 88.7)
14	NEP2	(272.8 , 66.0)	(95.8 , 28.7)	(334.8 , 88.7)
15	LL21	(332.3 , 30.2)	(86.0 , -20.8)	(347.6 , 38.4)
16	LL10	(311.8 , 60.1)	(96.6 , 10.4)	(0.7 , 70.6)
R1	M12on[b]	(44.0 , 19.5)	(159.2 , -34.5)	(47.2 , 2.6)
R2	MP235[c]	(113.3 , -19.5)	(235.0 , 0.0)	(119.5 , -40.6)

[a] This direction is near the local emission structure Radio Loop I where the standard criteria for region selection is inapplicable. It is noted that the emission from this direction can be possibly affected by the local one.
[b] The observation is towards the molecular cloud. The line emission of O VII and O VIII from this direction is expected to be local within the distance 275 pc.
[c] The observation is towards midplane ($b = 0°$), the line emission of O VII and O VIII from this direction is expected to be local within ∼400 pc.

4.2 Data reduction

4.2.1 Data screening

In all the observations, the XIS was set to the normal clocking mode and the data format was either 3 × 3 or 5 × 5. The Spaced-raw Charge Injection (SCI) was used for the data FORNAX(FOR), PKS2155_obs2(PKS2), PKS2155_obs1(PKS1), Low latitude 86-21(LL21), Low latitude 97+10 (LL10) and Midplane235 (MP235). We used version 2.0 processed *Suzaku* data and the event files of 3 × 3 and 5 × 5 observation mode were merged. As described in Chapter 3, XIS-BI has a larger effective area than the sum of XIS-FIs below 1 keV. Since we were interested in energy band below 1 keV and in order to avoid increasing systematic errors by adding different CCD data, only XIS-BI was used for the later analysis.

Although no unpredicted background flare occurs to *Suzaku* observations, the count rate of non X-ray events of the XIS depends on the angle of the sight line against the Earth's rim. The contamination of the fluorescence lines of the atmosphere of the Earth is significant when the field of view (FOV) of the satellite is near the sunlit Earth. In addition, it is known that the background level becomes extremely high when the satellite is in South Atlantic Anomaly (SAA) or in regions where the cut-off rigidity (COR) of the cosmic ray is low. Therefore we first cleaned the data using the selection criteria: elevation from sunlit/dark earth rim > 20/5 deg, cut off rigidity > 8 GV.

4.2.1.1 Exclusion of the Solar X-ray

Solar X-ray can scatter off the earth's atmosphere into the telescope, which is either by Thompson scattering or fluorescence, and could contaminate the spectrum. As *Suzaku* orbits the Earth with the fixed pointing, the column density of the atmosphere along the line of sight, which depends on the elevation of the satellite, varies rapidly and can affects the intensity of scattered X-ray. As we have great interest in O VII emission lines around 0.56 keV, we checked the dependency of the 0.4 - 0.7 keV counting rate on the Oxygen column density of the sunlit atmosphere in the line of sight using the MSIS atmosphere model (see Fujimoto et al. (2007); Smith et al. (2007b); Miller et al. (2008)). As shown in Figure 4.2, we found that the counting rate was constant as a function of the column density for the cleaned data. Thus there is no significant neutral O emission from Earth atmosphere in the filtered data.

4.2.1.2 Exclusion of the geocoronal SWCX

The spectrum below 1 keV could be contaminated by the solar wind charge exchange (SWCX) induced emission from the geocorona. For some data sets of soft X-ray diffuse emission observed with *Suzaku* XIS1, we extracted the spectra sorted by proton flux of solar wind, and investigated the relation of the threshold of proton flux with O VII line intensity in the spectrum while proton flux is below the threshold. We found that O VII line intensity could be affected by geocoronal SWCX when the threshold of proton flux is larger than 4×10^8 protons s^{-1} cm^{-2} (see also Mitsuda et al. (2007)). For example, Figure 4.3 is the comparison of two spectra of High latitude B (HL-B) observation while the proton flux was higher and lower than 4×10^8 protons s^{-1} cm^{-2} and shows a significant difference between the two spectra in the energy bins containing the O VII emission. Therefore, as the last stage of the data reduction, we removed time intervals in which the data is contaminated by the SWCX from the geocorona. We calculated the solar-wind proton flux using ACE SWEPAM data[1]. The ACE SWEPAM data is not available for certain time periods. In that cases we used WIND SWE data [2] or OMNI data from CDAWeb (Coordinated Data Analysis Web) [3]. The proton flux and XIS-BI light curve in energy range of 0.3-2 keV in each observation period are shown in Figure 4.4.

In Table 4.3, we summarize the process that we applied to remove the time interval which are suspected to be contaminated by the SWCX from the geocorona.

For Low latitude 86-21(LL21), Lockman hole 1 (LH-1), Off Filament(Off-FIL), PKS2155_obs2(PKS2) and GB1428+4217 (GB), the proton flux was always below 4×10^8 protons s^{-1} cm^{-2}. We thus decided to use the whole data(Table 4.3 case (1)).

[1] The data available at http://www.srl.caltech.edu/ACE/ACS/
[2] The data available at http://web.mit.edu/afs/athena/org/s/space/www/wind.html
[3] The data available at http://cdaweb.gsfc.nasa.gov/cdaweb/sp_phys/

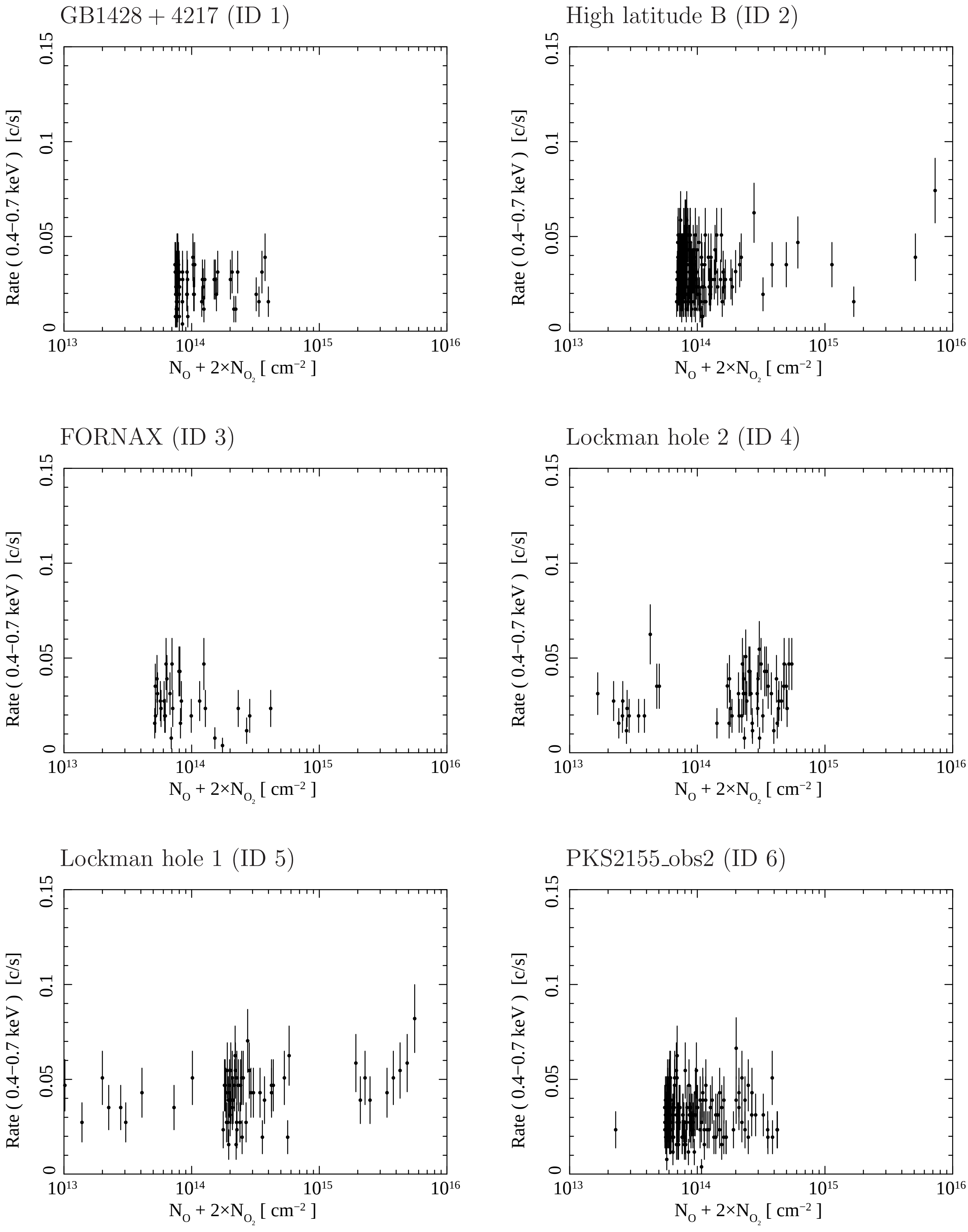

Figure 4.2: The 0.4-0.7 keV count rate of each observation in 256 sec bins as a function of Oxygen column density of the sunlit atmosphere in the line of sight using the MSIS atmosphere model (see Fujimoto et al. (2007), Smith et al. (2007b), Miller et al. (2008)).

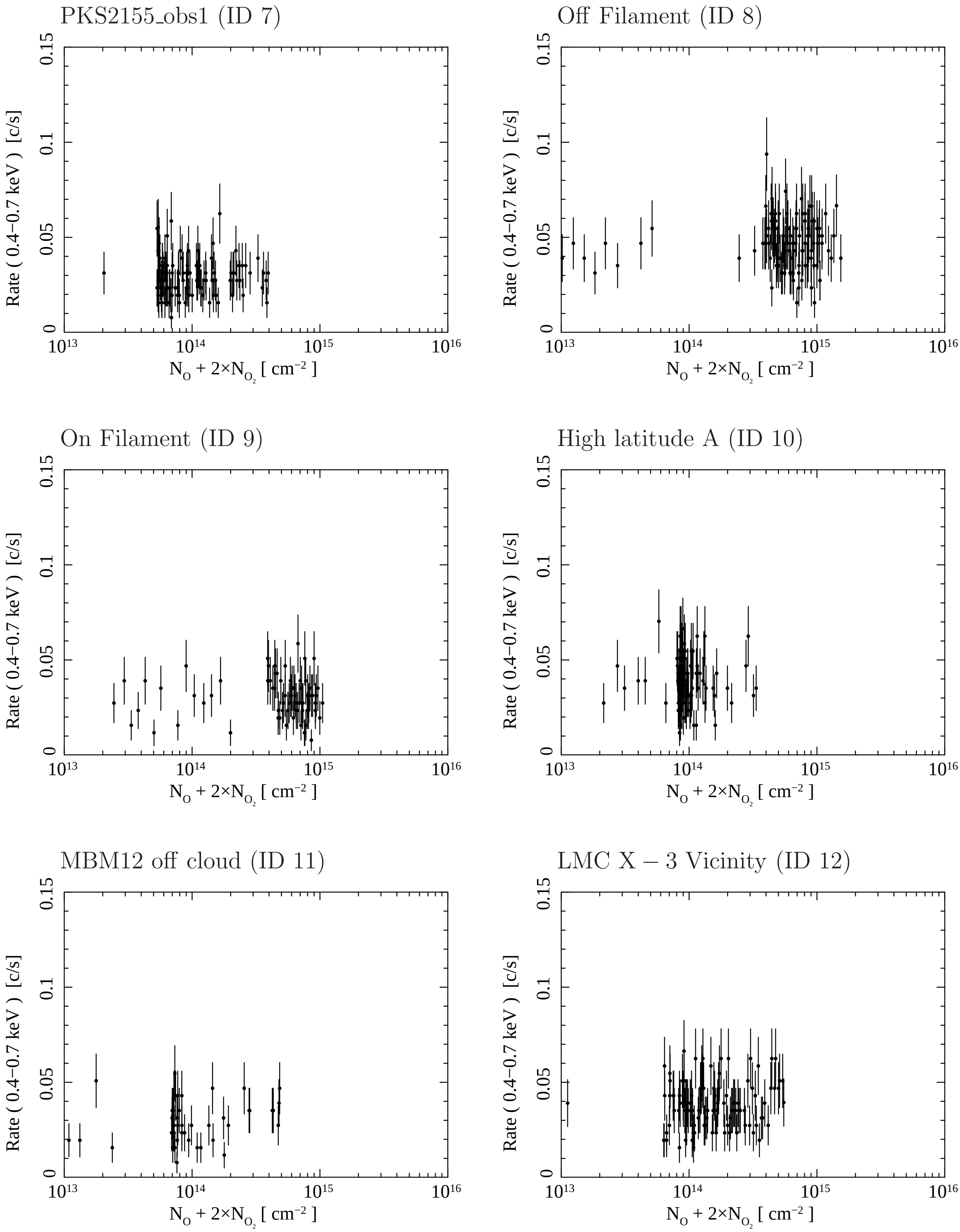

Figure 4.2: *Continued*

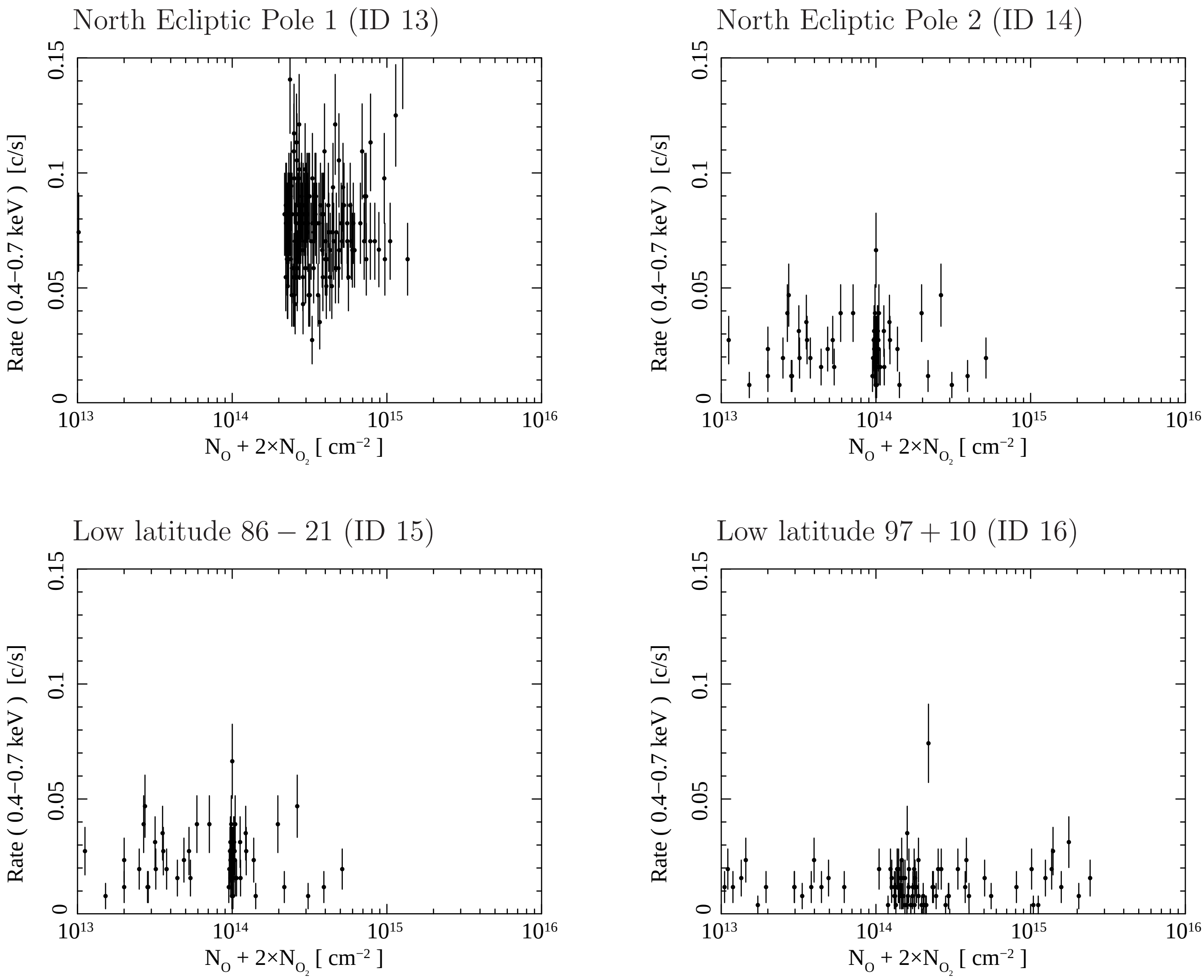

Figure 4.2: *Continued*

On the other hand, for North Ecliptic Pole 1 (NEP1), North Ecliptic Pole 2 (NEP2) Low latitude 97+10 (LL10) , Lockman hole 2 (LH-2), High latitude B (HL-B), LMC X-3 Vicinity (LX-3), On Filament(On-FIL), PKS2155_obs1(PKS1) and FORNAX(FOR), the proton flux exceeded the threshold during a significant fraction of observation time, but there still remains observation time in which the proton flux was lower than the threshold (Table 4.3 case (2)). Thus we subdivided those data into two subsets according to the proton flux, respectively. Then we constructed the energy spectra and compared them. We found significant (more than 2σ) difference as shown in Figure 4.3 between the two spectra for five data sets(Table 4.3 case (2a)): High latitude B (HL-B) , Lockman hole 2 (LH-2), North Ecliptic Pole 1 (NEP1), North Ecliptic Pole 2 (NEP2), On Filament(On-FIL) and PKS2155_obs1(PKS1). Therefore, for these data sets, we decided to use only the time intervals in which the proton flux was lower than 4×10^8 protons s^{-1} cm^{-2}.

For the observation of FORNAX(FOR), LMC X-3 Vicinity (LX-3) and Low latitude 97+10 (LL10), we found no significant difference between the two spectra with proton flux is higher and lower than threshold (Table 4.3 case (2b)).

The probability of a contamination by the SWCX from the geocorona increases if the shortest Earth-to-magnetopause (ETM) distance is $\lesssim 10$ Earth radius ($R_{\rm E}$) (Fujimoto et al., 2007). Here, the magnetopause is defined to be the lowest position along the line of sight where geomagnetic field is open to interplanetary space. We calculated the ETM distance every 256 s of all the observation periods using the T96 magnetic field model (Tsyganenko & Sitnov, 2005). We obtained the interplanetary plasma parameters required for the calculations from the CDAWeb. Figure 4.5 shows the calculated ETM distance and position of magnetopause in GSM coordinates in the observation period of High latitude A(HL-A), MBM12 off cloud (M12off), LMC X-3 Vicinity (LX-3), Low latitude 97+10 (LL10) and FORNAX(FOR).

For the FORNAX(FOR), the two spectra while higher and lower proton flux than 4×10^8 protons s^{-1} cm^{-2} do not show the significant difference. The ETM distance always stayed above $\sim 10\ R_{\rm E}$ during the proton flux above the threshold (Table 4.3 case (2b-1)). We decided to use the whole data.

During the Low latitude 97+10 (LL10) and Off Filament (Off-FIL) observation, the ETM distance occasionally dropped down to $< 10R_{\rm E}$ while proton flux are higher than threshold. We decided to simply discard the time intervals with high proton fluxes, because we still have enough statistics (Table 4.3 case (2b-2)).

For the High latitude A(HL-A), the proton flux stayed in the range of $(4-7)\times10^8$ protons s^{-1} cm^{-2}. Thus we can not compare spectra with low and high proton fluxes. We thus subdivided both the data according to the ETM distance and created two energy spectra with the ETM distance $= 5 - 10R_{\rm E}$ and $> 10R_{\rm E}$, respectively. There were small fraction of data with the ETM distance $< 5R_{\rm E}$. We decided to discard them. We found that the two spectra with different ETM distances show no significant difference (Table 4.3 case (3)). Thus we will use the data with the ETM distance $> 5R_{\rm E}$.

For the MBM12 off cloud (M12off), the proton flux stayed at a level of $\sim 5\times10^8$ protons s^{-1} cm^{-2}. In addition, the ETM distance stayed in the range of $7 - 9R_{\rm E}$. Therefore we cannot compare the spectrum as in the case of High latitude A(HL-A). Considering the relatively long ETM distance and the moderate proton flux, we decided to use the whole data (Table 4.3 case (4)). However, we should keep it in mind that two data sets of HL-Aand M12offcould still be contaminated by the SWCX from the geocorona.

As reported in Yao et al. (2009), the ETM distance for LMC X-3 Vicinity (LX-3) observation was always longer than $5R_{\rm E}$ when the magnetic field is open to the Sun direction and that it becomes as short as $1.4R_{\rm E}$ when the magnetic field is open to anti-Sun direction during which however solar-wind particles cannot penetrate (Table 4.3 case (5)). We thus decided to adopt all the data for this observation.

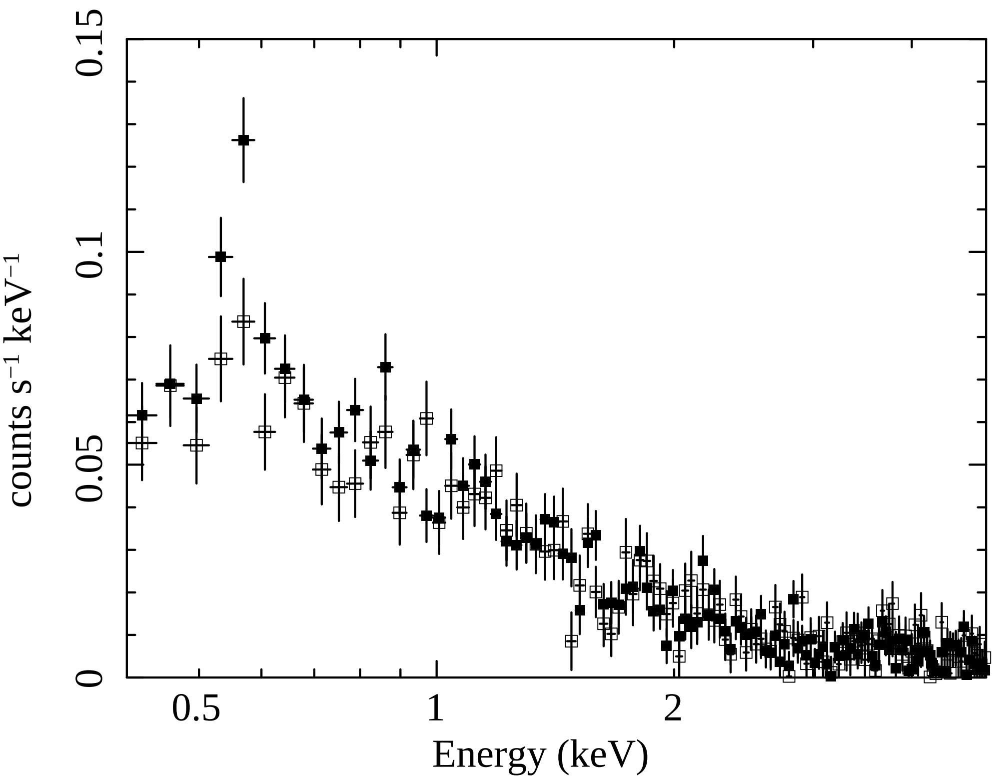

Figure 4.3: Energy spectra of High latitude B (HL-B) for the time intervals with solar wind proton flux higher (filled squares) or lower (open squares) than 4×10^8 protons s^{-1} cm^{-2}. There are large ($> 3\sigma$) discrepancy between the two spectra in the energy bins containing O VII emissions (~ 0.56 keV).

Table 4.3: Summary of Geocoronal SWCX removal process

(ID)	(1)	(2)	(2a)	(2b)	(2b-1)	(2b-2)	(3)	(4)	(5)
1 (GB)	○								
2 (HL-B)		○	○						
3 (FOR)		○		○	○				
4 (LH-2)		○	○						
5 (LH-1)	○								
8 (Off-FIL)		○		○		○			
9 (On-FIL)	○								
6 (PKS2)	○								
7 (PKS1)		○	○						
10 (HL-A)							○		
11 (M12off)								○	
12 (LX-3)		○		○					○
13 (NEP1)		○	○						
14 (NEP2)		○	○						
15 (LL21)	○								
16 (LL10)		○		○		○			

(1) The solar wind flux was alway $< 4 \times 10^8$ protons s^{-1} cm^{-2}. All time intervals were adopted.

(2) Enough statistics both for high ($> 4 \times 10^8$ protons s^{-1} cm^{-2}) and low solar wind fluxes.

(2a) Excess in the high-solar-wind-flux spectrum. Time intervals with high solar wind flux were discarded.

(2b) No excess in the high-solar-wind-flux spectrum.

(2b-1) Always high ETM distance ($> 10R_{\rm E}$) during high solar wind flux. All time intervals were adopted.

(2b-2) Occasionally low ETM distance during high solar wind flux. Time intervals with high solar wind flux were discarded.

(3) Proton flux stayed at $> 4 \times 10^8$ protons s^{-1} cm^{-2}. No significant difference in spectra with $5R_{\rm E} <$ ETM distance $< 10R_{\rm E}$ and ETM distance $> 10R_{\rm E}$. Time intervals with ETM distance $< 5R_{\rm E}$ were discarded.

(4) The solar wind flux is $\sim$ 5protons s^{-1} cm^{-2} and ETM distance is in the range from 7 to 9 $R_{\rm E}$. All time intervals were adopted.

(5)ETM distance was always $> 5R_{\rm E}$ when the magnetic field is open to the Sun direction and that it becomes as short as $1.4R_{\rm E}$ when the magnetic field is open to anti-Sun direction. All time intervals were adopted.

4.2.1.3 Exclusion of the point source

We then constructed an X-ray image in 0.3 to 2 keV energy range. For all the data sets except for Low latitude 97+10 (LL10), PKS2155_obs1 (PKS1) and PKS2155_obs2 (PKS2), point sources are detected in the field of view. We removed a circular region centered at the source position from the further analysis. The detected source position and removed radius are shown in Table B.1. Note that the data of GB1428+4217 (GB) is the observation for high-z blazar. This point source of an intensity of 2.6×10^{-13} erg s^{-1} cm^{-2} in the energy band of 0.3 to 1 keV (22×10^{-13} erg s^{-1} cm^{-2} in 1 to 10 keV) was detected at the center of the field of view. We removed a circular region of a 5 arc minute radius for this observation. The images in the 0.3-2 keV with point sources removed are shown in Figure 4.6. In all analysis, we did not exclude the two corners of the image where the calibration sources ^{55}Fe illuminates, because it does not affect low energy spectra ($\lesssim$ 1 keV)in which we are interested and the data can show better statistics.

Point source analysis: LH-2 **field as an example**

In this section, we show the analysis for point sources in LH-2 field as an example. In the field of view in the direction of LH-2, two point sources, denoted PS1 and PS2 in Figure 4.7, are detected. We extracted the spectra of the circular regions at the center of $(l, b) = (149.765, 53.228)$ and $(l, b) = (149.767, 53.139)$ and with the radius of 2 arcmin and 1.5 arcmin for PS1 and PS2, respectively. Then we extracted each background spectrum of the circular region at which is symmetrical about the region of point source with the radius of 2 arcmin as shown in Figure 4.7. Each background subtracted spectrum is shown in Figure 4.8. We fitted the each spectrum with the model which consists of absorbed power-law (wabs*power-law model) whose photon index is fixed to 1.4 and hydrogen column density is fixed to that of LH-2 field and unabsorbed thin thermal plasma model (APEC model) whose temperature and normalization are free. Results are shown in Table 4.4. Flux in the band of 0.47 – 1.21 keV for PS1 and PS2 were, respectively, 3.3 $\times 10^{-14}$ and 2.2×10^{-14} erg s^{-1} cm^{-2}. We also analyzed the point sources in other observation fields with the same procedure as above, and the flux in 0.47 - 1.21 keV band are shown in Table B.1. The counts from the point source outside the circular region is less than 4 % of the diffuse X-ray emission in 0.47 to 1.21 keV energy range. Thus the contribution of point sources to diffuse background emission can be ignored in following analysis.

4.2.2 Background and Response

When the FOV of the XRT points at the night Earth where the atmosphere is not illuminated by the Sun, no X-rays from the source hits the detectors, i.e. all the events are due to charged particle or the noise of the circuit. The non X-ray background (NXB) spectrum based on this night Earth data is the background for our analysis. The NXB spectrum was created using the software of *Suzaku* FTOOLS **xisnxbgen** version 2008-03-08 (Tawa et al., 2008). The NXB spectrum was constructed from the dark Earth database using the standard method in which the cut off rigidity distributions of the on-source and the background data were made identical.

We found 5 to 10 % discrepancy in the counting rates above 10 keV energy range between the non X-ray background and the observation data, suggesting background uncertainty of

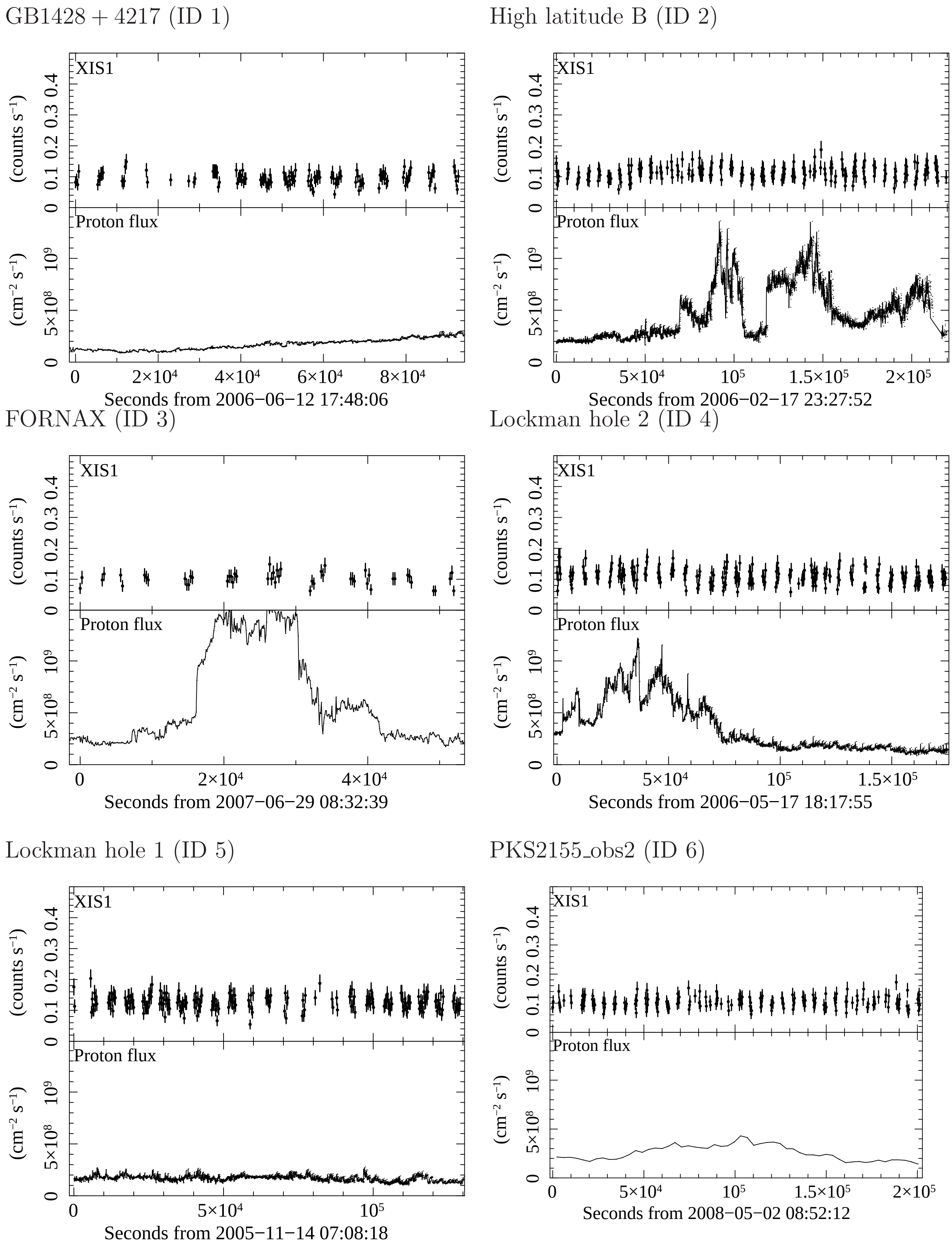

Figure 4.4: XIS-BI light curve in 0.3-2.0 keV (top panel) and solar wind proton flux (bottom panel) in each observation period calculated using the data of ACE SWEPAM (64 sec bin) or WIND SWE (64 sec bin) or OMNI (1 hours average) from CDAWeb. The origin is set to the beginning of each observation with *Suzaku* . For the data calculated from ACE and WIND, each bin was shifted in time to correct for the travel time of the solar wind from the satellites to the Earth (typically $\sim$ 3000 sec).

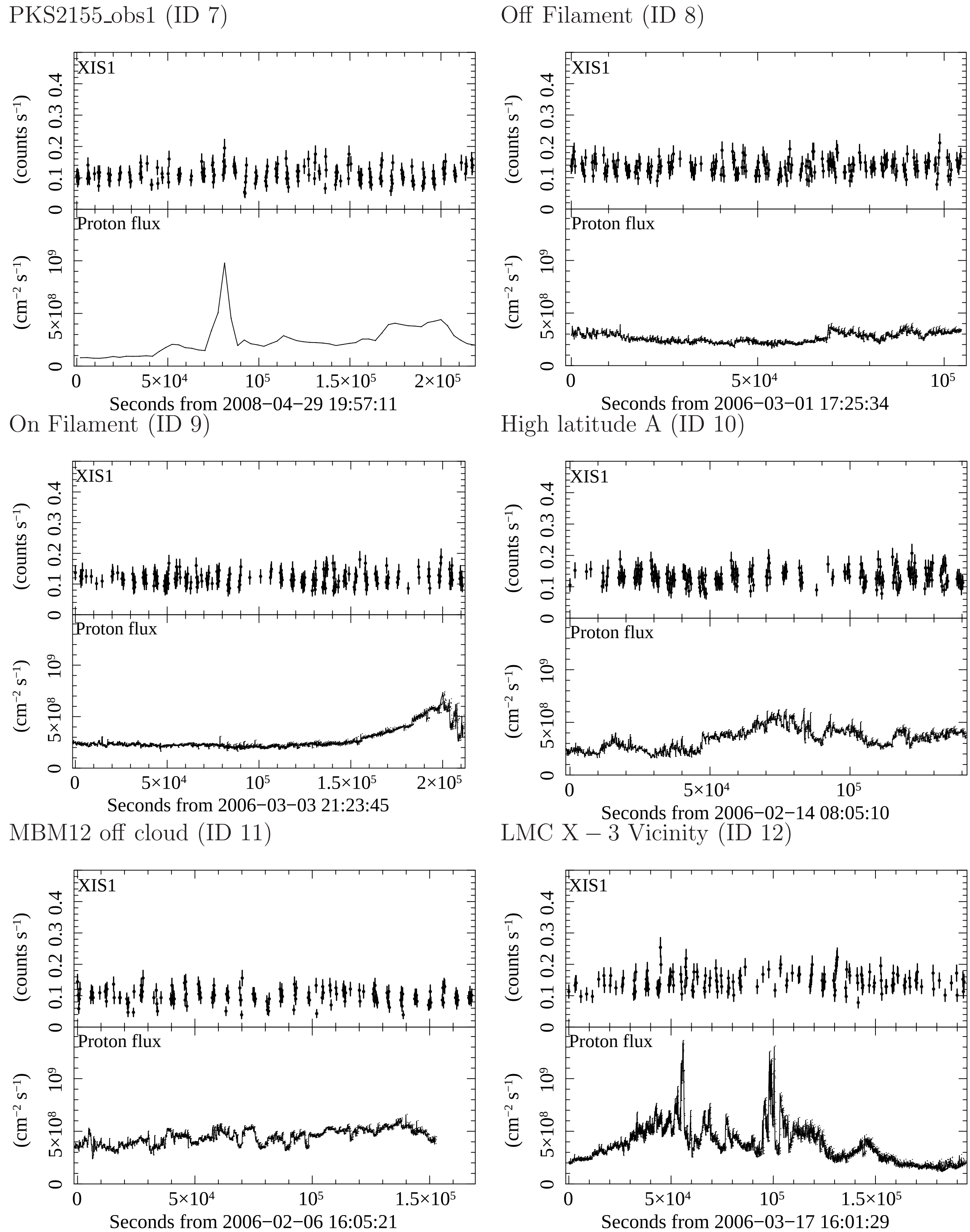

Figure 4.4: *Continued*

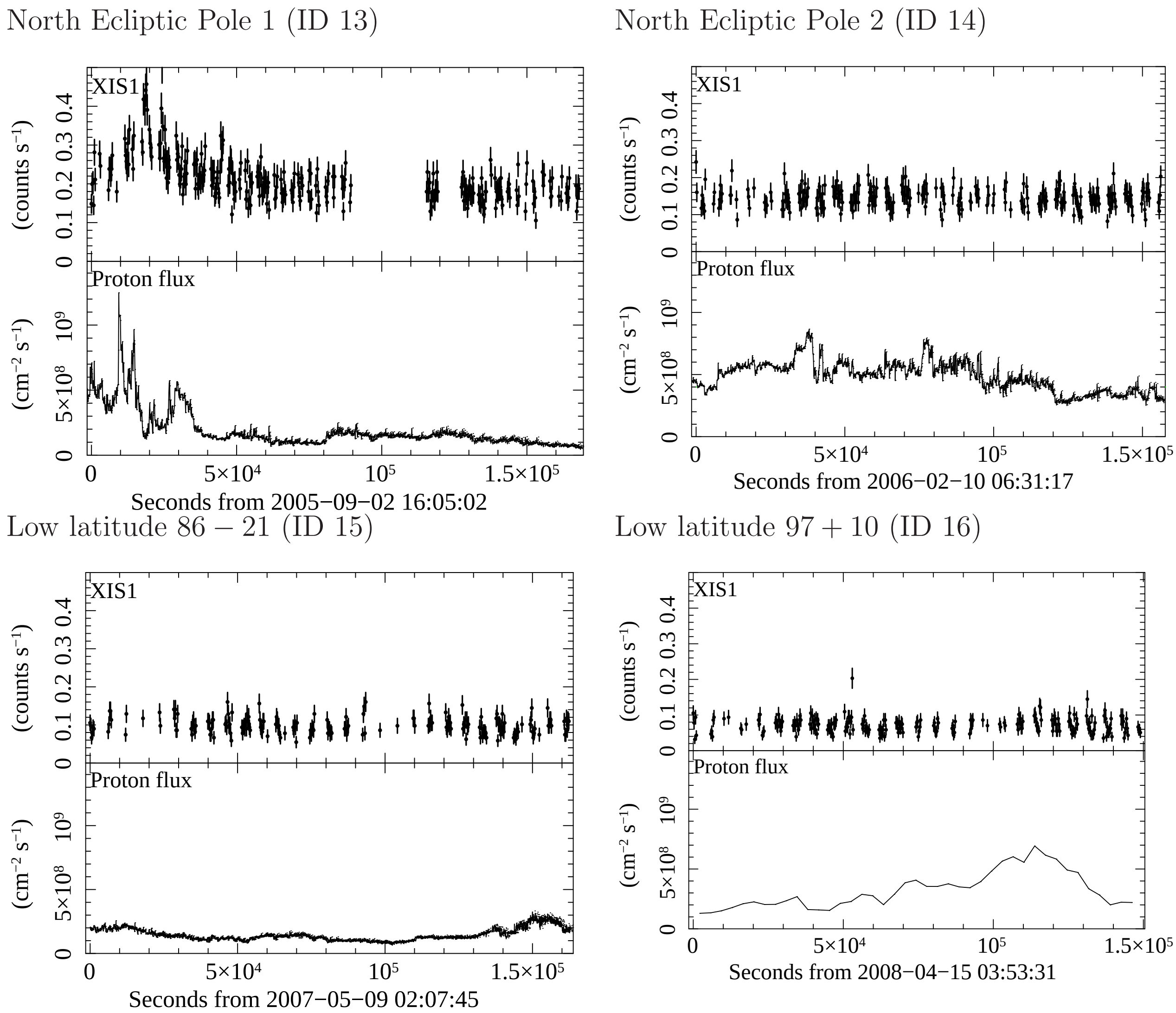

Figure 4.4: *Continued*

this level. However, since in the energy range below 1 keV, the non X-ray background is only about 10 % of the diffuse X-ray background, this level of the background uncertainty is negligible.

In order to perform spectrum fitting, we generated the efficiency file (so-called arf file) for a flat field, using *Suzaku* FTOOLS **xissimarfgen** version 2008-04-05 (Ishisaki et al., 2007) and the file for contamination thickness of ae_xi1_contami_20071224.fits, assuming a 20′-radius flat field as the input emission of the generator. The pulse height re-distribution matrix (so called rmf file) was created by *Suzaku* FTOOLS **xisrmfgen** version 2007-05-14.

The data reductions for data sets MBM12 on cloud (M12on) and Midplane235 (MP235) by Masui et al. (2008) have been done essentially the same methods. Only the difference is in point source removal of MBM12 on cloud data: this field contains a strong Cataclysmic Variable, thus its contribution was included in the model function of the spectral fitting, instead of removing image area contaminated by the source (Smith et al., 2007b; Masui et al., 2008).

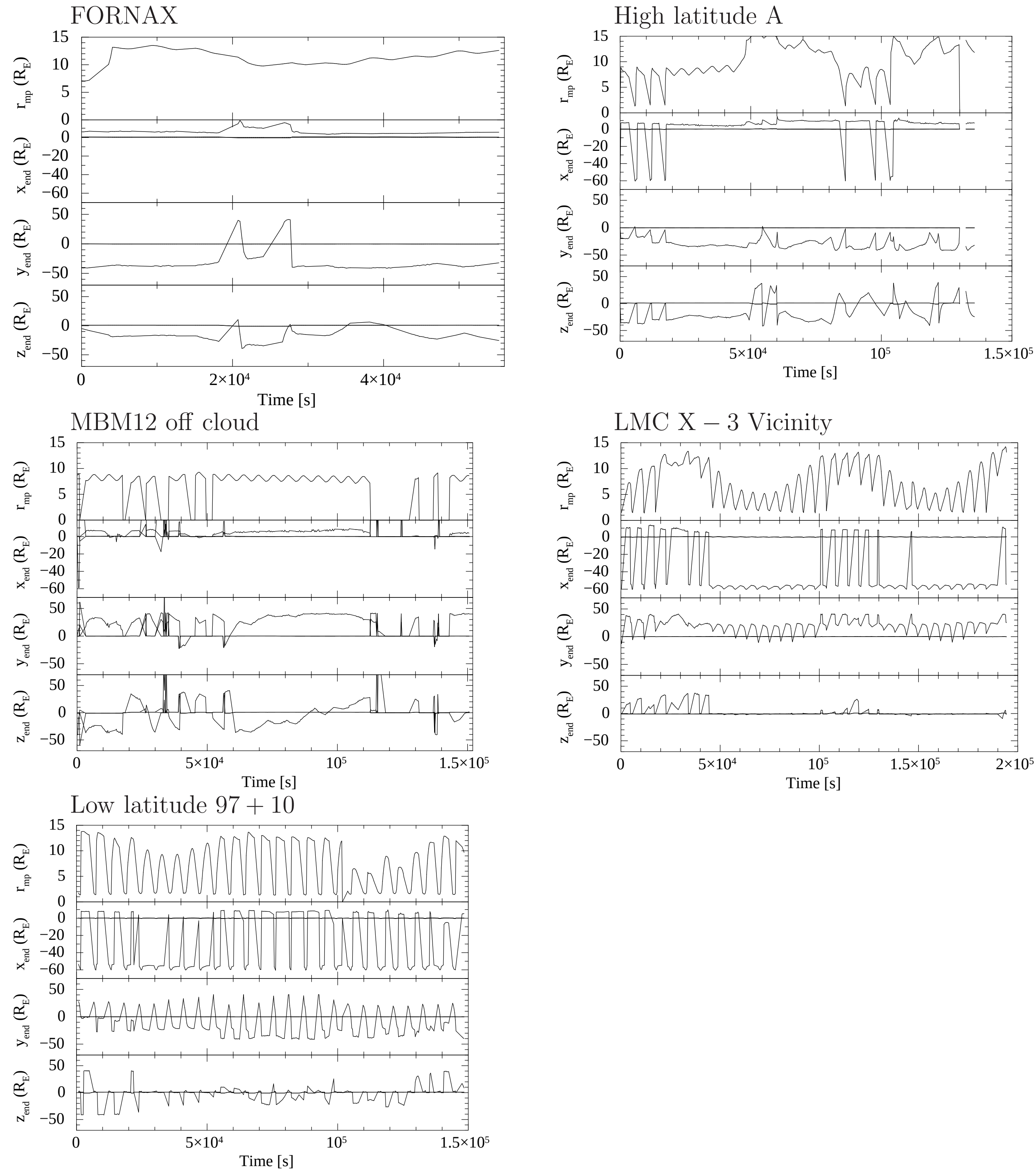

Figure 4.5: Magnetopause, which is defined to be the lowest position along the line of sight where geomagnetic field is open to the interplanetary space, in each observation period as a function of time calculated using T96 magnetic field model[a] (Tsyganenko & Sitnov (2005)). Top panel are earth-to-magnetopause distance, second, third and fourth panel are respectively the x, y, z value of the magnetopause in GSM (Geocentric Solar Magnetosheric[b]) coordinates every 256 sec in unit of earth radius R_E . [a] The parameters of this model are Geodipole tilt angle, Solar wind pressure, Dst index, Interplanetary magnetic filed and GSM position of the observation point. [b] The x-axis of the GSM coordinate system is defined along the line connecting the center of the Sun to the center of the earth. The origin is defined at the center of the earth, and ins positive towards the Sun. The y-axis is defined as the cross product of the GSM x-axis and the magnetic dipole axis; directed positive towards dusk. The z-axis is defined as the cross product of the x- and y-axis. The magnetic dipole axis lies within the xz plane.

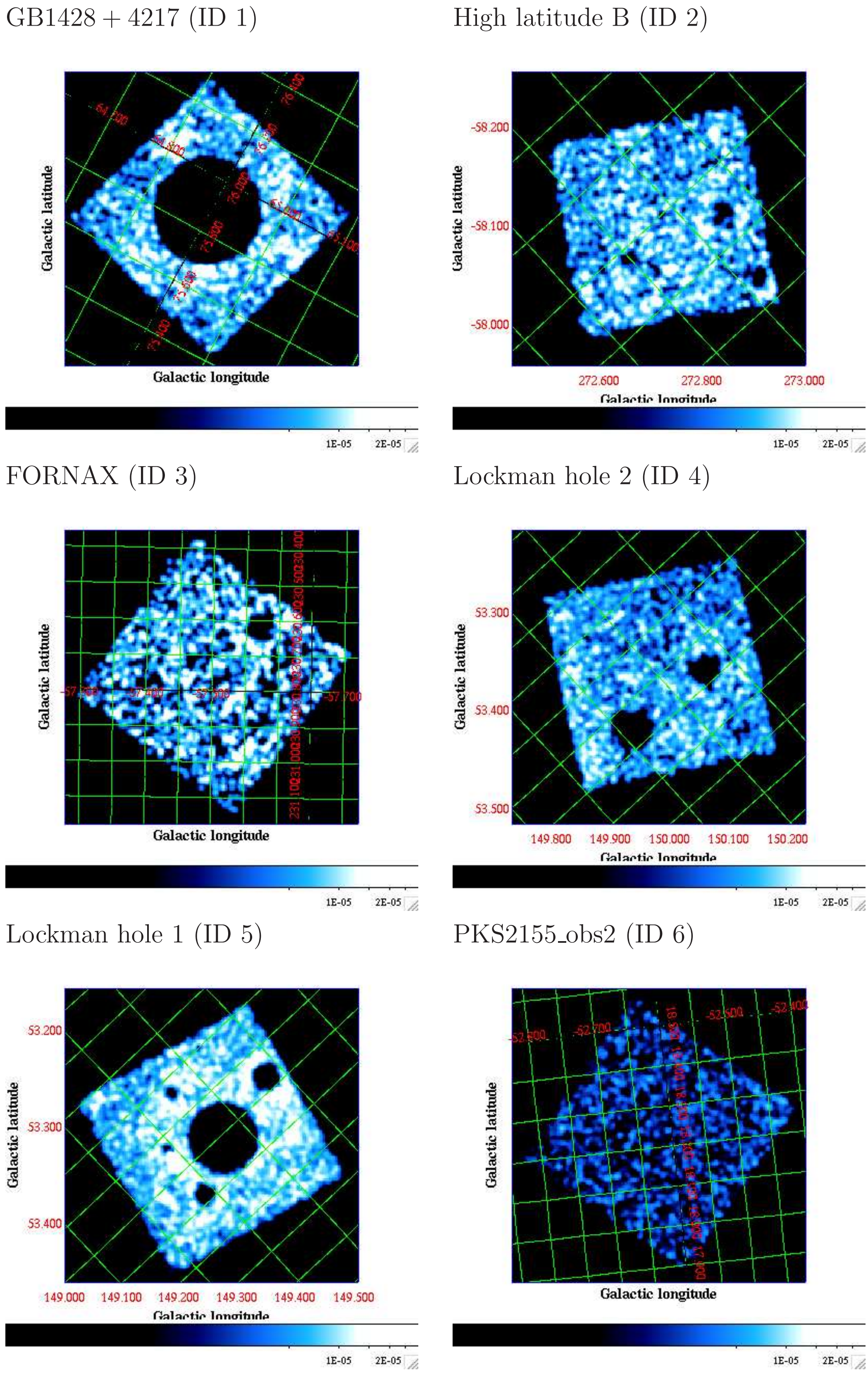

Figure 4.6: XIS 1 images in the 0.3-2 keV band. Point sources are excluded. No point source was detected in the observation of Low latitude 97+10, PKS2155_obs1 and PKS2155_obs2.

PKS2155_obs1 (ID 7)

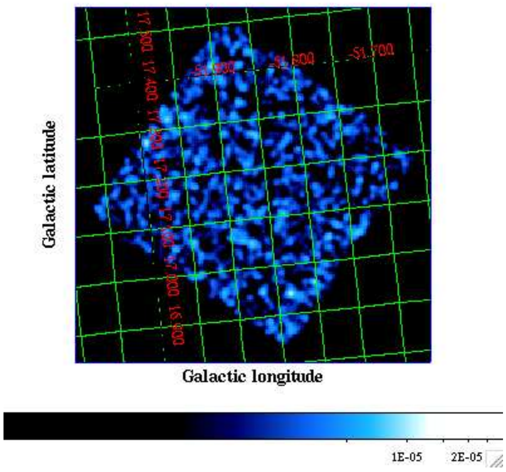

Off Filament (ID 8)

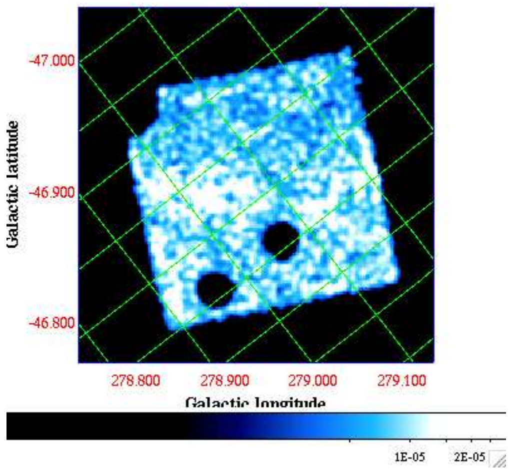

On Filament (ID 9)

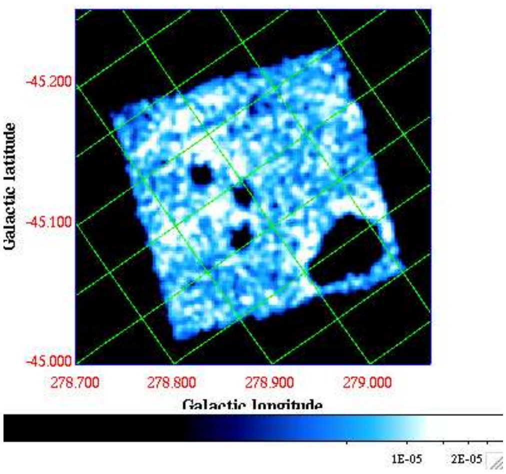

High latitude A (ID 10)

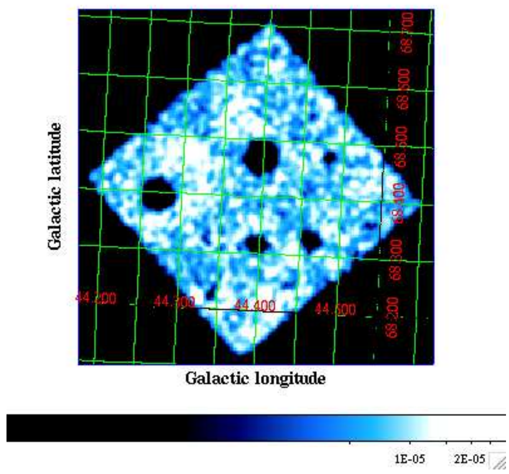

MBM12 off cloud (ID 11)

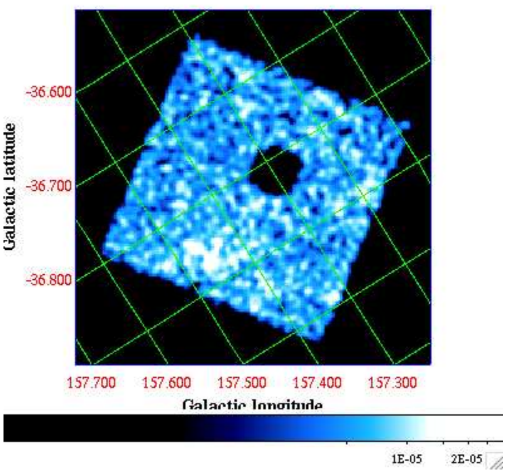

LMC X − 3 Vicinity (ID 12)

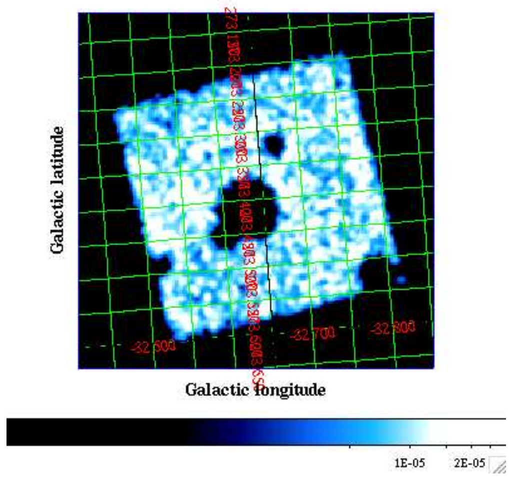

Figure 4.6: *Continued*

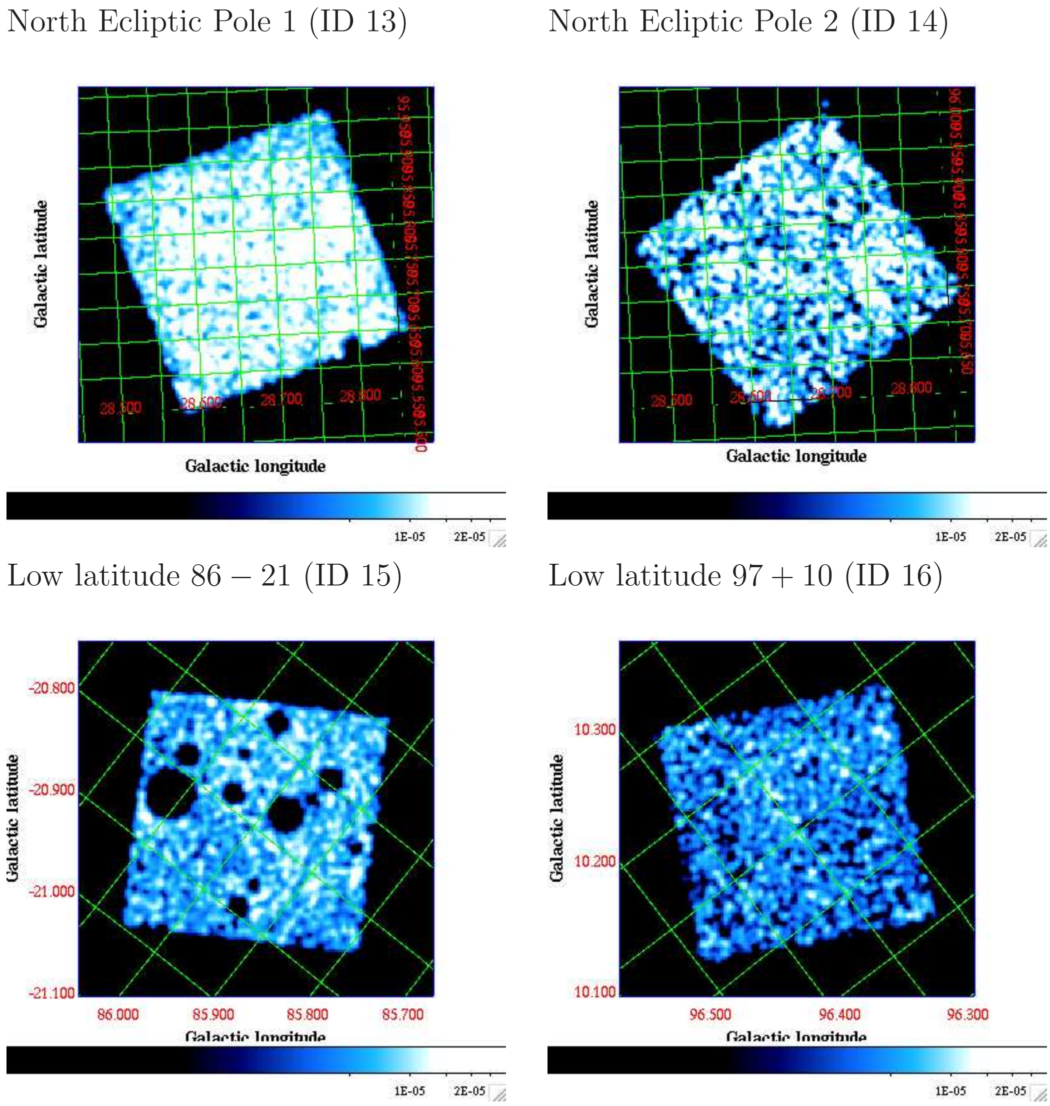

Figure 4.6: *Continued*

Table 4.4: Fitting results and flux of two point sources in Lockman hole 2 field with $wabs * power - law + APEC$ model

	wabs*power-law			APEC		χ^2/d.o.f	Flux[d]
region[a]	$N_{\rm H}$	index	Norm[b]	kT(keV)	Norm[c]		erg s^{-1} cm^{-2}
PS1	0.56	1.4	$0.05^{+0.05}_{-0.04}$	$0.402^{+0.271}_{-0.108}$	$0.13^{+0.06}_{-0.07}$	9.56/13	$3.3^{+0.4}_{-0.4}$
PS2	0.56	1.4	$0.08^{+0.03}_{-0.06}$	$0.715^{+0.592}_{-0.463}$	$0.06^{+0.03}_{-0.03}$	2.8/5	$2.2^{+0.2}_{-0.2}$

[a] See in Figure 4.7

[b] In unit of photons s^{-1}cm^{-2} keV^{-1}str^{-1}@1keV.

[c] The emission measure integrated over the line of sight, i.e. $(1/4\pi)\int n_{\rm e}n_{\rm H}ds$ in the unit of 10^{14} cm^{-5} str^{-1}.

[d] 0.47-1.21 keV range. Error is 68 % confidence range.

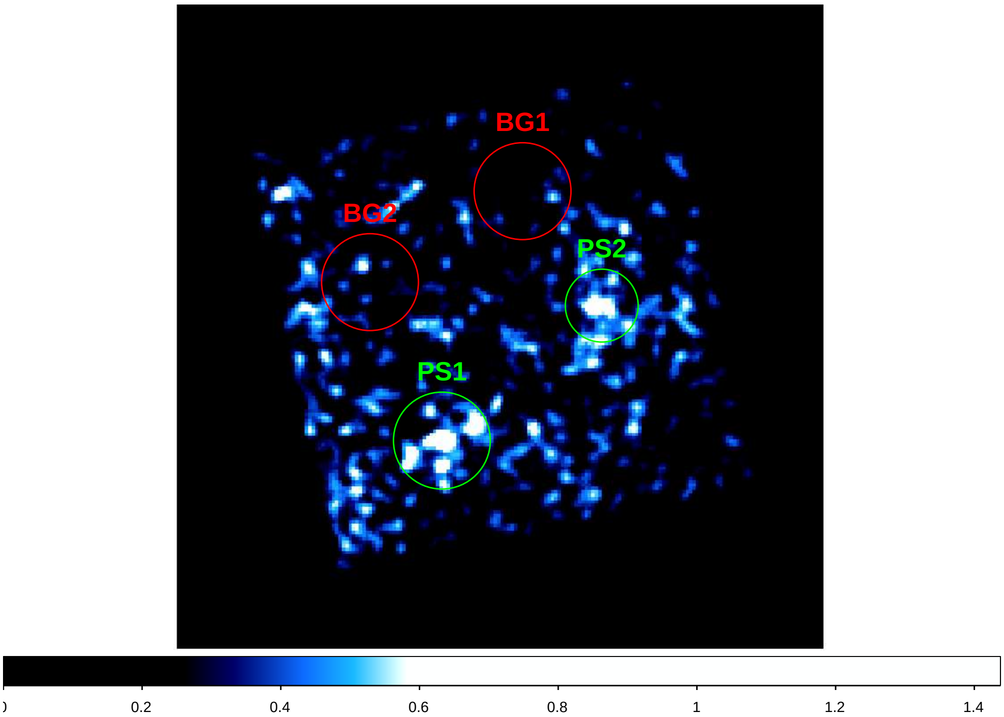

Figure 4.7: 0.3-2.0 keV XIS1 image of LH-2 field in detector coordinates. Two circles in green are extracted region as point sources and that in red is the region as the background for point sources.

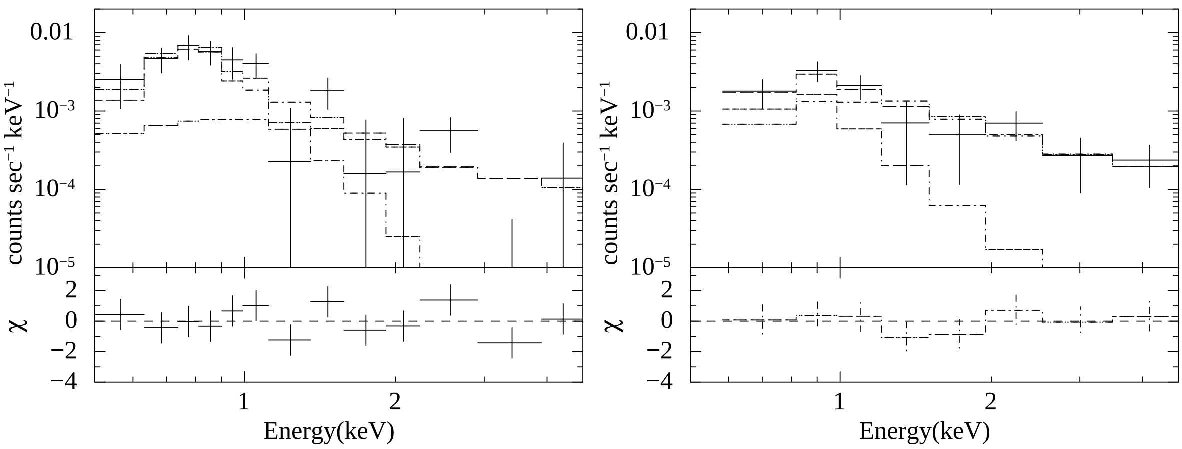

Figure 4.8: Left and right are the spectra and the best-fit model of point sources in LH-2 field denoted PS1 and PS2 in Figure 4.7, respectively.

Chapter 5

Analysis and Results

5.1 Basics of the spectral fittings

The energy spectra of 16 data sets obtained with *Suzaku* XIS1 and reduced as described in Chapter 4 are shown in Figure 5.1. We can clearly see emission lines in all spectra: O VII ($\sim$ 0.56 keV) , O VIII ($\sim$ 0.65 keV) and/or Ne IX ($\sim$ 0.91 keV). In the energy range below 0.4 keV, there are many complex emission lines that cannot be resolved with the XIS. As the X-ray diffuse background emission has low surface brightness, the source counts become comparable to the NXB above $\sim$ 5 keV. Therefore we used the energy spectra in the range of 0.4 – 5.0 keV for the spectral fittings with models. The production of energy responses are described in Chapter 4. We used *XSPEC* v12.4.0 as a fitting tool throughout this Chapter.

We assumed that the observed energy spectra consist of the diffuse X-ray background, the Cosmic X-ray Background (CXB), and non X-ray background (NXB) which is made by particles irradiated on the CCD. We firstly evaluate the reproductivity of the CXB and NXB.

5.1.1 Modeling of the CXB components

The CXB component was included in the spectral fitting as a model function, since the uniformity of the surface brightness of the CXB is well known. The absorption column density of the CXB is fixed to the value derived by 21 cm observations (Dickey & Lockman, 1990), "WABS" model in Xspec package are used as the interstellar absorption model which is photo-electric absorption using Wisconsin cross section(Morrison & McCammon, 1983). The model of the CXB in 2-10 keV band is a power-law of a photon index of 1.4. The average of AGN spectra below $\sim$ 1 keV becomes steeper than that above $\sim$ 1 keV (Hasinger et al., 1993). We thus tried two different models for the CXB: a single power-law model with a photon index fixed to 1.4, and a double broken power-law model used in Smith et al. (2007b). The latter model consists of two broken power-law functions with photon indices of 1.54 and 1.96 below 1.2 keV and a photon index of 1.4 above the energy. We fixed the normalization of one broken power law component with a low-energy photon index of 1.54 to 5.7 photons s^{-1} keV^{-1} str^{-1} at 1keV and set the normalization of the other broken power-law component free.

5.1.2 Reproductivity of the NXB components

Basically, the NXB component can be reproduced by the averaged spectra when *Suzaku* pointed toward the night Earth direction. We follow the formulation by Tawa et al. (2008), and subtract the estimated background spectra from the observed spectra before the spectral fitting. This NXB spectrum is basically flat, but contains emission lines at 1.486, 1.740, and 2.123 keV which are considered as fluorescence lines of materials in the instrument (Tawa et al., 2008). If the reproductivity of these lines are not enough, the subtracted spectra show spiky structure between 1.3 and 2.1 keV. Therefore, we first fitted the spectrum in the energy range 1.1 to 5 keV by an absorbed power-law model and narrow Gaussians in order to study the NXB-residual lines. There can be residual lines at which is different from the centroid energy of intrinsic NXB line due to the difference of energy resolution. We found that we needed to include a line at 1.828 keV for High latitude B (HL-B), a line at 2.157 keV for Low latitude 97+10 (LL10) and a line at 1.537 keV for FORNAX(FOR) in order to obtain an acceptable fit. In the further spectral fits, we include these lines with the parameters fixed at the best fit values.

Note that if we concentrated on the soft X-ray emission below 1 keV, the best-fit parameters of the soft X-ray emissions derived in later analysis are not sensitive to these structures. We include these structures to evaluate the errors by reliable χ^2 statistics.

5.1.2.1 Cases of North Ecliptic Pole 1 and North Ecliptic Pole 2

In the observations of North Ecliptic Pole 1 (ID 13, NEP1) and North Ecliptic Pole 2 (ID 14, NEP2), the observation dates are separated about 5 months from each other, but the aim points of theirs are same and only the roll angles of satellite were different(See Table 4.1 and 4.2). However their normalizations of the CXB component are different from each other about the XIS-BI (XIS1) data. We also created the other three XIS-FI spectra (XIS0, XIS2 and XIS3) of NEP1 and NEP2 and fitted the spectra in the energy range of 2 keV to 5 keV with the absorbed single power-law model whose photon index is fixed to 1.4. Only the normalization of in XIS-BI spectrum of NEP1 are inconsistent with the other seven results within the statistical error as shown in Table 5.1. It is hard to consider that the CXB varies. There is a discrepancy by at most 10 % in the counting rate between source spectrum and the NXB above 10 keV, therefore 10% uncertainty exists in the NXB level. Although we corrected the normalization of the NXB within this uncertainty and fitted the spectra of NEP1 and NEP2 in the same way described above, the inconsistency remained. We divided the spectrum of NEP1 into the former and the latter half of observation time when proton flux is in stable, and checked the normalization of them, the normalization of XIS-BI spectra are still significantly higher than the other three in both spectra of two periods. From these results, we suspected that the NXB for XIS-BI has the uncertainty not only the counting rate above 10 keV energy range but also the spectral shape, therefore the NXB spectrum for XIS-BI of NEP1 could not be reproduced well. This is thought to be valid considering that, as shown in Figure 3.15, the NXB level of XIS-BI above 10 keV is about 10 times larger than that in the range of 2 – 5 keV except for emission lines and that the XIS-FIs has low and stable background than XIS-BI and good reproducibility. Therefore in the analysis of NEP1, we corrected about 30 % of the NXB level of XIS-BI for NEP1 so that the CXB normalization of NEP1 become consistent with that of XIS0, XIS2, XIS3 and those of NEP2. It is noted that all parameters of spectra in the case of uncorrected and corrected normalization of the

NXB are consistent with each other within the statistical error in the fitting with model 1 and model 2 (listed later). It is important that the line intensities of O VII and O VIII with and without the NXB correction were consistent within statistical error. Finally we checked the normalization of CXB for all the observations in this thesis with *wabs*power-law* model applying the same procedure described above. The normalization of CXB are consistent to each XIS detector within statistical error(See Table C.1). Thus we do not correct the NXB level in their analysis except for the NEP1 observation.

Table 5.1: The CXB normalization of NEP1and NEP2with single power-law component fit. NXB level is not corrected.

observation	CXB norm[a] (90% error)			
	XIS0	XIS1	XIS2	XIS3
NEP1	7.4 (6.8,8.0)	10.7 (10.0, 11.4)	7.5 (6.9, 8.1)	8.6 (8.0, 9.2)
NEP2	8.1 (7.0, 9.2)	8.0 (6.9, 9.1)	8.5 (7.3, 9.7)	7.7 (6.6, 8.8)

[a] The normalization of the power-law function with the unit of photons $s^{-1}cm^{-2}$ $keV^{-1}str^{-1}$@1keV.

5.2 A simple TAE model

As described in the Chapter 2, soft X-ray diffuse background (SXDB) is considered to consist of the Solar-wind charge exchange (SWCX) within the Heliosphere, the emission from the local hot bubble (LHB), transabsorption emission (TAE) within our Galaxy and the Cosmic X-ray background (CXB). As a start, we try to represent the energy spectra by a simple model to characterize the soft X-ray emission below 1 keV. Following Smith et al. (2007b) and Masui et al. (2008), the (SWCX+LHB) components are modeled by an APEC model [1] which is the emission spectrum model from diffuse gas in collisional ionization equilibrium . We do not adopt an absorption by ISM since they come from $\leq$ a few hundred pc from the Sun. As for the transabsorption emission (TAE), we adopt an absorbed APEC model whose HI column density is derived from 21 cm emission line measurements, and which is also applied for the absorption column for the CXB component. The atomic abundance of both APEC components, we fixed those to the solar value (Anders & Grevesse, 1989). We call these models with the double broken power-law CXB model, and with the power-law CXB model, respectively, model 1 and model 1', respectively. In Tables 5.2 and 5.3 we summarized the results of the spectral fits. The best fit model functions convolved with the instrument response are plotted in Figures 5.1 and 5.2 for respective models 1 and 1'. The best-fit value CXB normalization for each fields are consistent with the past CXB studies (see compilation by Revnivtsev et al. (2005)) and the fluctuation of it can be understood by considering the size of field of view.

The temperatures of the two thermal components could not be constrained well for data HL-B(ID 2) and HL-A(ID 10) with model 1, and for data GB(ID 1) and HL-B(ID 2) for model 1', because of strong coupling between the two components. In these cases, we fixed the temperature of the SWCX+LHB components to the average values of other spectra, i.e.,

[1] http://hea-www.harvard.edu/APEC/

0.120 keV and 0.112 keV, respectively. For data GB(ID 1) and LH-2(ID 4) with model 1, the existence of the TAE component was not significant. Thus for these two cases we fixed the temperature of the TAE component to the average value of other spectra (0.264 keV) except for the data FOR(ID 3), On-FIL(ID 9) and LL10(ID 16), and estimated the upper limit of the normalization parameter.

Although different fitting procedure was necessary between models 1 and 1' for data GB(ID 1), LH-2(ID 4), and HL-A(ID 10) as described above, the best-fit parameter values of the TAE and SWCX+LHB components determined using different CXB models are consistent to each other within the statistical errors. We performed all the fits shown in this thesis using two different CXB models. However, since all of those results are consistent with each other within the statistical errors, we will only show the results with the double broken power-law model for the CXB for the further analysis.

The resultant χ^2 values were generally good (reduced χ^2 is 0.95 – 1.39 for 59 – 196 degrees of freedom.) The best-fit values of the temperatures of the two thin-thermal models are contained in a relatively narrow ranges. They are between 0.09 and 0.14 keV for the LHB + SWCX component and between 0.22 and 0.48 keV for the TAE, except for the TAE temperature of LL10(ID 16), PKS2(ID 6) and FOR(ID 3).

The temperature of the TAE for data LL10(ID 16) is significantly higher than other spectra and is similar to the temperature (0.77 keV) obtained for MP235(ID R2), the midplane direction $(\ell, b) = (235, 0)$, Masui et al. (2008)), which is discussed in Appendix D.

For the data On-FIL(ID 9), the TAE temperature is also significantly high compared with the other observations. This is because the TAE component is need to have high temperature or large Neon abundance in order to reproduce the strong Ne IX emission line or excess around the Fe-L lines in about 0.7-0.8 keV range shown in the spectrum of On-FIL(ID 9) with one TAE component. This can lead to the relatively high temperature of the SWCX+LHB component.

Table 5.2: Results of three-component (CXB, TAE, SWCX+LHB) spectral fits with the double broken power-law CXB model (model 1)

	$N_{\rm H}$[a]	CXB[b]	TAE		SWCX+LHB		χ^2/dof
ID	(10^{20}cm^{-2})	Norm[c]	kT (keV)	Norm[d]	kT (keV)	Norm[d]	
1 (GB)	1.40	$5.8^{+0.6}_{-0.6}$	0.264[e]	< 1.7[e]	$0.142^{+0.049}_{-0.020}$	$6.2^{+1.4}_{-1.4}$	91.25/92
2 (HL-B)	3.36	$2.7^{+0.6}_{-0.6}$	$0.272^{+0.081}_{-0.076}$	$1.6^{+1.6}_{-0.8}$	0.120[f]	$6.8^{+1.9}_{-3.6}$	94.45/87
3 (For)	1.35	$0.6^{+0.8}_{-0.6}$	$0.745^{+0.315}_{-0.423}$	$1.5^{+0.7}_{-0.6}$	$0.143^{+0.027}_{-0.032}$	$11.6^{+14.7}_{-2.0}$	65.84/59
4 (LH-2)	0.56	$3.6^{+0.5}_{-0.5}$	0.264[e]	< 1.0[e]	$0.099^{+0.027}_{-0.027}$	$16.3^{+5.4}_{-3.9}$	94.74/99
5 (LH-1)	0.56	$5.6^{+0.4}_{-0.5}$	$0.476^{+0.279}_{-0.149}$	$1.3^{+0.8}_{-0.5}$	$0.137^{+0.011}_{-0.017}$	$8.3^{+3.7}_{-1.4}$	154.08/127
6 (PKS2)	1.67	$2.1^{+0.4}_{-0.4}$	$0.237^{+0.037}_{-0.044}$	$5.8^{+4.0}_{-0.9}$	$0.088^{+0.013}_{-0.041}$	$54.7^{+143.7}_{-23.1}$	107.26/103
7 (PKS1)	1.76	$3.3^{+0.5}_{-0.5}$	$0.290^{+0.050}_{-0.041}$	$3.6^{+1.1}_{-1.0}$	$0.091^{+0.016}_{-0.012}$	$53.8^{+45.8}_{-25.0}$	107.18/90
8 (Off-FIL)	4.19	$3.0^{+0.4}_{-0.4}$	$0.271^{+0.018}_{-0.023}$	$7.2^{+1.7}_{-1.0}$	$0.118^{+0.006}_{-0.008}$	$25.5^{+5.5}_{-5.5}$	173.17/122
9 (On-FIL)	4.61	$4.8^{+0.5}_{-0.5}$	$0.644^{+0.081}_{-0.075}$	$1.9^{+0.5}_{-0.2}$	$0.182^{+0.012}_{-0.013}$	$7.0^{+0.7}_{-0.7}$	128.57/117
10 (HL-A)	1.02	$4.9^{+0.5}_{-0.5}$	$0.237^{+0.045}_{-0.039}$	$3.5^{+1.9}_{-1.1}$	0.120[f]	$10.0^{+3.2}_{-4.5}$	141.01/116
11 (M12off)	8.74	$1.8^{+0.5}_{-0.5}$	$0.245^{+0.104}_{-0.118}$	$2.4^{+3.4}_{-1.4}$	$0.102^{+0.016}_{-0.080}$	$21.4^{+21.1}_{-6.5}$	86.27/89
12 (LX-3)	4.67	$8.7^{+0.5}_{-0.5}$	$0.310^{+0.087}_{-0.029}$	$6.0^{+1.3}_{-2.5}$	$0.140^{+0.031}_{-0.019}$	$9.9^{+4.1}_{-1.9}$	211.71/196
13 (NEP1)	4.40	$3.0^{+0.5}_{-0.4}$	$0.244^{+0.023}_{-0.017}$	$9.5^{+1.7}_{-1.9}$	$0.113^{+0.009}_{-0.011}$	$23.8^{+6.3}_{-4.1}$	158.44/120
14 (NEP2)	4.40	$2.8^{+0.8}_{-0.8}$	$0.271^{+0.040}_{-0.039}$	$7.7^{+3.1}_{-2.3}$	$0.116^{+0.020}_{-0.025}$	$18.9^{+17.3}_{-8.5}$	60.85/55
15 (LL21)	7.24	$4.3^{+0.5}_{-0.5}$	$0.284^{+0.042}_{-0.035}$	$6.8^{+2.1}_{-1.7}$	$0.109^{+0.019}_{-0.020}$	$24.5^{+27.0}_{-9.6}$	105.03/97
16 (LL10)	27.10	$2.6^{+0.6}_{-0.6}$	$0.732^{+0.233}_{-0.180}$	$1.5^{+0.6}_{-0.7}$	$0.116^{+0.065}_{-0.035}$	$6.6^{+22.8}_{-3.9}$	86.47/89

[a] The absorption column densities for the CXB and TAE components were fixed to the tabulated values that are estimated from Dickey & Lockman (1990)

[b] Two broken power-law model was adopted. The photon indices below 1.2 keV were fixed to 1.54 and 1.96 . The normalization of the former index component is fixed to 5.7, and only the normalization of the other component was allowed to vary.

[c] The normalization of one of the broken power-law components with the unit of photons s^{-1}cm^{-2} keV^{-1}str^{-1}@1keV. Add 5.7 to obtain the total CXB flux at 1 keV.

[d] The emission measure integrated over the line of sight, i.e. $(1/4\pi)\int n_{\rm e} n_{\rm H} ds$ in the unit of 10^{14} cm^{-5} str^{-1}.

[e] The TAE component was not significant. Thus the upper limit of the normalization was determined for the temperature fixed to the average of TAE components of other observations.

[f] Because of the strong coupling between the TAE and LHB+SWCX components, the temperatures of the two components were not well determined. We thus fixed the temperature of the SWCX+LHB component to the average values of other observations.

Table 5.3: Results of three-component (CXB, TAE, SWCX+LHB) spectral fits with the single power-law CXB model (model 1')

	N_{H}[a]	CXB[b]	TAE		SWCX+LHB		χ^2/dof
ID	(10^{20}cm^{-2})	Norm[c]	kT (keV)	Norm[d]	kT (keV)	Norm[d]	
1 (GB)	1.40	$10.9^{+0.6}_{-0.6}$	$0.203^{+0.086}_{-0.050}$	$3.3^{+4.1}_{-1.4}$	0.112[e]	$8.1^{+6.3}_{-4.7}$	89.86/91
2 (HL-B)	3.36	$8.0^{+0.5}_{-0.5}$	$0.273^{+0.066}_{-0.043}$	$2.3^{+1.0}_{-0.9}$	0.112[e]	$9.5^{+2.6}_{-2.9}$	96.37/87
3 (FOR)	1.35	$6.2^{+0.8}_{-0.7}$	$0.634^{+0.384}_{-0.356}$	$1.6^{+0.6}_{-0.8}$	$0.139^{+0.032}_{-0.035}$	$12.8^{+31.7}_{-4.0}$	67.54/59
4 (LH-2)	0.56	$8.7^{+0.5}_{-0.6}$	$0.335^{+0.160}_{-0.148}$	$1.0^{+1.7}_{-0.6}$	$0.087^{+0.021}_{-0.030}$	$36.4^{+128.5}_{-23.9}$	89.76/97
5 (LH-1)	0.56	$10.6^{+0.4}_{-0.5}$	$0.354^{+0.069}_{-0.038}$	$2.5^{+0.6}_{-0.6}$	$0.116^{+0.013}_{-0.008}$	$15.2^{+4.2}_{-4.1}$	172.90/127
6 (PKS2)	1.67	$7.4^{+0.4}_{-0.4}$	$0.246^{+0.033}_{-0.025}$	$6.1^{+1.7}_{-1.6}$	$0.088^{+0.011}_{-0.019}$	$60.4^{+127.0}_{-23.5}$	109.73/103
7 (PKS1)	1.76	$8.5^{+0.5}_{-0.5}$	$0.295^{+0.042}_{-0.026}$	$4.2^{+0.9}_{-1.0}$	$0.090^{+0.011}_{-0.013}$	$63.4^{+63.4}_{-25.3}$	112.78/90
8 (Off-FIL)	4.19	$8.2^{+0.4}_{-0.4}$	$0.273^{+0.017}_{-0.019}$	$7.9^{+1.5}_{-1.0}$	$0.115^{+0.009}_{-0.006}$	$28.9^{+5.4}_{-5.8}$	178.04/122
9 (On-FIL)	4.61	$10.0^{+0.5}_{-0.4}$	$0.626^{+0.073}_{-0.065}$	$2.1^{+0.5}_{-0.5}$	$0.182^{+0.011}_{-0.011}$	$7.8^{+0.7}_{-0.6}$	124.99/ 117
10 (HL-A)	1.02	$10.1^{+0.4}_{-0.4}$	$0.242^{+0.036}_{-0.049}$	$4.9^{+3.0}_{-1.3}$	$0.093^{+0.020}_{-0.046}$	$27.8^{+56.1}_{-13.3}$	142.17/115
11 (M12off)	8.74	$7.2^{+0.4}_{-0.4}$	$0.260^{+0.071}_{-0.069}$	$2.7^{+2.8}_{-1.0}$	$0.101^{+0.015}_{-0.012}$	$23.9^{+10.6}_{-10.6}$	86.99/89
12 (LX-3)	4.67	$13.4^{+0.5}_{-0.5}$	$0.308^{+0.032}_{-0.023}$	$7.6^{+1.2}_{-1.5}$	$0.125^{+0.021}_{-0.013}$	$14.7^{+5.8}_{-4.1}$	214.27/196
13 (NEP1)	4.40	$8.1^{+0.4}_{-0.4}$	$0.250^{+0.023}_{-0.016}$	$9.9^{+1.7}_{-1.8}$	$0.112^{+0.008}_{-0.011}$	$26.8^{+7.7}_{-4.1}$	171.74/120
14 (NEP2)	4.40	$8.1^{+0.7}_{-0.7}$	$0.275^{+0.036}_{-0.036}$	$8.3^{+2.9}_{-1.9}$	$0.113^{+0.024}_{-0.023}$	$21.8^{+19.2}_{-9.0}$	63.15/55
15 (LL21)	7.24	$9.5^{+0.5}_{-0.5}$	$0.287^{+0.033}_{-0.031}$	$7.6^{+1.7}_{-1.5}$	$0.101^{+0.018}_{-0.012}$	$33.5^{+25.7}_{-14.5}$	104.43 /97
16 (LL10)	27.10	$7.9^{+0.6}_{-0.6}$	$0.716^{+0.166}_{-0.165}$	$1.7^{+0.6}_{-0.7}$	$0.118^{+0.069}_{-0.032}$	$6.3^{+18.4}_{-4.3}$	87.23/89

[a] The absorption column densities for the CXB and TAE components were fixed to the tabulated values that are estimated from Dickey & Lockman (1990).

[b] A power-law model with a photon index of 1.4 was adopted.

[c] The normalization of the power-law function with the unit of photons s^{-1}cm^{-2} keV^{-1}str^{-1}@1keV.

[d] The emission measure integrated over the line of sight, i.e. $(1/4\pi)\int n_{\mathrm{e}} n_{\mathrm{H}} ds$ in the unit of 10^{14} cm^{-5} str^{-1}.

[e] Because of the strong coupling between the TAE and LHB+SWCX components, the temperatures of the two components were not well determined. We thus fixed the temperature of the SWCX+LHB component to the average values of other observations.

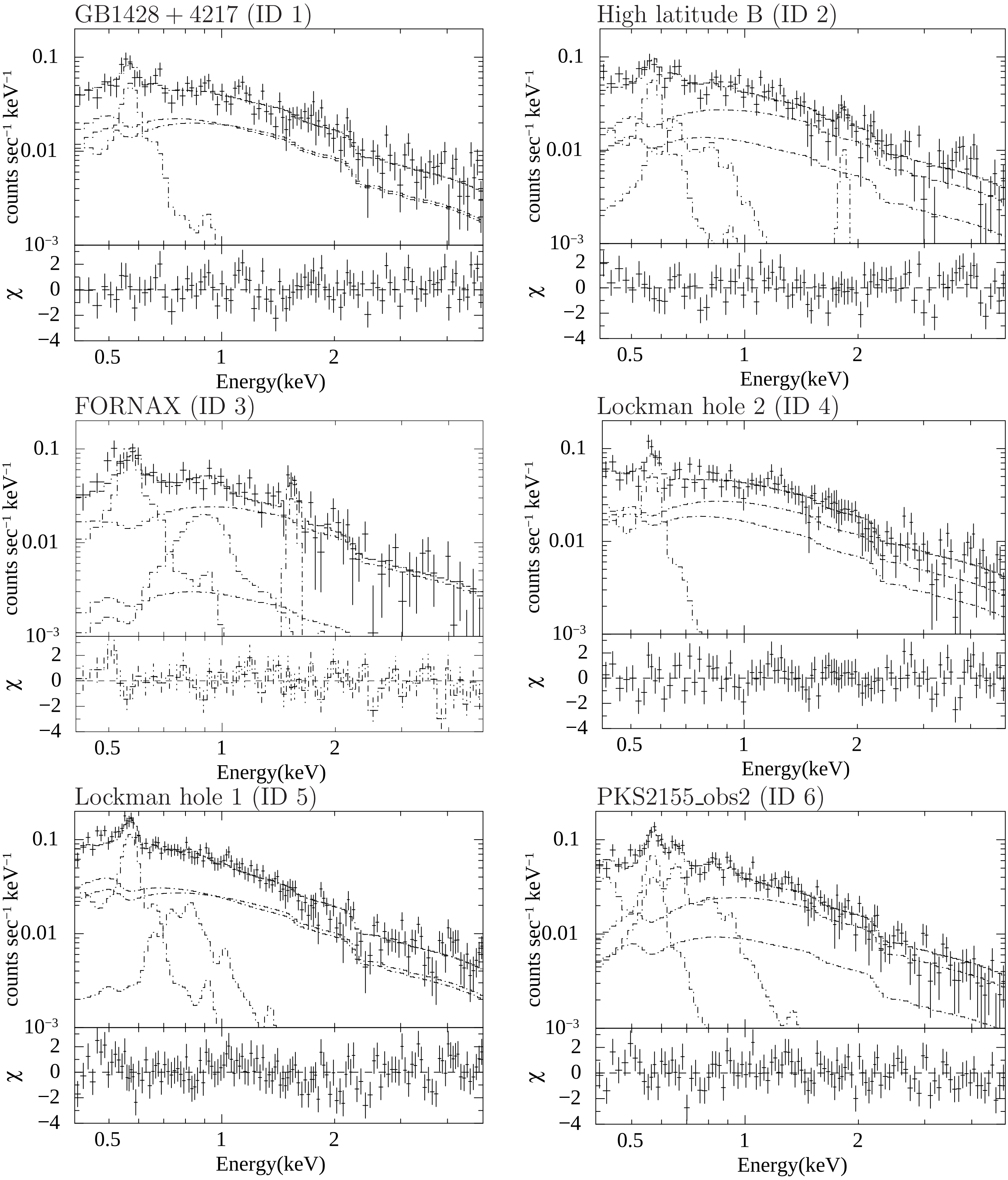

Figure 5.1: Spectra (crosses), best-fit model and its components (step functions) convolved with the instrument response function and residuals of the fit (bottom panels). The model function consists of three spectral components (CXB, TAE, SWCX+LHB). The CXB component was represented by a double broken power-law model (model 1). See Table 5.2 for parameters.

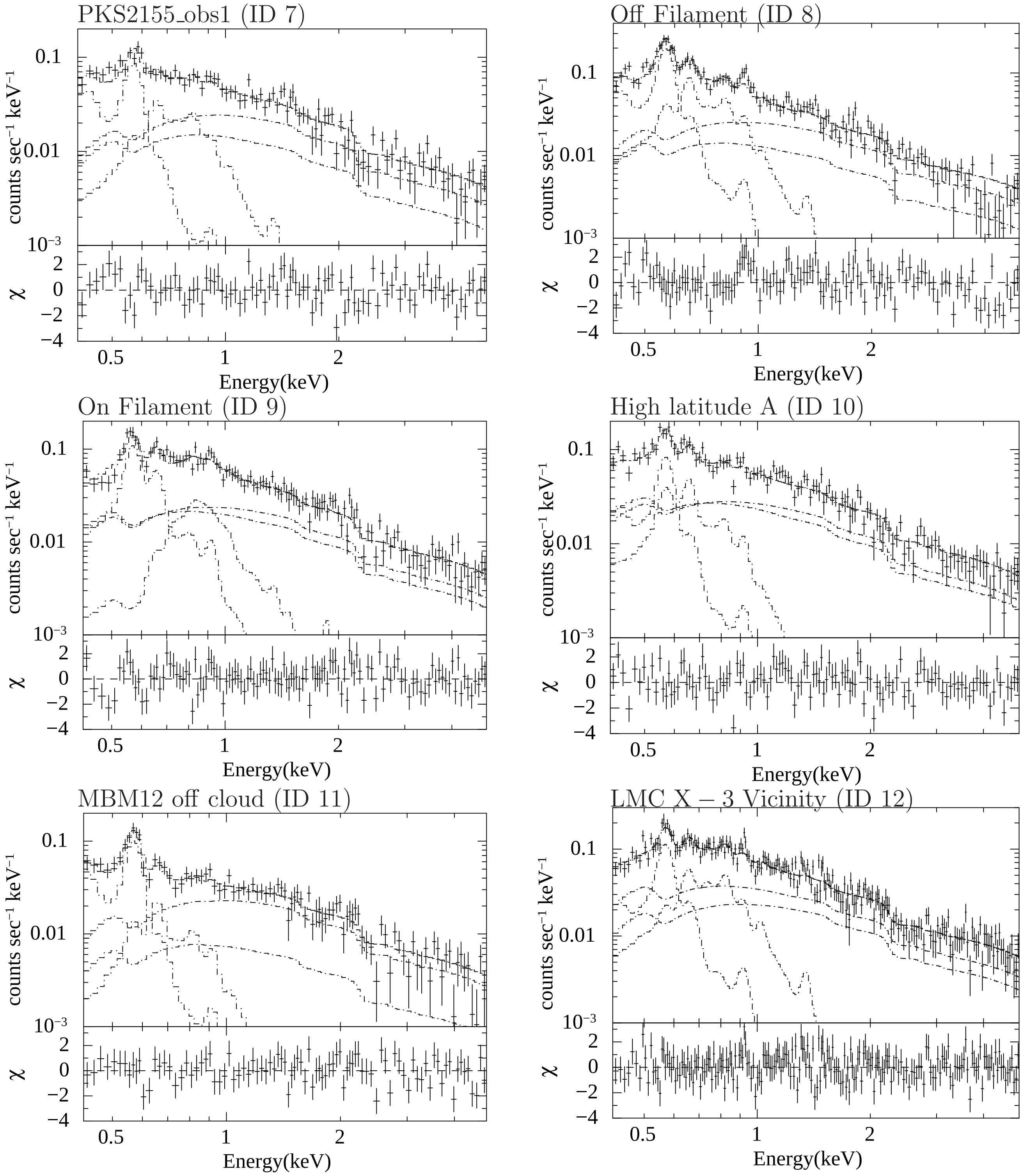

Figure 5.1: *Continued*

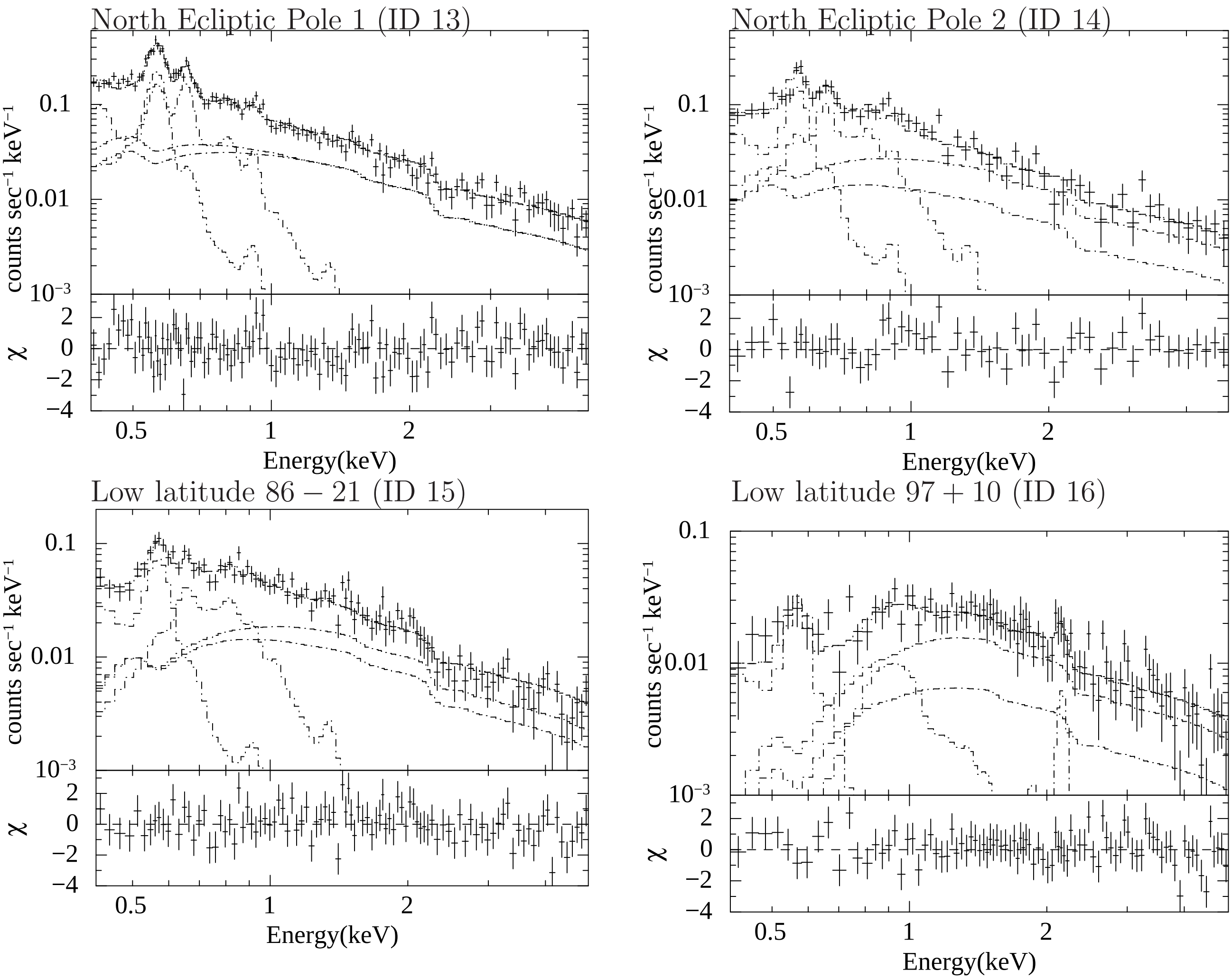

Figure 5.1: *Continued*

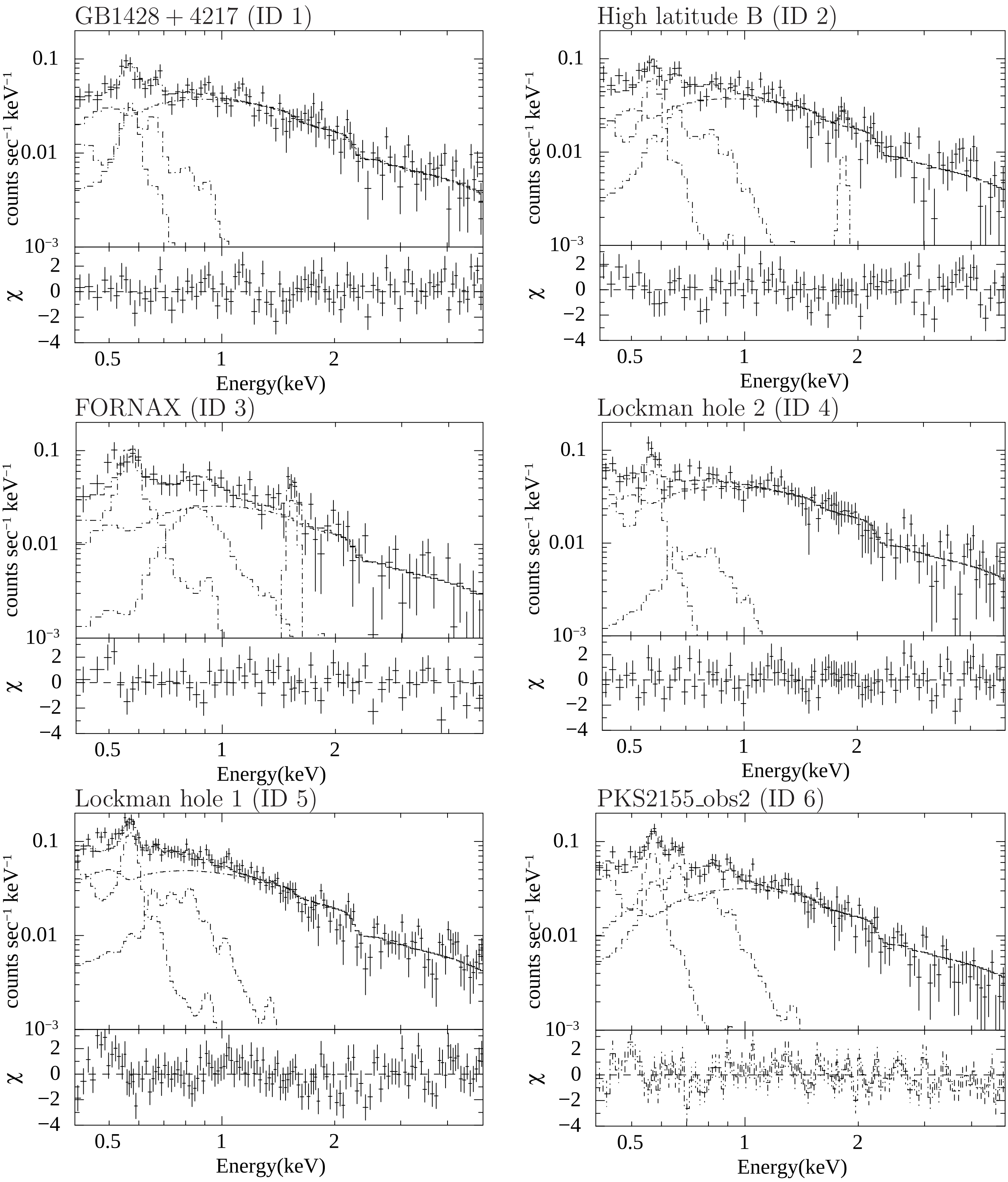

Figure 5.2: Spectra (crosses), best-fit model and its components (step functions) convolved with the instrument response function and residuals of the fit (bottom panels). The model function consists of three spectral components. The CXB component was represented by a single power-law model (model 1'). See Table 5.3 for parameters.

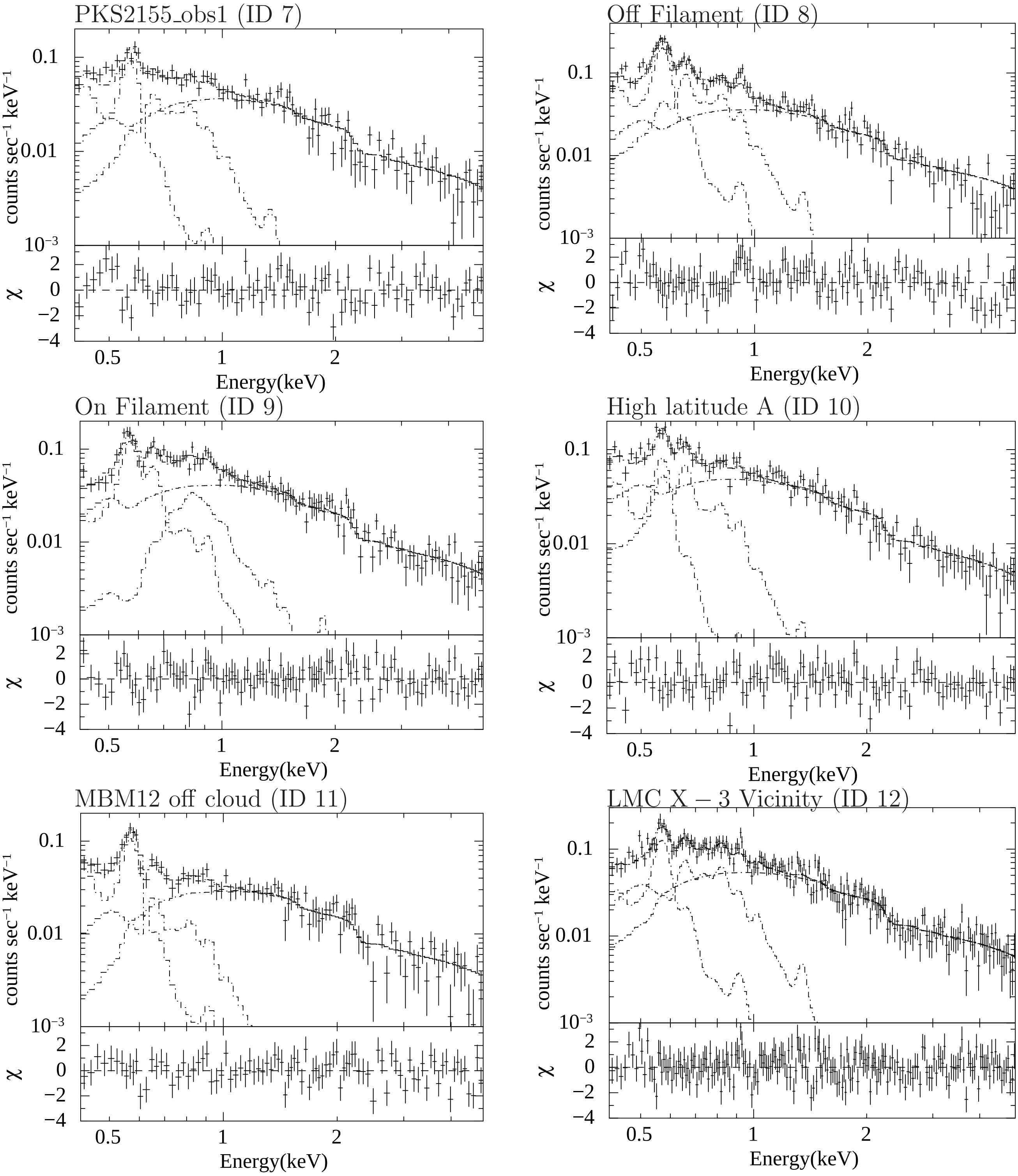

Figure 5.2: *Continued*

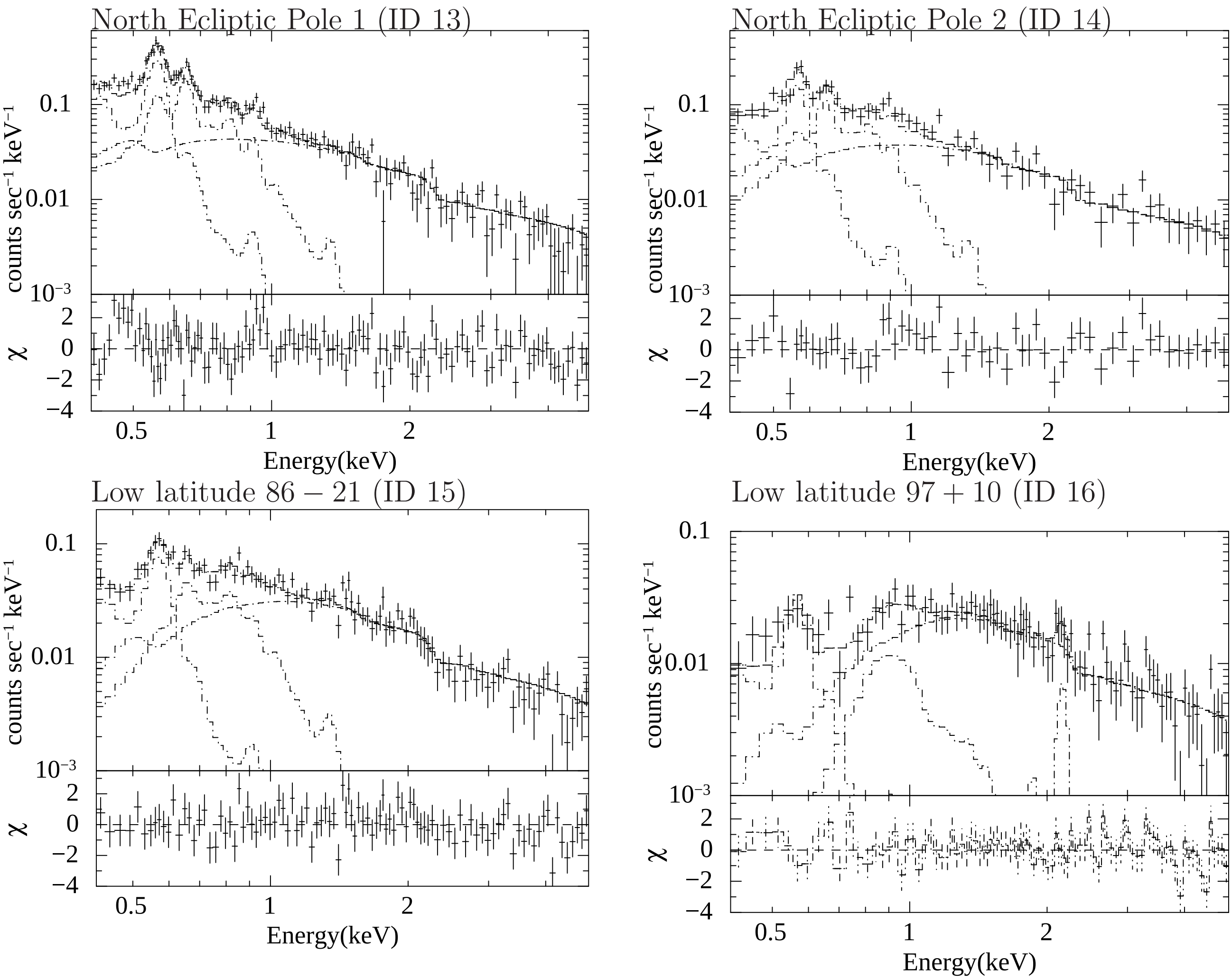

Figure 5.2: *Continued*

5.2.1 Evaluation of the apparent intensities of emission line

The surface brightness of O VII Kα and O VIII Kα emissions are evaluated with an application of this simple model. We will replace the APEC models in model 1 with the VAPEC models , in which abundance can be varied by elements. We set the abundance of Oxygen to be 0 and add two Gaussian functions that represent O VII Kα and O VIII Kα emissions, respectively. The intrinsic width of the Gaussian functions are set to be small enough compared to the detector energy resolution. The temperatures of these VAPEC components (SWCX+LHB, TAE) are set to the best-fit value of the model 1, and the centroid energies, the surface brightness without convolved by the ISM absorption are derived by the spectral fitting. The normalization of the CXB, the SWCX+LHB and the TAE are also renormalized. We set the intensities of the TAE component to 0 for data GB(ID 1) and LH-2(ID 4), because we obtained only the upper limit. Then the surface brightness of a line is calculated from the best-fit value of the Gaussian normalization. In Table 5.4 and Figure 5.3, we summarize the results of spectral fits. The centroid energy of O VIII had to be fixed to the theoretical value for data LH-2(ID 4), because we obtained only the upper limit for this data. For data FOR(ID 3), the centroid energy of O VIII line had to be fixed as for data LH-2(ID 4) in order not to blend with O VII line. Except for these cases, the centroid energies are consistently determined with the average energy of O VII Kα and O VIII Kα emission lines from thermal plasma in collisional equilibrium within the systematic errors of energy scale calibration (5 eV, Koyama et al. (2007), also see Section 3.1)

5.2.1.1 Possible systematic error for the determination of line intensities

In the following, we check the systematic uncertainties in the estimation of O VII and O VIII line intensities.

1. CXB modeling
   The spectral shape of continuum component below 1 keV can affect the estimation of line intensity. We estimated the line intensity using a single power-law with photon index fixed to 1.4 for CXB (model 1'). The best-fit values of the O VII O VIII line intensities are at most 10 % higher than those by the double broken power-law model for CXB, which are within the statistical error (See Table E.1 for parameters).

2. NXB level

   The uncertainty of non X-ray background level can affect the estimation of line intensity. Between the source spectrum and the non X-ray background above 10 keV in which all the counts are considered as background, there is a discrepancy by at most 10 % in the count rate. This means that 10 % uncertainty exists in the NXB level. The NXB level, however, is 10 % of the source spectrum below 1 keV range, therefore does not affect the line intensity estimation.

   On the other hand, NXB level of XIS-BI in the range below 10 keV can have larger uncertainty than that above 10 keV. As shown in Section 5.1.2.1, NXB level of XIS-BI for NEP1 field is larger than that of other XIS-FI sensors. We corrected 30 % of NXB level to be consistent to that of XIS-FIs in the spectral fitting. However, the O VII and O VIII line intensities are $8.9^{+0.5}_{-0.5}$ LU and $3.4^{+0.3}_{-0.3}$ LU for corrected NXB case, respectively, $8.7^{+0.5}_{-0.5}$ LU and $3.2^{+0.3}_{-0.3}$ LU for not corrected case. Thus the systematic error for the line intensities are within the statistical error. We also checked NXB level of XIS-BI and XIS-FI sensors for each observation field, and confirmed that they are consistent.

3. Energy resolution:
   There is an uncertainty in the calibration of the XIS energy resolution. In order to take the degradation of energy resolution from the calibration data into account, we first fitted the spectra with the double broken power-law model (model 1) multiplied by the gaussian smoothing model *gsmooth* in *XSPEC* whose width does not depend on energy. The best-fit values of the gaussian width of *gsmooth* are less than 10 eV. We determined the statistic error for the width except for the data HL-B(ID 2), FOR(ID 3), PKS1(ID 7), On-FIL(ID 9) and LL10(ID 16), whose statics around the O VII and O VIII lines is poor to determine the error. Then we estimated the surface brightness using this model with the sigma of *gsmooth* fixed to upper limit of the 90 % confidence obtained above. The best-fit values of O VII and O VIII surface brightness are within the 90 % statistical error of those by the model 1 without smoothing.

4. Contamination thickness
   The degradation of low energy efficiency due to the contamination on the XIS optical blocking filter was included in the arf file. The gradient of the contaminant thickness over the optical blocking filter is also taken into account. The uncertainty in the contaminant thickness can have large influence on the estimation of O VII and O VIII intensity. Systematic errors in the contaminant thickness are estimated to be about 10 % (Chapter 3.1 , see also Fujimoto et al. (2007) for early data and Yamasaki et al. (2008b) for recent data).

   We performed all the same analysis to obtain the line intensities described in the previous section for 10% thicker and thinner contaminants than nominal value. Because the contaminant thickness is gradually increasing with time, we created the arf files of 10% thicker or thiner contaminants by shifting the observation dates from the real dates changing the input parameter 'date-obs' in *xissimarfgen* script, except for the 10 % thicker cases of the data of PKS2(ID 6), PKS1(ID 7), LL21(ID 15) and LL10(ID 16). For the four cases, the +10 % thickness is larger than that of the most recent date in the latest calibration database. We thus added an absorption model in the model spectra to represent the extra contamination. For all data set, we found that the best-fit parameters when we assume ±10 % thickness changes within the 90 % statistical errors(See Table E.2). Among the parameters, the O VII emission intensity is most sensitive to the contaminant thickness. The O VII emission intensity varied at most by 0.6 LU (LU = photons $s^{-1}cm^{-2}str^{-1}$ for Off-FIL(ID 8) data, which is smaller than the statistical errors (See Table E.3).

5. Contamination of O VII Kβ line in O VIII line
   The uncertainty of line intensity ratio of O VII Kβ to O VII Kα that is expected by model and used in excluding the contamination of O VII Kβ to O VIII line can affect the O VIII line intensity. We estimated O VIII intensity using the O VII Kβ/O VII Kα of 0.04 for collisional ionization equilibrium plasma at 0.1 keV and 0.08 for solar wind charge exchange(SWCX). The best-fit value of O VIII line intensities are at most 10 %

higher and lower for the case of plasma at 0.1 keV and SWCX, respectively, which are within the statistical errors.

As a consequence, the systematic uncertainties above does not affect the results of O VII and O VIII surface brightness.

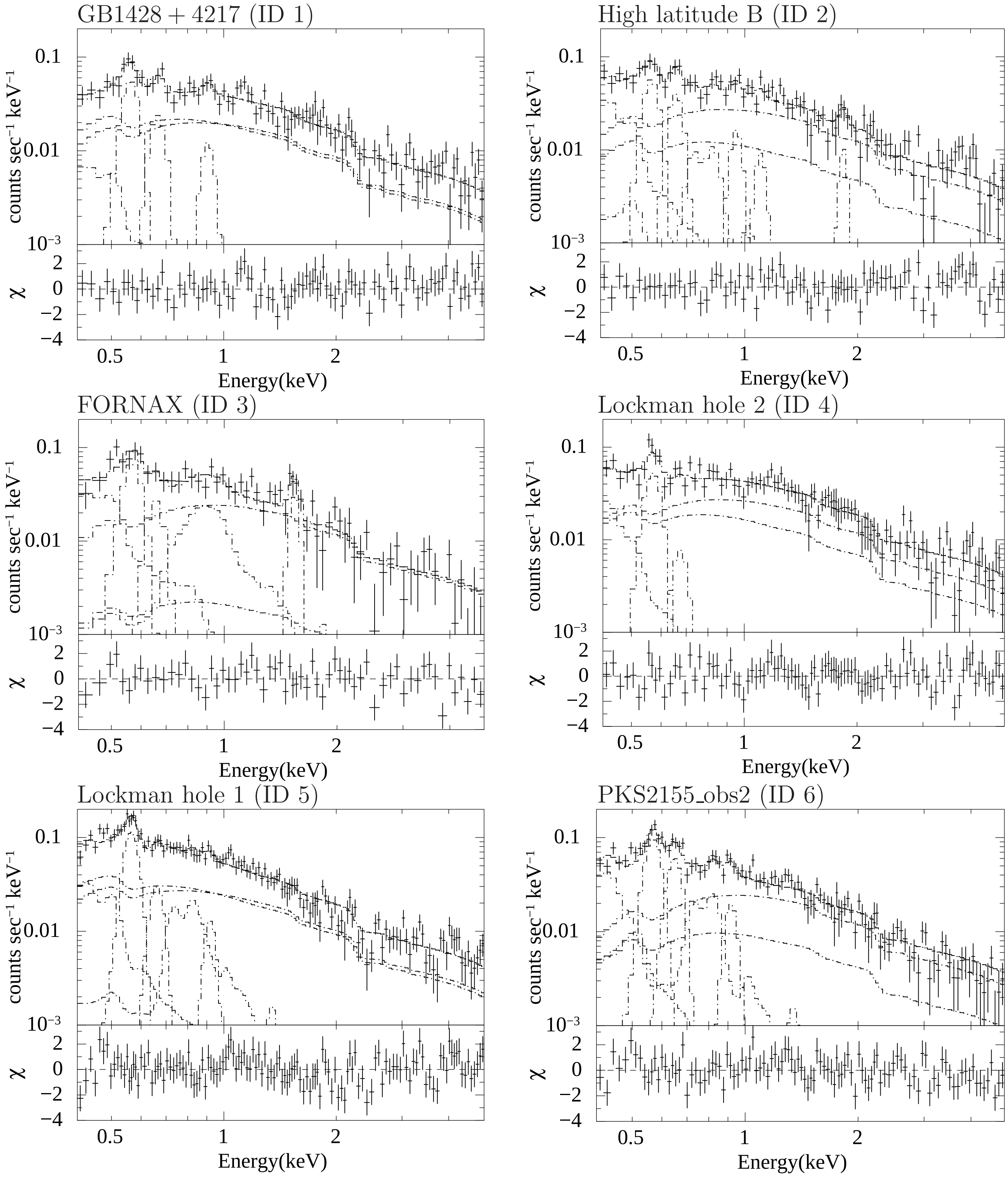

Figure 5.3: Spectra (crosses), best-fit model and its components (step functions) convolved with the instrument response function and residuals of the fit (bottom panels). The model function consists of three spectral components (CXB, TAE, SWCX+LHB) and gaussian lines to determine O VII and O VIII and/or Ne IX lines. The CXB component was represented by a double broken power-law model and the abundance oxygen and/or Neon in TAE and SWCX+LHB model are set to be 0. See Table 5.4 for parameters.

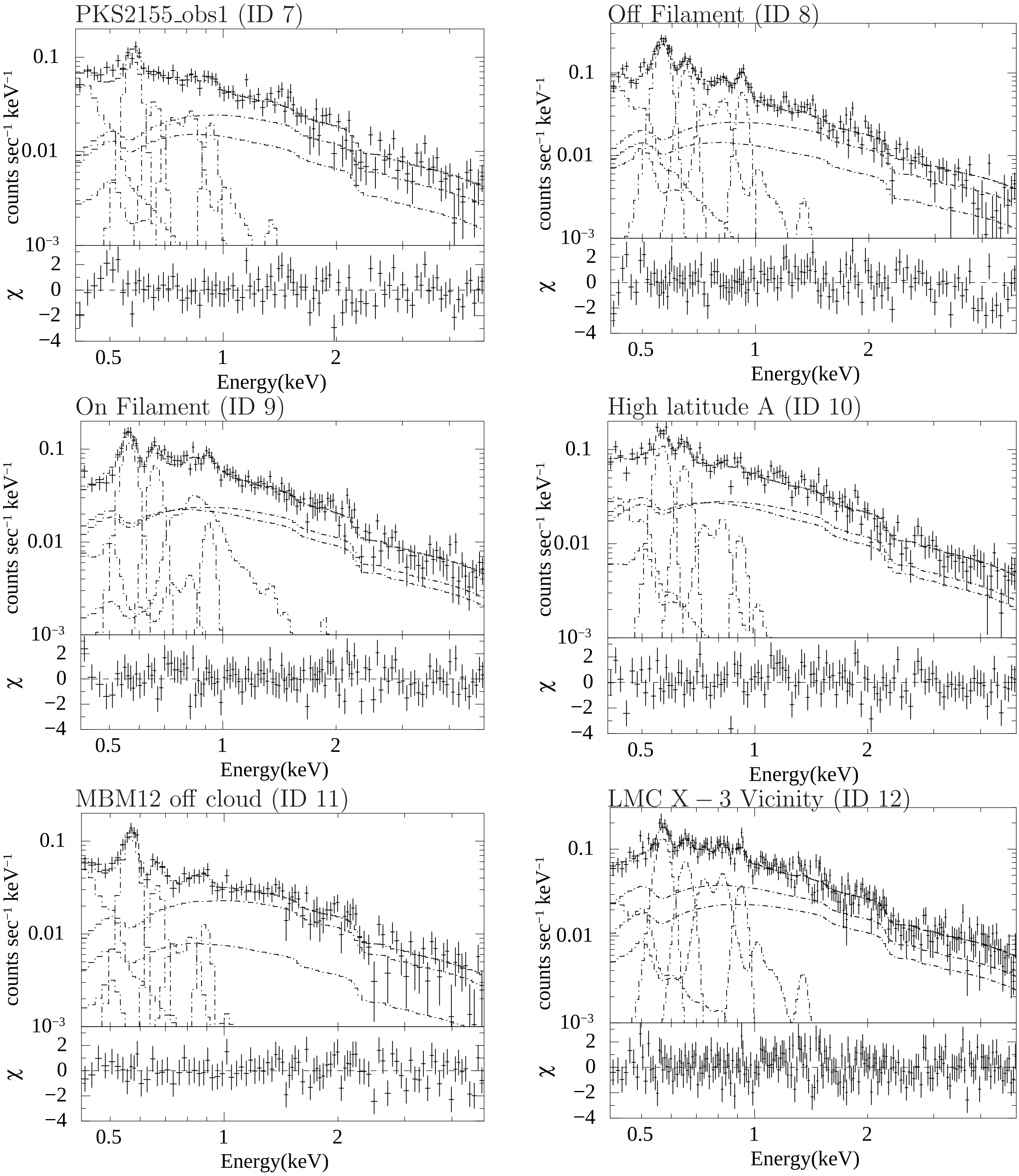

Figure 5.3: *Continued*

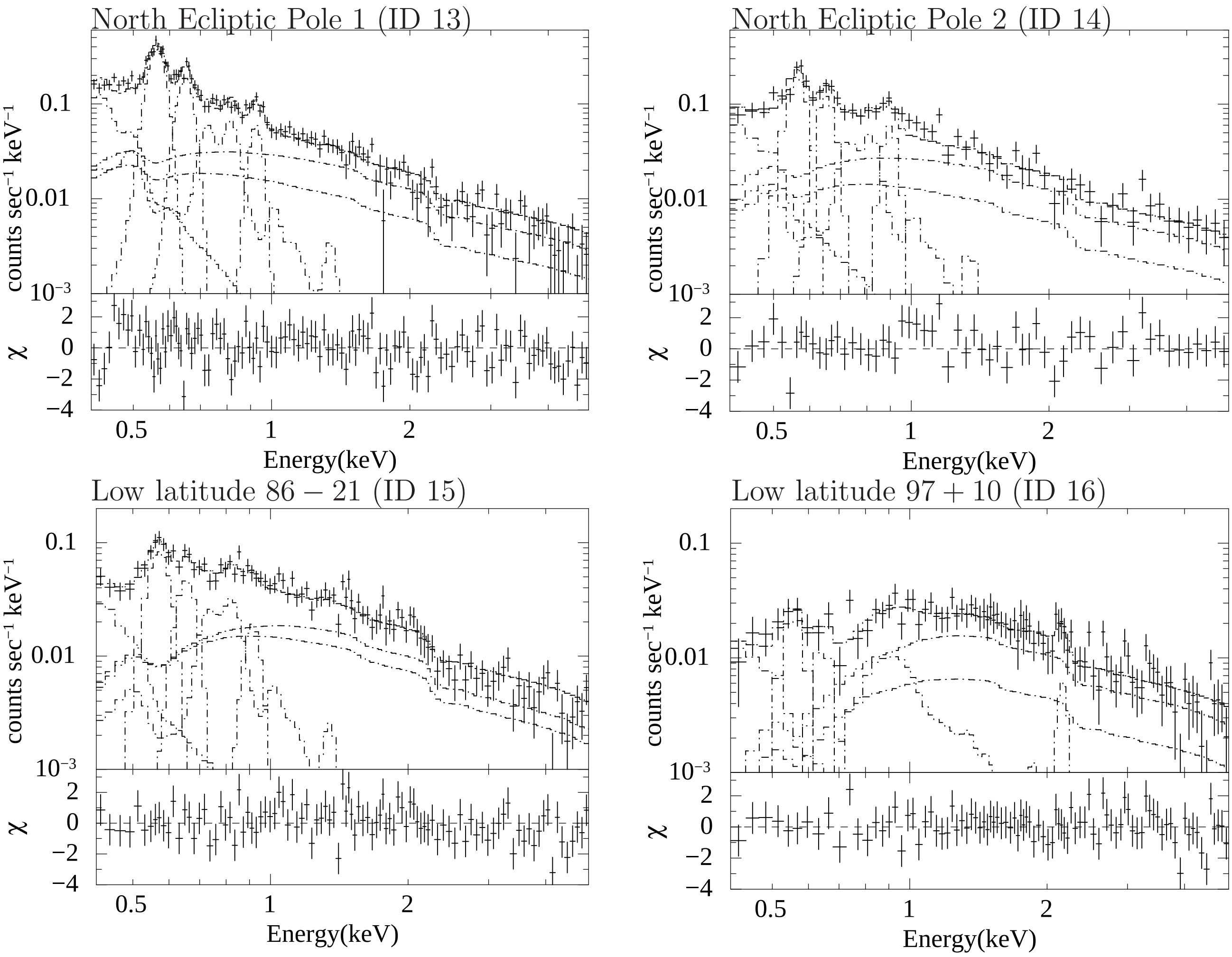

Figure 5.3: *Continued*

Table 5.4: Results of spectral fits to determine O VII and O VIII line intensities with broken-power-law CXB model.

	CXB[a]	TAE[a,b]	SWCX+LHB[b]	O VII		O VIII		χ^2/dof
ID	Norm[c]	Norm[d]	Norm[d]	Centroid	SB[e]	Centroid	SB[e]	
1 (GB)	$5.7^{+0.6}_{-0.6}$	-	$4.5^{+5.6}_{-4.5}$	$0.560^{+0.010}_{-0.008}$	$3.6^{+0.9}_{-1.0}$	$0.664^{+0.017}_{-0.018}$	1.0 ± 0.5	83.19/87
2 (HL-B)	$2.4^{+0.6}_{-0.6}$	$1.9^{+1.6}_{-1.5}$	$14.9^{+5.4}_{-5.4}$	$0.560^{+0.009}_{-0.010}$	$2.3^{+0.7}_{-0.7}$	$0.654^{+0.010}_{-0.014}$	1.1 ± 0.4	80.06/80
3 (For)	$0.5^{+0.8}_{-0.5}$	$1.8^{+0.7}_{-0.7}$	$26.3^{+9.5}_{-9.7}$	$0.568^{+0.014}_{-0.015}$	$5.0^{+1.1}_{-1.5}$	0.654[f]	$1.2^{+0.7}_{-0.8}$	61.69/58
4 (LH-2)	$3.6^{+0.5}_{-0.5}$	-	$18.3^{+9.1}_{-10.1}$	$0.568^{+0.008}_{-0.006}$	$2.5^{+0.7}_{-0.7}$	0.654[f]	< 0.6	93.58/97
5 (LH-1)	$5.6^{+0.5}_{-0.5}$	$1.2^{+0.4}_{-0.4}$	$11.8^{+3.2}_{-3.3}$	$0.562^{+0.003}_{-0.002}$	$4.1^{+0.5}_{-0.5}$	$0.659^{+0.015}_{-0.017}$	0.8 ± 0.3	124.53/ 92
6 (PKS2)	$2.2^{+0.4}_{-0.5}$	$8.4^{+2.3}_{-2.1}$	$61.6^{+12.4}_{-12.6}$	$0.567^{+0.005}_{-0.005}$	$6.3^{+0.8}_{-0.8}$	$0.648^{+0.006}_{-0.008}$	$2.5^{+0.4}_{-0.5}$	105.03/99
7 (PKS1)	$3.4^{+0.5}_{-0.5}$	$4.6^{+1.4}_{-1.3}$	$65.7^{+13.0}_{-12.7}$	$0.574^{+0.008}_{-0.008}$	$5.9^{+0.8}_{-0.9}$	$0.656^{+0.018}_{-0.020}$	$1.3^{+0.5}_{-0.5}$	103.12/86
8 (Off-FIL)	$2.8^{+0.5}_{-0.3}$	$7.5^{+1.2}_{-1.2}$	$27.3^{+4.3}_{-4.8}$	$0.566^{+0.001}_{-0.004}$	$9.3^{+0.6}_{-1.1}$	$0.652^{+0.006}_{-0.004}$	$3.0^{+0.4}_{-0.4}$	148.84/118
9 (On-FIL)	$5.3^{+0.5}_{-0.5}$	$2.9^{+0.6}_{-0.6}$	$11.2^{+3.3}_{-3.3}$	$0.564^{+0.002}_{-0.004}$	$5.6^{+0.6}_{-0.6}$	$0.660^{+0.006}_{-0.006}$	$2.2^{+0.3}_{-0.3}$	117.55/113
10 (HL-A)	$5.0^{+0.5}_{-0.5}$	$4.9^{+2.1}_{-2.1}$	$13.7^{+4.7}_{-4.7}$	$0.564^{+0.004}_{-0.004}$	$4.5^{+0.6}_{-0.6}$	$0.647^{+0.007}_{-0.011}$	1.9 ± 0.4	134.71/111
11 (M12off)	$1.9^{+0.4}_{-0.5}$	$2.9^{+2.1}_{-2.1}$	$24.3^{+5.2}_{-5.3}$	$0.564^{+0.004}_{-0.004}$	$4.4^{+0.5}_{-0.5}$	$0.662^{+0.011}_{-0.010}$	0.9 ± 0.3	79.05/85
12 (LX-3)	$8.8^{+0.5}_{-0.5}$	$7.3^{+1.2}_{-1.3}$	$11.9^{+4.1}_{-4.2}$	$0.570^{+0.004}_{-0.004}$	$6.0^{+0.7}_{-0.7}$	$0.654^{+0.006}_{-0.006}$	2.2 ± 0.4	206.76/192
13 (NEP1)	$3.1^{+0.3}_{-0.5}$	$13.4^{+2.0}_{-1.7}$	$29.1^{+3.5}_{-3.4}$	$0.567^{+0.003}_{-0.001}$	$8.9^{+0.5}_{-0.5}$	$0.653^{+0.004}_{-0.002}$	$3.4^{+0.3}_{-0.3}$	165.23/116
14 (NEP2)	$3.4^{+0.8}_{-0.7}$	$8.2^{+2.6}_{-2.7}$	$25.1^{+7.3}_{-7.2}$	$0.568^{+0.006}_{-0.004}$	$7.0^{+1.1}_{-1.1}$	$0.656^{+0.006}_{-0.008}$	$3.0^{+0.6}_{-0.7}$	56.20/51
15 (LL21)	$4.6^{+0.5}_{-0.5}$	$8.4^{+1.7}_{-1.8}$	$27.3^{+7.4}_{-7.5}$	$0.568^{+0.006}_{-0.005}$	$6.4^{+0.8}_{-0.9}$	$0.652^{+0.010}_{-0.010}$	2.2 ± 0.5	108.14 /93
16 (LL10)	$2.6^{+0.6}_{-0.6}$	$1.7^{+0.7}_{-0.7}$	$10.5^{+5.6}_{-5.6}$	$0.554^{+0.019}_{-0.018}$	$1.7^{+1.3}_{-0.7}$	$0.642^{+0.022}_{-0.034}$	$0.5^{+0.3}_{-0.3}$	80.63/87

[a] The absorption column densities for the CXB and TAE components were fixed to the values tabulated in Table 5.2.

[b] The temperature of TAE and SWCX+LHB components were fixed to the best fit values tabulated in Table 5.2. The O abundance of the both components was set to 0 in the fits.

[c] The unit is photons $\mathrm{s^{-1} cm^{-2}\ keV^{-1} str^{-1}}$@1keV.

[d] The emission measure integrated over the line of sight ,i.e. $(1/4\pi)\int n_{\mathrm{e}} n_{\mathrm{H}} ds$ in the unit of 10^{14} $\mathrm{cm^{-5}\ str^{-1}}$.

[e] Surface brightness in the unit of LU =photons $\mathrm{s^{-1}\ cm^{-2}\ str^{-1}}$.

[f] The centroid energy was fixed to O VIII Kα line energy to obtain the upper limit of the intensity.

5.3 A "floor" of the O_{VII} line intensity and an uniform temperature component

5.3.1 Correlation between O_{VII} and O_{VIII} lines

In Figure 5.5, we plot the derived O VIII emission intensity as a function of the O VII intensity, and include the data points for M12on and MP235 from Masui et al. (2008). It is noted that the evaluated O VIII line intensities in Table 5.4 has a contribution from O VII Kβ since XIS cannot resolve the O VIII Kα (654 eV) and O VII Kβ (666 eV) lines. Therefore, O VIII line intensities in Figure 5.5 are corrected by using the line intensity ratio of O VII Kβ to O VII Kα of 0.06 that is expected by collisional ionization equilibrium model (APEC model) at 0.2 keV and O VII Kα line intensities in Table 5.4.

In Figure 5.5, we notice two remarkable characteristics. First, there is a floor in the O VII intensity at ~ 2 LU. Second, all the data points except for three (HL-B, MP235, and LL10) approximately follow the relation (O VIII intensity) = 0.5 × [(O VII intensity) - 2 LU]. Masui et al. (2008) proposed that the O VIII emission line of the midplane field, MP235, is associated with a ~ 0.8 keV component that may arise from faint young dM stars in the Galactic disk. As we discuss later, the low latitude field at $b = 10°$, LL10, is also considered to contain emission of similar origin. Such high temperature emission produces little O VII.

We thus consider that the floor of O VII emission and the strong correlation between additional O VII and O VIII intensities suggest two different origins for the O VII emission. The second component emits O VII and O VIII with an intensity ratio of about 2 to 1 and shows point-to-point variations of ~ 0 to ~ 7 LU in O VII intensity. The lines in Figure 5.5 show O VII - O VIII intensity relations for different temperatures and absorption column densities. In calculating these lines, we summed up the intensities of the forbidden (561 eV), inter-combination (568 eV) and resonance (574 eV) lines as the O VII line intensity, and O VIII Kα (654 eV) as O VIII line intensity using the absorbed thin thermal model (WABS×APEC) model in *XSPEC* as to the various temperature and absorption column density, since XIS observed the blend of these lines. We have assumed 2.1 LU as the O VII floor intensity, using the value for the midplane field (MP235). The lines suggest that the average temperatures along each line of sight of the plasmas emitting the O VIII emission and the O VII emission above the floor are in a relatively narrow range of $kT \sim 0.19$ to 0.23 keV if they are arising from collisionally equilibrium plasma in spite of the large O VII intensity variations (~ 0 to ~ 7 LU).

5.3.2 Latitude dependence of O_{VII} and O_{VIII} emission lines

In Figure 5.4, we plotted the O VII and O VIII emission intensities as a functions of absolute Ecliptic latitude (top panel) and absolute Galactic latitude $|b|$ (bottom panel). The two data points marked with an open circle are M12on and MP235. If the main origin of the O VII is the SWCX, we expect a correlation between the intensity and the ecliptic latitude. Solar activity affects the solar wind densities and ionization temperature. Near the solar maximum, the slow solar winds which have high ionization temperatures and high densities are ejected from the sun resulting in stronger SWCX induced O VII and O VIII emissions (Koutroumpa et al., 2006) than in solar minimum. Near the solar minimum, slow solar winds are emitted from the equator region of the sun, and high speed, low-density, low-ionization-temperature winds are emitted from the high latitude region of the sun. As the results, in solar minimum, the SWCX induced X-ray emission from the Heliosphere is expected to be stronger near the ecliptic equator than in high ecliptic latitude areas. The observed O VII intensity in Figure 5.4 does not show such a dependence at all. Therefor, it can be interpreted that the spatially dependent components of O VII is associated with the TAE component and not with the SWCX. It is, however, not seen in Figure 5.4 (a). Figure 5.4 (b) suggests that the O VII and O VIII emission intensities are enhanced in $20° \lesssim b \lesssim 50°$. The low intensities of two data points at low latitude can be due to high absorption column density. Since there are only four data points with $b > 50°$, we need more observations to conclude low emission intensities in high latitude. The spatially variable ~ 0.2 keV emission component is likely related to the Galactic TAE.

5.3.3 Temporal variation of the O_{VII} floor

The remaining component which corresponds to the floor of O VII emission is most likely from the Heliospheric SWCX and the LHB. As shown in Figure 5.5, O VIII surface brightness of NEP1 and NEP2 are consistent within statistical error, on the other hand, there is more than ~ 1 LU difference of the surface brightness of O VII. Considering that the date of observation is different but the aiming point is same in the NEP1 and NEP2 observation, the difference of O VII intensity is thus thought to be caused by the temporal variability of the SWCX within the Heliosphere.

The O VII emission intensities of the five fields on the floor of in Figure 5.5 are in the range of 2–3 LU. These results indicate that the O VII intensity in the SWCX+LHB component contain temporal and spatial variations of the order of 1 LU.

5.3.4 The value of O_{VII} floor

The fitting of the O VII vs O VIII in Figure 5.5 excluding the data points of MP235, LL10 and HL-B with a linear function showed that slope and offset are 0.5 ± 0.1 and 0.9 ± 0.3 LU, respectively, and that O VII line intensity at which O VIII corresponds to 0 LU (i.e. floor) is 1.9 ± 0.7 LU. The O VII line intensities of MP235, LL10 and M12on whose mean free path of O VII emission line is a few hundred pc are consistent with floor value, therefore, the emission in these direction is thought to arise from heliospheric SWCX. The O VII line intensity induced by heliospheric SWCX is suggested to have a time variability of ~ 1 LU from the observation of NEP1 and NEP2. These indicate that O VII floor value is $\sim 2 \pm 1$ LU.

5.4 Separation of the TAE and SWCX+LHB components

If the emission which makes a "floor" of the O VII line intensity comes from the LHB+SWCX, and the emission which include O VII and O VIII lines with a fixed ratio indicates a uniform-temperature ($kT \sim 0.2$ keV) ISM in the Galaxy, we expect a constant temperature normalization for the SWCX+LHB component and a constant temperature for the TAE component. However, the results of the spectral fits shown in Table 5.2 (and Table 5.3) do not show

(a)

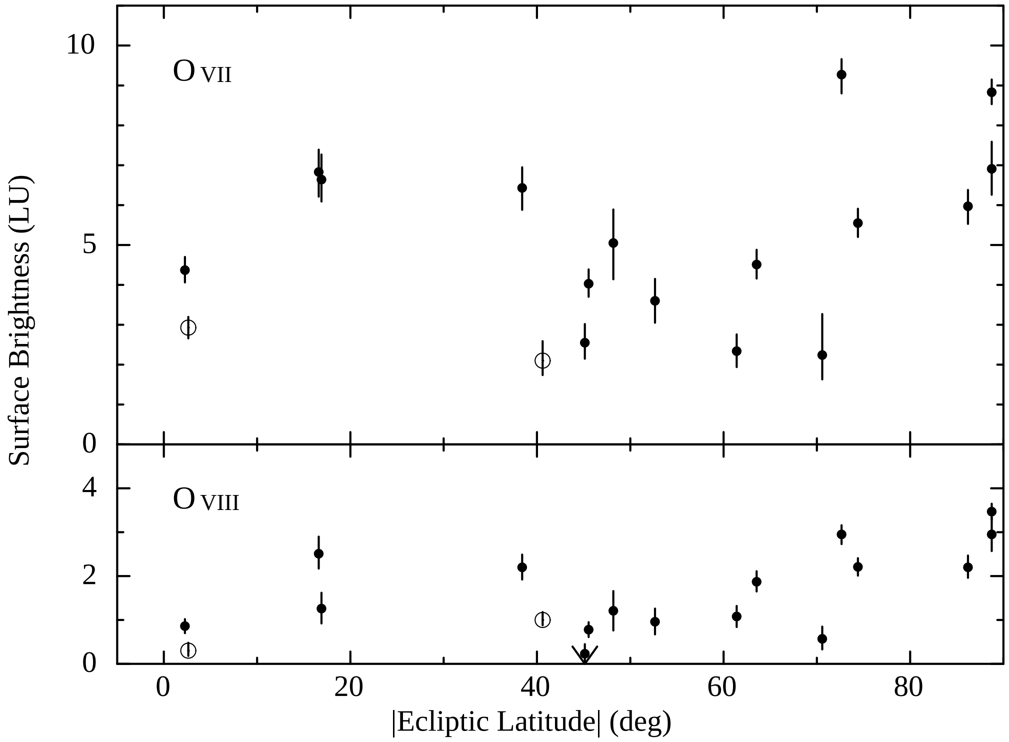

(b)

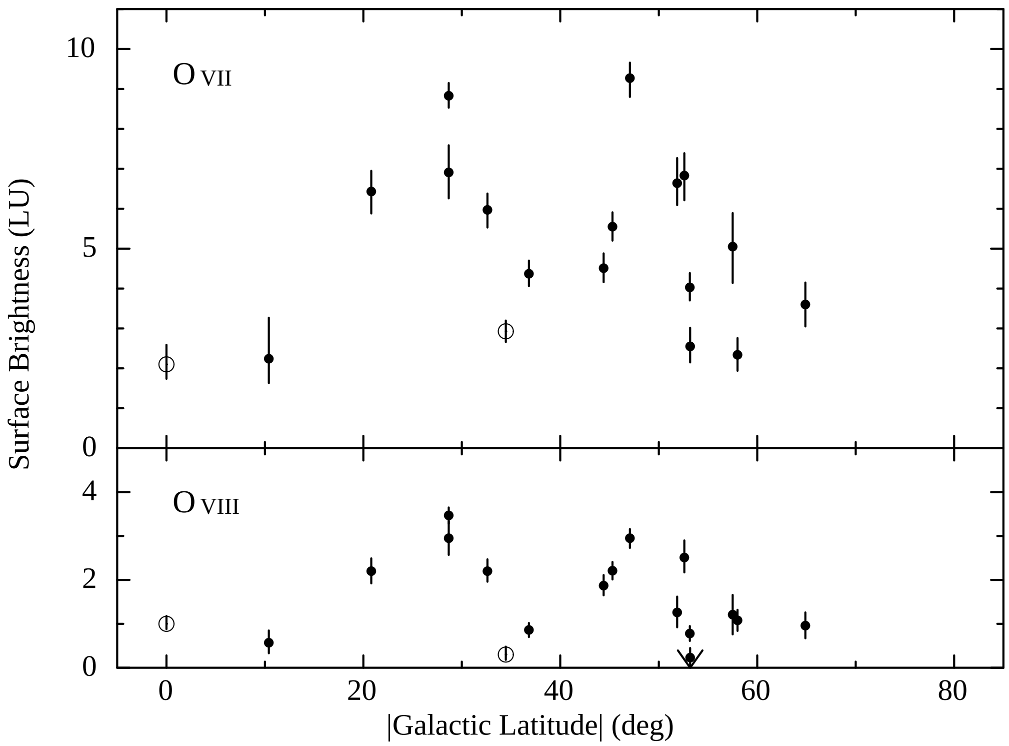

Figure 5.4: O VII and O VIII line emission intensities as a function of absolute ecliptic latitude (a), and as a function of absolute Galactic latitude(b). The two data points marked with an open circle are MBM on cloud direction (l,b)=(159°.2, -34°.5) and Midplane235 (l,b)=(235°, 0°) direction.

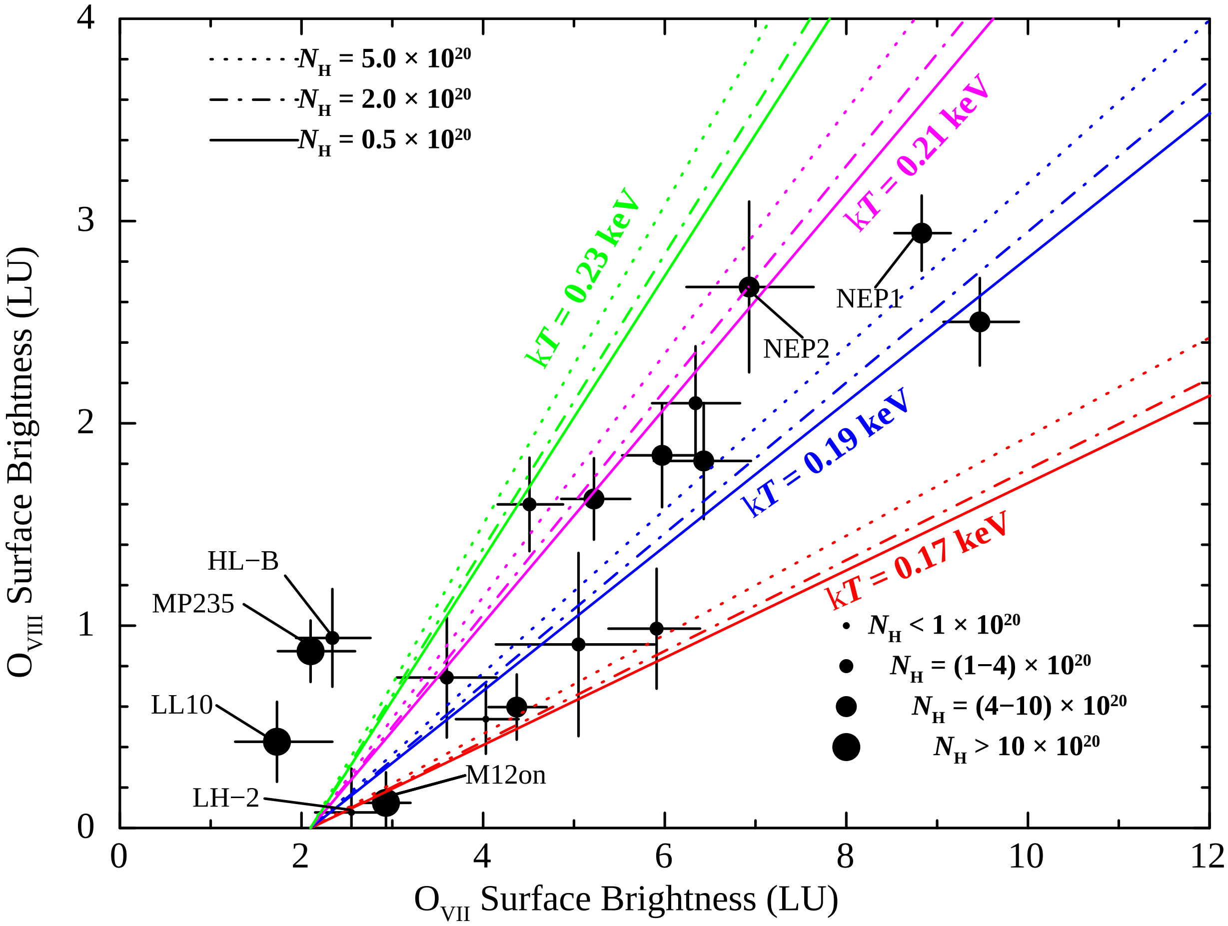

Figure 5.5: Relation between O VII and O VIII surface brightnesses for the 17 sky fields observed with *Suzaku* . The horizontal and vertical bars of data points show the 1 σ errors of the estimation. The diagonal lines show the relation between O VII and O VIII, assuming an offset O VII emission of 2.1 LU and emission from a hot plasma of the temperature and the absorption column density shown in the figure. The Galactic absorption column density of the observation fields are indicated by the maker size of the data points. The short names of five data points on the intensity floor of O VII emission, NEP1 and NEP2 are also shown.

such tendency. The O VII emission intensities of the SWCX+LHB component estimated using the best-fit parameters in Table 5.2 vary from 2 to 5.5 LU. The temperature of the TAE component is significantly higher than 0.2 keV and is far from constant.

The discrepancy is caused by the Fe and Ne emission lines. When we fixed the abundances (Fe to O, and Ne to O ratios) of the hot gas in the spectral fits, the temperature of the TAE component was mostly determined by Fe-L and/or Ne-K emission rather than O emission. Then the temperature and the intensity of the SWCX+LHB component was optimized to fill the remaining emission. We will now try fixing the temperature and the normalization of the SWCX+LHB component, and allowing the Ne and Fe abundances of the TAE component to vary to see if we can still get good fits and if the temperatures of the second component will be closer to 0.2 keV. This is called as "model 2".

5.4.1 Modeling of the SWCX+LHB component

Among the five data points at the floor of O VII in Figure 5.5, M12on, MP235, and LL10 are on special directions, since MBM-12 cloud blocks the TAE, and since no TAE is expected in midplane directions and LL10 field also has a large Galactic absorption. Thus the intensities in these two directions can be regarded as the O VII emission only from SWCX+LHB.

The temperature and the normalization (emission measure) of the SWCX+LHB components are, respectively, $0.109^{+0.006}_{-0.012}$ keV and $13.4^{+6.1}_{-2.4}$ cm^{-5} str^{-1} for MBM12 on cloud (ID R1), and $0.105^{+0.051}_{-0.032}$ keV and $14.1^{+6.9}_{-9.6}$ cm^{-5} str^{-1} for the midplane direction (Midplane235). These values are also consistent with the parameters assumed for the model fitting for LMC X-3 Vicinity (ID 12) by Yao et al. (2009) (0.103 keV and 18.4 cm^{-5} str^{-1}), which were derived from previous *XMM-Newton* and *Suzaku* observations of directions with absorption gas.

5.4.2 Variable abundance TAE model

Thus in following we fitted the spectra using the three component model (CXB, TAE, SWCX+LHB) with both the temperature and the normalization of the SWCX+LHB component fixed, and instead, the Ne and Fe abundances of the TAE component varied. As the nominal SWCX+LHB parameters we adopted the best-fit values of the midplane observation ($kT = 0.105$ keV and an emission measure of 14.1×10^{14} cm^{-5}str^{-1}) because the O VII emission intensity of this observation is the lowest among the 17 spectra.

In Table 5.5 and Figure 5.6 we show the results of the fits. The χ^2 values are generally good with the reduced χ^2 values in the range of 0.95 – 1.34 for the degrees of freedom of 61 – 196, although most of them are larger than those for the fit with the first model shown in Table 5.5. For six spectra GB (ID 1), HL-B (ID 2), FOR (ID 3), PKS1 (ID 7), M12off (ID 11) and LL10 (ID 16), the abundances were not constrained. We thus fixed them to the solar value. For data LH-2 (ID 4), the existence of the TAE was not significant. We estimated the upper limit of the intensity fixing the temperature to the average value of the other spectra. Excluding HL-B and LL10, the temperature of the TAE component is in the range of 0.18 to 0.24 keV with an average of 0.22 keV, which is significantly lower than the temperatures obtained by the model 1.

As noted in Section 5.3.3, there can be an uncertainty of the intensity of heliospheric SWCX emission about 1 LU. Then we check the influence of this uncertainty by changing the normalization of the SWCX+LHB component to 50 % of the nominal (model 2') and 150 % (model 2"), which corresponds to O VII line intensity of 1 LU and 3LU, respectively. The fitting results with model 2' and 2" are shown in Table 5.6 and 5.7. In the case of model 2', the temperature of TAE component is in the range of 0.15 keV to 0.22 keV with an average of 0.19 keV. In the case of model 2", excluding the case of LH-1, the temperature of TAE component is in the range of 0.19 keV to 0.30 keV with an average 0.26 keV. Thus there is uncertainty of the temperature of TAE component about 0.04 keV as to the heliospheric SWCX emission.

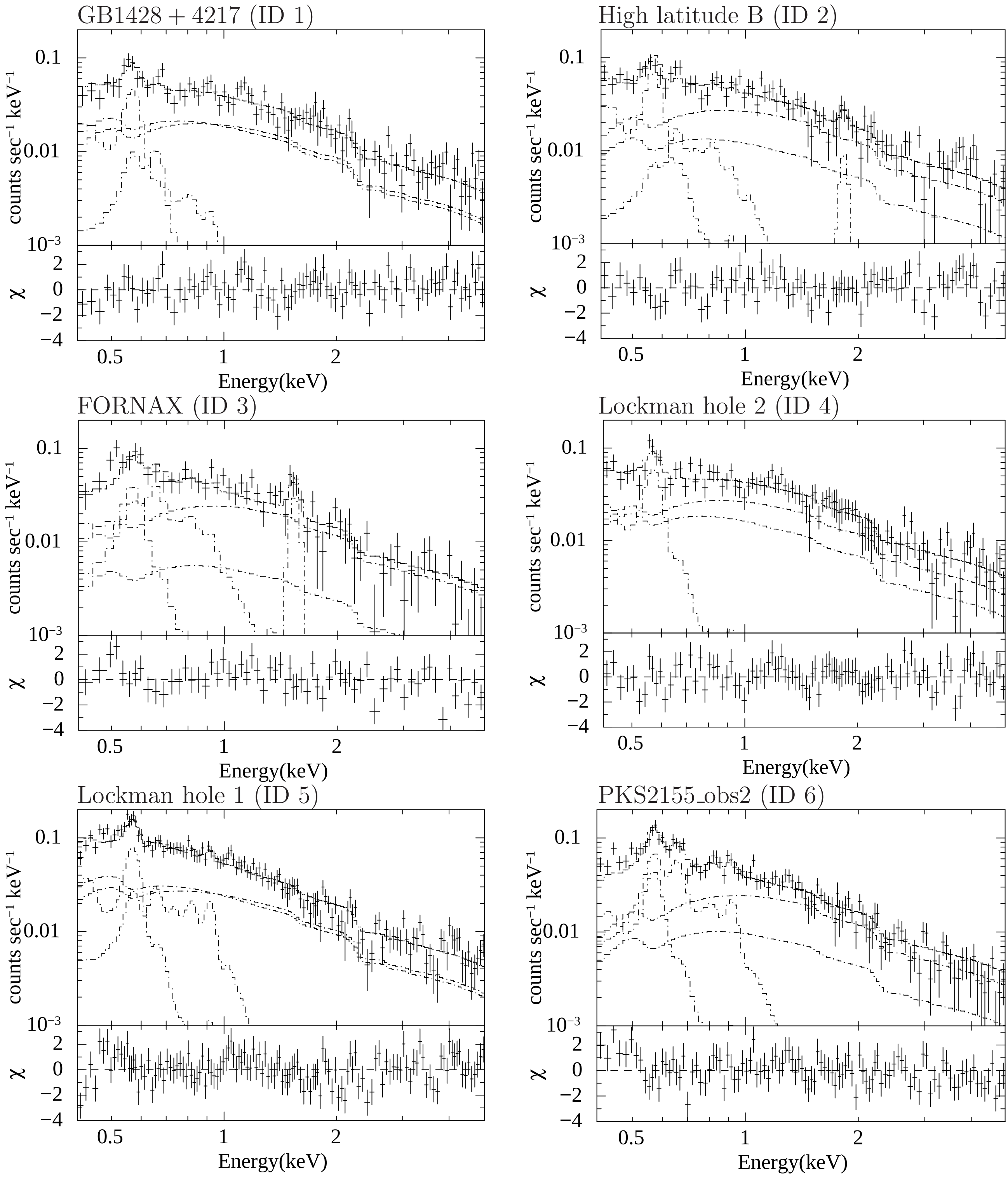

Figure 5.6: Observed spectra (crosses), best-fit model and its components (step functions) convolved with the instrument response function and residuals of the fit (bottom panels) are respectively shown. Results of three-component (CXB, TAE, SWCX+LHB) spectral fit with SWCX+LHB component fixed and with double broken power law CXB (model 2). See Table 5.5 for parameters.

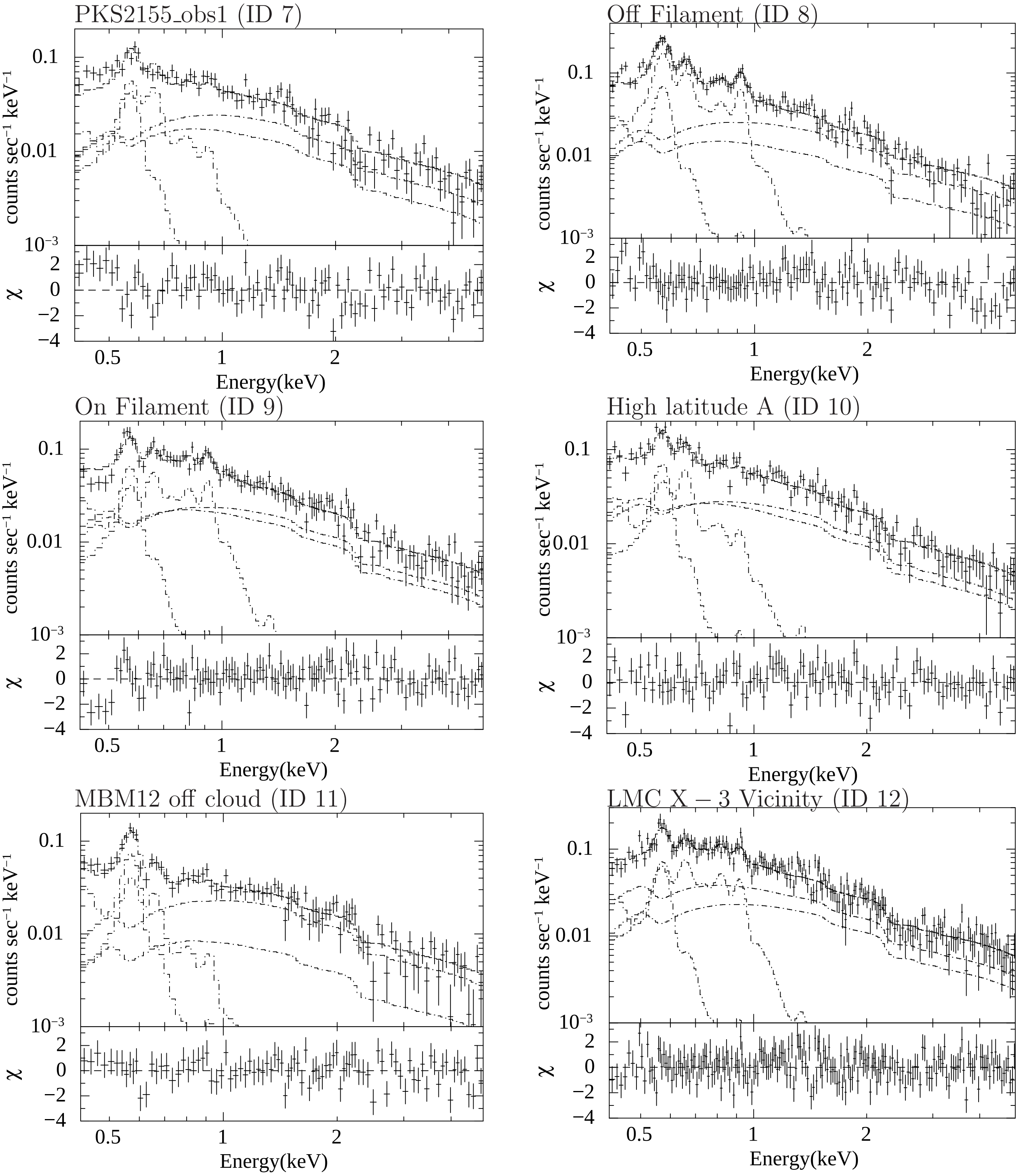

Figure 5.6: *Continued*

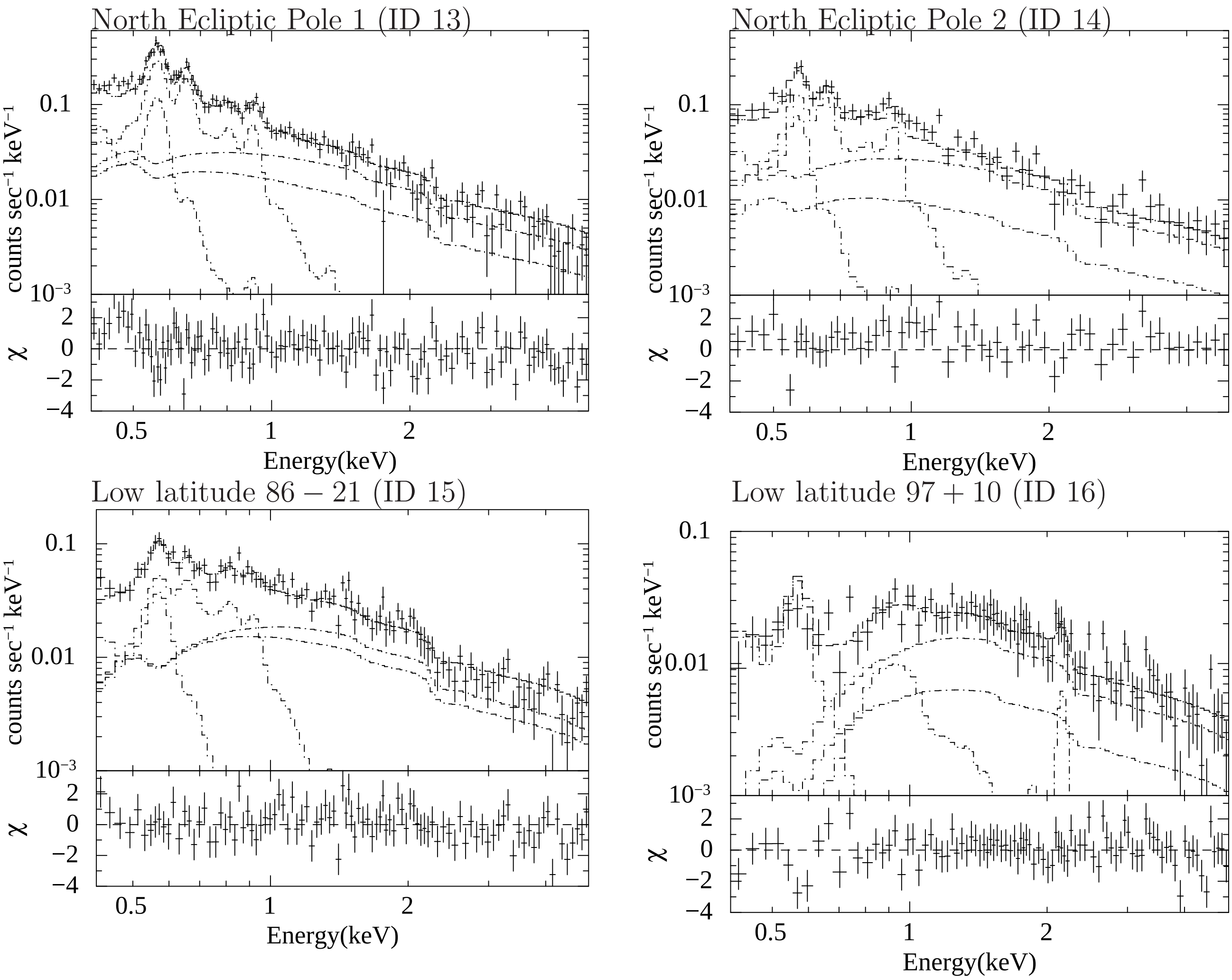

Figure 5.6: *Continued*

Table 5.5: Results of three-component (CXB, TAE, SWCX+LHB) spectral fit with SWCX+LHB component fixed and with double broken power law CXB (model 2). The temperature and normalization of SWCX+LHB component are fixed to 0.105 keV and 14.1 10^{14} cm^{-5} str^{-1} which is the best-fit value of Midplane235.

ID	$N_{\rm H}$[a]	CXB[b]	TAE				χ^2/dof
	10^{20}cm^{-2}	Norm[c]	kT (keV)	Ne	Fe	Norm[d]	
1 (GB)	1.40	$5.6^{+0.7}_{-0.7}$	$0.222^{+0.111}_{-0.068}$	1[e]	1[e]	$1.2^{+1.0}_{-1.0}$	95.12/92
2 (HL-B)*	3.36	$2.5^{+0.5}_{-0.6}$	$0.296^{+0.093}_{-0.049}$	1[e]	1[e]	$1.6^{+0.9}_{-0.7}$	95.14/88
3 (For)*	1.35	$1.2^{+0.8}_{-0.8}$	$0.242^{+0.058}_{-0.054}$	1[e]	1[e]	$4.4^{+1.3}_{-1.3}$	72.67/61
4 (LH-2)	0.56	$3.5^{+0.4}_{-0.5}$	0.217	1[e]	1[e]	< 0.6	95.33/100
5 (LH-1)	0.56	$5.6^{+0.5}_{-0.5}$	$0.237^{+0.262}_{-0.058}$	$3.79^{+6.43}_{-2.02}$	$2.49^{+13.60}_{-1.98}$	$2.0^{+0.6}_{-0.6}$	162.31/127
6 (PKS2)	1.67	$2.2^{+0.4}_{-0.4}$	$0.198^{+0.017}_{-0.015}$	$1.77^{+1.00}_{-0.803}$	$1.22^{+1.50}_{-0.82}$	$7.9^{+1.0}_{-1.0}$	121.74/103
7 (PKS1)	1.76	$3.9^{+0.5}_{-0.5}$	$0.198^{+0.021}_{-0.015}$	1[e]	1[e]	$6.5^{+1.1}_{-1.1}$	131.85/92
8 (Off-FIL)	4.19	$3.1^{+0.4}_{-0.4}$	$0.181^{+0.008}_{-0.008}$	$3.53^{+1.01}_{-0.80}$	$2.99^{+2.75}_{-1.21}$	$15.3^{+1.1}_{-1.1}$	159.33/122
9 (On-FIL)	4.61	$5.0^{+0.5}_{-0.5}$	$0.239^{+0.027}_{-0.025}$	$3.46^{+1.91}_{-1.19}$	$1.88^{+1.97}_{-0.85}$	$5.2^{+0.9}_{-0.9}$	130.94/117
10 (HL-A)	1.02	$4.9^{+0.5}_{-0.5}$	$0.243^{+0.031}_{-0.032}$	$0.91^{+1.06}_{-0.78}$	$0.51^{+1.16}_{-0.48}$	$4.3^{+0.8}_{-0.8}$	138.89/115
11 (M12off)	8.74	$2.0^{+0.4}_{-0.4}$	$0.184^{+0.023}_{-0.030}$	1[e]	1[e]	$4.9^{+1.2}_{-1.2}$	89.83/91
12 (LX-3)	4.67	$8.8^{+0.5}_{-0.5}$	$0.213^{+0.026}_{-0.018}$	$3.04^{+1.28}_{-1.17}$	$3.12^{+1.98}_{-1.59}$	$7.7^{+1.2}_{-0.5}$	210.94/196
13 (NEP1)	4.40	$3.2^{+0.5}_{-0.4}$	$0.191^{+0.006}_{-0.006}$	$2.09^{+0.53}_{-0.47}$	$1.69^{+0.75}_{-0.55}$	$15.3^{+0.9}_{-0.9}$	164.60/120
14 (NEP2)	4.40	$3.4^{+0.7}_{-0.7}$	$0.206^{+0.041}_{-0.019}$	$2.65^{+1.43}_{-1.34}$	$1.59^{+1.743}_{-1.177}$	$10.8^{+1.8}_{-1.8}$	57.94/55
15 (LL21)	7.24	$4.7^{+0.5}_{-0.5}$	$0.193^{+0.019}_{-0.016}$	$2.00^{+1.15}_{-0.86}$	$2.88^{+3.53}_{-1.33}$	$11.1^{+1.7}_{-1.7}$	112.77/97
16 (LL10)*	27.10	$2.5^{+0.7}_{-0.7}$	$0.742^{+0.232}_{-0.174}$	1[e]	1[e]	$1.5^{+0.7}_{-0.7}$	97.54/91

* A fixed gaussian model as NXB-residual line is added at 1.828 keV, 2.157 keV, 1.537 keV for ID 2, ID 3 and ID 16, respectively.

[a] The absorption column densities for the CXB and TAE components were fixed to the tabulated values.

[b] Two broken power-law model was adopted. The photon indices below 1.2 keV were fixed to 1.54 and 1.96. The normalization of the former index component is fixed to 5.7, and only the normalization of the other component was allowed to vary.

[c] The normalization of one of the broken power-law components with the unit of photons s^{-1}cm^{-2} keV^{-1}str^{-1}@1keV. Add 5.7 to obtain the total flux at 1 keV.

[d] The emission measure integrated over the line of sight, i.e. $(1/4\pi)\int n_{\rm e} n_{\rm H} ds$ in the unit of 10^{14} cm^{-5} str^{-1}.

[e] The abundance was not constrained well, thus fixed to the solar value.

Table 5.6: Results of three-component (CXB, TAE, SWCX+LHB) spectral fit with SWCX+LHB component fixed and with double broken power law CXB (model 2'). The temperature and normalization of SWCX+LHB component are fixed to 0.105 keV and 7.0 $\times 10^{14}$ cm^{-5} str^{-1} which is the half of the best-fit value of Midplane235.

ID	$N_{\rm H}$[a]	CXB[b]	TAE				χ^2/dof
	10^{20}cm^{-2}	Norm[c]	kT (keV)	Ne	Fe	Norm[d]	
1 (GB)	1.40	$5.6^{+0.6}_{-0.7}$	$0.181^{+0.041}_{-0.039}$	1[e]	1[e]	$3.0^{+1.1}_{-1.1}$	90.94/92
2 (HL-B)*	3.36	$2.7^{+0.5}_{-0.6}$	$0.226^{+0.038}_{-0.039}$	1[e]	1[e]	$2.6^{+0.9}_{-0.8}$	93.39/88
3 (For)*	1.35	$1.6^{+0.8}_{-0.7}$	$0.189^{+0.031}_{-0.034}$	1[e]	1[e]	$6.7^{+1.8}_{-1.7}$	75.74/61
4 (LH-2)	0.56	$3.5^{+0.5}_{-0.5}$	0.185	1[e]	1[e]	$1.4^{+0.8}_{-0.8}$	97.96/100
5 (LH-1)	0.56	$6.2^{+0.4}_{-0.4}$	$0.188^{+0.017}_{-0.015}$	1[e]	1[e]	$3.8^{+0.6}_{-0.6}$	175.50/129
6 (PKS2)	1.67	$2.4^{+0.4}_{-0.4}$	$0.190^{+0.009}_{-0.009}$	1[e]	1[e]	$10.0^{+1.0}_{-1.0}$	134.19/105
7 (PKS1)	1.76	$3.9^{+0.5}_{-0.5}$	$0.183^{+0.012}_{-0.011}$	1[e]	1[e]	$8.7^{+1.1}_{-1.1}$	141.54/92
8 (Off-FIL)	4.19	$3.2^{+0.4}_{-0.4}$	$0.162^{+0.013}_{-0.010}$	$4.28^{+1.14}_{-0.91}$	$6.94^{+4.07}_{-3.12}$	$20.1^{+2.3}_{-2.5}$	165.87/122
9 (On-FIL)	4.61	$5.2^{+0.5}_{-0.5}$	$0.198^{+0.016}_{-0.014}$	$4.12^{+1.59}_{-1.16}$	$3.22^{+1.70}_{-1.21}$	$7.3^{+1.0}_{-1.0}$	126.06/117
10 (HL-A)	1.02	$5.1^{+0.5}_{-0.5}$	$0.197^{+0.016}_{-0.015}$	$1.18^{+1.18}_{-1.02}$	$1.05^{+1.50}_{-0.98}$	$5.8^{+0.8}_{-0.8}$	142.17/115
11 (M12off)	8.74	$2.1^{+0.4}_{-0.4}$	$0.146^{+0.015}_{-0.030}$	1[e]	1[e]	$12.3^{+2.8}_{-2.8}$	95.31/91
12 (LX-3)	4.67	$8.9^{+0.5}_{-0.5}$	$0.190^{+0.012}_{-0.011}$	$3.21^{+1.32}_{-0.99}$	$4.19^{+3.45}_{-1.57}$	$10.6^{+1.1}_{-1.1}$	208.68/196
13 (NEP1)	4.40	$3.3^{+0.4}_{-0.5}$	$0.181^{+0.005}_{-0.005}$	$2.18^{+0.56}_{-0.50}$	$2.22^{+1.24}_{-0.79}$	$18.1^{+0.9}_{-0.9}$	183.33/120
14 (NEP2)	4.40	$3.5^{+0.7}_{-0.7}$	$0.191^{+0.016}_{-0.014}$	$2.74^{+1.51}_{-1.08}$	$1.97^{+2.88}_{-1.17}$	$13.6^{+1.8}_{-1.8}$	60.89/55
15 (LL21)	7.24	$4.7^{+0.5}_{-0.5}$	$0.177^{+0.014}_{-0.023}$	$2.15^{+1.44}_{-0.95}$	$4.74^{+9.25}_{-2.67}$	$14.6^{+3.7}_{-1.7}$	117.68/97
16 (LL10)*	27.10	$2.6^{+0.7}_{-0.7}$	$0.716^{+0.198}_{-0.154}$	1[e]	1[e]	$1.6^{+0.7}_{-0.7}$	89.50/91

* A fixed gaussian model as NXB-residual line is added at 1.828 keV, 2.157 keV, 1.537 keV for ID 2, ID 3 and ID 16, respectively.

[a] The absorption column densities for the CXB and TAE components were fixed to the tabulated values.

[b] Two broken power-law model was adopted. The photon indices below 1.2 keV were fixed to 1.54 and 1.96 . The normalization of the former index component is fixed to 5.7, and only the normalization of the other component was allowed to vary.

[c] The normalization of one of the broken power-law components with the unit of photons s^{-1}cm^{-2} keV^{-1}str^{-1}@1keV. Add 5.7 to obtain the total flux at 1 keV.

[d] The emission measure integrated over the line of sight, i.e. $(1/4\pi)\int n_{\rm e} n_{\rm H} ds$ in the unit of 10^{14} cm^{-5} str^{-1}.

[e] The abundance was not constrained well, thus fixed to the solar value.

Table 5.7: Results of three-component (CXB, TAE, SWCX+LHB) spectral fit with SWCX+LHB component fixed and with double broken power law CXB (model 2”). The temperature and normalization of SWCX+LHB component are fixed to 0.105 keV and 21.2 $\times 10^{14}$ cm^{-5} str^{-1} which is the 1.5 times best-fit value of Midplane235.

ID	$N_{\rm H}$[a]	CXB[b]	TAE				χ^2/dof
	10^{20}cm^{-2}	Norm[c]	kT (keV)	Ne	Fe	Norm[d]	
1 (GB)	1.40	$5.4^{+0.7}_{-0.7}$	0.262	1[e]	1[e]	< 1.2	109.66/93
2 (HL-B)*	3.36	$2.6^{+0.6}_{-0.5}$	0.262	1[e]	1[e]	< 1.3	129.51/89
3 (For)*	1.35	$1.0^{+0.8}_{-0.8}$	$0.304^{+0.090}_{-0.063}$	1[e]	1[e]	$3.2^{+1.2}_{-1.2}$	68.63/61
4 (LH-2)	0.56	$3.2^{+0.4}_{-0.4}$	0.262	1[e]	1[e]	< 0.3	113.95/100
5 (LH-1)	0.56	$5.2^{+0.5}_{-0.5}$	$0.398^{+0.226}_{-0.061}$	1[e]	1[e]	$1.7^{+0.6}_{-0.6}$	175.55/129
6 (PKS2)	1.67	$2.2^{+0.4}_{-0.4}$	$0.231^{+0.016}_{-0.015}$	1[e]	1[e]	$5.9^{+0.8}_{-0.8}$	115.02/105
7 (PKS1)	1.76	$3.6^{+0.5}_{-0.5}$	$0.248^{+0.026}_{-0.023}$	1[e]	1[e]	$4.5^{+0.9}_{-0.9}$	119.22/92
8 (Off-FIL)	4.19	$3.0^{+0.4}_{-0.4}$	$0.193^{+0.010}_{-0.009}$	$3.36^{+0.92}_{-0.74}$	$2.17^{+1.31}_{-0.78}$	$12.5^{+1.1}_{-1.1}$	153.77/122
9 (On-FIL)	4.61	$4.7^{+0.5}_{-0.5}$	$0.290^{+0.050}_{-0.032}$	$3.00^{+1.66}_{-1.26}$	$1.26^{+1.11}_{-0.66}$	$4.2^{+1.4}_{-1.1}$	148.68/117
10 (HL-A)	1.02	$4.7^{+0.5}_{-0.5}$	$0.269^{+0.022}_{-0.022}$	1[e]	1[e]	$3.0^{+0.6}_{-0.7}$	147.57/117
11 (M12off)	8.74	$1.8^{+0.5}_{-0.5}$	$0.274^{+0.063}_{-0.050}$	1[e]	1[e]	$1.9^{+0.8}_{-0.7}$	86.78/91
12 (LX-3)	4.67	$8.6^{+0.5}_{-0.5}$	$0.258^{+0.043}_{-0.031}$	$2.21^{+1.38}_{-0.89}$	$1.58^{+1.54}_{-0.80}$	$6.5^{+1.3}_{-1.1}$	217.84/196
13 (NEP1)	4.40	$3.1^{+0.4}_{-0.4}$	$0.205^{+0.008}_{-0.008}$	$2.02^{+0.508}_{-0.455}$	$1.40^{+0.54}_{-0.43}$	$12.4^{+0.9}_{-0.9}$	154.13/120
14 (NEP2)	4.40	$3.2^{+0.8}_{-0.8}$	$0.250^{+0.073}_{-0.032}$	$1.90^{+1.35}_{-1.00}$	$0.75^{+0.89}_{-0.55}$	$9.3^{+1.7}_{-1.7}$	54.76/55
15 (LL21)	7.24	$4.5^{+0.5}_{-0.5}$	$0.245^{+0.131}_{-0.036}$	$1.39^{+1.04}_{-0.64}$	$1.16^{+1.69}_{-0.95}$	$8.2^{+1.4}_{-1.4}$	107.53/97
16 (LL10)*	27.10	$2.4^{+0.7}_{-0.7}$	$0.770^{+-0.770}_{-0.173}$	1[e]	1[e]	$1.5^{+0.7}_{-0.7}$	154.20/91

* A fixed gaussian model as NXB-residual line is added at 1.828 keV, 2.157 keV, 1.537 keV for ID 2, ID 3 and ID 16, respectively.

[a] The absorption column densities for the CXB and TAE components were fixed to the tabulated values.

[b] Two broken power-law model was adopted. The photon indices below 1.2 keV were fixed to 1.54 and 1.96 . The normalization of the former index component is fixed to 5.7, and only the normalization of the other component was allowed to vary.

[c] The normalization of one of the broken power-law components with the unit of photons s^{-1}cm^{-2} keV^{-1}str^{-1}@1keV. Add 5.7 to obtain the total flux at 1 keV.

[d] The emission measure integrated over the line of sight, i.e. $(1/4\pi)\int n_{\rm e} n_{\rm H} ds$ in the unit of 10^{14} cm^{-5} str^{-1}.

[e] The abundance was not constrained well, thus fixed to the solar value.

5.4.3 A hotter components in the TAE

In model 2 fit shown in Table 5.5 and Figure 5.6, the strong Fe-L and Ne K lines are explained by over-abundance of those elements. In particular, $\sim 3\times$ solar abundance was required for Ne for four fields LH-1, Off-FIL, On-FIL, LX-3. We consider that the strong Ne and Fe emissions could be also represented by a higher temperature emission component with solar abundances. For model 3, we fixed the temperature and the abundance of the TAE component to the average of model 2 (0.217 keV) and to the solar value, respectively. We introduce a fourth emission component with higher temperature which we denote TAE'. In Table 5.8 and Figure 5.7, we show the results for the four fields. The resultant χ^2 values are comparable to those for model 2. In model 3, the excess Ne and Fe emissions are explained by emission with a temperature in the range of 0.5 to 0.9 keV, and an emission measure of $(1-2)\times 10^{14}$ cm^{-5} str^{-1}.

Table 5.8: Results of four-component (CXB, TAE, TAE', SWCX+LHB) spectral fit with SWCX+LHB normalization and temperature, and TAE temperature fixed and with double broken power law CXB (model 3)

ID	$N_{\rm H}$[a]	CXB[b]	TAE		TAE'		χ^2/dof
	10^{20}cm^{-2}	Norm[c]	kT (keV)	Norm[d]	kT (keV)	Norm[d]	
5 (LH-1)	0.56	$5.4^{+0.6}_{-0.5}$	0.217	$2.0^{+0.6}_{-0.5}$	$0.738^{+0.258}_{-0.312}$	$0.9^{+0.3}_{-0.5}$	160.51/128
8 (Off-FIL)	4.19	$2.7^{+0.5}_{-0.5}$	0.217	$12.6^{+0.8}_{-0.9}$	$0.860^{+0.120}_{-0.128}$	$0.9^{+0.4}_{-0.4}$	211.39/123
9 (On-FIL)	4.61	$4.6^{+0.5}_{-0.5}$	0.217	$4.8^{+0.8}_{-0.9}$	$0.661^{+0.082}_{-0.080}$	$1.8^{+0.5}_{-0.4}$	136.26/118
12 (LX-3)	4.67	$8.5^{+0.6}_{-0.5}$	0.217	$7.4^{+1.0}_{-0.9}$	$0.555^{+0.091}_{-0.172}$	$1.8^{+0.5}_{-0.5}$	215.76/197

[a] The absorption column densities for the CXB and TAE components were fixed to the tabulated values.
[b] Two broken power-law model was adopted. The photon indices below 1.2 keV were fixed to 1.54 and 1.96. The normalization of the former index component is fixed to 5.7, and only the normalization of the other component was allowed to vary.
[c] The normalization of one of the broken power-law components with the unit of photons s^{-1}cm^{-2} keV^{-1}str^{-1}@1keV. Add 5.7 to obtain the total flux at 1 keV.
[d] The emission measure integrated over the line of sight, i.e. $(1/4\pi)\int n_{\rm e} n_{\rm H} ds$ in the unit of 10^{14} cm^{-5} str^{-1}.

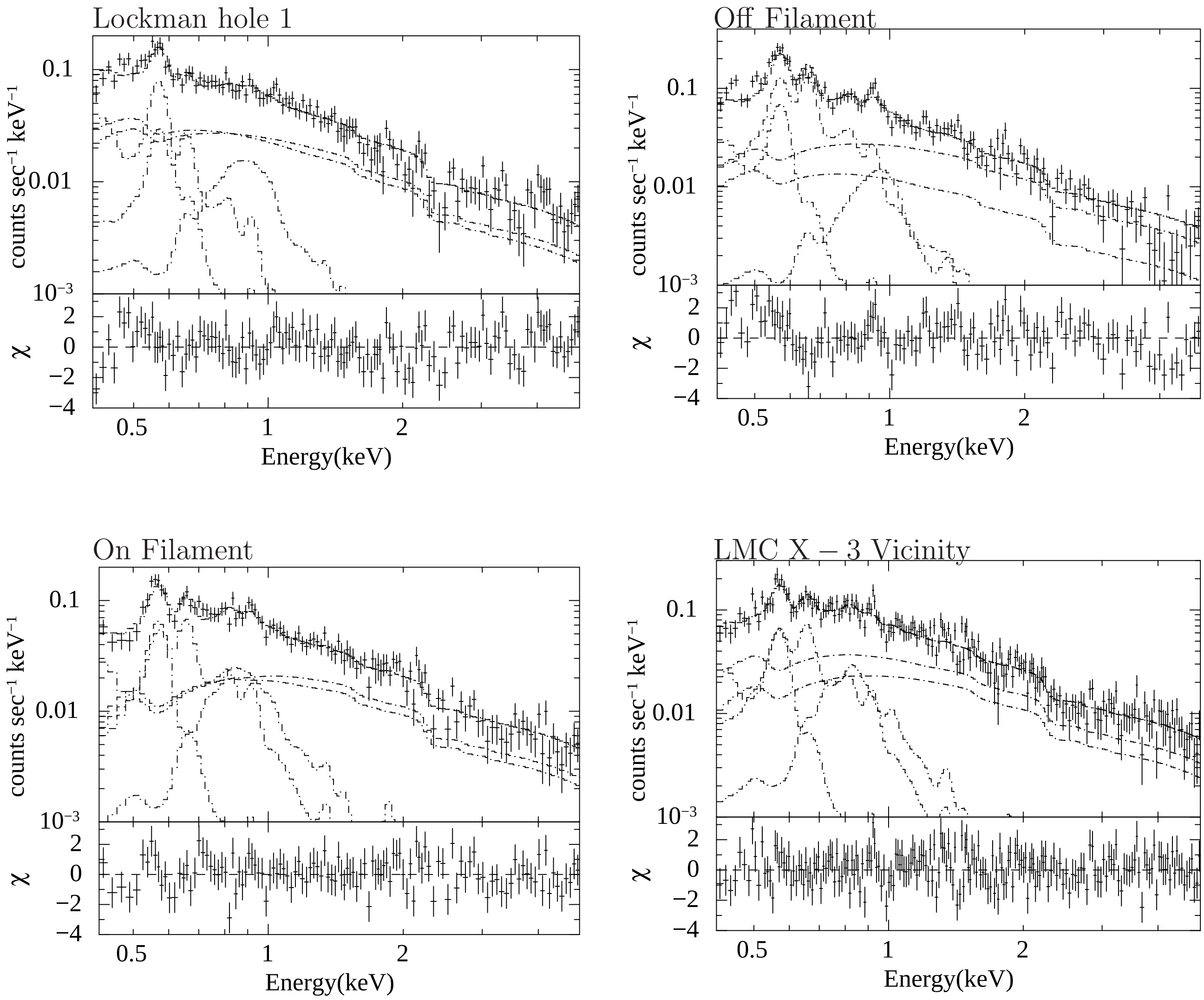

Figure 5.7: Observed spectra (crosses), best-fit model and its components (step functions) convolved with the instrument response function and residuals of the fit (bottom panels) are respectively shown. Results of four-component (CXB, TAE, TAE', SWCX+LHB) spectral fit with SWCX+LHB normalization and temperature, and TAE temperature fixed and with double broken power law CXB (model 3). See Table 5.8 for parameters.

5.5 The trend of Oxygen line intensities with Variable abundance TAE model or hotter component model

The surface brightness of O VII Kα and O VIII Kβ based on the model 2 (Section 5.4.3) and model 3 (Section 5.4.2) are evaluated with the same manner described in Section 5.2.1. As for the case based on the model 3, the temperature of TAE' component is also fixed to the best-fit value. The results of spectral fits based on the model 2 and 3 are summarized in Table 5.9 and 5.10, respectively. The centroid energy of O VIII needs to be fixed for FOR and LH-2 because the same reason as for model1, except for these the centroid energies are consistently determined with the average energy of O VII Kα and O VIII Kα emission lines in collisional equilibrium within the systematic errors of energy scale.

The surface brightness of O VII and O VIII with model 2 and 3 are plotted in Figure 5.8. In this figure, the O VIII line intensities are corrected using the line intensity ratio of O VII Kβ to O VII Kα. Figure 5.8 shows the same trend obtained with model1 as shown in Figure ??, which O VII has a floor, and O VIII line intensity has tight correlation with O VII above the floor. Therefore, the model 2 or 3 can consistently explain both the observed spectra and the trend of O VII and O VIII line intensities.

Table 5.9: Results of spectral fits to determine O VII and O VIII line intensities with model 2.

	CXB[a]	TAE[a,b]	SWCX+LHB[b]	O VII		O VIII		χ^2/dof
ID	Norm[c]	Norm[d]	Norm[d]	Centroid	SB[e]	Centroid	SB[e]	
1 (GB)	$5.7^{+0.6}_{-0.6}$	-	$6.7^{+7.5}_{-6.7}$	$0.560^{+0.008}_{-0.008}$	$3.6^{+1.0}_{-0.9}$	$0.663^{+0.015}_{-0.018}$	$1.0^{+0.5}_{-0.5}$	82.76/87
2 (HL-B)	$2.8^{+0.6}_{-0.6}$	$1.3^{+1.2}_{-1.2}$	$17.2^{+6.4}_{-6.4}$	$0.560^{+0.008}_{-0.010}$	$2.4^{+0.7}_{-0.7}$	$0.652^{+0.012}_{-0.012}$	$1.0^{+0.4}_{-0.4}$	86.29/84
3 (For)	$1.2^{+0.8}_{-0.7}$	$8.5^{+3.4}_{-3.6}$	$21.5^{+13.3}_{-13.9}$	$0.566^{+0.014}_{-0.016}$	$5.2^{+1.1}_{-1.4}$	0.654[f]	$1.0^{+0.7}_{-0.8}$	72.65/58
4 (LH-2)	$3.6^{+0.4}_{-0.5}$	-	$14.9^{+8.2}_{-8.2}$	$0.568^{+0.007}_{-0.009}$	$2.5^{+0.7}_{-0.7}$	0.654[f]	< 0.6	94.47/97
5 (LH-1)	$5.9^{+0.5}_{-0.5}$	$2.5^{+0.8}_{-0.8}$	$11.3^{+4.1}_{-4.3}$	$0.561^{+0.005}_{-0.004}$	$4.2^{+0.5}_{-0.5}$	$0.654^{+0.016}_{-0.016}$	$0.8^{+0.3}_{-0.3}$	158.79/123
6 (PKS2)	$2.1^{+0.5}_{-0.4}$	$18.4^{+3.7}_{-5.1}$	$27.4^{+9.4}_{-8.2}$	$0.570^{+0.004}_{-0.006}$	$6.1^{+0.8}_{-0.9}$	$0.649^{+0.007}_{-0.007}$	$2.4^{+0.4}_{-0.5}$	96.89/99
7 (PKS1)	$3.3^{+0.5}_{-0.5}$	$24.6^{+4.6}_{-6.2}$	$26.1^{+10.9}_{-10.6}$	$0.578^{+0.006}_{-0.006}$	$5.5^{+0.8}_{-0.9}$	$0.661^{+0.017}_{-0.018}$	$1.2^{+0.5}_{-0.4}$	89.71/86
8 (Off-FIL)	$3.2^{+0.4}_{-0.4}$	$23.9^{+3.4}_{-3.5}$	$21.9^{+6.0}_{-5.8}$	$0.567^{+0.002}_{-0.005}$	$9.2^{+0.7}_{-0.7}$	$0.654^{+0.004}_{-0.006}$	$3.0^{+0.4}_{-0.4}$	153.47/118
9 (On-FIL)	$5.4^{+0.4}_{-0.5}$	$6.2^{+1.3}_{-1.3}$	$4.0^{+5.0}_{-4.0}$	$0.562^{+0.004}_{-0.004}$	$5.2^{+0.7}_{-0.6}$	$0.658^{+0.006}_{-0.006}$	$1.9^{+0.3}_{-0.3}$	108.72/113
10 (HL-A)	$4.9^{+0.5}_{-0.5}$	$8.9^{+3.5}_{-3.5}$	$13.1^{+2.9}_{-5.9}$	$0.564^{+0.004}_{-0.004}$	$4.5^{+0.6}_{-0.6}$	$0.646^{+0.008}_{-0.008}$	$1.9^{+0.4}_{-0.4}$	134.10/111
11 (M12off)	$1.9^{+0.4}_{-0.4}$	$11.5^{+7.5}_{-6.7}$	$17.8^{+6.2}_{-6.2}$	$0.566^{+0.004}_{-0.004}$	$4.3^{+0.5}_{-0.6}$	$0.664^{+0.010}_{-0.011}$	$0.8^{+0.3}_{-0.3}$	77.66/85
12 (LX-3)	$9.1^{+0.5}_{-0.5}$	$10.0^{+1.6}_{-1.6}$	$11.8^{+5.3}_{-5.4}$	$0.570^{+0.003}_{-0.003}$	$6.0^{+0.7}_{-0.7}$	$0.654^{+0.006}_{-0.007}$	$2.2^{+0.4}_{-0.4}$	212.32/192
13 (NEP1)	$3.0^{+0.4}_{-0.4}$	$36.0^{+4.0}_{-4.5}$	$15.3^{+4.8}_{-4.6}$	$0.571^{+0.001}_{-0.003}$	$8.7^{+0.5}_{-0.5}$	$0.655^{+0.006}_{-0.003}$	$3.3^{+0.3}_{-0.3}$	148.15/116
14 (NEP2)	$3.5^{+0.7}_{-0.7}$	$21.7^{+6.0}_{-6.3}$	$18.4^{+9.3}_{-8.7}$	$0.570^{+0.004}_{-0.008}$	$6.8^{+1.1}_{-1.1}$	$0.655^{+0.009}_{-0.007}$	$2.9^{+0.7}_{-0.7}$	55.08/51
15 (LL21)	$4.8^{+0.5}_{-0.5}$	$14.8^{+3.2}_{-3.4}$	$23.4^{+8.4}_{-8.1}$	$0.570^{+0.006}_{-0.006}$	$6.3^{+0.9}_{-0.9}$	$0.654^{+0.010}_{-0.009}$	$2.2^{+0.5}_{-0.5}$	112.44/93
16 (LL10)	$2.5^{+0.7}_{-0.6}$	$1.8^{+0.6}_{-0.8}$	$11.9^{+6.4}_{-6.5}$	$0.554^{+0.016}_{-0.018}$	$1.8^{+1.6}_{-0.7}$	$0.642^{+0.022}_{-0.035}$	$0.6^{+0.3}_{-0.3}$	81.17/87

[a] The absorption column densities for the CXB and TAE components were fixed to the values tabulated in Table 5.5.
[b] The temperature of TAE and SWCX+LHB components were fixed to the best fit values tabulated in Table 5.5. The O abundance of the both components was set to 0 in the fits.
[c] The unit is photons $s^{-1}cm^{-2}$ $keV^{-1}str^{-1}$@1keV.
[d] The emission measure integrated over the line of sight ,i.e. $(1/4\pi)\int n_e n_H ds$ in the unit of 10^{14} cm^{-5} str^{-1}.
[e] Surface brightness in the unit of LU =photons s^{-1} cm^{-2} str^{-1}.
[f] The centroid energy was fixed to O VIII Kα line energy to obtain the upper limit of the intensity.

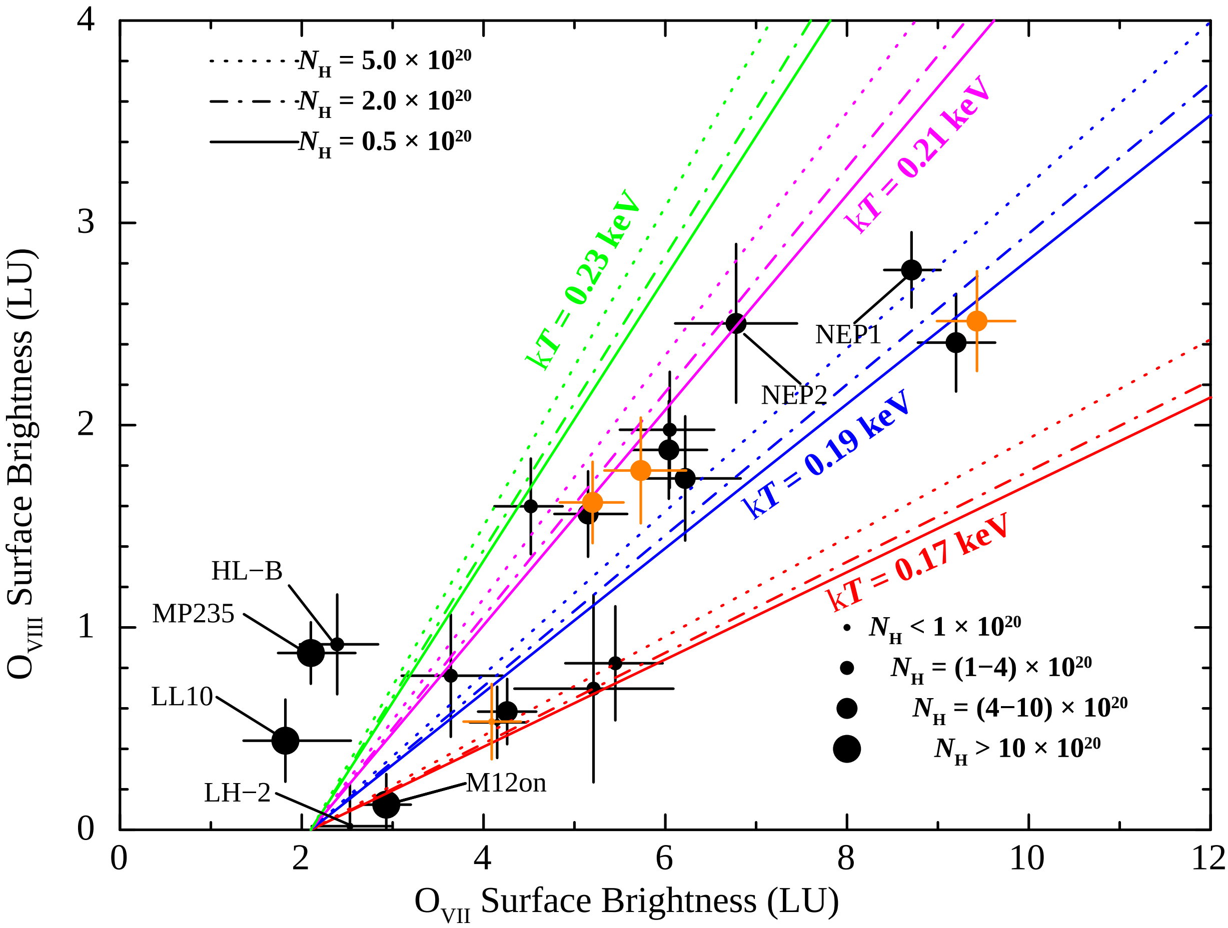

Figure 5.8: Relation between O VII and O VIII surface brightnesses determined by using the model 2 (black) and model 3 (orange) for the 17 sky fields observed with *Suzaku* . The horizontal and vertical bars of data points show the 1 σ errors of the estimation. The diagonal lines show the relation between O VII and O VIII, assuming an offset O VII emission of 2.1 LU and emission from a hot plasma of the temperature and the absorption column density shown in the figure. The Galactic absorption column density of the observation fields are indicated by the maker size of the data points. The short names of five data points on the intensity floor of O VII emission, NEP1 and NEP2 are also shown.

Table 5.10: Results of spectral fits to determine O VII and O VIII line intensities with model 3.

	CXB[a]	TAE[a,b]	TAE'[a,b]	SWCX+LHB[b]	O VII		O VIII		χ^2/dof
ID	Norm[c]	Norm[d]	Norm[d]	Centroid	SB[e]	Centroid	SB[e]		
5	$5.5^{+0.6}_{-0.5}$	$8.5^{+4.3}_{-4.2}$	$0.5^{+0.7}_{-0.5}$	$6.9^{+5.4}_{-5.4}$	$0.562^{+0.004}_{-0.004}$	$4.0^{+0.5}_{-0.5}$	$0.656^{+0.015}_{-0.018}$	$0.8^{+0.3}_{-0.3}$	150.71/122
8	$2.7^{+0.5}_{-0.5}$	$21.8^{+3.5}_{-3.7}$	$0.8^{+0.5}_{-0.6}$	$27.7^{+7.5}_{-5.5}$	$0.566^{+0.002}_{-0.002}$	$9.4^{+0.7}_{-0.8}$	$0.654^{+0.004}_{-0.006}$	$3.1^{+0.4}_{-0.4}$	147.96/117
9	$5.0^{+0.5}_{-0.5}$	$5.4^{+4.0}_{-5.4}$	$1.8^{+0.9}_{-0.9}$	$4.9^{+6.8}_{-4.9}$	$0.563^{+0.004}_{-0.005}$	$5.2^{+0.7}_{-0.6}$	$0.660^{+0.008}_{-0.006}$	$1.9^{+0.3}_{-0.3}$	110.23/112
12	$8.9^{+0.5}_{-0.6}$	$25.7^{+5.6}_{-6.0}$	$0.2^{+1.5}_{-0.2}$	$3.1^{+9.0}_{-3.1}$	$0.570^{+0.003}_{-0.003}$	$5.8^{+0.8}_{-0.7}$	$0.655^{+0.007}_{-0.007}$	$2.1^{+0.4}_{-0.4}$	206.15/191

[a] The absorption column densities for the CXB and TAE components were fixed to the values tabulated in Table 5.8.

[b] The temperature of TAE and SWCX+LHB components were fixed to the best fit values tabulated in Table 5.8. The O abundance of the both components was set to 0 in the fits.

[c] The unit is photons $s^{-1}cm^{-2}$ $keV^{-1}str^{-1}$@1keV.

[d] The emission measure integrated over the line of sight ,i.e. $(1/4\pi)\int n_e n_H ds$ in the unit of 10^{14} cm^{-5} str^{-1}.

[e] Surface brightness in the unit of LU =photons s^{-1} cm^{-2} str^{-1}.

[f] The centroid energy was fixed to O VIII Kα line energy to obtain the upper limit of the intensity.

5.6 Long-term variation of the soft X-ray background

To evaluate the time variability of the soft X-ray background, we compare the *Suzaku* spectra with past *ROSAT* counting rate. We calculated the R45 band counting rate expected from the best-fit model parameters of model1(Section 5.2). We used the *ROSAT* response function, 'pspcc_gain1_256.rsp', in CALDB at NASA/GSFC[2]. In estimating the *Suzaku* counting rate in R45 band for each direction, we created a simulated spectrum with the source which has *Suzaku* best-fit model (model1) obtained in this thesis, using $fakeit$ command in *XSPEC* with the best-fit model and the response of pspcc_gain1_256.rsp, and calculated the counting rate of the simulated spectrum in the 52-90 channel which corresponds to R45 band. Using the database at NASA/GSFC[3], we extracted the *ROSAT* R45 average counting rate in a circular region of 36 arcminute diameter centered at the *Suzaku* XIS aim point. We summarized the values in Table 5.11, and plotted the observed *ROSAT* counting rate in R45 band as a function of expected counting rate from the *Suzaku* observations in Figure 5.9. In the figure we included M12on and MP235 fields using the results from Masui et al. (2008). The horizontal error bars in this figure is 1σ statistical errors estimated from the spectral model fits of *Suzaku* data: we searched for the minimum and maximum expected *Suzaku* R45 count rate for the combination of parameters on the $\chi^2 = \chi^2_{\rm min} + 1$ surface in the 5 dimensional model parameter space (normalization of broken power-law and temperature and normalization of two APEC models).

The counting rates in R45 band of *ROSAT* and those expected from *Suzaku* result are well correlated. However the observed *ROSAT* counting rates are systematically higher than the rates expected from *Suzaku* best-fit model. The sky directions of the seven data points marked with an open rectangle are on streaks of bright areas which meets together at the north/south ecliptic poles in the *RASS* map. We thus consider that they are possibly contaminated with the long-term enhancement, i.e. with the SWCX from the geocorona, or by the solar X-ray scattering during the *ROSAT* observations (Snowden et al., 1994). If we exclude these data points, the scatter of the data points from a linear relation reduces significantly. We then fitted the relation of the remaining nine data points with a linear function: (*ROSAT* observed rate) $=p \times$ rate expected from *Suzaku* $+ q$. We obtained $p = 1.08 \pm 0.12$ and $q = (16.1^{+12.5}_{-13.6})\times 10^{-6}$ c s^{-1} arcmin^{-2}. The slope p is consistent with unity within the 90% statistical errors, while the offset q is positive.

Since Figure 5.9 is a comparison of diffuse emission where point sources are excluded, there can be a large fraction of the positive offset by the difference in point source sensitivity of the *ROSAT* and *Suzaku* observations. The contribution of X-ray point sources to the intensities is estimated as following procedure. For *RASS* map used in the present thesis, the point sources with the count rate >0.020 cts/s in R45 band were removed (Snowden et al., 1997). We first calculated the detection limit of *ROSAT* in 0.47–1.21 keV assuming the absorbed broken power-law model whose photon index are 1.96 and 1.4 below and above 1.2, respectively, and with various absorption column densities from 5.6 $\times 10^{19}$cm^{-2} (LH-1 and LH-2 fields) to 1 $\times 10^{21}$ cm^{-2}. These detection limit is in the range of $(3.8 - 4.0) \times 10^{-13}$ erg s^{-1} cm^{-2}in 0.47-1.21 keV. On the other hand, from the energy fluxes and their statistical errors of the point sources we removed from the present *Suzaku* analysis, we estimate the typical detection threshold for point sources to be 1×10^{-14} erg cm^{-2} s^{-1} in

[2]available from ftp://legacy.gsfc.nasa.gov/ROSAT/calib_data/pspc/cpf/matrices/pspcc
[3]available from http://heasarc.gsfc.nasa.gov/cgi-bin/Tools/xraybg/xraybg.pl

0.47–1.21 keV. Thus there is a factor of $\sim$ 40 difference in the detection threshold. We then estimated the average surface brightness of point sources in the flux range of (1–40) $\times 10^{-14}$ erg s^{-1} cm^{-2} in 0.47–1.21 keV, assuming the log$N$-log$S$ relations (approximately, $N(> S) = 7.5 \times 10^{-20} S^{-1.5}$ [degree^{-2}], where N is the number of point sources whose flux is larger than S) in 0.5-2.0 keV band obtained by $ROSAT$ observation of Lockman Hole field (Hasinger et al., 1993). To convert the energy flux in 0.5-2 keV to the R45 band, we assumed the absorbed power-law described above. We integrated the total flux in the range between detection limit of *Suzaku* and $ROSAT$ using $\int SdN = \int S(dN/dS)dS$. Finally, we calculated the count rate in R45 band using the broken power-law model whose flux in 0.47-1.21 keV corresponds to that estimated above and $fakeit$ with $ROSAT$ response.

As the results we obtained , (10–14)$\times$ 10^{-6} c s^{-1} arcmin^{-2}in the R45 band for $N_{\rm H}$ = (1–0.056)$\times 10^{-21}$cm^{-2} (shown in Figure 5.10). Thus the offset q is consistent with zero if we correct for contribution of point sources in the $ROSAT$ data. After correcting the average value in the $N_{\rm H}$ range, 12×10^{-6} c s^{-1} arcmin^{-2}, we obtain $q = (4^{+13}_{-14}) \times 10^{-6}$ c s^{-1} arcmin^{-2}.

Solar activities affects the solar wind densities and ionization temperature. Near the solar maximum, the slow solar winds which have high ionization temperatures and high densities are ejected from the sun resulting in stronger SWCX induced O VII and O VIII than in solar minimum (Koutroumpa et al., 2006). Near the solar minimum, slow solar winds are emitted from the equator region of the sun, and high speed, low-density, low-ionization-temperature winds are emitted from the high latitude region of the sun. Discrepancies between early *XMM-Newton* or *Chandra* observations which were also made near the solar maximum in 2000-2002 and *Suzaku* observation near the solar minimum were suggested by Koutroumpa et al. (2007) and Henley & Shelton (2008). For example, Lockman Hole $(l, b) = (149.1, 53.6)$ by *XMM-Newton* observations taken in October 2002 shows much higher O VII intensities (7 to 18 LU Koutroumpa et al. (2007)) than that of *Suzaku* (2.5 and 4.1 from the present LH-1 and LH-2 fields). Henley & Shelton (2008) showed that O VII line intensities on and off directions of the shadowing filament, (On-FIL, and Off-FIL fields) were $10.65^{+0.77}_{-0.82}$ and $13.86^{+1.58}_{-1.49}$ LU for the *XMM-Newton* observations in 2002 March, while they reported that the intensities for the *Suzaku* observation were $6.51^{+0.37}_{-0.45}$ and $10.53^{+0.68}_{-0.55}$ LU (statistically consistent with the present results, $5.2^{+1.0}_{-0.6}$ and $9.5^{+0.7}_{-0.7}$ LU). If this difference is due to the different SWCX intensity as the authors suggest, it was brighter by about 5 LU during the *XMM-Newton* observations than *Suzaku* . However, the O VII emission intensity in the MBM12 on-cloud direction (M12on) determined by *Chandra* (1.79$\pm$0.55) and *Suzaku* (2.93$\pm$ 0.45) were marginally consistent within the 90 % statistical errors, although the O VIII emission intensity by *Chandra* (2.34 ± 0.36 LU) was larger than that of *Suzaku* (0.30 ± 0.20 LU).

Although the $ROSAT$ all sky survey was also carried out near the solar maximum in 1990, the present results show that *Suzaku* and $ROSAT$ R45 band intensities at least ten directions were consistent to each other. The intensity of the spectral component for SWCX+LHB in model 2, which contains O VII emission of 2.1 LU is converted to a $ROSAT$ R45 counting rate of 14×10^{-6} c s^{-1} arcmin^{-2}. This is comparable to the 90 % confidence upper limit of offset q (=17×10^{-6} c s^{-1} arcmin^{-2}). This suggests that on average, the difference in O VII intensity between the $ROSAT$ and *Suzaku* is at most $\sim$ 2 LU. In Chapter 4, we tried to remove the time intervals in which the X-ray spectrum was contaminated by the SWCX from the geocorona. However, for the HL-A and M12off data, we could not exclude possible contaminations. Since both data points are on the same trend of other data points in the plot of Figure 5.9, we consider the contaminations by the SWCX from geocorona were small for these data sets.

Table 5.11: Comparison of *ROSAT* with *Suzaku* in R45 band count rate. The errors in this table are all at 1σ significance.

ID	*Suzaku* [a]	*RASS*[b] R45 band
	10^{-6} c s^{-1} arcmin^{-2}	
1 (GB)	85.4 ± 2.6	186 ± 21
2 (HL-B)	65.6 ± 2.2	150 ± 21
3 (FOR)	83.6 ± 4.2	96 ± 30
4 (LH-2)	68.4 ± 1.9	85 ± 15
5 (LH-1)	103.5 ± 2.0	103 ± 16
6 (PKS2)	104.3 ± 2.6	186 ± 24
7 (PKS1)	107.9 ± 3.0	162 ± 23
8 (Off-FIL)	130.4 ± 2.3	227 ± 34
9 (On-FIL)	105.3 ± 2.1	118 ± 27
10 (HL-A)	103.7 ± 2.2	112 ± 17
11 (M12off)	60.0 ± 1.8	99 ± 20
12 (LX-3)	140.1 ± 2.4	180 ± 16
13 (NEP)	136.6 ± 1.8	158 ± 4
14 (LL21)	109.3 ± 2.8	123 ± 14
15 (LL10)	31.6 ± 1.8	44 ± 9
R1 (M12on)	20.8 ± 0.9	37 ± 11
R2 (MP235)	58.0 ± 2.3	109 ± 21

[a] The intensity in R45 band expected from the *Suzaku* best-fit model function.
[b] Average intensity for a circular region of 36 arcminute diameter centered at the *Suzaku* observation aim point.

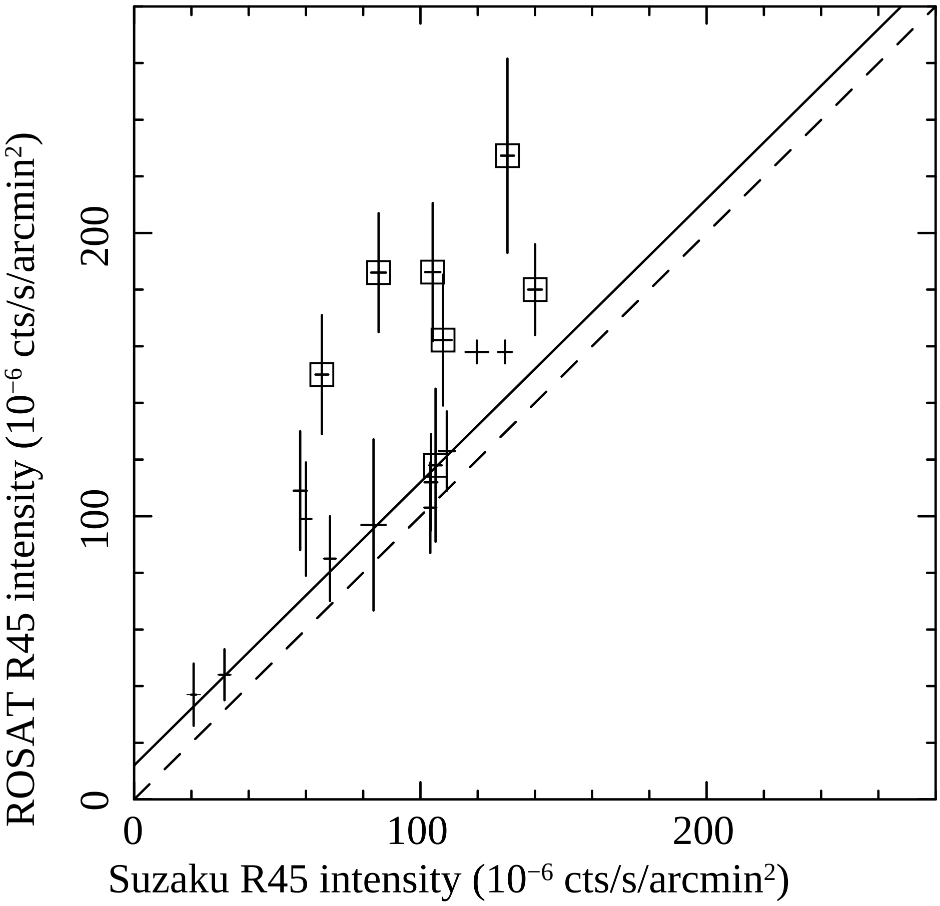

Figure 5.9: Observed *ROSAT* R45 band count rate v.s. R45 count rate expected from *Suzaku* best-fit model functions. The vertical error bars are the 1σ statistical errors of the *ROSAT* observation. The horizontal error bars are the 1σ statistical errors from the spectral model fits of the *Suzaku* data. The data in open rectangle are the directions which are possibly contaminated by LTEs in *RASS* map. Dashed line shows a slope of unity and solid line shows a slope of unity and 12×10^{-6} c s^{-1} arcmin^{-2} offset that is an average point source removal correction due to the detection limit of *Suzaku* and *ROSAT* (See Figure 5.10).

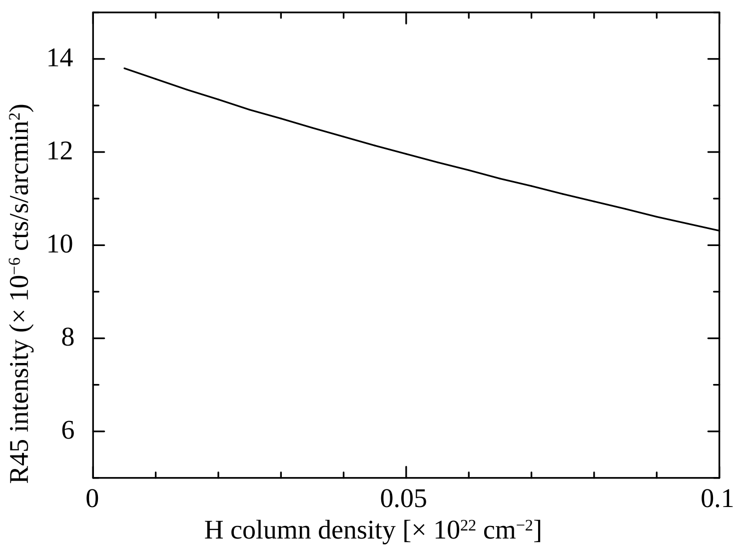

Figure 5.10: The contribution of the point sources whose flux is between the detection limit of *Suzaku* and *ROSAT* to the counting rate in R45 band as a function of hydrogen column density. In calculating the count rate, we assumed the model of an absorbed broken power-law whose photon indices is 1.96 and 1.4 below and above 1.2 keV, respectively and used the log$N$-log$S$ relation in Hasinger et al. (1993).

Chapter 6

Discussion

6.1 Summary of the Observational Results

In the present thesis, we have studied the feature of Soft X-ray diffuse Background (SXDB) emission in the seventeen directions which do not show the local X-ray emission enhancements such as Radio Loop I. We analyzed the *Suzaku* XIS-BI spectrum and utilize the O VII and O VIII emission lines as a main probe of investigating the SXDB. Specifically, we carefully exclude the contribution of the geocoronal charge exchange to the analyzed spectra. Below we summarize the obtained observational results.

1. The observed spectra clearly show the O emission lines and could be fitted with the model function which consists of three components(model 1): absorbed double broken power-law for the extragalactic cosmic X-ray background (CXB), unabsorbed thin thermal plasma model for the sum of heliospheric solar wind charge exchange and Local Hot Bubble(SWCX+LHB), and absorbed thin thermal plasma model for the plasma extending beyond the galactic HI (so-called transabsorption emission: TAE).

2. The obtained line intensities of O VII and O VIII line intensities using three component model above are distributed from $\simeq 2$ to $\simeq 10$ photons s^{-1} cm^{-2} str^{-1} (LU) for O VII and from $\simeq 0$ to $\simeq 4$ LU for O VIII. There are two remarkable features as follows.

    (a) The O VII and O VIII intensities are correlated and suggest the existence of an intensity floor for O VII emission at ~ 2 LU. This floor of O VII line intensity is consistent with the result of shadowing observation of MBM on cloud and that of Midplane235 ($(l, b) = (235°, 0°)$) whose emission are attribute to SWCX+LHB component only.

    (b) In the observation fields above the floor, O VII and O VIII line intensity show the tight correlation that is approximated as (O VIII intensity) = 0.5 × [(O VII intensity) - 2 LU]. In spite of large variation in O VII, the average temperature of the line of sight of plasma emitting the O VII and O VIII lines above the floor are in a relatively narrow range of $kT \sim 0.19$ to 0.23 keV if they arise from collisionally equilibrium plasma.

3. O VII and O VIII line intensities show no correlation with ecliptic latitude. This indicates that the O VII emission above the floor and the O VIII emission are not from SWCX because the intensity of SWCX emission in solar minimum phase is expected to correlate with ecliptic latitude, in particular it is strong in the ecliptic latitude range of $-20°$ to $+20°$.

4. The properties of O emission were not consistent with the results of spectral fits with model 1. Thus we tried to fit the observed spectra with two other models. In model 2, both the normalization and the temperature of the SWCX+LHB component were fixed to the values obtained with Midplane235 observation, which we consider to represent the typical "floor" parameters. This model contains O VII emission of 2.1 LU. The Fe and Ne abundances of the TAE component were set free. In model 3, the parameters of the SWCX+LHB were fixed as model 2. In model 3, the Ne and Fe abundance are fixed to the solar value. Instead, a higher temperature component was added to represent the strong Ne and Fe lines in some of the spectra. With these models, the temperature of the TAE component were $\simeq 0.2$ keV, and the increase of o VII intensity above floor and the O VIII emission were explained by the increase of intensity of the TAE component.

5. We compared the R45 band intensity of *Suzaku* observation with *ROSAT* observation of each direction. In spite of the fact that the present *Suzaku* observations and the *ROSAT* all sky survey were respectively conducted in solar minimum and maximum, no significant difference were found, if we take the difference in the point source sensitivity of the two missions into account. We placed 2 LU as the 90 % upper limit in the O VII intensity difference from *ROSAT* to *Suzaku*.

To obtain the above results, it was essential to determine the O VII and O VIII intensities reliably, which was only possible with *Suzaku* . In Figure 6.1, we show the relation between the O VII intensity and the *ROSAT* R45 band intensity. Although the O VII intensity is positively correlated with the R45 band intensity, there is large point-to-point fluctuations in the correlation. For example, if we estimate the O VII intensity from *RASS* map using this correlation, we will have typically 4 LU uncertainty. This demonstrates that it is essential to determine the line intensities using *Suzaku* .

6.2 Spatial distribution of emission measure of the TAE component

6.2.1 The patchy hot thick disk model

As shown in Chapter 2, Yao et al. (2009) showed that an isothermal hot gas cannot simultaneously explain the absorption lines observed in the energy spectra of LMC X-3, the X-ray binary in the LMC, with *Chandra* , and the emission lines in the energy spectra of the X-ray diffuse emission in the two directions about 30' away from LMC X-3 observed with *Suzaku*. On the other hand, we found that the temperature determined from the O VII and

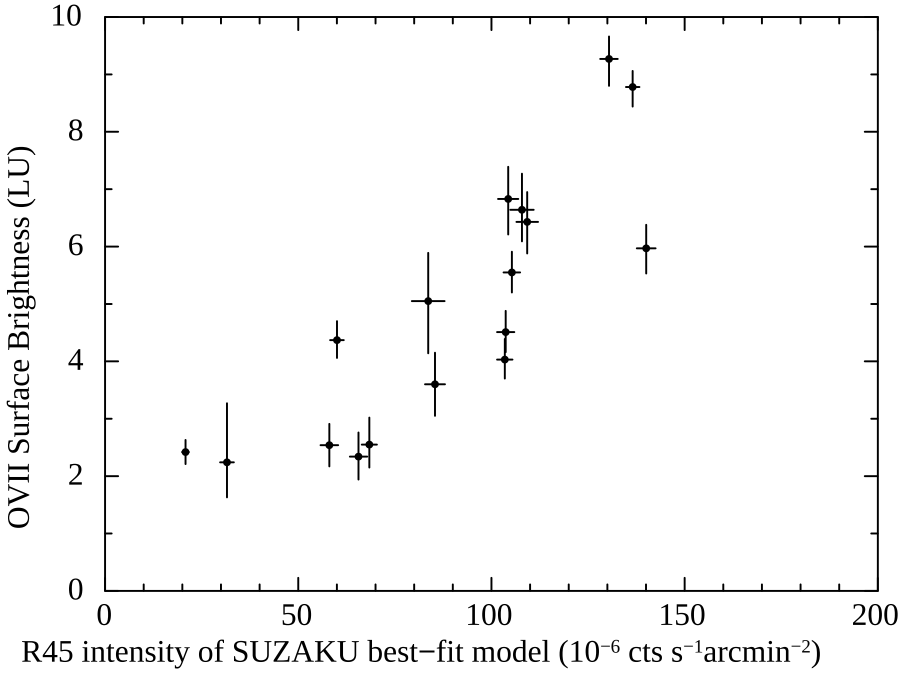

Figure 6.1: O VII surface brightness in unit of LU as a function of the count rate in R45 band expected from *Suzaku* best-fit model in Table 5.2. The horizontal and vertical errors are written in 68 % confidence level.

O VIII emission ratio shows only small point-to-point variations. How these two apparently contradicting observational results are explained?

Yao et al. (2009) constructed a thick hot disk model extending from the Galactic disk in order to simultaneously explain the absorption and emission lines towards the LMC X-3 direction. They assumed density and temperature distributions exponentially decreasing in the direction perpendicular to the Galactic disk. They obtained as the best-fit parameters the scale heights of $h_{\rm T}\xi = 1.4^{+3.8}_{-1.2}$ kpc and $h_{\rm n}\xi = 2.8^{+3.6}_{-1.8}$ kpc for temperature and density respectively, and the midplane gas temperature and H ion density of $T_0 = 3.6^{+1.1}_{-0.7} \times 10^6$ K and $n_0 = 1.4^{+2.0}_{-1.1} \times 10^{-3}$ cm^{-3}, where ξ is the filling factor of the hot gas. The emission-measure weighted average temperature along a line of sight is $T_0/(1+h_{\rm n}/(2h_{\rm T})) \sim 0.16$ keV. This is lower than the best-fit temperatures of the TAE component with model 2 shown in Table 5.5, although the discrepancy is not very large taking the the errors in T_0 and $h_{\rm n}/h_{\rm T}$ into account. If the TAE component comes from such a uniform thick disk, the O VII and O VIII emission ratio should be constant for all directions. Thus this model explains the two results consistently, which look contradicting to each other.

For a thick-disk with plane-parallel configuration, we expect the intensity of the emission to increase from high to low latitude as $\propto \sin^{-1}|b|$ because emission measure is proportional to $\sin^{-1}|b|$, on the other hand, at low latitude $\lesssim 10°$, it decreases rapidly because of the Galactic absorption. In Figure 6.2, instead of O VII emission intensity, we show the emission measure of TAE component for model 2 multiplied by $\sin|b|$ (denoted $EM\sin|b|$). The distribution of $EM\sin|b|$ is far from constant, showing a large direction-to-direction fluctuation. This suggests that the hot gas is patchy and consists of number of blobs. Particularly the short angular scale spatial variation between the two Lockman hole fields, LH-1 and LH-2 ($|b| =$

53.2), is puzzling. These are separated by only 0.42°, but the TAE component and O VII emission are significantly stronger for LH-1 (Table 6.2,Figure 5.4). The *ROSAT* map also show a difference in R45 intensities of the two fields (Table 5.11), although the field of view of the two *ROSAT* fields are overlapped to each other. Thus the difference of two fields are not due to time variations in Heliospheric SWCX. Since the distance between the two lines of sight is only 10 pc at 1kpc away from the Sun, the density contrast of hot plasma must be high between outside and inside the blobs. Because of the patchy distribution, the volume filling factor, ξ, of the hot gas must be low. On the other hand ξ may be larger than 0.1, so that the scale height of the hot disk model does not exceed the size of the Galaxy. If the typical blob size is 100 pc, there are ten blobs along the sight line of a 10 kpc length. Since the separations of line of sights of LH-1 and LH-2 is 100 pc even at 10 kpc, we have to assume unusual situation that the sight line to LH-1 is at the edge of most of blobs and the sight line of LH-2 does not go through most of them. Figure 6.2 may also indicate that $EM\sin|b|$ is systematically larger for $|b| \lesssim 50°$, than for $|b| \gtrsim 50°$. However, this could be a selection effect by chance, and we need more data points in order to conclude it.

A schematic view of our understanding about the origin of the SXDB, especially in Oxygen emission lines is presented in Figure 6.3 The SWCX process emit mainly O VII line within the geocorona and the heliosphere ($\leq$ 100 AU). The time scale of the variability of the SWCX is $\leq$ hour in the geocorona and $\leq$ an 11 years Solar cycle in the heliosphere. Due to the distribution of the neutral matters and the propagation of the Solar wind, they could not be spatially uniform. The LHB which is filled with a thin thermal plasma is considered to be surrounding us. It is actually not spherically symmetric. Typical size of this bubble is an order of 100 pc. The X-ray emission below the Carbon edge should come within the LHB. The sun and the LHB are embedded in the local Galactic disk. The properties of several kinds of the ISM within the disk is described in Chapter 2. The typical pressure of these ISM is $\sim 10^4$ K cm^{-3}, and scale heights are of a few times 100 pc order. In addition to these ISM, a hot ($kT \sim 0.2$ keV) and blobby plasma exists in our Galaxy with a thick (≥ 1 kpc) plane-parallel disk morphology. Its temperature may vary with the distance from the midplane. The emission from these hot blobs reaches us after absorbed by the cooler ISM.

6.2.2 Resonance scattering

The absorption cross section of the resonant line can be as high as 1×10^{-16}cm^{-2}. The O VII ion absorbed the photon instantly re-emits a photon at the energy of the resonant line. Thus this process can be regarded as scattering. Since the scattering probability per volume is proportional to the ion density while the emission probability is proportional to second power of ion density, the resonance scattering will level the spatial contrast in emission intensity.

The scattering cross section depends on the line broadening. There are three origins for the broadening; natural width, thermal doppler, and doppler effect due to macroscopic motion. The broadening function for natural broadening is given by

$$\phi(E) = \frac{(h\Gamma/4\pi)^2}{(E-E_0)^2 + (h\Gamma/4\pi)^2}, \tag{6.1}$$

where Γ is the transition rate. If we consider the spontaneous emission for the transition rate, the half width half maximum of the broadening function is estimated to be 1.1×10^{-3} eV for O VII resonant line.

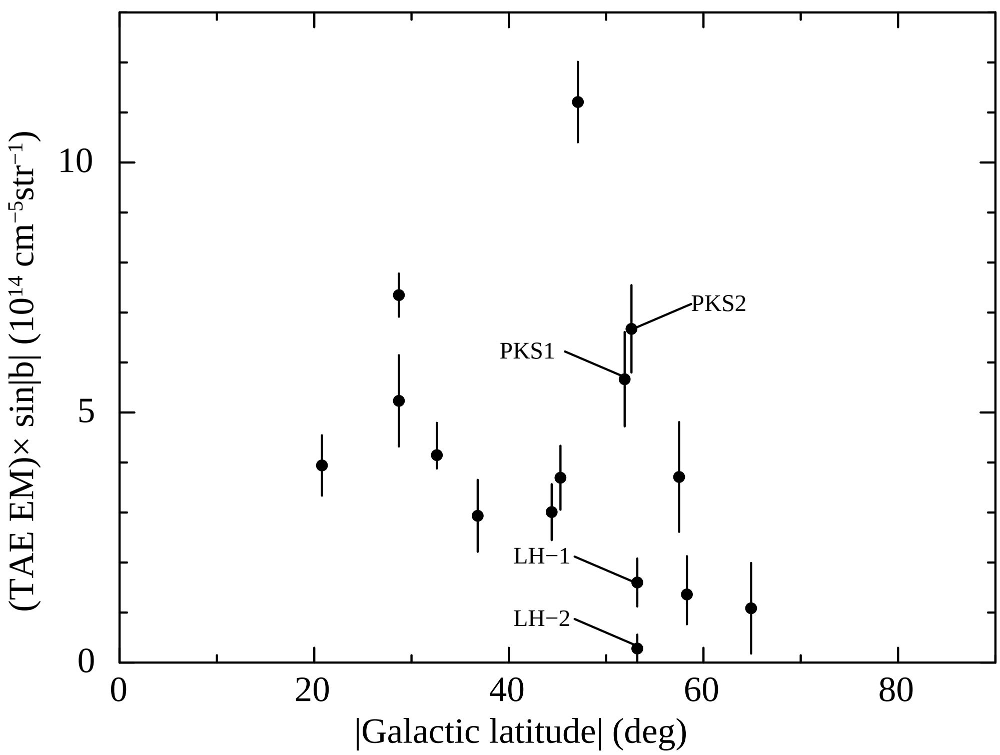

Figure 6.2: The emission measure of the TAE component multiplied by sin$|b|$ as a function of $|b|$. The TAE normalization factors are taken from model 2 (Table 5.5). The data point LL10 is not plotted because the higher temperature component of this field is like to have different origin from other fields.

On the other hand, the broadening function for the doppler effect is given by

$$\phi(E) = \frac{1}{\Delta E \sqrt{\pi}} \exp\left[-\frac{(E-E_0)^2}{\Delta E^2}\right], \tag{6.2}$$

where

$$\Delta E = \frac{E}{c}\sqrt{\frac{2kT}{m_{\rm ion}} + b^2}, \tag{6.3}$$

and $m_{\rm ion}$ and b are respectively the mass of the ion and the b parameter for macroscopic motion, i.e. the rms velocity dispersion times $\sqrt{2}$ in line of sight direction. $\Delta E = 0.093$ eV for $kT = 0.2$ keV and $b = 0$. Thus the natural broadening can be neglected compared to the thermal doppler broadening.

The scattering optical depth, $\tau(E)$ is given by

$$\tau(E) = \frac{\pi e^2}{m_{\rm e} c} f_{fi} \frac{h}{\Delta E \sqrt{\pi}} \exp\left[-\frac{(E-E_0)^2}{\Delta E^2}\right] N_{\rm ion} \tag{6.4}$$

where f_{fi} and $N_{\rm ion}$ are respectively the oscillator strength of the transition and the column density of the ion. $f_{fi} = 0.696$ for O VII K resonant line. Then the scattering probability after passing through the column density of $N_{\rm ion}$ is given by integrating the absorption probability

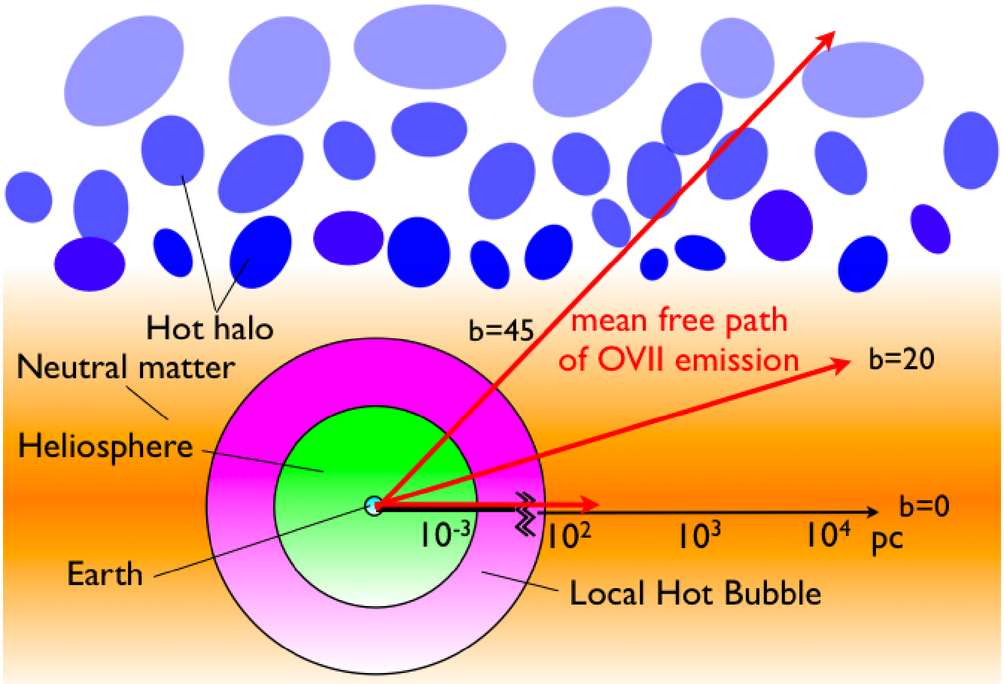

Figure 6.3: A schematic view of our understanding about the origin of the SXDB. Image is drawn in logarithmical scale.

weighted by the source photon energy distribution;

$$P = \int dE\ \phi(E)[1 - \exp\{-\tau(E)\}] \tag{6.5}$$

The total column densities of O VII and O VIII ions are respectively estimated to be 1×10^{15} cm^{-2} and 2×10^{15} cm^{-2} for the thick hot disk model. Yao & Wang (2007) and Wang et al. (2005) respectively estimated the velocity dispersion of the hot gas in the directions of Mrk421 ((l,b) = (179°.83, 65°.03)) and LMC X-3 ((l,b) = (273°.57, -32°.08)) to be 64^{+40}_{-16} kms^{-1} and 79^{+53}_{-19} km s^{-1} from the absorption line observations with *Chandra* . In Figure 6.4, we calculated the scattering probability as a function of ion column density for O VII and O VIII. From this figure we find that in maximum about 10% to 30 % of photons are scattered out from the line of sight and instead photons from other line of sights are observed as if they are emitted in the line of sight. The maximum O VII intensity from the TAE is $7.2^{+0.6}_{-1.0}$ in the Off-FIL field. Thus there is 1-2 LU uncertainty in the O VII emission intensity of this fields due to resonance scattering. Except for this field and NEP, the effect of resonance scattering is smaller than the statistical errors. Thus the effect of the resonance scattering is not crucial for the present results of O VII and O VIII intensities.

6.3 Order of magnitude estimates of hot gas properties

In this section, we estimate the physical paramters of the hot ionized plasma. For this purpose we simplify the assumption of the patchy hot thick disk model; we replace the exponential gradient in temperature with the constant temperature of $kT = 0.2$ keV, but

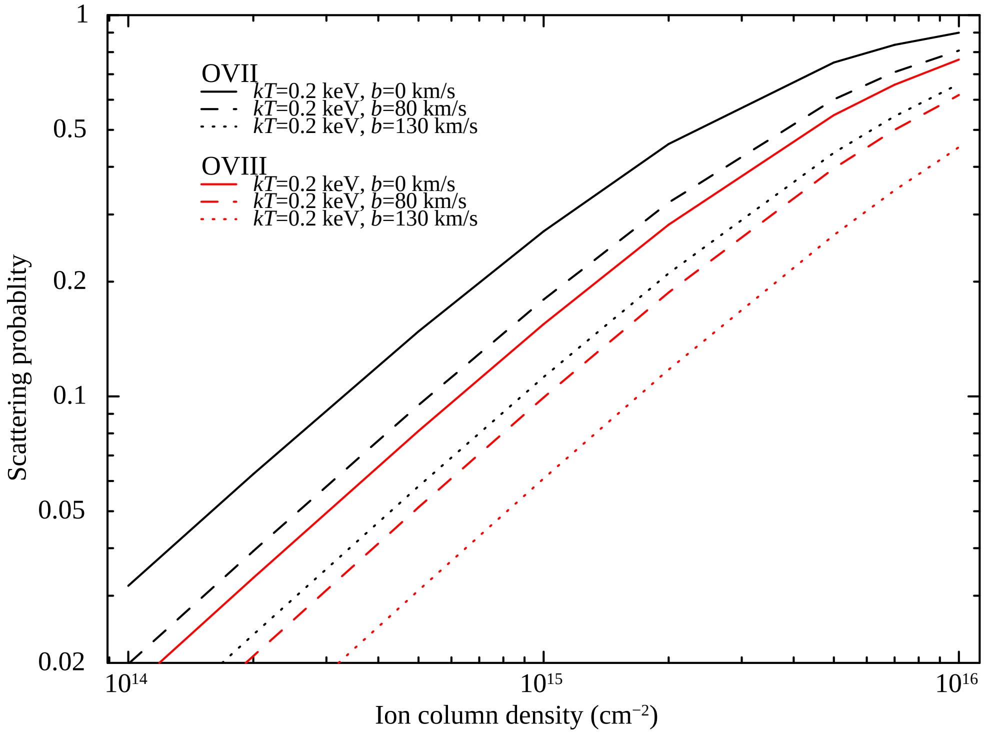

Figure 6.4: Resonance scattering probability for $kT = 0.2$ keV plasma with several b paramaters as a function of column density of each ion.

keep the exponential decrease of the density with scale height of $h_{\rm n} 1.4\xi^{-1}$ kpc. In order to estimate the average vertical emission measure we use the O VII line intensity obtained in Chapter 5, and assumed that the element abundance is solar abundance of Anders & Grevesse (1989) value.

6.3.0.1 Density

Assuming that the hot plasma is distributed in plane-parallel with the scale height of density $h_{\rm n}$ from the galactic plane, the density of plasma is expressed as $n(z) = n_0 \exp(-z/h_{\rm n})$, where the n_0 is midplane value. In such a configuration, we exptected the intensity of emission to increase from high to low latitude as $\propto \sin|b|$. Thus the observed intensity of emission line, denoted I_{ion} is expressed with the ion density in the line of site $n_{\rm ion}(x)$ as follows.

$$I_{ion} = \int_0^\infty \frac{1}{4\pi} n_{\rm e}(x) n_{\rm ion}(x) \Lambda(T) \xi dx = \frac{1}{4\pi} \frac{A_{\rm atom} f_{ion}(T)}{\mu_{\rm e}} \Lambda(T) \frac{n_0^2}{\sin|b|} \frac{h\xi}{2} \tag{6.6}$$

where $\mu_{\rm e}$, $\Lambda(T)$, $A_{\rm atom}$, $f_{\rm ion}$ and ξ are, the electron number density ratio to that of hydrogen (n_e/n_H=1.2), the line emission power per unit volume and per square electron density, the abundance of element($n_{\rm atom}/n_{\rm H}$), the ionization fraction($n_{\rm ion}/n_{\rm atom}$) and volume filling factor of hot plasma. We also defined $h = h_{\rm n}/2$. Assuming the scale height of density 2.8 kpc and using the temperature of 0.2 keV, the electron density at midplane using the avarage value of O VII line intensity multiplied by $\sin|b|$ line 2.3 LU is calculated to be

$$n_{\rm e} = 1.1 \times 10^{-3} {\rm cm}^{-3} \left(\frac{h\xi}{1.4 \text{ kpc}}\right)^{-\frac{1}{2}} \left(\frac{I_{ion}\sin|b|}{2.3 \text{ LU}}\right)^{\frac{1}{2}}. \tag{6.7}$$

6.3.0.2 Total luminosity and mass

Assuming that hot plasma fills a cylinder with a radius of 10 kpc centered on the Galactic center and with the scale height from galactic plane 2.8 kpc, total mass $M_{\rm total}$ and total luminosity $L_{\rm total}$ of the hot plasma are calculated to

$$M_{\rm total} = \int 1.4 n_e m_p {\rm d}V = 2.4 \times 10^7 M_{\odot} \left(\frac{h\xi}{1.4 \text{ kpc}}\right)^{\frac{1}{2}} \left(\frac{I_{ion}\sin|b|}{2.3 \text{ LU}}\right)^{\frac{1}{2}} \left(\frac{R}{10 \text{ kpc}}\right)^2 \tag{6.8}$$

$$L_{\rm total} = \int n_e n_t \Lambda_{\rm tot}(T) {\rm d}V = 1.3 \times 10^{39} \text{ erg s}^{-1} \left(\frac{I_{ion}\sin|b|}{2.3 \text{ LU}}\right) \left(\frac{R}{10 \text{ kpc}}\right)^2 \tag{6.9}$$

where we applied proton mass $m_{\rm p}$, the electron density (n_e) and total ion density (n_t) obtained above, and $\Lambda_{\rm tot}(T)$ is a cooling function at 0.2 keV of 6.3×10^{-23} erg s^{-1} cm^3, which is taken from Sutherland & Dopita (1993).

6.3.0.3 Cooling time scale

$$\tau_{cool} = \frac{3}{2}\frac{(n_e + n_t) k_{\rm B} T_e}{n_e n_i \Lambda(T)} = 4.6 \times 10^8 \text{ yr} \left(\frac{I_{ion}\sin|b|}{2.3 \text{ LU}}\right)^{-\frac{1}{2}} \left(\frac{h\xi}{1.4 \text{ kpc}}\right)^{\frac{1}{2}} \tag{6.10}$$

where n_t is the total ion density, $k_{\rm B}$ is Boltzman constant. We applied $\Lambda(T)$ value of 6.3×10^{-23} erg s^{-1} cm^3 in Sutherland & Dopita (1993), and $1.1 \times 10^{-3}{\rm cm}^{-3}$ of n_e obtained above.

6.3.0.4 Conduction time scale

The thermal conductivity κ is expresed as the classical electron thermal conductivity formula given by Spitzer(1962), which is applicable to a fully ionized plasma.

$$\kappa = 1.84 \times 10^{-5} T_e^{\frac{5}{2}} / {\rm ln}\Lambda_{\rm coul} \text{ erg s}^{-1} \text{ cm}^{-1} \text{ K}^{-1} \tag{6.11}$$

where an adequate approximation for the Coulomb integral factor for $T_e > 4 \times 10^5$ K is

$${\rm ln}\Lambda_{\rm coul} = 32 + {\rm ln}[n_e^{-\frac{1}{2}}(T_e/10^7 \text{ K})]. \tag{6.12}$$

Therefore, κ of hot ionized plasma is calculated to 5.4×10^9 erg s^{-1}cm^3. The conduction time scale $\tau_{\rm cond}$ in which the heat transfers to the length scale of δx is approximately expreseed as $\frac{c}{\kappa} \times \delta x^2$, where c is specific heat of hot plasma, which is equal to $\frac{3}{2}(n_e + n_t)k_{\rm B}$. Therefore, conduction time scale τ_{cond} with trasfering in the length scale 10 kpc is calculated to

$$\tau_{\rm cond} = \frac{1}{\kappa} \times \frac{3}{2}(n_e + n_t) k_{\rm B} \times \delta x^2 = 7.4 \times 10^9 \text{ yr} \left(\frac{h\xi}{1.4 \text{ kpc}}\right)^{-\frac{1}{2}} \left(\frac{I_{ion}\sin|b|}{2.3 \text{ LU}}\right)^{-\frac{1}{2}} \left(\frac{R}{10 \text{ kpc}}\right)^2 \tag{6.13}$$

In the presence of a magnetic field which is not parallel to the direction of heat condunction, the conductive heat flux is reduced, therefore the derived conduction time scale above is a lower limit.

6.3.1 Comparisons with other galaxies and origin of the hot plasma

Soft X-ray emission extending by ~ 10 kpc scales from galactic plane have been observed in some of nearby galaxies with relatively low star burst activities. The spectra of those halo emission are described by single or two-temperature models with kT's in the range of 0.1 to 0.8 keV (Strickland et al., 2004; Tüllmann et al., 2006; Yamasaki et al., 2008b). The total luminosities are typically 10^{38-39} erg s^{-1}. Thus, the TAE component found in this thesis could be similar to the halo hot gas in these galaxies. If our Galaxy is observed from outside, the average temperature of the halo emission should be observed as $kT = 0.2$ keV. Since in other galaxies the temperature ranges from 0.1 to 0.8 keV, there should be a reason why our Galaxy prefers $kT = 0.2$ keV. Possibly it is related to the virial temperature of our Galaxy. The virial temperature $T_{\rm vir} = \mu m_{\rm p} v^2/3k$ with rotational velocity of our Galaxy (200 km s^{-1}) is estimated to 0.195 keV, which is very close to the "average temperature" of hot plasma in our analysis.

A possible origin for this coincidence could be that the hot gas was formed by cosmological accretion (Toft et al., 2002; Rasmussen, 2007), i.e. the primordial gas around our galaxy was heated by falling along the gravitatinal potential of dark matter halo. Pointecouteau et al. (2005) investigated the relation between the virial mass and temperature of the nearby clusters, and the relation is fitted with the power-law model of

$$M_{\rm vir} = 10^{0.829} \left(\frac{T}{5\ \rm keV}\right)^{1.74} 10^{14} M_\odot \tag{6.14}$$

Shimizu et al. (2006). Using this model, $M_{\rm vir}$ at the gas temperature of 0.2 keV is calculated to $2.5 \times 10^{12} M_\odot$. This value is consistent with the estimated virial mass of our galaxy, $1.9^{+3.6}_{-1.7} \times 10^{12} M_\odot$ (Wilkinson & Evans, 1999), $2.5^{+0.5}_{-1.0} \times 10^{12} M_\odot$ (Sakamoto et al., 2003) and $1.42^{+1.14}_{-0.54} \times 10^{12} M_\odot$ (Smith et al., 2007a). However, the radiative cooling time of the hot gas is estimated to be only 5×10^8 years. Thus the gas cannot be primordial and the hot gas needs be supplied at least on this short time scale.

The most likely heating source is supernova explosion. Taking the heating efficiency (HE), which is the ratio of the fraction of the SN explosion energy that remains effectively stored in the ISM gas and is not radiated away, as 0.1, SN rates in our galaxy is 1 century^{-1} and the explosion energy is 10^{51} erg, the heating rate by SN explosion can be expressed by

$$3.2 \times 10^{40}\ \rm erg\ s^{-1} \left(\frac{U_{\rm SN}}{10^{51}\ \rm erg}\right) \left(\frac{\rm HE}{0.1}\right) \left(\frac{\rm SN\ rate}{1\ \rm century^{-1}}\right). \tag{6.15}$$

As this late is larger than the total luminosity of hot plasma, supernovae is a possible origin of hot plasma.

A possible interpretation for the coincidence of the hot gas average temperature with the virial tempearture is that the gas at higher temperarure than virial one has escaped from the gravitational potential. Then the gas at near or below the virial temperature remains in the halo, while the hot gas near the virial temperature is most efficiently emitting in O emission. This can be valid considering that the escape time scale that the gas at 200 km s^{-1} escaped away to 10 kpc scale is about half of the radiative cooling time scale.

Chapter 7

Conclusion

We have investigated the soft X-ray diffuse background (SXDB) from the regions apart from the atypical X-ray emission features, using the unprecedented spectroscopic capability for spatially extended emission below ∼1 keV of *Suzaku* . In the data reduction, we carefully removed the contributions of the solar wind charge exchange induced X-ray emission from the Earth's geocorona (Geocoronal SWCX). By analyzing the fifteen directions (sixteen observations) together with two other fields analyzed by Masui et al. (2008), we have obtained new insights on the SXDB.

1. O VII emission was clearly detected from all fields with intensity in the range of ~ 2 to ~ 9 LU. O VIII emission was also detected from most of the fields. The intensity was < 0.6 LU (upper limit) to 4 LU.

2. The O VII and O VIII correlation plot indicates that the O VII emission consists of two components; a component with intensity of ~ 2 LU and a small spatial variations, and the other component with intensity of 0–7 LU and a large filed to field variation. The O VIII intensity is about a half of the intensity of the latter O VII component. Thus the temperature of the latter component must be about $kT = 0.2$ keV. The temperature of the former component is much lower than this and likely $kT = 0.1$ keV, if it is thermal emission.

3. The likely origin of the former O VII emission component of approximately constant intensity is the Heliospheric SWCX with possible small contribution of emission from the Local Hot Bubble (LHB). Because two observations of the same directions near the north ecliptic pole showed ~ 1 LU intensity variation and because there is about 1 LU intensity variation on the O VII intensity floor, we consider the Heliospheric SWCX has about 1 LU temporal and spatial variations.

4. We consider that the latter, spatially variable O VII emission component comes from more distant part of the Galaxy than the SWCX+LHB component; thus mostly above or beyond the bulk of the Galactic absorption. We call this component Transabsorption component (TAE) following Kuntz and Snowden (2000).

5. In order to reproduce the constancy of the TAE temperature in the spectral model fits, the Fe and Ne abundance against O must be increased to 2 - 3 times solar value

for about four fields, or a higher temperature ($kT = 0.6 - 0.9$ keV) component which efficiently emits Fe-L and Ne lines must be included.

6. The present *Suzaku* results and the R45 band intensities of the same directions in the *ROSAT* all sky map were consistent with each other within the statistical uncertainties. We placed an upper limit of 2 LU for O VII intensity difference. This indicates that on average, the increase of the Heliospheric SWCX near the solar maximum (*ROSAT*) from near solar minimum (*Suzaku*) is at most 2 LU.

7. The constancy of the temperature of the TAE component is consistent with the plane parallel geometry of the thick hot disk model which was proposed by Yao et al. (2009) to explain simultaneously the absorption and emission spectra towards the sight line of LMC X-3. However, the O VII emission intensity and the emission measure of the TAE component show large field to field variations and thus their latitude dependencies are far from that expected for a plane parallel configuration. Thus the hot gas must be patchy. It may have a low volume filling factor.

8. Simplifying the model parameters of the patchy hot thick disk model, basic parameters of the hot gas, e.g. the total emission luminosity, the total mass of the hot gas, radiative cooling time, were estimated. The total luminosity, $\sim 1 \times 10^{39}$ erg s^{-1}, is within the range of luminosities observed in halo of some nearby normal galaxies.

9. The radiative cooling time scale is estimated to be ~ 0.5 G years. Hot gas or energy must be supplied to the TAE on this short time scale. The most likely heating source is supernovae. The apparent temperature of the TAE may be kept to a value close to the virial temperature of the Galaxy ($kT = 0.2$ keV), because a hotter gas from supernovae will escape from the halo of the Galaxy on the time scale shorter than the cooling time scale.

Appendix A

Charge Exchange

In the following, the charge exchange process and solar wind parameters are summarized.

A.1 Physical process of charge exchange

Most simple and main reaction of charge exchange is as follows.

$$A^{+q} + B \rightarrow A^{+(q-1)} + B^{+} \tag{A.1}$$

where A^{+q} is a projectile ion and B is a target atom. An electron of target atom transfers to the excited energy level of projectile, then the line is emitted by de-excitation of projectile ion(Figure A.1). This process is called Solar Wind Charge eXchange (SWCX) when A^{+q} is solar wind ion and B is the neutral matter in geocorona or heliosphere. For example, the reaction of O^{+7} ion and a Hydrogen atom produced a O^{+6} in excited state and hydrogen ion, then OVII line is emitted. The cross section of this reaction is relatively large $\sim 4\times10^{15}$ cm^{-2} at the collision velocity of $\sim$ 100 km/s. And the electron distribution of O^{+6} in excited state is different from that by other excitation process such as collisional ionization occurred in thermal plasma. Therefore, this process induces the difference of line intensity ratio due to the difference of main quantum number, and that of the fine structure of the line emission due to the difference of orbital angular momentum (e.g. resonance, intercombination, forbidden).

A.1.1 Solar Wind properties

Solar activities affects the density, ionization temperature and transfer direction of the solar wind, therefor also affects the intensity and distribution of SWCX. Table A.1 summarize the cross section of slow and fast solar wind for Charge exchange between solar wind heavy ions and H and He which is based on theoretical and experimental work. The slow solar wind (SSW) at an average velocity of 400 km s^{-1} has high ionization temperature and density which induces stronger O VII and O VIII line emission than the fast solar wind (FSW) at an average velocity of 750 km s^{-1} that has low temperature and low density. During solar minimum, SSW is emitted from the low latitude region of the sun which is below $\sim 200°$, and FSW from the high latitude region of the sun. On the other hand, during solar maximum, all the solar wind is in the SSW state.

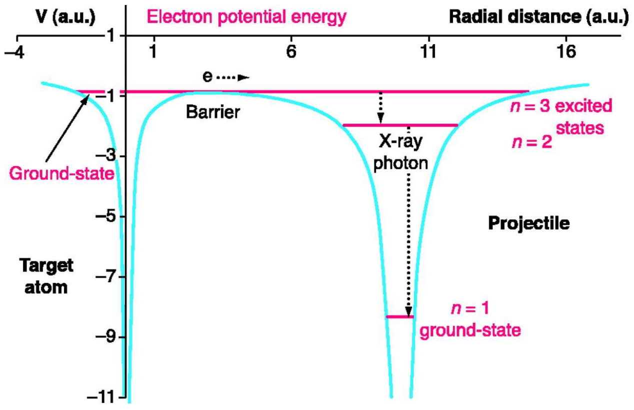

Figure A.1: Electron potential energy V [in atomic units (a.u.)] versus distance from the target atom nucleus (assumed to be atomic hydrogen here) for a charge transfer reaction involving projectile ion A^{q+} (calculated here for Be^{4+}). The internuclear distance chosen here [10 a.u. (1 a.u. = 1 Bohr radius = 5.29^{-11} m)] is the curve-crossing distance for the n = 3 ion final state. 1 atomic energy unit = 1 hartree = 27.2 eV. The target energy level (and binding energy) and product ion (Be^{3+}) energy levels are shown. In the classical overbarrier model, the electron is able to cross over from the target to the projectile for the favored principal quantum number (n approx 3, here). A possible cascading pathway for the de-excitation by photon emission is shown. Figure is taken from Cravens (2002)

Table A.1: Slow and Fast Solar Wind Parameters.

type			Slow			Fast	
V_{SW}			400 (km s^{-1})			750 (km s^{-1})	
$[\frac{O}{H^+}]$			1/1780			1/1550	
H^+ density at 1AU (cm^{-3})			6.5			3.2	
X^{Q+}	Lines (eV)[a]	fraction $[\frac{X^{Q+}}{O}]^b$	$\sigma_{(H,X^{Q+})}$ (10^{-15} cm^2)	$\sigma_{(He,X^{Q+})}$ (10^{-15} cm^2)	fraction $[\frac{X^{Q+}}{O}]^b$	$\sigma_{(H,X^{Q+})}$ (10^{-15} cm^2)	$\sigma_{(He,X^{Q+})}$ (10^{-15} cm^2)
O^{8+}	(33, 65, 77, 82, 84)	0.070	5.65	2.80	0.000	6.16	2.80
O^{7+}	(561, 569, 574)	0.200	3.40	1.80	0.030	3.70	1.97
O^{6+}	(72, 83, 94, 107)	0.730	3.67	0.96	0.970	3.91	1.31

[a] Including most important lines which is produced by $X^{(Q-1)+}$. [b] Charge exchange cross section of hydrogen.
[c] Charge exchange cross section of helium. Table is extracted from Koutroumpa et al. (2006)

Appendix B

Point source in each observation field

Table B.1 shows the position, excluded radius and flux in the range of 0.47-1.21 keV of the regions which are removed as X-ray point source in the analysis of Soft X-ray Diffuse background.

Table B.1: Position, removed circular radius and the flux for the point sources detected in each observation field. The flux of diffuse background region and the flux ratio of the leak to out side of the circular region of point source to diffuse background region are also shown.

Observation	ID	(l, b)	radius	Flux [a]	Flux [b]	Flux [c]	ratio (%)
1(GB)	1	(75.869, 64.893)	5'	28.9	22.98	49.29	0.02
2(HL-B)	1	(272.427, -58.200)	1'	0.7	0.58	1.39	0.56
	2	(272.511, -58.355)	1'	2.3	2.27	1.39	2.16
	3	(272.518, -58.339)	1'	0.8	0.67	1.39	0.63
	4	(272.727, -58.321)	1'	2.0	1.65	1.39	1.57
3(FOR)	1	(230.617, -57.568)	1.5'	6.4	5.08	1.87	1.80
4(LH-2)	1	(149.763, 53.283)	2'	3.3	2.75	1.48	0.61
	2	(149.769, 53.141)	1.5'	2.2	1.77	1.48	0.79
5(LH-1)	1	(148.967, 53.024)	1.5'	9.6	7.40	2.20	2.24
	2	(149.078, 53.214)	1'	3.6	3.04	2.20	1.83
	3	(148.929, 53.207)	0.7'	1.5	1.23	2.20	1.19
	4	(149.005, 53.135)	3'	12.2	10.27	2.20	0.51
	5	(148.835, 53.146)	0.7'	2.7	2.28	2.20	2.19
8(Off-FIL)	1	(278.816, -45.328)	1.7'	6.5	3.44	2.85	0.26
	2	(278.553, -45.264)	1.2'	1.8	0.72	2.85	0.16
	3	(278.624, -45.291)	1'	1.4	0.85	2.85	0.20
	4	(278.809, -45.368)	2.5'	22.1	5.16	2.19	1.01
	5	(278.685, -45.258)	1'	1.1	1.36	2.19	0.62
9(On-FIL)	1	(278.416, -47.015)	2.5'	4.3	1.08	2.19	0.65
	2	(278.785, -47.064)	1.5'	0.9	16.99	2.19	1.70
	3	(278.783, -46.960)	1.5'	1.1	0.87	2.19	0.53
10(HL-A)	1	(68.468, 44.398)	1.5'	1.3	1.17	2.23	0.35
	2	(68.328, 44.463)	1'	1.9	1.51	2.23	0.89
	3	(68.331, 44.396)	1'	1.3	1.07	2.23	0.63
	4	(68.395, 44.271)	1.5'	2.9	2.46	2.23	0.73
	5	(68.365, 44.338)	0.7'	1.6	1.33	2.23	2.39
	6	(68.475, 44.481)	0.5'	0.4	0.32	2.23	0.58
11(M12off)	1	(157.296, -36.815)	2'	1.0	0.91	1.34	0.22
12(LX-3)	1	(273.413, -32.630)	1.5'	14.5	12.01	2.89	2.76
	2	(273.322, -32.671)	1'	2.5	2.01	2.89	0.92
	3	(273.449, -32.602)	1.2'	1.9	1.47	2.89	0.50
	4	(273.527, -32.789)	1.7'	3.5	2.94	2.89	0.43
	5	(273.490, -32.512)	1'	2.3	1.93	2.89	0.88
13(NEP1)	1	(95.626, 28.793)	0.7'	2.5	2.01	2.93	1.45
15(LL21)	1	(85.975, -20.762)	1.5'	1.1	0.84	2.30	0.24
	2	(86.114, -20.831)	2'	3.8	3.46	2.30	0.50
	3	(85.949, -20.888)	1'	5.3	5.59	2.30	3.21
	4	(86.029, -20.746)	1'	2.5	2.47	2.30	1.42
	5	(85.951, -20.856)	0.7'	0.7	0.53	2.30	0.49
	6	(85.872, -20.740)	0.7'	1.1	0.88	2.30	0.81
	7	(86.131, -20.731)	1'	5.7	5.96	2.30	3.42
	8	(86.069, -20.734)	0.7'	0.7	0.56	2.30	0.51
	9	(86.046, -20.782)	1'	1.2	1.20	2.30	0.69
	10	(85.960, -20.727)	0.7'	0.7	0.53	2.30	0.49
	11	(86.127, -20.778)	1'	1.2	1.09	2.30	0.63

[a] Flux in 0.47-1.21 keV range in unit of 10^{-14} erg s^{-1} cm^{-2}

[b] Flux of point source in 0.47-1.21 keV range in unit of 10^{-3} counts s^{-1} cm^{-2}

[c] Flux in diffuse background region in 0.47-1.21 keV range in unit of 10^{-5} counts s^{-1} cm^{-2}

Appendix C

The normalization of Cosmic X-ray Background (CXB) components

The results of spectral fit with $wabs * power - law$ model for observation in the present thesis about all XIS sensors are shown in Table C.1.

Table C.1: Results of CXB normalization for single power-law component fit in 2.0–5.0 keV range. NXB level is not corrected.

observation	CXB norm[a]			
	XIS0	XIS1	XIS2	XIS3
1(GB)	$11.4^{+1.3}_{-1.3}$	$11.5^{+1.1}_{-1.1}$	$11.8^{+1.4}_{-1.4}$	$10.6^{+1.3}_{-1.3}$
2(HL-B)	$7.3^{+0.6}_{-0.6}$	$8.0^{+0.9}_{-0.9}$	$8.6^{+0.7}_{-0.7}$	$7.9^{+0.6}_{-0.6}$
3(FOR)	$6.5^{+1.3}_{-1.3}$	$5.0^{+1.1}_{-1.1}$	N/A[b]	$8.0\ ^{+1.4}_{-1.4}$
4(LH-2)	$9.1^{+0.7}_{-0.7}$	$8.4^{+0.9}_{-0.9}$	$8.5^{+0.8}_{-0.8}$	$9.4^{+0.7}_{-0.7}$
5(LH-1)	$10.2^{+0.9}_{-0.9}$	$10.2^{+0.8}_{-0.8}$	$10.5^{+1.0}_{-1.0}$	$11.4^{+0.9}_{-0.9}$
6(PKS2)	$7.1^{+0.6}_{-0.6}$	$6.5^{+0.7}_{-0.7}$	N/A[b]	$6.8\ ^{0.6}_{-0.6}$
7(PKS1)	$8.4^{+0.7}_{-0.7}$	$8.0^{+0.7}_{-0.7}$	N/A[b]	$7.9\ ^{+0.7}_{-0.7}$
8(Off-Fil)	$7.1^{+0.6}_{-0.6}$	$7.0^{+0.6}_{-0.6}$	$6.1^{+0.7}_{-0.7}$	$6.8^{+0.7}_{-0.7}$
9(On-Fil)	$9.2^{+0.6}_{-0.6}$	$9.9^{+0.7}_{-0.7}$	$9.0^{+0.7}_{-0.7}$	$9.6^{+0.7}_{-0.7}$
10(HL-A)	$9.2^{+1.0}_{-1.0}$	$9.0^{+0.7}_{-0.7}$	$10.0^{+1.1}_{-1.1}$	$9.0^{+1.0}_{-1.0}$
11(M12off)	$7.5^{+0.9}_{-0.9}$	$6.7^{+0.7}_{-0.7}$	$7.8^{+1.0}_{-1.0}$	$6.6^{+0.9}_{-0.9}$
12(LX-3)	$11.4^{+0.7}_{-0.7}$	$13.0^{+0.8}_{-0.8}$	$12.6^{+0.8}_{-0.8}$	$10.7^{+0.7}_{-0.7}$
13(NEP1)	$7.4^{+0.6}_{-0.6}$	$10.7^{+0.7}_{-0.7}$	$7.5^{+0.6}_{-0.6}$	$8.6^{+0.6}_{-0.6}$
14(NEP2)	$8.1^{+1.1}_{-1.1}$	$8.0^{+1.1}_{-1.1}$	$8.5^{+1.2}_{-1.2}$	$7.7^{+1.1}_{-1.1}$
15(LL21)	$8.2^{+0.8}_{-0.8}$	$8.5^{+0.7}_{-0.7}$	N/A[b]	$7.5\ ^{+0.8}_{-0.8}$
16(LL10)	$7.2^{+0.8}_{-0.8}$	$8.0^{+0.8}_{-0.8}$	N/A[b]	$6.8\ ^{+0.7}_{-0.7}$

[a] The normalization of the power-law function with the unit of photons $s^{-1}cm^{-2}\ keV^{-1}str^{-1}$@1keV.
[b] XIS-S2 is not available.

Appendix D

The spectrum of the $b = 10^\circ$ sample

We obtained significantly higher temperature (0.75 keV) for the TAE component for LL10 than that of other samples (average = 0.2 keV). This direction has a high Galactic absorption of $2.71\times10^{21}\mathrm{cm}^{-2}$, and the transmission of O VII and O VIII emissions are respectively only about 10 % and 20 %. Thus the emissions from the thick disk of the temperature ~ 0.2 keV will be significantly absorbed and hard to be detected, if it exists in this direction. Masui et al. (2008) detected an emission component of the similar temperature in the energy spectrum of the midplane direction, MP235. They suggested that the component is a sum of emission from unresolved faint dM stars existing between the bulk of Galactic absorption and the Earth, and constructed model spectra assuming an average dM star spectrum of the double temperature thermal emissions, the X-ray luminosity distribution functions, and the spatial densities of dM stars in literature. The model spectrum could consistently explain the observed spectrum not only in the spectral shape but also in the absolute intensity within 30 %. We fitted the LL10 spectrum using their dM star model spectrum constructed for $(l, b) = (90^\circ, 30^\circ)$, instead of the TAE component in model 1. As shown in Figure D.1, this model reproduces the observed spectrum well ($\chi^2 = 89.2$ for 90 degrees of freedom). However, it was necessary to increase the intensity of the emission by a factor of about 5 from the model. This suggests that th emission from dM stars does not decrease so rapidly with increasing b as the model predicts, or that the there is a large spatial fluctuations at b $\sim 10^\circ$.

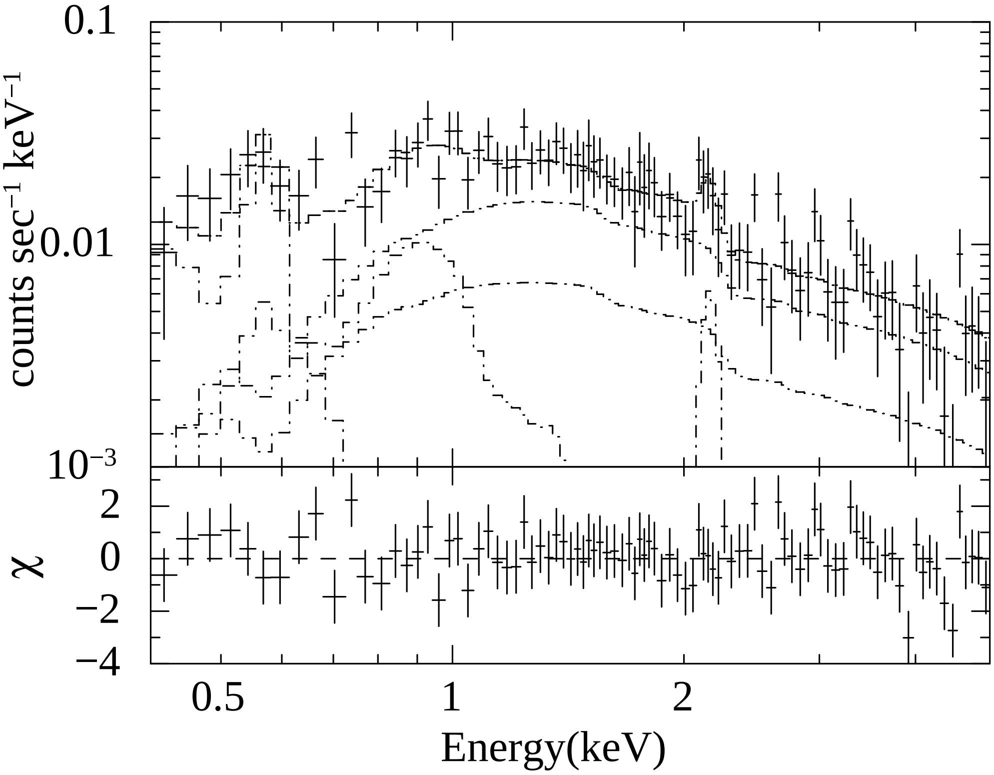

Figure D.1: Fit result of the Low latitude 97+10 (data ID 16) spectrum using the faint dM star model by Masui et al. (2008) instead of TAE component.

Appendix E

Systematic errors of fit

Results of spectral fits to determine O VII and O VIII line intensities with single power-law CXB model are shown in Table E.1.

Table E.2 shows th results of spectral fits with three component model (CXB, TAE, SWCX+LHB) with double broken power-law model for CXB in the case that the contaminants thickness on optical blocking filter is 10 % thicker and thinner than nominal value used in the fit of Chapter 5. And the results of spectral fits to determine O VII and O VIII line intensities with double broken power-law CXB model in the case of 10 % thicker and thinner contaminants are shown in Table E.3. Obtained parameters are all within the statistical error in the case of nominal contaminants thickness.

Table E.1: Results of spectral fits to determine O VII and O VIII line intensities with single power-law CXB model.

	CXB[a]	TAE[a,b]	SWCX+LHB[b]	O VII		O VIII		χ^2/dof
ID	Norm[c]	Norm[d]	Norm[d]	Centroid	SB[e]	Centroid	SB[e]	
1 (GB)	$10.9^{+0.6}_{-0.3}$	$3.0^{+6.2}_{-3.0}$	$11.7^{+11.3}_{-8.0}$	$0.560^{+0.008}_{-0.006}$	$4.1^{+0.9}_{-1.0}$	$0.663^{+0.014}_{-0.014}$	$1.3^{+0.5}_{-0.5}$	81.80/86
2 (HL-B)	$7.7^{+0.6}_{-0.6}$	$2.8^{+1.6}_{-1.5}$	$19.1^{+5.8}_{-5.7}$	$0.560^{+0.008}_{-0.010}$	$2.6^{+0.7}_{-0.7}$	$0.652^{+0.012}_{-0.010}$	$1.2^{+0.4}_{-0.4}$	79.36/ 80
3 (FOR)	$6.1^{+0.7}_{-0.7}$	$1.9^{+0.6}_{-0.6}$	$27.4^{+9.5}_{-9.7}$	$0.568^{+0.014}_{-0.015}$	$5.2^{+1.4}_{-1.5}$	0.654	$1.2^{+0.7}_{-0.8}$	63.39/58
4 (LH-2)	$8.7^{+0.5}_{-0.5}$	$1.1^{+0.7}_{-0.8}$	$38.1^{+13.4}_{-13.6}$	$0.568^{+0.007}_{-0.007}$	$3.0^{+0.7}_{-0.7}$	0.654	$0.4^{+0.4}_{-0.4}$	89.12/96
5 (LH-1)	$10.8^{+0.4}_{-0.5}$	$2.7^{+0.7}_{-0.6}$	$19.7^{+3.9}_{-3.5}$	$0.562^{+0.004}_{-0.005}$	$4.7^{+0.5}_{-0.5}$	$0.654^{+0.012}_{-0.012}$	$1.1^{+0.3}_{-0.3}$	145.02/92
6 (PKS2)	$7.5^{+0.4}_{-0.4}$	$8.5^{+2.0}_{-1.7}$	$68.8^{+12.6}_{-12.0}$	$0.566^{+0.006}_{-0.003}$	$6.6^{+0.8}_{-0.8}$	$0.648^{+0.006}_{-0.008}$	$2.6^{+0.5}_{-0.4}$	108.84/99
7 (PKS1)	$8.6^{+0.4}_{-0.5}$	$5.4^{+1.3}_{-1.2}$	$77.2^{+13.5}_{-13.5}$	$0.574^{+0.006}_{-0.008}$	$6.2^{+0.9}_{-0.8}$	$0.654^{+0.016}_{-0.018}$	$1.6^{+0.5}_{-0.5}$	109.62/86
8 (Off-FIL)	$8.2^{+0.3}_{-0.4}$	$8.1^{+1.3}_{-1.1}$	$32.0^{+4.8}_{-4.5}$	$0.566^{+0.002}_{-0.004}$	$9.5^{+0.7}_{-0.7}$	$0.653^{+0.005}_{-0.005}$	$3.1^{+0.4}_{-0.3}$	153.93/118
9 (On-FIL)	$10.3^{+0.5}_{-0.4}$	$3.2^{+0.5}_{-0.7}$	$14.8^{+3.5}_{-3.4}$	$0.563^{+0.003}_{-0.003}$	$5.7^{+0.6}_{-0.6}$	$0.660^{+0.006}_{-0.007}$	$2.4^{+0.3}_{-0.3}$	118.93/113
10 (HL-A)	$10.1^{+0.4}_{-0.4}$	$7.3^{+1.8}_{-2.0}$	$30.6^{+7.3}_{-7.2}$	$0.563^{+0.005}_{-0.004}$	$5.0^{+0.6}_{-0.6}$	$0.646^{+0.006}_{-0.006}$	$2.2^{+0.4}_{-0.4}$	137.74/111
11 (M12off)	$7.3^{+0.4}_{-0.4}$	$3.2^{+1.5}_{-1.5}$	$27.6^{+5.4}_{-5.5}$	$0.564^{+0.004}_{-0.004}$	$4.5^{+0.5}_{-0.5}$	$0.662^{+0.010}_{-0.010}$	$1.0^{+0.3}_{-0.3}$	80.05/85
12 (LX-3)	$13.5^{+0.5}_{-0.5}$	$9.3^{+1.1}_{-1.3}$	$20.1^{+4.3}_{-4.4}$	$0.570^{+0.003}_{-0.004}$	$6.5^{+0.7}_{-0.7}$	$0.653^{+0.007}_{-0.005}$	$2.6^{+0.4}_{-0.4}$	211.14/192
13 (NEP1)	$8.3^{+0.3}_{-0.5}$	$13.5^{+1.8}_{-1.5}$	$33.2^{+3.6}_{-3.3}$	$0.567^{+0.003}_{-0.001}$	$9.1^{+0.6}_{-0.5}$	$0.653^{+0.004}_{-0.002}$	$3.6^{+0.3}_{-0.3}$	182.41/116
14 (NEP2)	$8.7^{+0.6}_{-0.7}$	$9.2^{+2.5}_{-2.6}$	$28.8^{+7.8}_{-7.1}$	$0.568^{+0.006}_{-0.004}$	$7.2^{+1.1}_{-1.1}$	$0.654^{+0.008}_{-0.007}$	$3.1^{+0.7}_{-0.6}$	59.72/51
15 (LL21)	$9.7^{+0.5}_{-0.5}$	$9.4^{+1.7}_{-1.6}$	$38.0^{+8.9}_{-9.4}$	$0.570^{+0.004}_{-0.008}$	$6.7^{+0.9}_{-0.9}$	$0.653^{+0.008}_{-0.009}$	$2.4^{+0.5}_{-0.5}$	109.42/93
16 (LL10)	$7.9^{+0.5}_{-0.6}$	$1.9^{+0.8}_{-0.6}$	$10.7^{+5.6}_{-5.4}$	$0.556^{+0.016}_{-0.018}$	$1.8^{+1.1}_{-0.7}$	$0.644^{+0.020}_{-0.031}$	$0.6^{+0.3}_{-0.3}$	80.62/87

[a] The absorption column densities for the CXB and TAE components were fixed to the values tabulated in Table 5.3.
[b] The temperature of TAE and SWCX+LHB components were fixed to the best fit values tabulated in Table 5.3. The O abundance of the both components was set to 0 in the fits.
[c] The unit is photons $\mathrm{s^{-1}cm^{-2}\ keV^{-1}str^{-1}}$@1keV.
[d] The emission measure integrated over the line of sight ,i.e. $(1/4\pi)\int n_\mathrm{e} n_\mathrm{H} ds$ in the unit of 10^{14} $\mathrm{cm^{-5}\ str^{-1}}$.
[e] Surface brightness in the unit of LU =photons $\mathrm{s^{-1}\ cm^{-2}\ str^{-1}}$.

Table E.2: Results of three-component (CXB, TAE, SWCX+LHB) spectral fits with the double broken power-law CXB model (model 1) in the case that the contaminants on optical blocking filter is 10% thicker and thiner than nominal value. The + and – mark in the table are for 10% thicker and thiner case, respectively.

	$N_{\rm H}$[a]	CXB[b]	TAE		SWCX+LHB		χ^2/dof
ID	(10^{20}cm^{-2})	Norm[c]	kT (keV)	Norm[d]	kT (keV)	Norm[d]	
1 (GB)+	1.40	$5.9^{+0.6}_{-0.6}$	0.264	< 1.6[e]	$0.158^{+0.027}_{-0.025}$	$6.0^{+1.2}_{-1.3}$	89.51/92
1 (GB)–	1.40	$5.5^{+0.6}_{-0.6}$	0.264	< 1.6[e]	$0.170^{+0.020}_{-0.035}$	$4.0^{+0.9}_{-1.0}$	91.74/92
2 (HL-B)+	3.36	$2.7^{+0.6}_{-0.6}$	$0.271^{+0.078}_{-0.070}$	$1.8^{+1.2}_{-0.9}$	0.120[f]	$7.3^{+2.0}_{-3.4}$	95.77/87
2 (HL-B)–	3.36	$2.6^{+0.6}_{-0.5}$	$0.271^{+0.081}_{-0.081}$	$1.6^{+1.7}_{-0.9}$	0.120[f]	$6.2^{+1.8}_{-3.7}$	93.41/87
3 (FOR)+	1.35	$0.5^{+0.7}_{-0.8}$	$0.745^{+0.317}_{-0.527}$	$1.6^{+0.8}_{-0.6}$	$0.143^{+0.014}_{-0.032}$	$11.7^{+14.9}_{-3.9}$	65.91/59
3 (FOR)–	1.35	$0.6^{+0.8}_{-0.6}$	$0.754^{+0.327}_{-0.430}$	$1.4^{+0.7}_{-0.7}$	$0.144^{+0.029}_{-0.031}$	$9.7^{+10.3}_{-3.5}$	64.24/59
4 (LH-2)+	0.56	$3.7^{+0.5}_{-0.5}$	0.264	< 1.0[e]	$0.096^{+0.025}_{-0.025}$	$21.3^{+3.8}_{-4.7}$	94.47/99
4 (LH-2)–	0.56	$3.4^{+0.5}_{-0.4}$	0.264	< 1.0[e]	$0.094^{+0.039}_{-0.021}$	$17.7^{+6.9}_{-4.6}$	95.54/99
5 (LH-1)+	0.56	$5.6^{+0.5}_{-0.5}$	$0.468^{+0.259}_{-0.136}$	$1.3^{+0.8}_{-0.5}$	$0.135^{+0.015}_{-0.019}$	$8.9^{+4.3}_{-1.6}$	155.75/127
5 (LH-1)–	0.56	$5.4^{+0.5}_{-0.5}$	$0.599^{+0.161}_{-0.253}$	$1.1^{+0.4}_{-0.4}$	$0.140^{+0.012}_{-0.016}$	$7.9^{+2.9}_{-1.3}$	152.87/127
6 (PKS2)+	1.67	$2.1^{+0.4}_{-0.5}$	$0.237^{+0.037}_{-0.040}$	$5.8^{+4.6}_{-1.6}$	$0.088^{+0.013}_{-0.041}$	$54.7^{+128.5}_{-23.1}$	107.24/103
6 (PKS2)–	1.67	$2.1^{+0.5}_{-0.4}$	$0.236^{+0.039}_{-0.046}$	$5.3^{+2.9}_{-1.5}$	$0.089^{+0.018}_{-0.045}$	$41.8^{+1229.3}_{-19.9}$	105.50/103
7 (PKS1)+	1.76	$3.4^{+0.5}_{-0.5}$	$0.290^{+0.050}_{-0.041}$	$3.6^{+1.1}_{-1.0}$	$0.091^{+0.016}_{-0.012}$	$53.8^{+45.1}_{-25.1}$	107.17/90
7 (PKS1)–	1.76	$3.3^{+0.5}_{-0.5}$	$0.291^{+0.054}_{-0.044}$	$3.2^{+1.0}_{-0.9}$	$0.094^{+0.017}_{-0.008}$	$40.2^{+21.7}_{-19.2}$	104.89/90
8 (OFF-FIL)+	1.90	$2.9^{+0.4}_{-0.4}$	$0.275^{+0.021}_{-0.024}$	$5.5^{+1.3}_{-0.9}$	$0.125^{+0.015}_{-0.010}$	$19.2^{+5.3}_{-4.9}$	169.78/122
8 (OFF-FIL)–	1.90	$2.9^{+0.4}_{-0.4}$	$0.273^{+0.019}_{-0.023}$	$6.2^{+1.5}_{-0.9}$	$0.120^{+0.013}_{-0.009}$	$25.4^{+6.0}_{-6.3}$	170.60/122
9 (ON-FIL)+	9.60	$5.2^{+0.5}_{-0.5}$	$0.628^{+0.073}_{-0.064}$	$2.6^{+0.6}_{-0.6}$	$0.183^{+0.011}_{-0.010}$	$7.6^{+0.6}_{-0.6}$	126.83/117
9 (ON-FIL)–	9.60	$5.2^{+0.5}_{-0.5}$	$0.621^{+0.070}_{-0.061}$	$2.7^{+0.6}_{-0.6}$	$0.182^{+0.010}_{-0.010}$	$8.8^{+0.7}_{-0.7}$	128.16/117
10 (HL-A)+	1.02	$5.0^{+0.5}_{-0.5}$	$0.243^{+0.042}_{-0.038}$	$3.6^{+1.2}_{-0.9}$	0.120[f]	$11.4^{+2.8}_{-4.0}$	142.53/116
10 (HL-A)–	1.02	$4.9^{+0.5}_{-0.5}$	$0.230^{+0.047}_{-0.039}$	$3.4^{+2.1}_{-1.2}$	0.120[f]	$8.4^{+3.3}_{-5.0}$	139.80/116
11 (M12off)+	8.74	$1.8^{+0.5}_{-0.5}$	$0.245^{+0.097}_{-0.124}$	$2.4^{+15.3}_{-1.3}$	$0.102^{+0.016}_{-0.080}$	$21.5^{+1913.7}_{-7.8}$	85.90/89
11 (M12off)–	8.74	$1.8^{+0.5}_{-0.5}$	$0.242^{+0.113}_{-0.098}$	$2.2^{+15.1}_{-1.4}$	$0.104^{+0.016}_{-0.086}$	$18.8^{+1107.3}_{-5.7}$	85.69/89
12 (LX-3)+	4.67	$8.7^{+0.6}_{-0.5}$	$0.306^{+0.064}_{-0.025}$	$6.6^{+1.2}_{-2.4}$	$0.136^{+0.025}_{-0.018}$	$11.3^{+5.4}_{-2.0}$	211.77/196
12 (LX-3)–	4.67	$8.6^{+0.5}_{-0.5}$	$0.321^{+0.280}_{-0.037}$	$5.2^{+3.7}_{-3.5}$	$0.146^{+0.044}_{-0.022}$	$8.9^{+3.0}_{-1.9}$	212.97/196
13 (NEP)+	4.40	$2.9^{+0.4}_{-0.5}$	$0.243^{+0.023}_{-0.016}$	$9.7^{+1.8}_{-1.8}$	$0.113^{+0.009}_{-0.011}$	$24.2^{+6.5}_{-4.1}$	159.06/120
13 (NEP)–	4.40	$2.9^{+0.4}_{-0.5}$	$0.243^{+0.023}_{-0.017}$	$9.5^{+1.8}_{-1.8}$	$0.114^{+0.010}_{-0.011}$	$23.5^{+5.9}_{-4.0}$	158.39/120
14 (NEP2)+	4.40	$3.3^{+0.8}_{-0.8}$	$0.263^{+0.043}_{-0.035}$	$8.4^{+3.1}_{-2.5}$	$0.113^{+0.030}_{-0.024}$	$21.2^{+21.7}_{-9.6}$	59.97/55
14 (NEP2–	4.40	$3.3^{+0.8}_{-0.8}$	$0.267^{+0.052}_{-0.020}$	$7.3^{+3.0}_{-2.8}$	$0.118^{+0.037}_{-0.027}$	$16.2^{+15.1}_{-7.5}$	59.27/55
15 (LL21)+	7.24	$4.3^{+0.5}_{-0.5}$	$0.284^{+0.042}_{-0.038}$	$6.8^{+2.1}_{-1.7}$	$0.109^{+0.019}_{-0.020}$	$24.4^{+26.9}_{-9.6}$	105.04/102
15 (LL21)–	7.24	$4.3^{+0.5}_{-0.5}$	$0.286^{+0.044}_{-0.041}$	$6.0^{+2.1}_{-1.4}$	$0.111^{+0.024}_{-0.021}$	$19.1^{+19.9}_{-8.2}$	104.20/97
16 (LL10)+	27.10	$2.6^{+0.6}_{-0.6}$	$0.732^{+0.233}_{-0.174}$	$1.5^{+0.7}_{-0.7}$	$0.116^{+0.065}_{-0.035}$	$6.6^{+22.7}_{-3.9}$	86.47/89
16 (LL10)–	27.10	$2.6^{+0.6}_{-0.6}$	$0.737^{+0.253}_{-0.179}$	$1.4^{+0.6}_{-0.7}$	$0.116^{+0.067}_{-0.034}$	$5.8^{+17.4}_{-3.9}$	85.91/89

[a] The absorption column densities for the CXB and TAE components were fixed to the tabulated values. They were estimated from Dickey & Lockman (1990), except for 8' and 9'. The column densities were estimated from the 100 μm intensity of the direction (?).

[b] Two broken power-law model was adopted. The photon indexes below 1.2 keV were fixed to 1.54 and 1.96 . The normalization of the former index component is fixed to 5.7, and only the normalization of the other component was allowed to vary.

[c] The normalization of one of the broken power-law components with the unit of phtons s^{-1}cm^{-2} keV^{-1}str^{-1}@1keV.

[d] The emission measure integrated over the line of sight, $(1/4\pi)\int n_{\rm e} n_{\rm H} ds$ in the unit of 10^{14}cm^{-5} str^{-1}.

[e] The TAE component was not significant. Thus the upper limit of the normalization was determined for the temperature fixed to the average of TAE components of other observations.

[f] Because of the strong coupling between the TAE and LHB+SWCX components, the temperatures of the two components were not well determined. We thus fixed the temperature of the SWCX+LHB component to the average values of other observations.

Table E.3: Results of spectral fits to determine O VII and O VIII line intensities with double power-law CXB model in the case that the contaminants on optical blocking filter is 10% thicker and thiner than nominal value. The + and – mark in the table are for 10% thicker and thiner case, respectively.

	CXB[a]	TAE[a,b]	SWCX+LHB[b]	O VII		O VIII		χ^2/dof
ID	Norm[c]	Norm[d]	Norm[d]	Centroid	SB[e]	Centroid	SB[e]	
1 (GB)+	$5.8^{+0.7}_{-0.6}$	-	$6.9^{+6.1}_{-6.7}$	$0.562^{+0.008}_{-0.009}$	$3.9^{+1.1}_{-1.0}$	$0.662^{+0.016}_{-0.016}$	$1.1^{+0.5}_{-0.5}$	83.27/87
1 (GB)–	$5.6^{+0.7}_{-0.6}$	-	$1.2^{+5.5}_{-1.2}$	$0.560^{+0.009}_{-0.008}$	$3.2^{+0.9}_{-0.9}$	$0.662^{+0.018}_{-0.018}$	$0.9^{+0.5}_{-0.5}$	84.55/87
2 (HL-B)+	$2.6^{+0.5}_{-0.6}$	$1.9^{+1.5}_{-1.4}$	$15.8^{+6.1}_{-5.4}$	$0.560^{+0.010}_{-0.008}$	$2.4^{+0.8}_{-0.7}$	$0.652^{+0.012}_{-0.012}$	$1.1^{+0.4}_{-0.4}$	84.27/84
2 (HL-B)–	$2.5^{+0.6}_{-0.5}$	$1.7^{+1.3}_{-1.4}$	$12.5^{+5.0}_{-5.1}$	$0.560^{+0.011}_{-0.010}$	$2.1^{+0.7}_{-0.6}$	$0.652^{+0.012}_{-0.012}$	$1.0^{+0.4}_{-0.4}$	84.34/84
3 (FOR2)+	$0.7^{+0.8}_{-0.6}$	$1.4^{+0.7}_{-0.6}$	$24.6^{+9.7}_{-9.6}$	$0.568^{+0.014}_{-0.016}$	$5.0^{+1.5}_{-1.4}$	0.654[f]	$1.2^{+0.7}_{-0.8}$	63.39/58
3 (FOR2)–	$0.5^{+0.8}_{-0.5}$	$1.7^{+0.7}_{-0.7}$	$20.7^{+8.2}_{-8.3}$	$0.568^{+0.013}_{-0.016}$	$4.4^{+1.2}_{-1.3}$	0.654[f]	$1.1^{+0.7}_{-0.7}$	61.46/58
4 (LH-2)+	$3.7^{+0.5}_{-0.5}$	-	$24.1^{+11.3}_{-11.3}$	$0.568^{+0.009}_{-0.009}$	$2.9^{+0.7}_{-0.8}$	0.654[f]	$0.3^{+0.4}_{-0.3}$	93.93/97
4 (LH-2)–	$3.5^{+0.5}_{-0.5}$	-	$16.1^{+9.6}_{-10.5}$	$0.568^{+0.008}_{-0.008}$	$2.2^{+0.7}_{-0.6}$	0.654[f]	$0.1^{+0.4}_{-0.1}$	94.46/97
5 (LH-1)+	$5.6^{+0.5}_{-0.5}$	$1.4^{+0.4}_{-0.5}$	$12.8^{+3.4}_{-3.5}$	$0.562^{+0.003}_{-0.003}$	$4.2^{+0.6}_{-0.5}$	$0.656^{+0.015}_{-0.017}$	$0.8^{+0.3}_{-0.3}$	152.28/123
5 (LH-1)–	$5.4^{+0.5}_{-0.5}$	$1.2^{+0.4}_{-0.4}$	$11.1^{+3.2}_{-3.3}$	$0.562^{+0.003}_{-0.003}$	$3.9^{+0.6}_{-0.5}$	$0.658^{+0.016}_{-0.017}$	$0.8^{+0.3}_{-0.3}$	150.32/123
6 (PKS2)+	$2.2^{+0.4}_{-0.4}$	$8.5^{+2.3}_{-2.1}$	$61.6^{+12.3}_{-12.6}$	$0.567^{+0.005}_{-0.005}$	$6.3^{+0.8}_{-0.8}$	$0.648^{+0.007}_{-0.008}$	$2.5^{+0.4}_{-0.5}$	105.01/99
6 (PKS2)–	$2.1^{+0.2}_{-0.5}$	$7.6^{+2.3}_{-2.0}$	$47.1^{+10.4}_{-10.4}$	$0.568^{+0.004}_{-0.006}$	$5.6^{+0.8}_{-0.7}$	$0.647^{+0.007}_{-0.007}$	$2.2^{+0.4}_{-0.4}$	102.67/99
7 (PKS1)+	$3.3^{+0.5}_{-0.5}$	$4.8^{+1.2}_{-1.5}$	$65.7^{+12.9}_{-12.9}$	$0.574^{+0.008}_{-0.008}$	$5.9^{+0.8}_{-0.9}$	$0.655^{+0.018}_{-0.019}$	$1.3^{+0.5}_{-0.3}$	103.11/86
7 (PKS1)–	$3.3^{+0.5}_{-0.2}$	$4.3^{+1.1}_{-1.4}$	$49.8^{+10.3}_{-10.4}$	$0.574^{+0.007}_{-0.006}$	$5.3^{+0.7}_{-0.8}$	$0.656^{+0.018}_{-0.020}$	$1.2^{+0.5}_{-0.4}$	100.19/86
8 (OFF-FIL)+	$2.9^{+0.4}_{-0.4}$	$7.0^{+1.2}_{-1.3}$	$23.9^{+4.0}_{-4.3}$	$0.566^{+0.002}_{-0.001}$	$8.7^{+0.7}_{-0.7}$	$0.653^{+0.003}_{-0.005}$	$2.8^{+0.4}_{-0.4}$	147.35/118
8 (OFF-FIL)–	$2.9^{+0.4}_{-0.4}$	$7.9^{+1.2}_{-1.2}$	$31.5^{+4.9}_{-5.1}$	$0.566^{+0.001}_{-0.004}$	$9.9^{+0.7}_{-0.4}$	$0.652^{+0.006}_{-0.004}$	$3.1^{+0.4}_{-0.4}$	150.48/118
9 (ON-FIL)+	$5.3^{+0.5}_{-0.5}$	$2.8^{+0.6}_{-0.6}$	$9.9^{+3.2}_{-3.2}$	$0.564^{+0.002}_{-0.004}$	$5.2^{+0.4}_{-0.6}$	$0.660^{+0.007}_{-0.007}$	$2.1^{+0.3}_{-0.3}$	117.05/113
9 (ON-FIL)–	$5.4^{+0.5}_{-0.5}$	$3.0^{+0.6}_{-0.6}$	$12.7^{+3.5}_{-3.6}$	$0.563^{+0.002}_{-0.004}$	$5.9^{+0.6}_{-0.6}$	$0.660^{+0.006}_{-0.006}$	$2.3^{+0.3}_{-0.3}$	118.57/113
10 (HL-A)+	$5.0^{+0.5}_{-0.4}$	$5.1^{+1.7}_{-2.1}$	$16.6^{+4.9}_{-5.0}$	$0.564^{+0.004}_{-0.004}$	$4.9^{+0.6}_{-0.7}$	$0.646^{+0.007}_{-0.007}$	$2.0^{+0.4}_{-0.4}$	135.00/111
10 (HL-A)–	$4.9^{+0.5}_{-0.5}$	$5.1^{+2.3}_{-2.3}$	$10.8^{+4.4}_{-4.3}$	$0.564^{+0.004}_{-0.004}$	$4.2^{+0.6}_{-0.6}$	$0.647^{+0.007}_{-0.009}$	$1.8^{+0.4}_{-0.4}$	134.35/111
11 (M12off)+	$1.9^{+0.4}_{-0.5}$	$3.0^{+2.1}_{-2.1}$	$27.3^{+5.8}_{-5.8}$	$0.565^{+0.002}_{-0.005}$	$4.6^{+0.5}_{-0.6}$	$0.662^{+0.010}_{-0.010}$	$0.9^{+0.3}_{-0.3}$	78.83/85
11 (M12off)–	$1.8^{+0.4}_{-0.4}$	$2.7^{+2.1}_{-2.1}$	$21.2^{+4.8}_{-4.8}$	$0.565^{+0.004}_{-0.004}$	$4.1^{+0.5}_{-0.5}$	$0.662^{+0.011}_{-0.011}$	$0.8^{+0.3}_{-0.3}$	78.31/85
12 (LX-3)+	$8.9^{+0.5}_{-0.6}$	$8.0^{+1.4}_{-1.2}$	$14.5^{+4.5}_{-4.4}$	$0.570^{+0.004}_{-0.003}$	$6.4^{+0.8}_{-0.7}$	$0.654^{+0.006}_{-0.006}$	$2.4^{+0.4}_{-0.4}$	207.44/192
12 (LX-3)–	$8.7^{+0.6}_{-0.5}$	$6.4^{+1.0}_{-1.2}$	$10.2^{+3.9}_{-4.0}$	$0.570^{+0.004}_{-0.004}$	$5.6^{+0.6}_{-0.7}$	$0.655^{+0.005}_{-0.007}$	$2.1^{+0.4}_{-0.4}$	206.41/192
13 (NEP)+	$3.0^{+0.4}_{-0.5}$	$13.7^{+1.9}_{-1.8}$	$29.6^{+3.5}_{-3.5}$	$0.568^{+0.003}_{-0.001}$	$9.0^{+0.5}_{-0.5}$	$0.653^{+0.003}_{-0.002}$	$3.4^{+0.3}_{-0.3}$	165.59/116
13 (NEP)–	$3.0^{+0.4}_{-0.5}$	$13.4^{+1.9}_{-1.8}$	$28.8^{+3.4}_{-3.5}$	$0.568^{+0.002}_{-0.001}$	$8.9^{+0.5}_{-0.5}$	$0.653^{+0.004}_{-0.002}$	$3.4^{+0.3}_{-0.3}$	164.66/116
14 (NEP2)+	$3.6^{+0.6}_{-0.8}$	$9.5^{+3.0}_{-2.7}$	$27.5^{+8.2}_{-7.7}$	$0.568^{+0.006}_{-0.004}$	$7.3^{+1.2}_{-1.1}$	$0.654^{+0.008}_{-0.006}$	$3.1^{+0.7}_{-0.7}$	56.93/51
14 (NEP2)–	$3.5^{+0.7}_{-0.8}$	$8.2^{+2.7}_{-2.7}$	$21.6^{+6.6}_{-6.7}$	$0.568^{+0.004}_{-0.004}$	$6.5^{+1.1}_{-1.0}$	$0.656^{+0.007}_{-0.008}$	$2.8^{+0.6}_{-0.6}$	55.44/51
15 (LL21)+	$4.5^{+0.5}_{-0.6}$	$8.3^{+1.4}_{-1.3}$	$27.1^{+7.6}_{-7.3}$	$0.570^{+0.005}_{-0.006}$	$6.4^{+0.9}_{-0.9}$	$0.652^{+0.010}_{-0.010}$	$2.2^{+0.5}_{-0.5}$	103.91/95
16 (LL21)–	$4.6^{+0.4}_{-0.6}$	$7.2^{+1.8}_{-1.5}$	$20.9^{+6.6}_{-6.2}$	$0.570^{+0.005}_{-0.006}$	$5.6^{+0.8}_{-0.7}$	$0.652^{+0.009}_{-0.010}$	$2.0^{+0.5}_{-0.4}$	106.30/93
16 (LL10)+	$2.6^{+0.6}_{-0.6}$	$1.6^{+0.7}_{-0.7}$	$10.6^{+5.5}_{-5.5}$	$0.554^{+0.018}_{-0.018}$	$1.7^{+1.3}_{-0.7}$	$0.642^{+0.021}_{-0.034}$	$0.5^{+0.3}_{-0.3}$	80.49/97
16 (LL10)–	$2.5^{+0.6}_{-0.6}$	$1.6^{+0.7}_{-0.7}$	$9.1^{+4.8}_{-4.9}$	$0.554^{+0.018}_{-0.017}$	$1.5^{+1.2}_{-0.7}$	$0.642^{+0.022}_{-0.036}$	$0.5^{+0.3}_{-0.3}$	80.37/87

[a] The absorption column densities for the CXB and TAE components were fixed to the values tabulated in Table E.2.
[b] The temperature of TAE and SWCX+LHB components were fixed to the best fit values tabulated in Table E.2. The O abundance of the both components was set to 0 in the fits.
[c] The unit is phtons $s^{-1}cm^{-2}\ keV^{-1}str^{-1}$@1keV.
[d] The emission measure integrated over the line of sight ,i.e. $(1/4\pi)\int n_e n_H ds$ in the unit of $10^{14}cm^{-5}\ str^{-1}$.
[e] Surface brightness in the unit of LU =phtons $s^{-1}\ cm^{-2}\ str^{-1}$.
[f] The centroid energy was fixed to O VIII Kα line energy to obtain the upper limit of the intensity.

Bibliography

Anders, E., & Grevesse, N. 1989, Geochim. Cosmochim. Acta , 53, 197

Bronfman, L., Cohen, R. S., Alvarez, H., May, J., & Thaddeus, P. 1988, ApJ, 324, 248

Clemens, D. P., Sanders, D. B., & Scoville, N. Z. 1988, ApJ, 327, 139

Cox, D. P. 1998, "The Local Bubble and Beyond", proceedings of IAU Colloquium 166, 113, 271

—. 2005, Annual Rev. A&A, 43, 337

Cravens, T. E. 1997, GeoRL , 24, 105

—. 2000, ApJ, 532, L153

—. 2002, Science , 296, 1042

Cravens, T. E., Robertson, I. P., Ledvina, S. A., Mitchell, D. G., Krimigis, S. M., & Waite, J. H. 2007, AGU Fall Meeting Abstracts, A1011+

Dickey, J. M., & Lockman, F. J. 1990, Annual Rev. A&A, 28, 215

Diplas, A., & Savage, B. D. 1991, ApJ, 377, 126

Ferrière, K. M. 2001, Reviews of Modern Physics, 73, 1031

Field, G. B., Goldsmith, D. W., & Habing, H. J. 1969, ApJ, 155, L149+

Freyberg, M. J. 1994, PhD thesis, , Technische Univ. München, (1994)

Fujimoto, R., Mitsuda, K., Mccammon, D., Takei, Y., Bauer, M., Ishisaki, Y., Porter, S. F., Yamaguchi, H., Hayashida, K., & Yamasaki, N. Y. 2007, PASJ, 59, 133

Garmire, G. P., Nousek, J. A., Apparao, K. M. V., Burrows, D. N., Fink, R. L., & Kraft, R. P. 1992, ApJ, 399, 694

Hasinger, G., Burg, R., Giacconi, R., Hartner, G., Schmidt, M., Trumper, J., & Zamorani, G. 1993, A&A, 275, 1

Henley, D. B., & Shelton, R. L. 2008, ApJ, 676, 335

Hurwitz, M., Sasseen, T. P., & Sirk, M. M. 2005, ApJ, 623, 911

Ishisaki, Y., Maeda, Y., Fujimoto, R., Ozaki, M., Ebisawa, K., Takahashi, T., Ueda, Y., Ogasaka, Y., Ptak, A., Mukai, K., Hamaguchi, K., Hirayama, M., Kotani, T., Kubo, H., Shibata, R., Ebara, M., Furuzawa, A., Iizuka, R., Inoue, H., Mori, H., Okada, S., Yokoyama, Y., Matsumoto, H., Nakajima, H., Yamaguchi, H., Anabuki, N., Tawa, N., Nagai, M., Katsuda, S., Hayashida, K., Bamba, A., Miller, E. D., Sato, K., & Yamasaki, N. Y. 2007, PASJ, 59, 113

Koutroumpa, D., Acero, F., Lallement, R., Ballet, J., & Kharchenko, V. 2007, A&A, 475, 901

Koutroumpa, D., Lallement, R., Kharchenko, V., & Dalgarno, A. 2008, ArXiv e-prints 0805.3212

Koutroumpa, D., Lallement, R., Kharchenko, V., Dalgarno, A., Pepino, R., Izmodenov, V., & Quémerais, E. 2006, A&A, 460, 289

Koyama, K., Tsunemi, H., Dotani, T., Bautz, M. W., Hayashida, K., Tsuru, T. G., Matsumoto, H., Ogawara, Y., Ricker, G. R., Doty, J., Kissel, S. E., Foster, R., Nakajima, H., Yamaguchi, H., Mori, H., Sakano, M., Hamaguchi, K., Nishiuchi, M., Miyata, E., Torii, K., Namiki, M., Katsuda, S., Matsuura, D., Miyauchi, T., Anabuki, N., Tawa, N., Ozaki, M., Murakami, H., Maeda, Y., Ichikawa, Y., Prigozhin, G. Y., Boughan, E. A., Lamarr, B., Miller, E. D., Burke, B. E., Gregory, J. A., Pillsbury, A., Bamba, A., Hiraga, J. S., Senda, A., Katayama, H., Kitamoto, S., Tsujimoto, M., Kohmura, T., Tsuboi, Y., & Awaki, H. 2007, PASJ, 59, 23

Krasnopolsky, V. A., Greenwood, J. B., & Stancil, P. C. 2004, Space Science Reviews, 113, 271

Kuntz, K. D., & Snowden, S. L. 2000, ApJ, 543, 195

Lallement, R. 2004a, A&A, 422, 391

—. 2004b, A&A, 418, 143

Lallement, R., Bertaux, J. L., & Dalaudier, F. 1985, A&A, 150, 21

Lisse, C. M., Dennerl, K., Englhauser, J., Harden, M., Marshall, F. E., Mumma, M. J., Petre, R., Pye, J. P., Ricketts, M. J., Schmitt, J., Trumper, J., & West, R. G. 1996, Science, 274, 205

Liu, H., & Lühr, H. 2005, JOURNAL OF GEOPHYSICAL RESEARCH, VOL. 110, A09S29, 108, 1300

Lockman, F. J. 1984, ApJ, 283, 90

Marshall, F. J., & Clark, G. W. 1984, ApJ, 287, 633

Masui, K., Mitsuda, K., Yamasaki, N. Y., Takei, Y., Kimura, S., Yoshino, T., & McCammon, D. 2008, ArXiv e-prints 0810.2035

McCammon, D., Almy, R., Apodaca, E., Bergmann Tiest, W., Cui, W., Deiker, S., Galeazzi, M., Juda, M., Lesser, A., Mihara, T., Morgenthaler, J. P., Sanders, W. T., Zhang, J., Figueroa-Feliciano, E., Kelley, R. L., Moseley, S. H., Mushotzky, R. F., Porter, F. S., Stahle, C. K., & Szymkowiak, A. E. 2002, ApJ, 576, 188

McCammon, D., Burrows, D. N., Sanders, W. T., & Kraushaar, W. L. 1983, ApJ, 269, 107

McCammon, D., & Sanders, W. T. 1990, Annual Rev. A&A, 28, 657

Miller, E. D., Tsunemi, H., Bautz, M. W., McCammon, D., Fujimoto, R., Hughes, J. P., Katsuda, S., Kokubun, M., Mitsuda, K., Porter, F. S., Takei, Y., Tsuboi, Y., & Yamasaki, N. Y. 2008, PASJ, 60, 95

Mitsuda, K., Fujimoto, R., Yamasaki, N. Y., Yoshino, T., Hagihara, T., Masui, K., Bauer, M., Takei, Y., McCammon, D., Wang, Q. D., & Yao, Y. 2007, Progress of Theoretical Physics Supplement, 169, 79

Morrison, R., & McCammon, D. 1983, ApJ, 270, 119

Nousek, J. A., Fried, P. M., Sanders, W. T., & Kraushaar, W. L. 1982, ApJ, 258, 83

Østgaard, N., Mende, S. B., Frey, H. U., Gladstone, G. R., & Lauche, H. 2003, Journal of Geophysical Research (Space Physics), 108, 1300

Pointecouteau, E., Arnaud, M., & Pratt, G. W. 2005, A&A, 435, 1

Rasmussen, J. 2007, New Astronomy Review, 51, 99

Revnivtsev, M., Gilfanov, M., Jahoda, K., & Sunyaev, R. 2005, A&A, 444, 381

Rosner, R., Avni, Y., Bookbinder, J., Giacconi, R., Golub, L., Harnden, Jr., F. R., Maxson, C. W., Topka, K., & Vaiana, G. S. 1981, ApJ, 249, L5

Sakamoto, T., Chiba, M., & Beers, T. C. 2003, A&A, 397, 899

Sanders, W. T., Burrows, D. N., McCammon, D., & Kraushaar, W. L. 1983, in IAU Symposium, Vol. 101, Supernova Remnants and their X-ray Emission, ed. J. Danziger & P. Gorenstein, 361–365

Savage, B. D., Sembach, K. R., Wakker, B. P., Richter, P., Meade, M., Jenkins, E. B., Shull, J. M., Moos, H. W., & Sonneborn, G. 2003, ApJS, 146, 125

Shimizu, M., Kitayama, T., Sasaki, S., & Suto, Y. 2006, PASJ, 58, 291

Smith, M. C., Ruchti, G. R., Helmi, A., Wyse, R. F. G., Fulbright, J. P., Freeman, K. C., Navarro, J. F., Seabroke, G. M., Steinmetz, M., Williams, M., Bienaymé, O., Binney, J., Bland-Hawthorn, J., Dehnen, W., Gibson, B. K., Gilmore, G., Grebel, E. K., Munari, U., Parker, Q. A., Scholz, R.-D., Siebert, A., Watson, F. G., & Zwitter, T. 2007a, MNRAS, 379, 755

Smith, R. K., Bautz, M. W., Edgar, R. J., Fujimoto, R., Hamaguchi, K., Hughes, J. P., Ishida, M., Kelley, R., Kilbourne, C. A., Kuntz, K. D., McCammon, D., Miller, E., Mitsuda, K., Mukai, K., Plucinsky, P. P., Porter, F. S., Snowden, S. L., Takei, Y., Terada, Y., Tsuboi, Y., & Yamasaki, N. Y. 2007b, PASJ, 59, 141

Smith, R. K., Edgar, R. J., Plucinsky, P. P., Wargelin, B. J., Freeman, P. E., & Biller, B. A. 2005, ApJ, 623, 225

Snowden, S. L., Egger, R., Finkbeiner, D. P., Freyberg, M. J., & Plucinsky, P. P. 1998, apj, 493, 715

Snowden, S. L., Egger, R., Freyberg, M. J., McCammon, D., Plucinsky, P. P., Sanders, W. T., Schmitt, J. H. M. M., Truemper, J., & Voges, W. 1997, ApJ, 485, 125

Snowden, S. L., McCammon, D., Burrows, D. N., & Mendenhall, J. A. 1994, ApJ, 424, 714

Snowden, S. L., McCammon, D., & Verter, F. 1993, ApJ, 409, L21

Strickland, D. K., Heckman, T. M., Colbert, E. J. M., Hoopes, C. G., & Weaver, K. A. 2004, ApJS, 151, 193

Sutherland, R. S., & Dopita, M. A. 1993, ApJS, 88, 253

Tanaka, Y., & Bleeker, J. A. M. 1977, Space Science Reviews, 20, 815

Tawa, N., Hayashida, K., Nagai, M., Nakamoto, H., Tsunemi, H., Yamaguchi, H., Ishisaki, Y., Miller, E. D., Mizuno, T., Dotani, T., Ozaki, M., & Katayama, H. 2008, PASJ, 60, 11

Toft, S., Rasmussen, J., Sommer-Larsen, J., & Pedersen, K. 2002, MNRAS, 335, 799

Tsyganenko, N. A., & Sitnov, M. I. 2005, Journal of Geophysical Research (Space Physics), 110, 3208

Tüllmann, R., Pietsch, W., Rossa, J., Breitschwerdt, D., & Dettmar, R.-J. 2006, A&A, 448, 43

Wang, Q. D., Yao, Y., Tripp, T. M., Fang, T.-T., Cui, W., Nicastro, F., Mathur, S., Williams, R. J., Song, L., & Croft, R. 2005, ApJ, 635, 386

Wilkinson, M. I., & Evans, N. W. 1999, MNRAS, 310, 645

Yamasaki, N. Y., Sato, K., Mitsuishi, I., & Ohashi, T. 2008a, Proceedings of Local Hot Bubble and beyond

—. 2008b, ArXiv e-prints 0809.0109

Yao, Y., & Wang, Q. D. 2007, ApJ, 658, 1088

Yao, Y., Wang, Q. D., Hagihara, T., Mitsuda, K., McCammon, D., & Yamasaki, N. Y. 2009, ApJ, 690, 143